Quantum coherence and correlations in photonic qubits and photoactive hybrid organometallic Perovskite systems

Thesis by
Carlos Andres Melo Luna

In Partial Fulfillment of the Requirements for the
degree of
Doctor in Natural Sciences-Physics, Dr. rer. nat

UNIVERSIDAD DEL VALLE, BAYREUTH UNIVERSITÄT
Cali-Colombia, Bayreuth-Germany

2019
Defended January 17th

Carlos Andres Melo Luna
ORCID: https://orcid.org/0000-0002-9204-7900

ACKNOWLEDGEMENTS

Nature behavior is hidden, in such a way we have to perform complicated procedures to know it into more gentle interpretation.

I would like to acknowledge to the Professors J. H. Reina and R. Hildner for its helpful advice and orientation during the development of this research. I want to remark the kindness and the valuable discussions with the EPIV group colleagues at Universität Bayreuth during my stay in Germany. Mainly to: Prof. Dr. J. Köhler, Werner Reichstein "Werni", Stefan Schlicht, Uwe Gerken, Kevin Wilma, Bern Wittmann, Christian Schörner, Sebastian Stäter, Sebastian Pickles, Dominic Raithel, Johannes Maier, Daniel Zalami, Carmen Wolfring, Caroline Reichel, Dominic Raithel, Alexander Löhner, Lisa Günther, Inga Elvers, and Sebastian Baderschneider. In the same direction, I say thanks to everyone which contribute to my professional formation from Universidad del Valle side as professors (mainly from the Physics Department) and colleagues (J. D. Perea, C. W. Sanchez, C. Susa, A. Ducuara, A. Gonzalez, J. Ordoñez, M. Quiñonez, D. Madrid, J. Cespedes, V. Lizcano, A. Perez, A. Barreiro, B. Diaz, C. Parra, G. Parra). Furthermore, I express gratitude to the financial support institutions as DFG (Deutsche Forschungsgemainschaft) Research Training group GRK1640 (Graduiertenkolleg 1640 Research Training Group 1640), Research grant (CT 015-2015 cod: 1106-658-42624, CI:71003) Colciencias (Departamento Administrativo de Ciencia, tecnología e innovación), and CibioFi (Research centre for bioinformatics and Photonics). Finally, I give special thanks to my friends (German-Colombians), my mother Lourdes, my sister Melissa and my girlfriend Angelica, which have contributed to my personal and moral formation and were fundamental to finishing this work supporting me in any circumstance.

ABSTRACT

The past two decades have witnessed tremendous advances and breakthroughs in quantum information science and technology, due mainly to the use of quantum physical resources such as coherence and entanglement. The formalization of the concept of universal quantum computing by D. Deutsch in 1985 has matured into commercial initiatives that aim to accelerate the physical implementation of a practical quantum computer. So far, such quantum technology has been pushed forward as information processors that are mainly on superconducting quantum bits (qubits) based. Other developments make use of quantum states of photons in conjunctions with other quantum registers based on electrons, atoms, molecules, artificial systems, between others. Although in any case, multiple qubit technologies are still under intense research and developments and the temperature and size of the quantum register are essential issues. However, all possible physical implementation of quantum information processing devices have in common the fundamental properties of quantum systems: interference, coherence, and entanglement.

In this thesis, we concerned the study of quantum coherence and entanglement in qubits (encoded on the polarisation basis) and quantum materials (operating at room temperature) to analyze the role of quantum correlations and decoherence for information processing purposes. The current research is divided into two main parts, the first one begins with the analysis of the influence of a birefringent medium over the entanglement of a photonic qubit state. We employ a polarisation maintaining fiber (PMF) as a decohering environment to test the theoretical model in which the symmetry of the coupling between the qubit and environment defines the death and revival of the information correlations. This finding establishes a tool to keep the entanglement independent of the fiber length employing the symmetry properties of the physical system.

Additionally, to demonstrate that the entanglement is not the only crucial factor in information schemes, we employ the prisoner's dilemma game (in a two parameters strategy space and extended up to three) to evidence that quantum advantages in this protocol are by the quantum superposition instead of the entanglement of the physical system. Here we also pose an experimental setup with photons to verify our findings with photonic qubits.

The second part of the thesis examines a novel nanomaterial which could serve up

a bridge to the interaction of photons and electrons toward a physical representation of photonic qubits conditioned by external registers (as electrons or ions). The first stage in this direction considers the implementation of single photon emitters. However, previous to it is necessary to recognize the photophysical capabilities of the Perovskites as structure selected. As a complement, the novelty of this nanostructure allow us to give answers to some open questions in this characterization direction in the frame of this research.

The MA-halide (*methylammonium-halide*) perovskites are structurally composed by small domains which ranging from nano to micrometer sizes presenting strong photoluminescence intermittency (blinking). We attribute this response to the Auger-nonradiative recombination of additional electrons photogenerated in a trap-filling process due to defects or ion movement. We verified this through the application of an absorbing layer (quencher) of charges of PCBM (Phenyl-C61-butyric acid methyl ester) resulting in considerably decreases in blinking. We also provide a novel technique for real-time observation of the ion movement effect over this material. Additionally, this behavior indicates appropriate conditions for the existence of a few emitters which are useful in quantum protocols and become a motivation to analyze and explain this phenomenon. Then, we prepare two chemical compositions of inorganic Perovskites with a high structural order to explore the necessary conditions to produce single emitter with this material. We visualized the samples through electron microscopy, and both systems were spectrally characterized decreasing dilutions up to observe emission intermittency. We verified the nonclassical behavior of the emission employing a Hanbury Brown-Twiss interferometer by measuring the degree of the second-order coherence correlation function. Finally, but not less important, the additional information presents the laboratories implemented during this doctoral research and the prototype of signals counting device to analyze temporal coincidences in correlated photonic events.

RESUMEN

Las últimas dos décadas han sido testigos de tremendos avances y desarrollos en la ciencia y tecnología de la información cuántica, debido principalmente al uso de recursos físico-cuánticos, tales como la coherencia y el entrelazamiento. La formalización del concepto de computación cuántica universal por D. Deutsch en 1985 ha madurado hacia iniciativas comerciales que apuntan a acelerar la implementación física de una computadora cuántica práctica. Hasta ahora, dicha tecnología cuántica se ha impulsado como procesadores de información que se basan principalmente en bits cuánticos (qubits) superconductores. Otros desarrollos hacen uso de los estados cuánticos de los fotones en conjunción con otros registradores cuánticos basados en electrones, átomos, moléculas, sistemas artificiales, entre otros. Aunque, para cualquier caso, las tecnologías de qubit múltiples aún están bajo intensa investigación y desarrollos en los que la temperatura y el tamaño del registrador cuántico son cuestiones esenciales. Sin embargo, toda posible implementación física de dispositivos de procesamiento de información cuántica tiene en común las propiedades fundamentales de los sistemas cuánticos: interferencia, coherencia y entrelazamiento.

En esta tesis, tratamos el estudio de la coherencia cuántica y el entrelazamiento en qubits (codificados en base a la polarización) y los materiales cuánticos (que operan a temperatura ambiente) para analizar el papel de las correlaciones cuánticas y la decoherencia para fines de procesamiento de información. La investigación actual se divide en dos partes principales: la primera comienza con el análisis de la influencia de un medio birrefringente sobre el entrelazamiento de un estado de qubit fotónico. Empleamos una fibra que mantiene la polarización (PMF) como un entorno de decoherencia para probar el modelo teórico en el que la simetría del acoplamiento entre el entorno y el qubit define la muerte y reactivación de las correlaciones de información. Este hallazgo establece una herramienta para mantener el entrelazamiento independiente de la longitud de la fibra empleando las propiedades de simetría del sistema físico.

Como complemento, para demostrar que el entrelazamiento no es el único factor crucial en los esquemas de información, empleamos el juego del dilema del prisionero (en un espacio de estrategia de dos parámetros y extendido hasta tres) para demostrar que las ventajas cuánticas en este protocolo son debido a la superposición cuántica en lugar del entrelazamiento del sistema físico. Aquí también presentamos

una configuración experimental con fotones para verificar nuestros hallazgos con qubits fotónicos.

La segunda parte de la tesis examina un nuevo nanomaterial que podría servir de puente para la interacción de fotones y electrones hacia una representación física de qubits fotónicos condicionados mediante registros externos (como electrones o iones). La primera etapa en esta dirección considera la implementación de emisores de fotones individuales. Sin embargo, antes de esto es necesario reconocer las capacidades fotofísicas de las Perovskites como estructura seleccionada. Como complemento, la novedad de esta nanoestructura nos permite dar respuestas a algunas preguntas abiertas en esta dirección de caracterización en el marco de esta investigación.

Las perovskitas de MA-haluro (*metilamonio-haluro*) están estructuralmente formadas por pequeños dominios que van desde tamaños de nano a micrómetros y que presentan una fuerte intermitencia de fotoluminiscencia (Blinking). Atribuimos esta respuesta a la recombinación noradiativa de Auger de electrones adicionales fotogenerados en un proceso de relleno de trampas ocasionadas por defectos o móvimiento de iones. Esto lo verificamos mediante la aplicación de una capa absorbente (quencher) de cargas de PCBM (fenil-éster metílico del ácido butírico C61), lo que resultó en una disminución considerable del parpadeo. También proporcionamos una técnica novedosa para la observación en tiempo real del efecto del movimiento de iones sobre este material. Adicionalmente, este comportamiento indica condiciones adecuadas para la existencia de pocos emisores que son útiles en protocolos cuánticos y se convierten en una motivación para analizar y explicar este fenómeno. Luego, preparamos dos composiciones químicas de perovskitas inorgánicas con un alto orden estructural para explorar las condiciones necesarias para producir un emisor cuántico con este material. Visualizamos las muestras a través de microscopía electrónica, y ambos sistemas se caracterizaron espectralmente para disminuir las diluciones hasta observar la intermitencia de la emisión. Se verificó el comportamiento no clásico de la emisión empleando un interferómetro Hanbury-Brown y Twiss mediante la medición del grado de función de correlación de coherencia de segundo orden. Finalmente, pero no menos importante, la información adicional presenta los laboratorios implementados durante esta investigación doctoral y el prototipo de un dispositivo de conteo de señales para analizar las coincidencias temporales en eventos fotónicos correlacionados.

ZUSAMMENFASSUNG

In den letzten beiden Dekaden wurden sehr große Fortschritte und Durchbrüche auf dem Gebiet der Quanteninformationstechnologie erzielt, was auf die Ausnutzung quantenphysikalischer Eigenschaften, wie zum Beispiel Kohärenz und Verschränkung, zurückzuführen ist. Im Jahr 1985 entwickelte D. Deutsch das formale Konzept eines universellen Quantencomputers, das mittlerweile von kommerziellen Initiativen aufgegriffen wurde mit dem Ziel, die physikalische Implementierung eines funktionsfähigen Quantencomputers voranzutreiben. Bislang werden hauptsächlich supraleitende Quantenbits (Qubits) als Grundlage für den Prozessor eines Quantencomputers eingesetzt. Alternative Entwicklungen nutzen Quantenzustände von Photonen aus in Verbindung mit Quantenregistern, die auf Elektronen, Atomen, Molekülen, etc. basieren. Da die Arbeitstemperatur und die Größe der Quantenregister wesentliche Gesichtspunkte für die weitere Entwicklung sind, werden solch unterschiedliche Ansätze für die Implementierung von Quantenprozessoren weiter intensiv untersucht. Trotz dieser verschiedenen physikalischen Implementierungen basieren alle Ansätze auf den fundamentalen Eigenschaften von Quantensystemen, d.h. auf Interferenz, Kohärenz und Verschränkung.

Diese Arbeit beschäftigt sich mit der Untersuchung von Quantenkohärenz und Verschränkung von Qubits (hier die Polarisationszustände von Photonen) und von Quantenmaterialien (bei Raumtemperatur), um die Rolle von Quantenkorrelationen und Dekohärenz für die Quanteninformationsverarbeitung besser zu verstehen. Im ersten Teil der Arbeit wird analysiert, wie ein doppelbrechendes Medium die Verschränkung eines photonischen Qubits beeinflusst. Eine polarisationserhaltende Faser stellt hier eine Umgebung bereit, die Dekohärenz induziert. Damit konnten wir ein theoretisches Modell testen, in dem die Symmetrie der Wechselwirkung zwischen dem Qubit und der Umgebung die Vernichtung und das Wiederaufleben von Informationskorrelation bestimmt. Durch das Ausnutzen dieser Symmetrie konnten wir zeigen, dass die Verschränkung unabhängig von der Faserlänge erhalten werden kann. Ergänzend dazu konnten wir anhand des Gefangenen-Dilemma-Spiels demonstrieren, dass Verschränkung von Qubits nicht der einzige wesentliche Faktor in Quanteninformationstechnologien ist, sondern dass auch Quantensuperposition einen Vorteil in der Quantenversion des Gefangenen-Dilemma-Spiels bietet. Im Rahmen dieser theoretischen Arbeit entwickelten wir auch einen Vorschlag für die experimentelle Umsetzung dieses Spiels mit Hilfe photonischer Qubits.

Im zweiten Teil dieser Arbeit wurde ein neues Material – Nanostrukturen so genannter (metallorganischer) Perovskite – untersucht, das eine Brücke zwischen photonischen und elektronischen Realisierungen von Qubits schlagen könnte. Der erste Schritt in dieser Richtung ist die Implementierung einer Einzelphotonenquelle basierend auf diesen neuen Materialien. Zunächst wurde aber ein tieferes Verständnis der photophysikalischen Eigenschaften dieser hier untersuchten Methylammonium-halid Perovskite entwickelt und einige diesbezüglich offene Fragestellungen beantwortet.

Filme aus Methylammonium-halid Perovskiten sind strukturell aus Domänen kleiner Einkristalle aufgebaut, deren Größe von Nanometern bis zu einigen Mikrometern reicht. Diese Domänen zeigen starke Photolumineszenz-Intermittenz, die auf nicht-strahlende Auger-Rekombination mit zusätzlichen photogenerierten Ladungen zurückzuführen ist. Dieser Effekt konnte durch das Aufbringen eines "Quencher"-Films aus dem C_{60}-Derivat PCBM verifiziert werden. Durch Elektronentransfer zum PCBM wird die Dichte der Ladungen im Perovskit-Film reduziert, was die Intermittenz signifikant reduziert. In diesem Zusammenhang entwickelten wir auch einen neuen Ansatz, um die Bewegung von Ionen im elektrischen Feld im Perovskit in Echtzeit zu verfolgen.

Das Auftreten der Intermittenz in Perovskit-Filmen war ein klarer Hinweis, dass Perovskit-Nanostrukturen grundsätzlich als Einzelphotonenquelle in Frage kommen und für Quantenprotokolle eingesetzt werden können. Daher untersuchten wir dieses Phänomen an zwei chemisch unterschiedlichen anorganischen Perovskit-Nanokristallen mit hoher struktureller Ordnung. Basierend auf elektronenmikroskopischen und spektralen Messungen, reduzierten wir die Konzentration der Nanokristalle, bis wir auch in diesem System Intermittenz beobachten konnten. Das nicht-klassische Verhalten der Emission wiesen wir durch die Messung der Kohärenz-Korrelationsfunktion zweiter Ordnung durch ein Hanbury-Brown-Twiss Interferometer nach.

Den Abschluss dieser Arbeit bildet die Beschreibung der Messplätze in neuen Laboren an der Universidad del Valle in Cali, die im Rahmen dieser Arbeit realisiert wurde. In diesem Zusammenhang wurde auch ein Prototyp eines Photonenzählers entwickelt, der zum Nachweis zeitlicher Koinzidenzen bei korrelierter Photonenemission dient.

PUBLISHED CONTENT AND CONTRIBUTIONS

[1] Carlos Andres Melo-Luna, Cristian E. Susa, Andrés F. Ducuara, Astrid Barreiro, and John H. Reina. “Quantum Locality in Game Strategy”. In: *Sci. Rep.* 7 (2017), pp. 1–11.

[2] Cheng Li, Yu Zhong, Carlos Andres Melo-Luna, Thomas Unger, Konstantin Deichsel, Anna Gräser, Jürgen Köhler, Anna Köhler, Richard Hildner, and Sven Huettner. “Emission Enhancement and Intermittency in Polycrystalline Organolead Halide Perovskite Films”. In: *Molecules* 21 (2016), p. 1081.

[3] Cheng Li, Antonio Guerrero, Yu Zhong, Anna Gräser, Carlos Andres Melo-Luna, Jürgen Köhler, Juan Bisquert, Richard Hildner, and Sven Huettner. “Real-Time Observation of Iodide Ion Migration in Methylammonium Lead Halide Perovskites”. In: *Small* 1701711 (2017), pp. 1–10.

[4] Carlos Andres Melo-Luna and John H. Reina. “Experimental quantum control of entangled photonic qubits under decoherence”. to be submitted. 2018.

[5] Carlos Andres Melo-Luna, M. Ritter, R. Hildner, J. Köhler, Stephan Förster, and John H. Reina. “Trihalide Perovskite Quantumdots as a Reliable Quantum Source”. to be submitted.

[6] Erick Ipus, Carlos Andres Melo-Luna, Luis Giraldo, Otto Vergara, and John H. Reina. “Implementation of a Cost-Efficient Device for Wireless Photon Coincidence Detection”. to be submitted, arXiv:1706.04927. 2018.

TABLE OF CONTENTS

LIST OF ILLUSTRATIONS

LIST OF TABLES

Chapter 1

BACKGROUND

1.1 Quantum Information

Information is physical, and as such, its manipulation, its storage, and its reading convey physical processes. Since the physical world is described ultimately by the fundamental laws of quantum theory, the basics of information theory and computer science appear naturally linked to quantum mechanics [1, 2]. The first approach to this statement seems to be a seminal theoretical work in 1935 by Einstein, Podolsky and Rosen-EPR [3] which considered a particular quantum state in a two-particle Hilbert space. The particles appear related in some weird fashion- or *verschränkung*, a term used by *Schrödinger* and translated from German to English as "*entanglement*"- that implies an incomplete description of the reality by the wave-function of quantum mechanics or the impossibility of a simultaneous reality for both particles giving rise to the so-called "EPR paradox". In fact, from the information theory point of view, this would imply an infinite speed for the information transmission [4–6].

Later in 1959 in a celebrated talk [7], Richard Feynman would introduce the concept of miniaturization within the scope of manipulating information in the scale of angstroms. And over two decades later [8], Feynman provided a description of information quantities in the frame of the quantum mechanics, allowing the use of the phenomena of quantum superposition within a novel information scheme. This description gives an advantage over the classical counterpart of the information, as first formalized by David Deutsch in 1985 in his quantum computing seminal work [9].

In 1964 John Bell [10], confronting the main argument proposed by the EPR paper, established a theorem that settled the discussion raised by EPR on the realism and the non-locality implied by the quantum theory. In the language of information theory [2], we introduce quantum states that represent a two-state system, the so-called quantum bits or "qubits". If $|0\rangle$ and $|1\rangle$ denote the fundamental and excited state of a qubit (two-level) system, respectively, the Bell states (or "EPR pairs") stated in

Bell's theorem [10] denote the set of four maximally entangled quantum states [2]:

$$|\Psi^{\pm}\rangle \equiv \frac{|00\rangle \pm |11\rangle}{\sqrt{2}}, \qquad |\Phi^{\pm}\rangle \equiv \frac{|01\rangle \pm |10\rangle}{\sqrt{2}}.$$

Clauser and collaborators [11] were the first to achieve a formal description of Bell's theorem, a form of Bell inequalities that proposed a method to evaluate the relationship between realism and locality.

Over a century ago, the fundamentals of quantum physics were established, but their interpretation, from the information/thermodynamics point of view, goes back only three decades. The non-locality, a conceptual cornerstone of quantum physics, proposes the interaction capability between spatially separated systems, without any intermediate mechanism [10], in clear contrast with the original EPR argument [3]. This concept has been precisely the physical resource that has allowed the development of protocols for quantum computing and communication, which are of fundamental interest to problems that appear irresolvable from the classical point of view, and propose a paradigm for the development of the future quantum technologies [2]. Such a development of novel technologies for the processing of quantum information has made possible the implementation of counterintuitive protocols such as quantum teleportation [2, 12] and quantum cryptography [2, 13, 14]. In this sense, these protocols require the control of the initial quantum state of the system under study in which, moreover, it is crucial to understand and model the dynamics to predict the state after interactions within the protocol. In this scheme of thought, a helpful tool to evaluate and quantify the dynamics followed by photonics and molecular systems are the quantum information correlations.

Findings in quantum optics take photons as robust candidates for the physical realization of qubits, because they are charge-less, can be guided for long distances using optical fibers, and can address the matter with great precision [15]. Furthermore, the polarisation of a photon beam is a quantum mechanical two level system which can be controlled and measured [16]. However, the inconvenient inability to completely isolate the physical system from its environment makes necessary to consider the decoherence processes which contribute to the deterioration of the quantum computing tasks [17]. Through the dynamics of classical [18], quantum correlations [19], and entanglement [20], the interactions involved in such process can be revealed. The understanding of the dynamical processes followed by these quantities opens up new perspectives in the search for efficient quantum information processing and novel quantum materials to optimize the robustness of the communication and measurement protocols.

Quantum entanglement [3, 21–23], and, in general, quantum correlations, reveal physical properties as manifestations of purely quantum features of multipartite systems. These correlations have received a great deal of attention within the scientific community because they are at the core of the physical implementation of quantum protocols and quantum nanotechnology development, which involve transdisciplinary features like quantum optics, molecular and atomic physics, condensed matter, quantum information science, and some branches of engineering [24], to name a few.

The Swedish Academy also acknowledged the importance of these quantum control processes, and in 2013 the Nobel Prize for Physics went to S. Haroche and D. J. Wineland, for their "ground-breaking experimental methods that enable measuring and manipulation of individual quantum systems" [25]. Haroche and Wineland designed and demonstrated the control of individual photons and atoms (qubits) in systems allocated within optical cavities and ion traps. These experimental advances opened the path in the search for the physical realization of controlled quantum systems with direct applications to information theory. However, the impossibility to reach the perfect isolation of the quantum system from its environment induces a process of decoherence [26] which modifies the correlation dynamics in a non-trivial way [15, 21, 26, 27].

After the physical demonstration of entangled photons emitted by atomic cascades [28], a couple of (now celebrated) experiments demonstrated the violation of Bell inequalities [29, 30]. In this context, two main facts marked the last two decades of the twentieth century [31]. First, the violation of the Bell inequalities was demonstrated experimentally, not only for internal variables like the spin of particles but also for external variables like the position, momentum, energy and time [30, 32, 33]. Second, a new kind of photons source based on the spontaneous parametric down conversion (SPDC) process was employed [34]. These advances in quantum optics were, in some way, away from the information theory developments until 1985, when Deutsch traveled through the laws of quantum mechanics to create a robust vision of the Church-Turing thesis [2].

Currently, in the experimental realization of quantum protocols and algorithms achievements in the field of quantum information are used, e.g., the accomplishment of the quantum key distribution between a satellite and a station on earth [35]. However, it is necessary to increase the control of the quantum systems to use it as the computing hardware. The success of this goal depends on the stability of the

controlled quantum systems, and the capacity to prepare the desired quantum state, in this direction, different physical systems have been explored, e.g., metallic bulk materials [36], defect-centers in diamonds [37], superconducting flux and charge quantum circuits [24], trapped ions and quantum dots [24], just to cite but a few.

1.2 Motivation

The current developments in quantum information have been limited by challenges such as scalability or information lost. In this research, we explore features of losing coherence and correlations as the causes of the problems above-mentioned, and the needed of the entanglement as an essential resource in quantum communications. Concisely, **the general aim of this doctoral project is to evaluate experimentally by means of single-molecule spectroscopy for organic photoactive perovskites and by quantum tomography for entangled photons, decoherence mechanisms and the suitability of such nanostructure and photonic qubits for quantum information processing**.

Quantum decoherence processes have been widely studied theoretically [38]. Experimentally, the dynamics of decoherence has been studied using different physical systems such as molecular magnets [39], single trapped ions [40], and photons [15, 16]. In photonics systems, in particular, it has been possible to demonstrate the existence of decoherence-free subspaces [41] and to simulate decoherence channels characterized by amplitude [42], and phase damping [43]. All these studies use the polarisation of photons to track the processes of decoherence induced by the coupling of the frequency or space variables with the environment [44].

Quantum correlations apart from entanglement (e.g., quantum discord) can be crucial in the performance of quantum computing tasks [45]. In this context, computational protocols like the "deterministic quantum computation with one pure qubit" (DQC1) proposed by Knill and LaFlamme [46] involve mixed states and have the quantum discord as an essential feature in the speed up of quantum computing processes. However, it is plausible to prove in some scenarios that even in the absence of discord and entanglement, the quantum properties as the quantum superposition offers advantages over the classical computing analog [47]. This last suggests further alternatives to the search of reliable quantum computer hardware [2].

In this sense, this thesis searches specifically:

1. To verify theoretically the importance of the physical resources as the entanglement and coherence in the control of quantum information tasks for physical bipartite systems as photons pairs.

2. To investigate experimentally novel physical representation of qubits as organic-inorganic perovskites due to its well defined geometry and highly efficient electronic structure.

1.3 Synopses of thesis chapters

This doctoral research plan is two-fold and addresses two complementary physical aspects developed resolving some questions through the chapters. Each chapter is self-content regarded to the theoretical descriptions. However, *Chapter 1* briefly describes the photons and nanostructures as qubits with a general description about both the experiments already performed, and the physical capabilities of the perovskite structures that made this material as a candidate for a novel quantum system to be explored in the quantum information sense.

The **Part I** is focussed on the understanding of photon correlations and composed by Chapter 2 and Chapter 3. In this first part, in the *Chapter 2*, we propose an all-optical setup that allows the experimental exploration of the dynamics control of correlations under decoherence, and the basic quantum information tasks to digging deeper into the answer to: can be the photon correlations controlled through the symmetry of the environment coherence?. The *Chapter 3* in the same line explores the nonlocality properties considering a particular scheme of "game theory" called the Prisoners' Dilemma through the analysis of information correlations. There, we verify that the advantages offered by the quantum attributes are not due to entanglement but the quantum superposition [47].

The first step for a novel physical representation of qubits comprises finding proper material able to control the dynamics of a quantum system (electrons) through the interaction with another one (photons). In this respect, an alternative to the above approach mentioned is to identify and use atomic, molecular or nanostructured systems that can serve as building blocks for quantum hardware [24, 48]. This situation motivates the **Part II: coherence and correlations in perovskite systems**, of the present doctoral research which consists of Chapters 4 and 5. We propose the use of organic-metallic and full-metallic halide perovskite systems due to the well defined geometric structure as an alternative to address the scalability problem in quantum information protocols. These system has been studied in the research

group of Prof. Dr. Richard Hildner associated to Prof. Dr.Jürgen Kühler's research group at the University of Bayreuth (*EPIV-Experimental Physics IV- Lehrstuhl für Spektroskopie weicher Materie*) [49–53]. *Chapter 4* answers the question: why the perovskite structures exhibit photoluminescence intermittency at interacting with coherent light?. Additionally, we explore the dependence of the light-matter interaction process with external electric fields, constituting the first step toward the understanding of interacting photon-electron systems. Finally, *Chapter 5* defines a protocol for the production of single photon emitters with the perovskite structure, answering questions such as: could be used the blinking an indicator of single emitters?. What are the parameters to control the single emission?.

1.4 Thesis contributions

We published the following articles during the development of this thesis: [47, 52, 53]. Although the additional content has been prepared to be submitted and helpfully published: [54–56]. This thesis has contributed to the "Quantum information theory" as follows:

- It evaluates the use of the coherence as a physical resource to keep the physical system without losing the quantum state information.
- It confirms that the entanglement is not the essential correlation in a particular quantum algorithm.
- It gives physical insight into the photophysical behavior of photon-electron interaction in a Perovskite structure.
- It evaluates the material ability as single photons emitter through the degree of second-order coherence $g^2(\tau)$ to produce quantum physical systems employed in quantum information tasks.

1.5 About source employed

This thesis discusses the coherence and correlation problems in photonic qubits and searches a discrete way to create them in an electro-active physical system (perovskites). This document is the summary of research works previously published as in Chapter 3 and 4 most of the used content comes from the published papers. Chapter 3 uses the information published in [47] developed at "Universidad del Valle", and Chapter 4 is a mixture of [52, 53] wrote at "Universitaet Bayreuth".

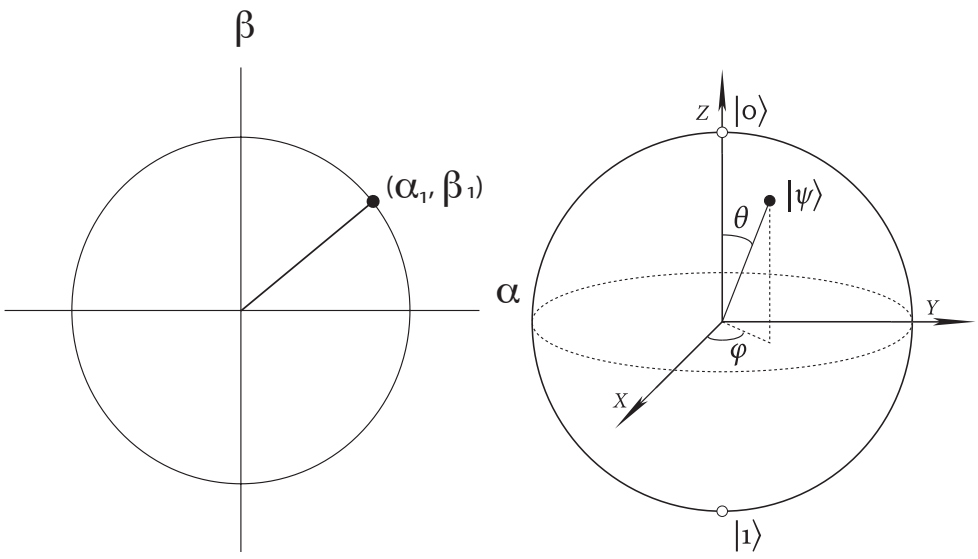

Figure 11: *Fundamental units of classical and quantum information:* a) classical "bit" represented as the geometrical results after taking all the possible values for α and β and plot it as the vector (α_1, β_1). In similar way, b) the qubit plot with all possible values of parameters θ and ϕ in the vector representation $|\psi\rangle \equiv \cos(\theta/2)|0\rangle + e^{i\phi}\sin(\theta/2)|1\rangle$, this sphere is known as the Bloch sphere in quantum mechanics [58].

1.6 Qubits and physical systems

The current chapter presents some fundamental concepts in quantum information to contextualize this document. Establishing first, the definition of a *qubit* and its formalism, after including a brief explanation of the locality and non-locality of quantum states, and finally closing this conceptual clarification with some considerations from other authors about the creation of states in photonic and molecular systems.

A *bit* is a primary unit in the classical computation and information scheme. In probability theory, it is possible to describe a "bit" as the state with probability p of equaling 0, and $1-p$ of being 1. Now, considering the bit as a vector (α, β) in which $\alpha^2 + \beta^2 = 1$, the complete set of this vectors form a circle, shown in the Fig.11 [57]. If we encode the classical bit into the simplest quantum system, a two-level system, we obtain:

$$0 \rightarrow |0\rangle, \quad 1 \rightarrow |1\rangle. \tag{1.1}$$

So far, we have used the Dirac notation to describe the fundamental states of a two-level system and the quantum theory establish that the above states are not the only possible states for these systems. Because, the linearity of the quantum theory

it allows arbitrary superpositions of the above two states. Then, using the inherited features from the two-level systems with the rules of linear algebra in a Hilbert space, this superposition can be expressed as follow:

$$|\psi\rangle \equiv \alpha|0\rangle + \beta|1\rangle = \begin{bmatrix}\alpha \\ \beta\end{bmatrix} \tag{1.2}$$

A subtle change to consider is the introduction of *probability amplitudes* instead of probabilities. This allows that α and β can be now complex numbers but not only real positives. Preserving this perspective, suppose the probability amplitudes as complex numbers in the following way:

$$\alpha = r_0 e^{i\phi_0}, \qquad \beta = r_1 e^{i\phi_1}. \tag{1.3}$$

Factoring out the phase $e^{i\phi_0}$ from both α and β, we achieve a physically equivalent to the state (1.2). Because, at the moment to measure any of those states we get the same physical result, and now reads:

$$|\psi'\rangle \equiv r_0|0\rangle + r_1 e^{i(\phi_1-\phi_0)}|1\rangle, \tag{1.4}$$

where $|\psi\rangle = |\psi'\rangle$ because of the equivalence mentioned above. Defining $\phi = \phi_1 - \phi_0$, $\in [0, 2\pi]$, and recalling the constraint $|r_0|^2 + |r_1|^2 = 1$, it is possible to parametrise the values of r_i in terms of one parameter θ arising from $r_0 = \cos(\theta/2)$ and $r_1 = \sin(\theta/2)$. Getting finally the general form of a *qubit*:

$$|\psi\rangle \equiv \cos(\theta/2)|0\rangle + e^{i\phi}\sin(\theta/2)|1\rangle. \tag{1.5}$$

In this sense, drawing all the possible values for θ and ϕ we arrive to the geometrical representation of a qubit as shown in Fig.11. A special mention here is that the definition arose so far, is a quantitative concept, hence, any physical two-level system could be, in principle, use as a qubit. However, in order to achieve the physical realization, additional requirements have to be fulfilled. The first point to accomplish by the physical qubits is to be controllable, i.e., the system should allow being prepared in the wanted initial state, freely evolve as the user needs, and be enabled to measure the output final quantum state after the evolution. The second aspect to consider, pose the existence of external interactions acting as unitary operators over the evolution of the system following a computational logic, known as *logic gates* [2]. Following these statements, other authors explored through different physical systems that could fulfill the mentioned requirements. Some of the first systems to be tested were the *photons*, entangling the first pair with high

intensity in 1995 by P.Kwiat et al. [59]. This system offered stability and versatility to create quantum states with different degrees of entanglement [60], and to probe the entanglement features [41–43, 61–65]. Also, it allows testing various quantum protocols such as teleportation [66], cryptography [67], factorization algorithm [68], multipartite state prepared employing up to 10 entangled qubits [69], and quantum key distribution [70, 71]. Currently, this is the ideal system to probe novel ideas about quantum information. However, the main difficulty to address is the scalability, in the sense of generating as many controllable and differentiable quantum states as the amount of processed information requires it. In this way, also has been researched QED Cavities [72–76], NMR systems [77–82], optical lattices and Bose-Einstein condensates [83, 84], and quantum dots [85, 86]. Even ion traps which due to the degree of control realized by David J. Wineland *et al.* and Serge Haroche *et al.* awarded the Nobel prize in 2012 [87, 88]. Because the central objective of the current chapter is not digging deeper into the detail about the qubits physical realization, hence, the principal achievements in this direction were introduced with some of the corresponding references, suggested as further readings.

1.7 Local and nonlocal quantum states

Most of the protocols in quantum information require multipartite systems, then whole states of quantum systems will depend on the subsystem states and even more on the *correlations* between each part of the quantum set. The nonlocality concept was implicitly introduced by Einstein, Podolsky, and Rosen in their famous EPR paper [3], and formalized time after by J. Bell in 1964 [10] in the form of an inequality independent from any physical theory [89]. This inequality was able to demonstrate the nonlocality of the two-level states as presented in Appendix A.1. Complementary, an extensive method posed by Clauser-Horne-Shimony-Holt (CHSH) defined an inequality for any set of dichotomic variables, and if the principle of local causes is valid, it establishes an upper limit to the correlation of distant events [11, 89], the formal description of this tool is given in Appendix A.

Then, any state ρ which violate these inequalities will be considered as *nonlocal* else will be *local*. In such a way, it is known that the nonlocality for multipartite pure states is equivalent to the entanglement [90–92],i.e., every nonlocal state as the states of Eq. 1.1 is entangled, known as the EPR's states or Bell's states. Nonetheless, this is not fulfilled by the mixed states as the entangled local states, in the following, some examples of this kind are presented:

Werner states

The first class of Werner states to consider is the called *Werner-Isotropic* The name isotropic is related with the two-qubit version of this state proposed by Werner in 1989 [93] which reads:

$$\rho_{WI}(p) = p|\psi_-\rangle\langle\psi_-| + \frac{(1-p)}{4}\mathbb{1}, \tag{1.6}$$

where $0 \leq p \leq 1$, and $|\psi_-\rangle := \frac{1}{\sqrt{2}}(|01\rangle - |10\rangle)$. This is a mixture state which combines a maximum entangled part with a non-entangled mixture in such a way that a parameter p defines the amount of entanglement, if $p = 0$ we get the pure entangled state $|\psi_-\rangle$ but else if $p = 1$ results a diagonal state different from the unity only by a scalar. This state was also proposed for a bipartite system bigger than two-level is the so-called two-qudit[1] *Werner state* defined as:

$$\rho_W^d(p) = \frac{p}{d(d-1)}2P_{anti} + \frac{(1-p)}{d^2}\mathbb{1}, \tag{1.7}$$

with $1 - \frac{2d}{d+1} \leq p \leq 1$, and $P_{anti} := \frac{1}{2}\left(\mathbb{1} - \sum_{ij}^{d} |i\rangle\langle j| \otimes |j\rangle\langle i|\right)$. Those states were posed as an explicit example to demonstrate that a classically correlated quantum system does not satisfy the generalized Bell's inequalities and currently constitutes a new family of states known as *mixed entangled local states*[93].

These states in its two-qubit version are called as Werner-Isotropic states and will lead to:

$$\rho_W I(p) = p|\psi^-\rangle\langle\psi^-| + \frac{(1-p)}{4}\mathbb{1}, \tag{1.8}$$

where $0 \leq p \leq 1$, and $|\psi_-\rangle := \frac{1}{\sqrt{2}}(|01\rangle - |10\rangle)$.

Werner-like states

Isotropic states

Time after following the assumptions of Werner and defining the generalised state for singlet, M. Horodecki & P. Horodecki proposed the isotropic states defined as [94]:

$$\rho_I^d(p) = p|\psi_d\rangle\langle\psi_d| + \frac{(1-p)}{d^2}\mathbb{1}, \tag{1.9}$$

considering $0 \leq p \leq 1$ and $|\psi_d\rangle := \frac{1}{\sqrt{2}}\sum_{i=1}^{d} |ii\rangle$.

[1] qudit is a physical system compose by two systems of d-levels each one.

Hirsch states

In 2013 Hirsch, Quintino, Bowles and Brunner [95] analysed the two-qubit state which holds:

$$\rho_F(p,q,\sigma) = p|\psi^-\rangle\langle\psi^-| + (1-p)\left[q\sigma + (1-q)\frac{\mathbb{1}}{2}\right] \otimes \frac{\mathbb{1}}{2}, \tag{1.10}$$

where $0 \leq p \leq 1$, $0 \leq q \leq 1$, $|\psi^-\rangle := \frac{1}{\sqrt{2}}(|01\rangle - |10\rangle)$, and σ is an arbitrary one-qubit state. This kind of states may be thought as a general form of the Werner-Isotropic states, see eqn.1.8. The importance of those states lies in that the amount of entanglement and nonlocality of these states will depend on the selected parameters. Nevertheless, under some considerations raised in the appendix A, it is possible to *activate* the nonlocality using different techniques which some of it were applied to the quantum game in the Chap. 4.

1.8 The Physical representation of qubits: experimental preparation of quantum states

The wide spreading of novel methods of the qubits states preparation can be divided commonly by its physical representation. Henceforth, the current section will examine the physical qubit systems from photons to molecular structures, describing the significant achievements which define a breakthrough in the preparation of these quantum states.

Photons

In 1995 P. Kwiat *et al.* [59] proposed using a nonlinear $\beta - BBO$ (Beta Barium Borate, $Ba(BO_2)_2$) type II crystal to achieve the preparation of the all Bell states characterized through the violation of the Bell inequalities. Time after in 1999 the same author [60] modified the posed scheme changing a crystal type II for a *two-type I crystal geometry* in which the optical axis of both crystals was perpendicular. This modification increased the correlations number and optimized the value of the inequalities violation. The proposal of P. Kwiat *et al.* popularised the use of non-linear media for the entangled photon preparation in polarisation basis in the research community (see fig. 12).

These techniques propel the preparation of complicated states like the Werner state as reported by Zhang *et al.* employing the parametric down-conversion phenomenon in 2002 [61]. This last include an additional nonlinear crystal, type I BBO, on the UV beam before the two-geometry crystal to prepared the bell state with the non-converted light. A novel direction here was the use of photon's decoherence through

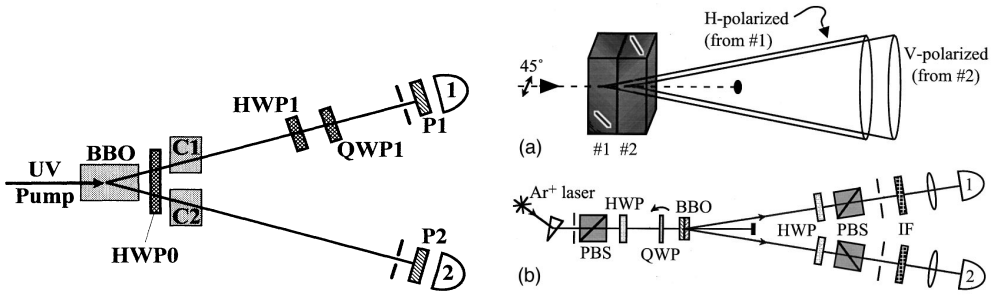

Figure 12: Illustration of the techniques posted by P. Kwiat *et al.* in the preparation of entangled states. Left: preparation setup of the four Bell's states using a type II nonlinear BBO crystal reprint from [59]. Right: (a) Detail of the two-crystal geometry, and (b) preparation scheme of the four Bell's states using a two-type I nonlinear BBO crystal geometry reprinted from [60].

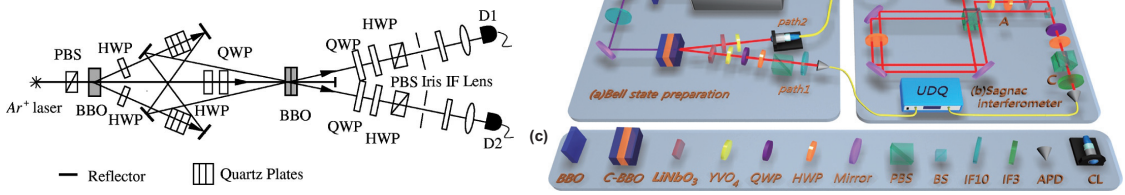

Figure 13: The preparation of Werner states with photons. Left: setup employed in the preparation of a Werner-Isotropic state reprinted from[61]. Right: experimental arrangement used by Liu *et al.*, the system comprises (a) Bell's states preparation, (b) the Sagnac-like interferometer and (c) the graphical indication of the optics employed.

quartz plates as a tool in the creation of polarisation quantum states of light as shown in Fig. 13. Currently, additional optical systems as the Sagnac-like interferometer, and a True-zero order half-wave plate between the two- BBO crystal geometry, and the high power of pulsed lasers affords the production of a tunable Werner-Isotropic state as the reported by Liu *et al.*[96], see Fig.13.

Since 2010 combinations of these experimental strategies have been used to characterize the decoherence of photons [43, 65, 97] with different theoretical methods, see Fig. 14. Those characterizations have defined a mechanism to achieve the preparation of Bell diagonal states which combines all the Bell basis [98]:

$$\rho_{ab} = \frac{1+k}{2}\left(\lambda_+|\Phi^+\rangle\langle\Phi^+| + \lambda_-|\Phi^-\rangle\langle\Phi^-|\right) + \frac{1-k}{2}\left(\lambda_+|\Psi^+\rangle\langle\Psi^+| + \lambda_-|\Psi^-\rangle\langle\Psi^-|\right), \tag{1.11}$$

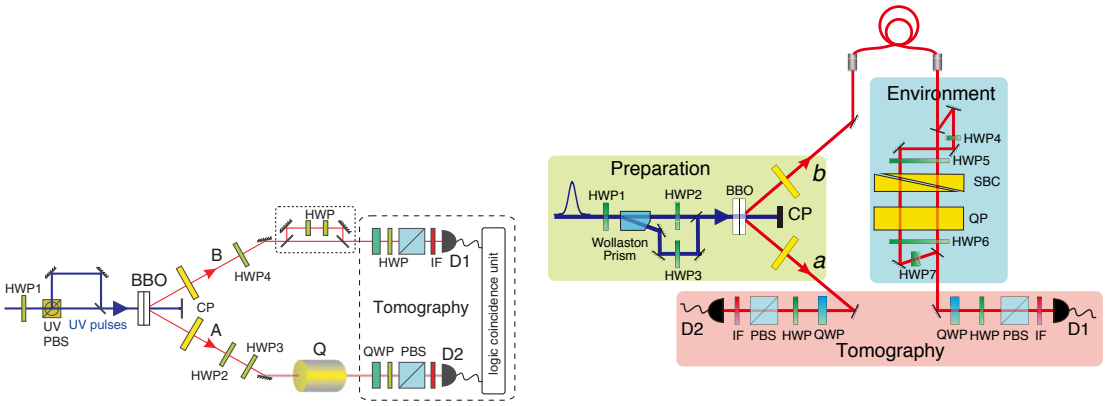

Figure 14: Decoherence analysis with photons. Left: Experimental setup for the analysis of the information correlations in Bell diagonal states, as eq. 1.11, in which the environment is simulated by a set of Quartz plates (Q) reprinted from [43] . Right: proposed experiment for the control of coherence under the action of a environment coupled to the photons in a Bell diagonal state reprinted from [98].

where k is the decoherence parameter, λ_+ is a quantity arbitrarily determined by the relative power between the paths created by the Wollaston prism in Fig.14 which follows $\lambda_+ + \lambda_- = 1$, and the Bell states in the polarisation basis $|\Phi^+_-\rangle = (1/\sqrt{2})(|HH\rangle \pm |VV\rangle)$, and $|\Psi^+_-\rangle = (1/\sqrt{2})(|HV\rangle \pm |VH\rangle)$.

These experimental ideas suggest the feasibility to expand these procedures to a large number of qubits. In 2016 were prepared16 photons in a maximum entangled state [69], even more considering the Orbital Angular Momentum (OAM) states of photons could serve as the perspectives in higher dimensions [99].

Through different techniques, the confirmation of those states is performed in which we can find the violation of the Bell's inequalities [59], the homodyne techniques, and the quantum tomography[100].

Nanostructured materials

Natural quantum states in molecules

Kasha's rule establishes that the fluorescence emission comes from the lowest excited state of a given excited band in a molecule [101]. This assumption allows considering fewer energy levels in a model of molecular photophysical behavior. Hence, considering a couple of non-interacting organic dimers with transition dipole moments $\vec{\mu_1}$ and $\vec{\mu_2}$. The total hamiltonian of the dimer reads $H_T = H_1 + H_2$, where the subindex 1 and 2 corresponds to the monomer 1 and 2, respectively. The ground

state ($|\Psi_g\rangle$) and the excited state wave functions ($|\Psi_1\rangle,\ |\Psi_2\rangle$) of the system holds:

$$\begin{aligned} |\Psi_g\rangle &= |0_1\rangle \cdot |0_2\rangle, \\ |\Psi_1\rangle &= |1_1\rangle \cdot |0_2\rangle, \\ |\Psi_2\rangle &= |0_1\rangle \cdot |1_2\rangle \end{aligned} \tag{1.12}$$

Here the Hamiltonian in basis of the wavefunctions of the excited state, $|\Psi_1\rangle,\ |\Psi_2\rangle$, is diagonal. Nevertheless, including an interaction potential (V) between the monomers we arrive at the coupled system in which the new Hamiltonian holds $H' = H_T + V$, and is not anymore diagonal in the excited state basis, but in a new coupled system basis can be written as:

$$\begin{aligned} |+\rangle &= \cos\frac{\theta}{2}|\Psi_1\rangle + \sin\frac{\theta}{2}e^{i\psi}|\Psi_2\rangle = \cos\frac{\theta}{2}|1_1 0_2\rangle + \sin\frac{\theta}{2}e^{i\psi}|0_1 1_2\rangle \\ |-\rangle &= -\sin\frac{\theta}{2}|\Psi_1\rangle + \cos\frac{\theta}{2}e^{i\psi}|\Psi_2\rangle = -\sin\frac{\theta}{2}|1_1 0_2\rangle + \cos\frac{\theta}{2}e^{i\psi}|0_1 1_2\rangle \end{aligned} \tag{1.13}$$

where the $\theta = \tan^{-1}\left(\frac{2|V_{12}|}{E_1 - E_2}\right)$, and $V_{12} = |V_{12}|e^{-i\psi}$. Where the E_i are the eigenenergies in the basis of the excited states, in the interaction frame the new eigenenergies are now:

$$E_\pm = \frac{1}{2}\left(E_1 + E_2\right) \pm \sqrt{\frac{1}{4}(E_1 - E_2)^2 + |V_{12}|^2} = E_m \pm \sqrt{\Delta^2 + |V_{12}|^2} \tag{1.14}$$

here $E_m = \frac{1}{2}\left(E_1 + E_2\right)$ and $\Delta = \frac{1}{2}(E_1 - E_2)$. Effectively, the coupling regime is now identified by the ratio $\frac{|V_{12}|}{\Delta}$ and is divided in two main regimes. On the one hand, the weak coupling, $\frac{|V_{12}|}{\Delta} \ll 1$, reduce the excited states to the proper states of any of the monomers showing a localized excitation in the monomer 1 or 2, in the following way:

$$\begin{aligned} |+\rangle &= \left(|\Psi_1\rangle + e^{-i\psi}\left|\frac{V_{12}}{\Delta}\right||\Psi_2\rangle + \cdots\right) \approx |\Psi_1\rangle \\ |-\rangle &= \left(-e^{-i\psi}\left|\frac{V_{12}}{\Delta}\right||\Psi_1\rangle + |\Psi_2\rangle + \cdots\right) \approx |\Psi_2\rangle \\ E_\pm &= E_m \pm \Delta \cdot \left(1 + \frac{1}{2}\left|\frac{V_{12}}{\Delta}\right|^2 + \cdots\right) \approx E_{1,2} \end{aligned} \tag{1.15}$$

On the other side, the strong coupling, $\frac{|V_{12}|}{\Delta} \gg 1$, gives rise to a delocalisation of the excitation on both monomers and the simplest case, for iso-energetic energy levels

($\Delta = 0$, $E_m = E_1 = E_2$), defines the *exciton states* as:

$$\begin{aligned} |+\rangle &= \frac{1}{\sqrt{2}}\left(|\Psi_1\rangle + e^{i\psi}|\Psi_2\rangle\right) = \frac{1}{\sqrt{2}}\left(|1_1 0_2\rangle + e^{i\psi}|0_1 1_2\rangle\right) \\ |-\rangle &= \frac{1}{\sqrt{2}}\left(-|\Psi_1\rangle + e^{i\psi}|\Psi_2\rangle\right) = \frac{1}{\sqrt{2}}\left(-|1_1 0_2\rangle + e^{i\psi}|0_1 1_2\rangle\right) \end{aligned} \tag{1.16}$$

In recent years various chromophores and photoactive molecules have been characterized finding of high photo-stability and fluorescence quantum yield [49, 50, 102–105]. Such properties let the molecular systems become a promising candidate for the study of quantum coherence control and information processing. Systems as the Perylene Bisimide (PBI) dimer have a short distance, 2.2 nm, between the monomers (subunits 1 and 2, see Fig. 15) yielding a reasonable dipole-dipole coupling strength which results in natural entanglement and correlations making it amenable to the implementation of quantum information protocols [106]. Such macromolecular quantum registers are suitable to overcome the scalability problem by the tunable size of the molecular structure through chemical synthesis controlling the dipolar interaction length.

The molecular quantum states are quantifiable by the absorption and fluorescence emission through spectroscopic techniques [107]. And we will identify a single molecular signal if we guarantee that: (i) only one molecule, in the irradiated volume, is in resonance with the laser, and (ii) the signal of the molecule is larger than the produced by the background signals [108].The latter condition holds although the fluorescence signal represents a small fraction of the incident light because the photons emitted are red-shifted in regard to the excitation energy, this shift is known as the Stokes shift [109]. Therefore, employing optical filters in the excitation band the signal of the single molecule will be detected with high a signal-to-noise ratio. A brief explanation of the first condition begins with the extinction cross section of a single two-level emitter [110]

$$\sigma = \frac{3\lambda^2}{2\pi}\frac{\gamma_0}{\gamma_{\mathrm{h}om}}\,, \tag{1.17}$$

where λ is the illumination wavelength , γ_0 the natural linewidth, and $\gamma_{\mathrm{h}om}$ the homogeneous width of the transition. Then, if $\gamma_0 \approx \gamma_{\mathrm{h}om}$, a condition which can be satisfied for an emitter embedded in a well-defined matrix at very low temperatures, the cross section is approximately $\lambda^2/2$ which is comparable to the area of a beam focused to the diffraction limit with high numerical aperture objective.

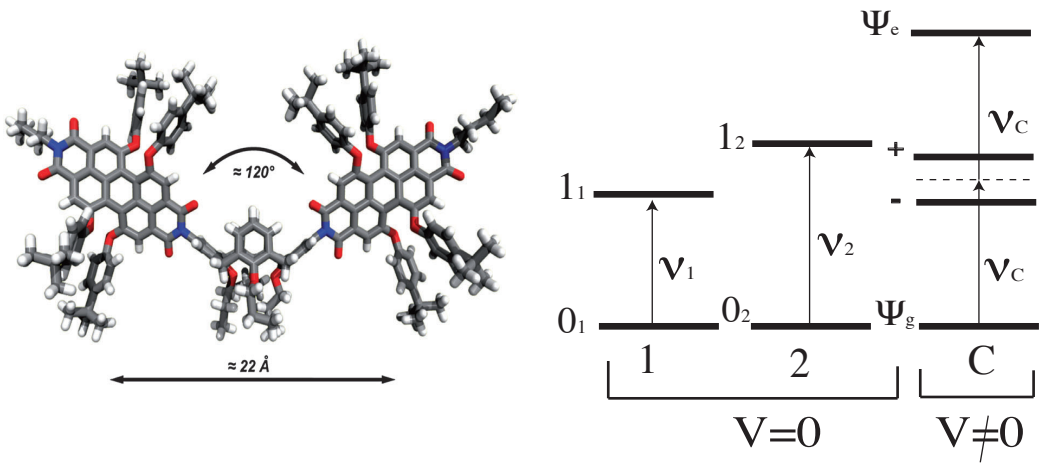

Figure 15: *Molecular structure of PBI dimers*. ***Left***: two PBI chromophores are covalently linked through a bridge of tetrakis(propyloxy)-calix[4]arene [50]. ***Right***: $|0_1\rangle$ and $|0_2\rangle$ are the ground singlet states of subunits 1 and 2, respectively. $|1_1\rangle$, and $|1_2\rangle$ denote their corresponding excited states. If the dipole-dipole interaction (V) between the subunits is zero, then the subunits 1 and 2 (the branches of the dimer) will be uncoupled. However, if $V \neq 0$, the dipole-dipole coupling generates a dimer energy structure that can be mapped into an effective four level system "C" that allows energy selectivity (e.g., for quantum logic gating), with ground state $|\Psi_g\rangle = |0_1 0_2\rangle$, upper doubly excited state $|\Psi_e\rangle = |1_1 1_2\rangle$, and entangled states $|-\rangle = \frac{1}{\sqrt{2}}\left(-|1_1 0_2\rangle + e^{i\psi}|0_1 1_2\rangle\right)$, and $|+\rangle = \frac{1}{\sqrt{2}}\left(|1_1 0_2\rangle + e^{i\psi}|0_1 1_2\rangle\right)$. ν_i denotes the transition frequencies of subunits 1 and 2, and ν_c is associated to the energy scheme of the interacting subunits.

The fundamental properties of quantum control on quantum states of physical systems pave the way to the implementation of quantum information protocols and can be accessible through the employment of photons and molecules as shown before. However, the definition of a qubit system which consider a mixture of the physical systems presented before is not a straightforward process. In the current research some insights are given in this direction opening a perspective for hybrid physical qubits.

Induced quantum states in molecular systems

In 2002, Hettich *et al.* [111] showed how to address two single Terrylene molecules separated by a distance of 12 nm; the molecules were close enough to effectively interact with each other via the resonant dipole-dipole coupling which in turn produced an energy level shift between the excitation levels of the pair, Fig. 16. The

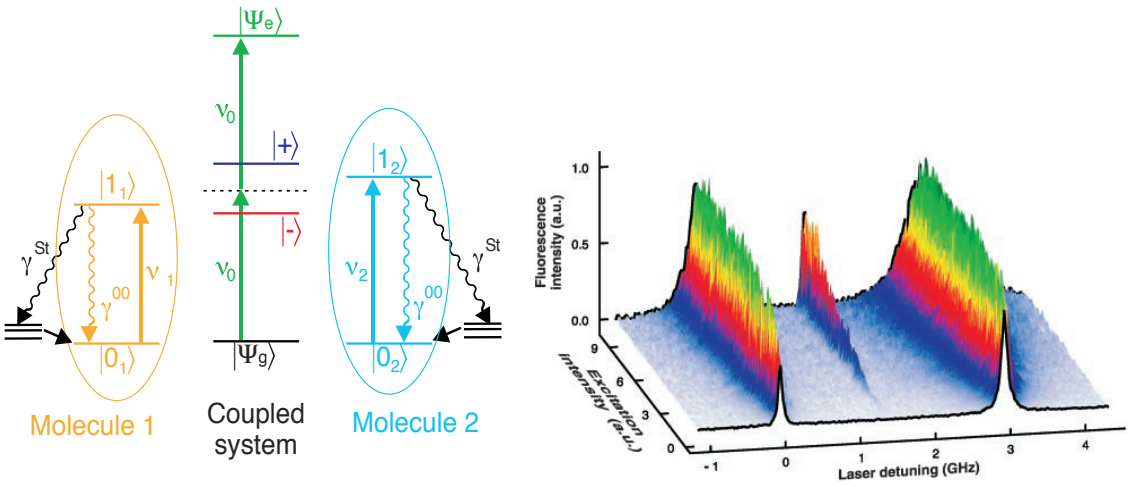

Figure 16: Molecular entangled system reprinted from [111]. Left: Electronic structure of the dipole-dipole interaction between the molecules 1 and 2, the notation has been modified to keep the coherence in the present chapter. Right: Excitation spectrum for a range of laser intensities tunable in frequency.

system was exposed to a simultaneous two-photon excitation process which allowed the experimental verification of a nonlinear optical effect. The demonstration of the dipole-dipole coupling opened the possibility of generating entangled states [2] between such single molecules. The use of photoactive organic molecules near enough to interact by means of the resonant dipolar coupling is an interesting prospect for the implementation of quantum logic [2]. Here, it is possible to characterize the molecular interaction in terms of decay rates of the coupled system, in the following way:

We assume two interacting molecules separated by a distance $|\vec{r_{12}}|$, with the transition dipole moment for each molecule $\vec{\mu_i} = \langle |0_i|\vec{D_i}|1_i\rangle$, where $\vec{D_i}$ is the dipole operator, $|1_i\rangle$ and $|0_i\rangle$ are the excited and ground state of the individual molecules, respectively. The dipole-dipole interaction energy $h\delta_{12}$ of the system is given by

$$h\delta_{12} = \frac{3h\sqrt{\gamma_1\gamma_2}}{8\pi(k_0 n r_{12})}\left[(\hat{\mu_1}\cdot\hat{\mu_2}) - 3(\hat{\mu_1}\cdot\hat{r_{12}})(\hat{\mu_2}\cdot\hat{r_{12}})\right], \tag{1.18}$$

where δ_{12} corresponds to the static dipole-dipole interaction potential, γ_i the spontaneous emission rate, h is the Planck's constant, n is the refraction index of the medium and $k_0 c = 2\pi\nu_0 \equiv \pi(\nu_1 + \nu_2)/2$, where ν_i is the transition frequency. An inter-molecular coupling in this way could be considered like a four-level system with $|\Psi_g\rangle = |0_1 0_2\rangle$ (the ground state), $|\Psi_e\rangle = |1_1 1_2\rangle$ (the upper state), and $|-\rangle$ and

$|+\rangle$ (the intermediate superpositions) as defined before by diagonalising the new Hamiltonian. The appropriate calculations lead to the decay rates for each energy level, and are given by:

$$\begin{aligned} \gamma_I &= (\cos\frac{\theta}{2})^2\gamma_1 + (\sin\frac{\theta}{2})^2\gamma_2 - 2(\sin\frac{\theta}{2}\cos\frac{\theta}{2})\gamma_{12}, \\ \gamma_J &= (\sin\frac{\theta}{2})^2\gamma_1 + (\cos\frac{\theta}{2})^2\gamma_2 + 2(\sin\frac{\theta}{2}\cos\frac{\theta}{2})\gamma_{12}, \\ \gamma_U &= \gamma_1 + \gamma_2, \end{aligned} \tag{1.19}$$

here γ_{12} is the incoherent cross-damping rate and if $k_0 r_1 \ll 1$ goes to $\gamma_{12} = \sqrt{\gamma_1\gamma_2}(\hat{\mu_1}\cdot\hat{\mu_2})$. With this decay rates we can characterise the transitions of the system under study and it is possible to calculate the steady-state density matrix from the complete master equation.

This experiment offered an possibility to obtain entangled states in the molecular regime. However, the fundamental condition to visualise these states, the intermolecular distance ~ 12 nm, could not be repeated and poses a serious drawback for one of the conditions of a reliable quantum computational scheme, the scalability.

Perovskites Structures

Trihalide perovskite semiconductors are a novel class of materials which attracted the attention of the scientific community due to the great ascend of the photovoltaic power conversion efficiency in just the 2012 year [112, 113].

The implementation of hardware for quantum information requires four fundamental conditions: i) the representation of a quantum information unit isolable from the interaction with the environment, ii) the preparation fiducial initial state, iii) the construction of a universal set of logical quantum gates, and iv) the capability to measure the final output. The first condition involves the production of pure quantum states reliable through the building of controllable single photon sources[70, 71]. The basic strategy consists of the quantum control over the two-level system. In systems as Quantum dots (QDs) in a microcavity[114–116] and three-level atom in an optical cavity[117], the coupling of the photons is mediated by an atom, hence increasing the atom-field coupling is profitable. Other physical arrangements as the fluorescence from a single nitrogen-vacancy[118], the emissions from defects in Silicon Carbide [119], molecules trapped in solids[120], QDs in silicon photonic circuits[121], excitons at oxygen defects in carbon nano tubes[122], or highly diluted organic molecules [123] have limited quantum yield which reduces the number of

qubits. In this sense, The perovskites structures are outstanding materials with quantum Yields $\sim 100\%$ [124–127] at room temperature, and the fluorescent emission is controllable through homogenous electric field due to the movement of the ions [53]. The coherence time (τ_Q) of these nanostructures are around the microseconds (10^{-6} seconds), and the operational times (τ_{Op}, time needed to perform a logical operation) is around the nanoseconds (10^{-9} seconds [128]) resulting in a number of logical operations of $\sim 10^3$ [2] able to the implementation of quantum information processing protocols with this perovskite structure.

Currently, this material has led the third-generation of solar harvesting systems and recent breakthroughs in perovskites formation have contributed to increasing the efficiency of this material up to 22.7% [129]. This perovskite material is the result of the crystallization of organic halide and metal halide salts forming the ABX_3 structure in which A and B are the organic and metallic cations together bound to X the halide anion, see Fig. 17. After the formation, the polar binding between the metal and halide ions determines the crystal cell size and the band structure in which the overlap between the orbitals defines the energy gaps [104, 130].

These conditions limit the metal to choose (metal ions as Cu, Ge, Ni, have been demonstrated [131, 132]) which form the structure because it requires a metal with the appropriate configuration in their outer orbitals and adequate valency. An outstanding capability of the organic-inorganic trihalide perovskite structures is the tunability of the emission and absorption band through the substitutions of the cation and the anion. The methylammonium (Ma) lead trihalide combination with stoichiometry $MAPbX_mY_{3-m}$ exhibits an emission range from 390 to 790 nm while the formamidinium (FA) lead trihalide structure ($FAPbI_mBr_{3-m}$) shows an absorption edge tuneable as shown in Fig. 17. This characteristic is not restricted only to the inorganic-organic structures, also through halide compositions and quantum-size adjusting the metal halide perovskites have an spectra tuneable entirely in the visible range from 410 to 700 nm [102].

In general, these structures have a low Urbach energy (< 16 meV) which means an ordered microstructure [133], Stokes shift smaller than 20 meV [104], high charge-carrier mobilities $\sim 30\ cm^2V^{-1}s^{-1}$, long diffusion lengths $\sim 10\ \mu$m [134], and low trap density $\sim 10^{14}\ cm^{-3}$. All those characteristics belongs to the Pb-based perovskites, however a big discussion arise about the toxicology issues that bring the use of this compound. Then, the lead-free structures principally based on Tin (Sn) have impulsed a new research tendency [135–138].

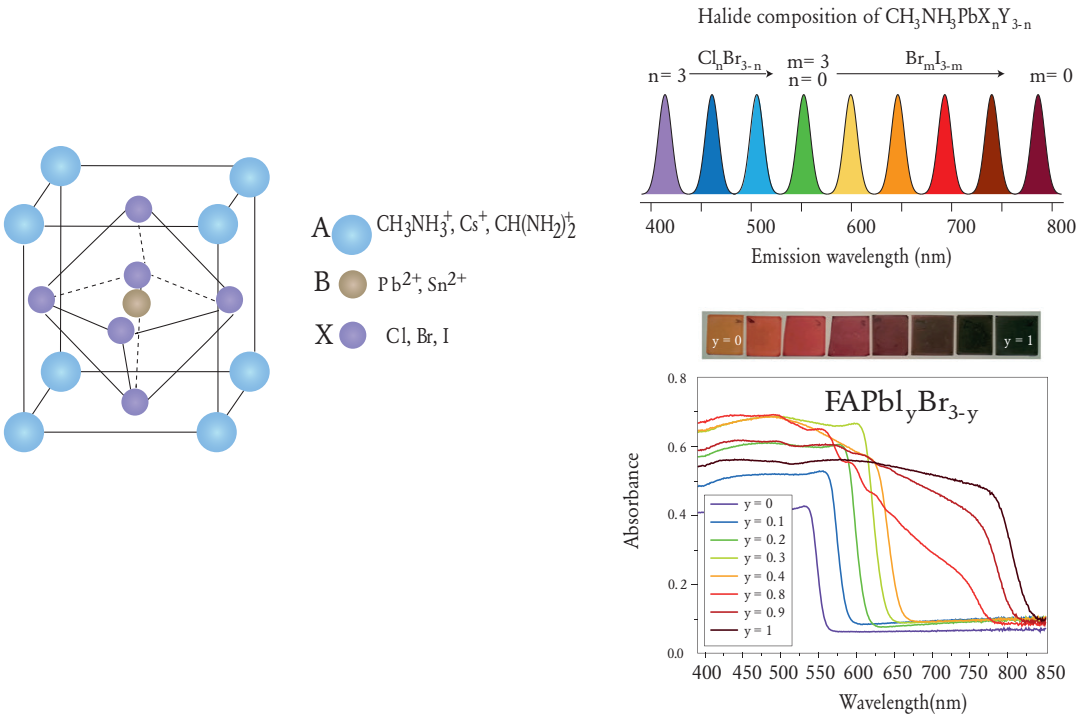

Figure 17: Perovskite molecular structure reprinted from [104, 105]. Left: Perovskite crystal structure ABX_3 and the possible combinations for the Ma-based structure. Right upper: variation of the emission spectra correlated with the halide composition changes. Right lower: Absorption tunability for the $FAPbI_yBr_{3-y}$.

The $MASnI_3$ has a bandgap in the range from 1.2 to 1.3 eV which allows the harvesting of light in a broader range than the counterpart made of lead but with a shorter diffusion length of $\sim$ 30 nm [139]. Nevertheless, the Sn-based perovskites are unstable and highly degradable in the air which is inconvenient for room temperature applications. Currently, organic-inorganic perovskites with alternative metal ions as Cu, Ge, Ni, among others, have been demonstrated [131, 132].

All those characteristics already described show that the $MAPbX_3$ have an electronic dynamics as a direct band semiconductor.

Assuming a small exciton binding energy, the photon absorption with quantized energy above the exciton resonance will create: an electron-hole pair with total momentum $\mu \approx 0$, or an exciton with whole momentum $\mu \neq 0$ called a geminate exciton formation, as shown in Fig. 18 lower part. The kind of processes depend on the amount of excitation energy, under low fluences with carrier densities typical

of photovoltaic conditions ($n_0 \approx 10^{13} - 10^{15} cm^{-3}$), the monomolecular processes as trap-assisted recombination or geminate recombination are inefficient with low recombination coefficients at first order ($k_1 \approx 10 \mu s^{-1}$) [140]. At higher carrier densities, $n_0 \approx 10^{16} - 10^{18} cm^{-3}$, bimolecular (nongeminate recombination) and trimolecular (Auger processes) effects are more probable, see Fig. 18 upper part.

The monomolecular annihilation of two Coulombically bound charges originates the geminate recombination, by another way, the bimolecular recombination of two free charges is the responsible for the nongeminate recombination. However, this last process has a recombination constant ($k_2 = 10^{-10} cm^3 s^{-1}$) four orders lower than determined by the electron-hole annihilation (Langevin rates). Nevertheless, the Auger rates are large ($k_3 \approx 10^{-28} cm^6 s^{-1}$) similar to the strongly confined colloidal quantum dots of $CdSe$.

In $MAPbI_3$ material, the exciton binding energy (E_b) at room temperature have the same order than the thermal energy $E_b \sim k_B T$ increasing up to $2 - 3k_b T$ changing the anions to Br or Cl. This condition benefits the prevalence of free carriers over the bound excitons which in turn favors the usage of this materials as the active layer in multi-junction solar cell architectures [143]. But if we alter the electronic density of states through the reduction of the dimensionality [142, 144], the bound excitons will be favored.

For our interest, the exciton production will define the behavior of the perovskites as a two-level system. In that sense, the necessary conditions to achieve it involve photons with energy slightly above the E_b, low energy fluences, reduced dimensionality (quantum dots) in such a way that the Auger recombination suppress emissions from biexcitons and other higher-order multiexcitons [145], and to consider the temperature effects on the structural changes which affect the Optical properties as has been reported [146]. Therefore, perovskite materials are a strong possibility to correlate photons and electrons within a quantum computational system becoming a candidate to solve the scalability problem in the quantum information protocols (increasing the number of accessible qubits states) controlling the system electro-optical response, and exploring detection arrangement to interact controlled with the qubit system.

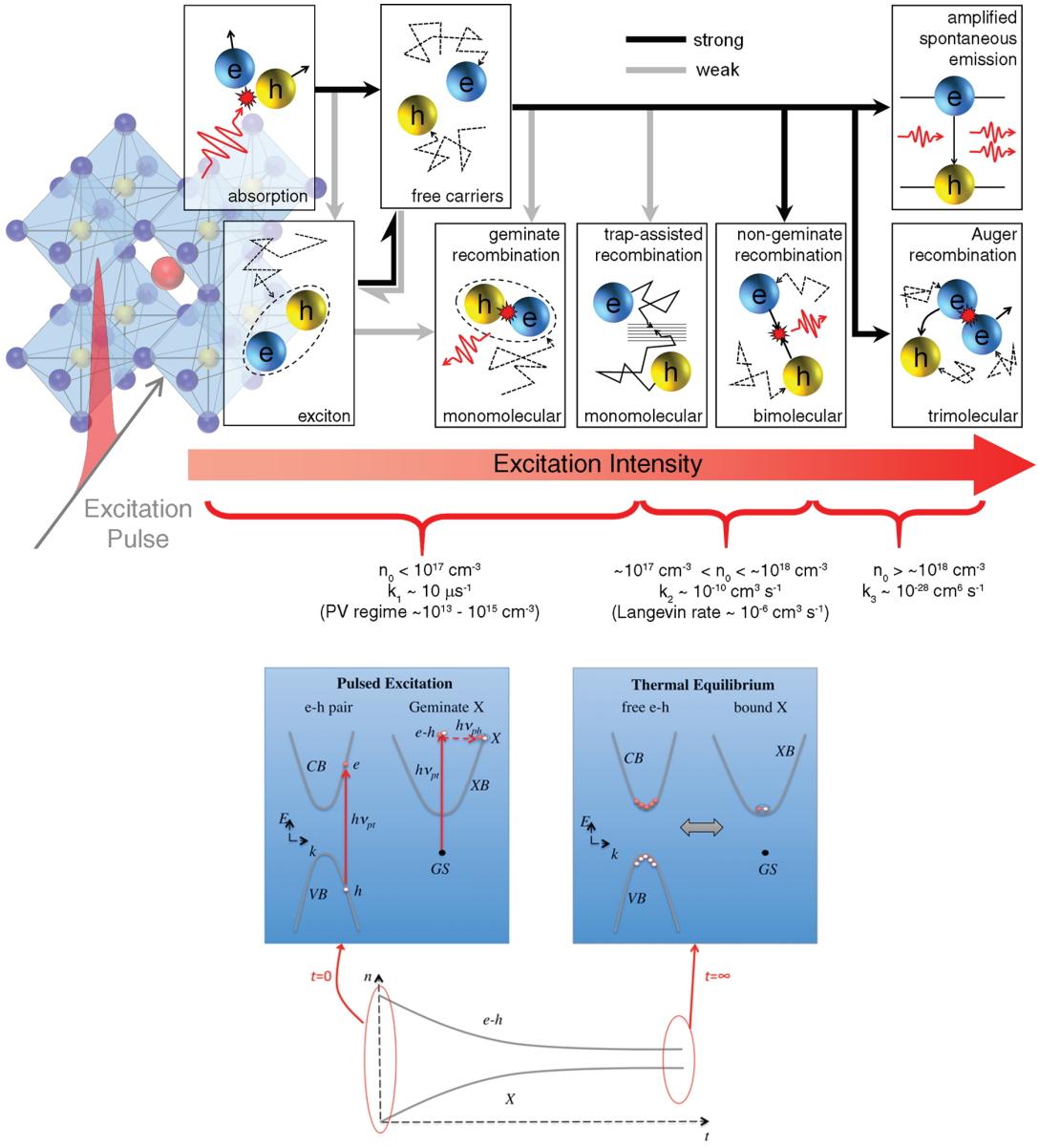

Figure 18: Perovskite molecular photoexcitation dynamics reprinted from [141, 142]. Upper: photoexcitation process due to pulsed excitation and thermal equilibrium in perovskite structures for the occurrence of free charge carrier and hole pair $(e-h)$ in a two body diagram, or geminate bound exciton (X) in a single-particle diagram, drawing the conduction band (CB), valence band (VB), and $e-h$ pair ground state (GS). Lower: Scheme for the photoexcitation dynamics under pulsed excitation and thermal equilibrium showing the predominance of the free carriers over the excitons a $t = 0$ to achieve a population equilibrium at $t = \infty$ between them.

Part I

Coherence and Correlations in Photonic Qubits

Chapter 2

DECOHERENCE ENVIRONMENT SYMMETRY DEPENDENCE ON ENTANGLED BIPARTITE PHOTONIC QUBITS

2.1 Introduction

Quantum systems are ubiquitous in nature—after all, we live in a world that is ultimately ruled by the laws of quantum physics. Such systems of course comprise the primary atoms, molecules and photons, biomolecular complexes, and, interestingly, man-made complex nanostructures such as arrays of artificial atoms and organic multichromophoric networks, to cite but a few. In particular, photons have appeared to be ideally suited to quantum technology development such as commercially available quantum key distribution systems, large-scale secure networks, enhanced measurement and lithography [147], and even quantum information processors[24, 48, 148]. For example, an experimental demonstration achieved the encoding of quantum information by means of 100-photon Schrödinger cat states [149]. These outstanding developments owe their success to the fact that photons are chargeless, can be guided over long distances at high-speed transmission (e.g., using optical fibers), and because photons do not interact with each other, which translates into highly desirable low-noise properties. This said, usually the external control of such photonic systems is performed via a radiation-matter coupling through systems like atoms or molecules[2, 24, 48, 111].

In addition, due to the photons have to pass through birefringent medium, different authors have demonstrate that the coupling with the frequency modes of the environment causes decoherence effects showed theoretically [41, 150–152] and experimentally [41, 43, 62]. Then, the understanding and control of decoherence are necessary steps in the development of robust experimental protocols of quantum information. Also, if this verification is complemented with the behaviour of correlations of a quantum information system (Entanglement, quantum discord, mutual information and classical correlations), it is possible to determine the efficiency of the physical system as resource for the quantum computation. In this way, coherence control of physical systems in the quantum regime is of utmost importance in the design and implementation of quantum information tasks. Thus, the present article will serve as evidence of the experimental production, the detection and

characterisation of entangled quantum states under controlled decoherence through homogeneous birefringent media. In order to evaluate the efficiency of the coherent control over the entangled states as a kernel for quantum information processing. Here, we encode quantum information in the polarisation states of photons to prepare and demonstrate quantum entanglement and nonlocality of photonic qubits under decoherence. A polarisation maintaining fibre (PMF) acts as a qubits noisy channel and output states are measured by applying a quantum tomography protocol. The PMF introduces decoherence in a similar way to a birefringent crystal and allows a controlable noise scenario to test how the symmetries due to collective and independent qubit-environment coupling affects the original input quantum states. We model the PMF and quantify measured output states with fidelities greater than 92%. We identify optical conditions (e.g. fiber's rotational angle) for the implementation of a decoherence-free subspace for different entangled states and interaction optical paths longer than 1 m.

2.2 Birefringent media as decoherent environment for photons

In 2010 S. Luo *et al.* showed that symmetry of quantum states and the operation of the decoherent environment define the behavior of the correlations in the quantum system [150, 151] finding an area where the classical correlations are lower than the quantum ones. Specifically, a statistical mixture of Bells states prepared as $\rho = dR|\Phi^+\rangle\langle|\Phi^+| + b(1-R)|\Phi^-\rangle\langle\Phi^-| + bR|\Psi^+\rangle\langle\Psi^+| + d(1-R)|\Psi^-\rangle\langle\Psi^-|$, where the coefficients b and d depend on the relative power between two polarisation species in the creation process and accomplish that $b + d = 1$, and R is the total reflectivity of two partially reflecting mirrors involved in the experimental setup described in [43]. This experiment found the appropriate thickness of quartz plates as decoherence environment to increases the value of the quantum correlations over the classical ones, at $L = 78\lambda_0$, with λ_0 as the central wavelength of the photonic quantum state.

The coupling of the polarisation modes with the frequency of photons gives account about the modification of the photonic state by the media. A single photon state which considers these variables can be written as:

$$|\Psi\rangle = \sum_{j=1}^{2} c_j|\gamma_j\rangle \otimes \int d\omega A(\omega)|\omega\rangle \tag{2.1}$$

where $|\gamma_j\rangle$ corresponds to the polarisation modes and $A(\omega)$ is the amplitude of the photons distribution around ω with $\int d\omega|A(\omega)|^2 = 1$. In the biphoton case,

we use a non-linear crystal to produce Spontaneous Parametric Down Conversion (SPDC) which in turn produces spatially separated and entangled photon pairs. These converted photons have frequencies $\omega^+ = \frac{\omega_0}{2} + \epsilon$ and $\omega^- = \frac{\omega_0}{2} - \epsilon$, with ω_0 as the central frequency of the pump photons in the SPDC process and ϵ as a perturbation fraction, in such a way that $\omega^+ + \omega^- = \omega_0$. If any of these photons pass through a birefringent medium is expected the decreasing of the coherence values in the density matrix of the whole system, this phenomenon is called decoherence. For photons in a Biphoton-state can be calculated by considering the coupling with the proper frequency before entering the birefringent environment as:

$$\begin{aligned} \rho_\omega(0) &= |\Psi(0)\rangle\langle\Psi(0)| \\ &= \sum_{i,j,k,l} c_{ij}c^*_{kl}|\gamma_{ij}\rangle\langle\gamma_{kl}| \otimes \int\int |A(\omega^+)|^2|A(\omega^-)|^2 \times |\omega^+\rangle|\omega^-\rangle\langle\tilde{\omega^+}|\langle\tilde{\omega^-}|d\epsilon d\tilde{\epsilon}, \end{aligned} \tag{2.2}$$

the subindex ω in the density matrix means that is considered the coupling frequency in this expression, and the argument (0) corresponds to the size of the birefringent medium crossed. The action of the medium with birefringence Δn and thickness L is modeled by an operator $\hat{U}(L)$ which acts over each path of the setup in the following way [41](see fig. 21):

$$\begin{aligned} \hat{U}(x_1)|\gamma_i\rangle &= e^{i\varphi_i(x_1)}|\gamma_i\rangle \\ \hat{U}(x_2)|\gamma_j\rangle &= e^{i\varphi_j(x_2)}|\gamma_j\rangle \end{aligned} \tag{2.3}$$

where x_1 and x_2 are the thickness of the birefringent medium on path one (1) and two (2) of the experimental arrangement, respectively, and $\varphi_i(x_1) = (n_i x_1)\omega/c$ is a dimensionless parameter which gives account about the ratio between the phase and the group velocity into the environment considering c as the speed of light in the vacuum. Hence, the total operator will be $\hat{\mathbf{U}}(x_1, x_2) = \hat{U}(x_1) \otimes \hat{U}(x_2)$ and performing a frequency-insensitive measurement, the result is:

$$\begin{aligned} \rho(x_1, x_2) &= \textstyle\sum_{i,j,k,l} \quad c_{ij}c^*_{kl}|\gamma_{ij}\rangle\langle\gamma_{kl}| \int d\epsilon |A(\omega^+)|^2|A(\omega^-)|^2 \\ &\times \qquad e^{i(\varphi_i(\omega^+,x_1)+\varphi_j(\omega^-,x_2)-\varphi_k(\omega^+,x_1)-\varphi_l(\omega^+,x_2))} \end{aligned} \tag{2.4}$$

For anisotropic media, the refraction index of a material is a spatially-dependent quantity, i.e., rotations over the optical axis affect its value. In the same way, this change in the refraction index affects the frequency of photons within a birefringent environment. Additionally, rotations over the optical axis produce coherence decreasing in the whole state of the photonics system, but under certain restrictions,

this modification is reversible. With the model described here, each part of the system can be to the same decoherence or collective decoherence exposed. For this, we should need to rotate the crystals of each subsystem keeping a difference of $\pi/2$ between their rotating angles. In such a way, the photons in a birefringent environment are a useful prototype for the analysis of decoherence in quantum systems. In this research, we use the birefringent properties of an optical polarisation-maintaining fiber (PMF) as a decoherent environment toward the study of control parameters on photons non-maximally entangled. In general, the PMF avoid the loss by dispersion of the polarisation states even if the fiber is bent like a long and flexible homogeneous crystal. This behavior is due to the introduction of stressed material cylinders, generally Quartz or compositions of modified glass [153], near to the kernel of the fiber. The insertion of this cylinders produces a strong birefringence related with the symmetry of the refractive index profile.

2.3 Experimental Methods

The actual experiment involves two principal steps. The first stage consists of the production of entangled photon pairs around 810 nm with a non-collinear source. In this step, we employ a continuous wave laser of GaN (405 nm) pumping two non-linear crystals of Beta Barium Borate ($\beta - BBO$, type II) of 2 mm thickness as shown in the Fig.21a. Due to the nonlinear process inside the crystal, the group velocity of the ordinary and the extraordinary polarization components are different producing a walk-off delay ($\delta\tau = L(\frac{1}{u_0} - \frac{1}{u_e})$) and displacement ($d = L\tan\gamma$), with L as the crystal length, the u_0 and u_e are the ordinary and extraordinary group velocities respectively, and γ the angle between the ordinary and extraordinary component [59]. Nevertheless, we compensate this walk-off employing a BBO with the half size in both optical paths. The crossing section of the polarization cones of the light converted is directly observed with a long time exposure CCD camera (STF-series). This cones crossing site defines the position of mechanical diaphragms to align the tomography optics and the fiber couplers (FC) connected to the detectors toward $5m$ multimode fibers (MMF) as in Fig.21b. the minimum exposure time to observe the entangled photons was 15 min, then each movement of the camera or the mechanical diaphragms were in time steps of 15 mins which increase the time of each experimental test.

We Include a filter with a double coating at 405 nm in the detection path which allows only the cross of photons at 810 nm, and the undesired counts can be reduced. This source produces photons in a quantum state like $|\Psi_{12}^{+}\rangle = \cos\alpha|H_1V_2\rangle + \sin\beta|V_1H_2\rangle$

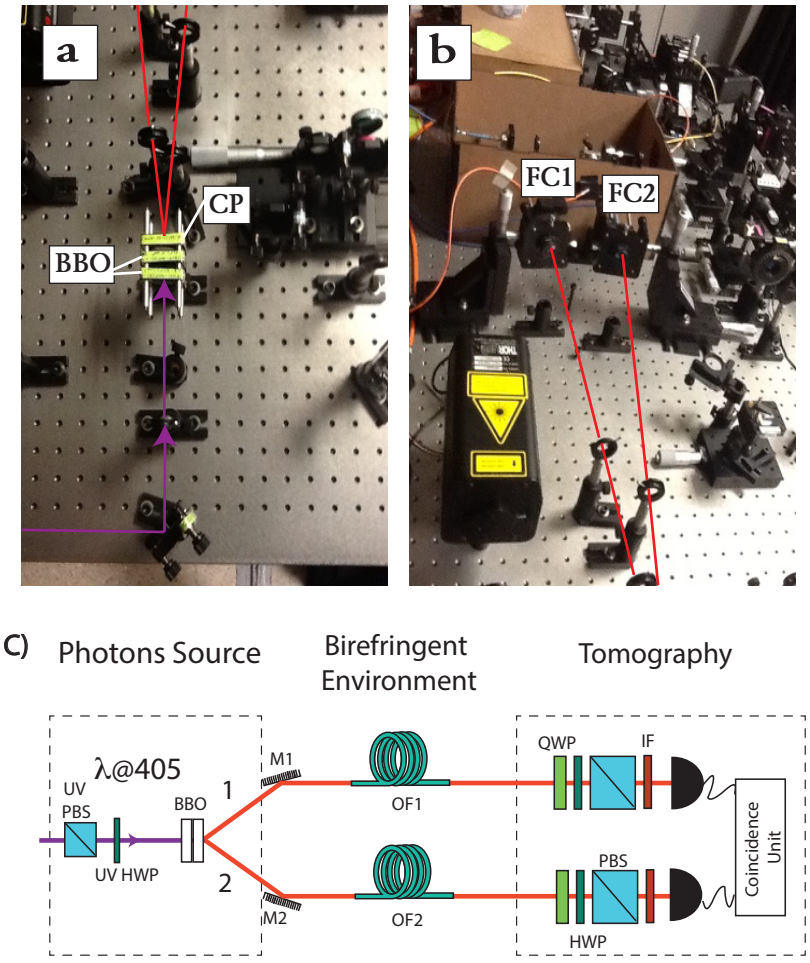

Figure 21: (a). Experimental arrangement of the double crystal setup employed in the production of entangled photon pairs through the spontaneous parametric down conversion process; the compensation plate (CP) is a BBO with the total half size, the pump laser of GaN is drawn in false color as well the output paths. (b) Experimentally the converted light is focused on a fiber coupler (FC) system to decrease the losses. (c) Sketch of the experimental setup used for the production of the input state and the inclusion of the PMF as a decoherence environment on the entangled photons paths. A continuous wave laser GaN (405 nm) pumps two non-linear BBO (Beta Barium Borate) type II Crystals to produce an entangled single photon source. The photons passing through the paths 1 and 2 are directed toward the detectors, after the plane mirrors M1 and M2. The tomography is performed using a Quarter-Wave Plate (QWP), a Half WavePlate (HWP), a polarisation Beam Splitter (PBS), and an Interference Filter (IF) of 10 nm Wideband on each optical path [100].

[60] due to the spontaneous parametric down-conversion process (SPDC), here the subindex "1" and "2" are related with the spatial way of the photons, see sketch on Fig. 21c. The parameters α and β depend on the experimental phase induced within the crystals.

The verifications of the prepared quantum state are performing through the experimental scheme proposed by D. F. V. James *et al.* [100], known as *"quantum tomography"*. This protocol requires two Quart wave-plates (QWP), two half-wave plates (HWP), two polarized beam splitter, two interference filter (IF), and two Avalanche Photodiode (APD). In our experiment, we obtained the projections on the polarisation basis through rotations of a quarter wave plate (QWP, $\frac{\lambda}{4}$) and a half wave plate (HWP, $\frac{\lambda}{2}$). This light is then filtered by a polarising beam splitter (PBS, $50/50$) and an interference Filter-IF (FWHM, 10 nm) at 810 nm on each photon's path, see the tomography square in sketch on Fig.21c. Afterward, the coincidences between single photons are counted and stored in a computer through a lab-made counting module. Finally, we produce sixteen ($4^2 = 16$) measurements corresponding to all the polarisation basis and their combinations (horizontal polarised $|H\rangle$, vertical polarised $|V\rangle$, diagonal polarised $|D\rangle$, and circularly right polarised $|R\rangle$). In our case, we arrange the measurement in such a way that the rotation of the wave-plates can be cycle performed as shown in the tab 21.

Each of the sixteen measurements gives a Stokes parameter ($S_{i,j}$) to reconstruct the quantum state of the system as $\hat{\rho} = \frac{1}{2^n}\sum_{i_1,i_2,i_3,\cdots,i_n}^{3} \frac{S_{i_1,i_2,i_3,\cdots,i_n}}{S_{0,0,\cdots,0}} \hat{\sigma}_{i_1} \otimes \hat{\sigma}_{i_2} \otimes \cdots \hat{\sigma}_{i_n}$ as shown in [100]. [1] Finally, we use an algorithm on the experimental data to compute the Stokes parameters and reconstruct the quantum state [100]. After this process, we obtain a sixteen components vector for the input state as: $(n_1 = 0.0125, n_2 = 0.2625, n_3 = 0.0, n_4 = 0.725, n_5 = 0.4, n_6 = 0.225, n_7 = 0.0875, n_8 = 0.3, n_9 = 0.2, n_{10} = 0.2375, n_{11} = 0.2875, n_{12} = 0.1375, n_{13} = 0.3125, n_{14} = 0.2875, n_{15} = 0.1125, n_{16} = 0.0875)$. The second part of this experiment consisted of the inclusion of two optical polarisation-maintaining fiber (PMF) of the same length (1 m) before the tomography process placed simultaneously on both photons line as shown in the Fig. 21c. In our experiment we have used a PMF with a birefringence[2] of $\Delta n = 3.5 \times 10^{-4}$ that induces a retardation length of $\approx 432\lambda_0$, where λ_0 is the center wavelength of the down-converted light. After the PMF inclusion we obtained the measurement set ($n_1 = 0.312977, n_2 =$

[1] Here is possible to modify the conventional scheme using four (4) instead of two (2) detectors to perform fewer measures to obtain the quantum state of the system

[2] specification belongs to panda fiber PM780-HP by Thorlabs.

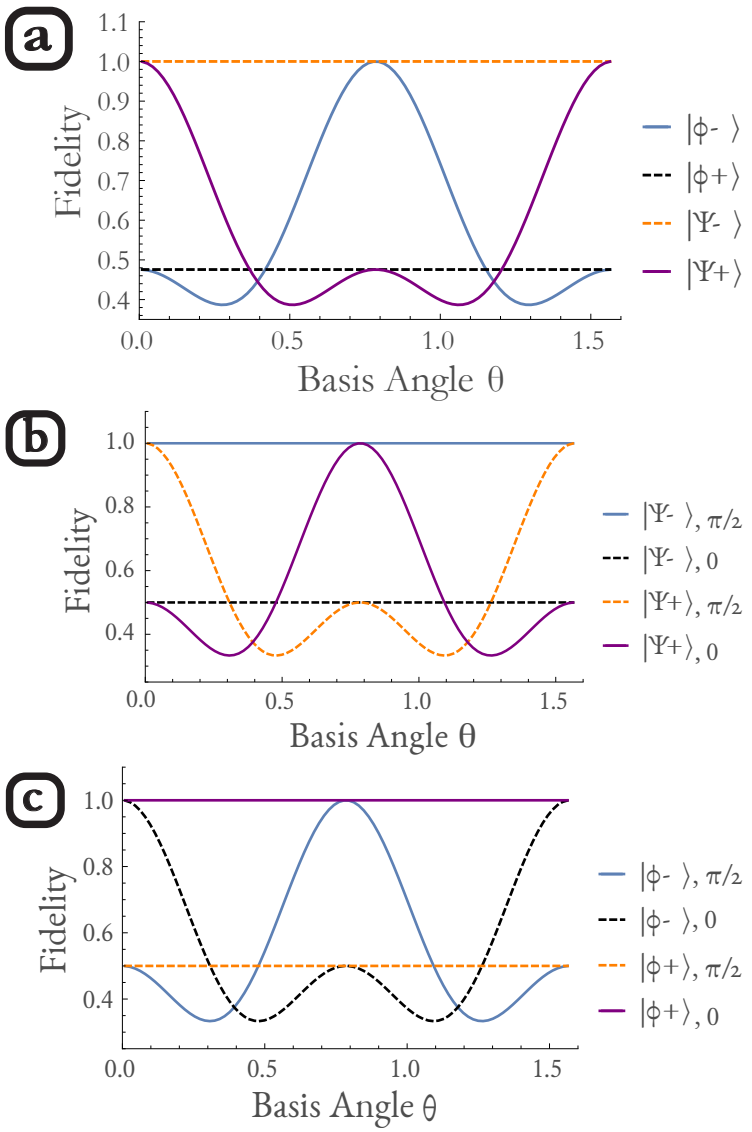

Figure 22: The fidelity of the input state with the calculated output after the state passes through the birefringent environment. Here, the $\pi/2$ after the name of the states symbolizes the collective decoherence, and the 0 describes the non-collective decoherence environment. a) All four Bell's states in a collective decoherence environment. b) the $|\Psi^{\pm}\rangle$ states in both the collective and the non-collective surroundings. c) the $|\phi^{\pm}\rangle$ states in both decoherence scenarios.

Table 21: Tomography measurement order, H and Q hold for Half wave-plate and Quart wave-plate respectively. The subindex 1 and 2 are related to the optical path measured. The values under each wave-plate symbol are the axial rotation angles for each device in degrees, and the measurement bases are horizontal (H), vertical (V), diagonal (D), right rotational (R), and left rotational (L).

Order	H_1	Q_1	H_2	Q_2	Measurement basis
1	0.0	0.0	0.0	0.0	VV
2	22.5	0.0	0.0	0.0	RV
3	45.0	0.0	0.0	0.0	HV
4	0.0	0.0	45.0	0.0	VH
5	22.5	0.0	45.0	0.0	RH
6	45.0	0.0	45.0	0.0	HH
7	22.5	45.0	0.0	0.0	DV
8	22.5	45.0	22.5	0.0	DR
9	22.5	45.0	45.0	0.0	DH
10	22.5	45.0	22.5	45.0	DD
11	0.0	0.0	22.5	45.0	VD
12	22.5	0.0	22.5	45.0	RD
13	45.0	0.0	22.5	45.0	HD
14	0.0	0.0	22.5	90.0	VL
15	22.5	0.0	22.5	90.0	RL
16	45.0	0.0	22.5	90.0	HL

$0.221374, n_3 = 0.290076, n_4 = 0.175573, n_5 = 0.244275, n_6 = 0.290076, n_7 = 2.17557, n_8 = 2.33588, n_9 = 2.16031, n_{10} = 2.17557, n_{11} = 2.93893, n_{12} = 3.10687, n_{13} = 2.96183, n_{14} = 3.32061, n_{15} = 1.31298, n_{16} = 2.39695$).

2.4 Results and Discussions

We control the collective change of the environment employing the coupling of the polarisation with the frequency modes in which the physical system (“ the twin photons”) is lead. The initial conditions for the rotational angle of the birefringent environment define the nature of the decoherence. Hence in a bipartite system, if both parts of the system are exposed to symmetrical rotations we have a *collective decoherence* otherwise it will be a *non-collective* or *independet coherence* scenario.

We consider the calculation of the *fidelity* to evaluate the decoherence effects. This quantity was defined by William Wootters to quantify the similarity of quantum states for pure states is $F = Tr(\rho_{out}\rho_{in})$, and $F = \left[Tr\left(\sqrt{\rho_{in}}\rho_{out}\sqrt{\rho_{in}}\right)^{1/2}\right]^2$ for other quantum states [154]. We calculate the fidelities for the maximally entangled

states in a collective decoherence environment employing the model before posed, as shown in Fig. 22a. In this graph, the fidelity is a function of the rotational angle around the propagation axis (in both arms). And as can be seen, the $|\psi^-\rangle$ state is not affected by changes in the birefringence surroundings. This find was observed before by P. Kwiat *et al.* and described as a decoherence-free subspace (DFS) for the $|\Psi^-\rangle$ state [41].

If we take only two Bell's states instead of all four, e.g. $|\Psi^{\pm}\rangle$, but considering the different scenarios for the decoherence environment. It is possible to confirm that $|\Psi^-\rangle$ is not any more decoherence-free within a non-collective environment ($|\Psi^-\rangle, 0$), as shown in the Fig.22b. In opposite way, the non-collective scenario is convenient to enhance the DFS behavior of the $|\phi^+\rangle$ state as shown for "$|\phi^+\rangle, 0$" in Fig. 22c. This performance shows the emergence of a DFS dependence on the matching of the symmetry of the environment and the quantum state of the system. In short, if the quantum state and the environment share the same symmetry, then this first will be DFS. In this sense, we can suggest that the $|\Psi^-\rangle$ shares the same symmetry with the collective decoherence environment as well as the $|\phi^+\rangle$ with the non-collective decoherence surrounding.

So far, the analysis considers the parameters employed by P. Kwiat *et al.* in their experiments, and only on maximally entangled states. However, it is interesting to identify the behavior of non-maximally entangled states and its correlations. We prepared experimentally the non-maximally entangled state $\rho_{ExInp} = 0.0125\rho_{(HH,HH)} + 0.0\rho_{(HH,HV)} + 0.06875\rho_{(HH,VH)} - 0.10625\rho_{(HH,VV)} + 0.0\rho_{(HV,HH)} + 0.2625\rho_{(HV,HV)} + 0.24375\rho_{(HV,VH)} + 0.04375\rho_{(HV,VV)} + 0.06875\rho_{(VH,HH)} + 0.24375\rho_{(VH,HV)} + 0.725\rho_{(VH,VH)} + 0.05\rho_{(VH,VV)} - 0.10625\rho_{(VV,HH)} + 0.04375\rho_{(VV,HV)} + 0.05\rho_{(VV,VH)} + 0.0\rho_{(VV,VV)}$, shown in the tomography of Fig. 23a, and employed the PMF as a decoherence medium (1 m of length) in a non-collective configuration. Then, the experimental input was transformed into the state in the tomography in the Fig.23b. Further, making use of the model already tested, the output state was calculated. We performed the calculation considering the following experimental parameters: retardation length $432\lambda_0$, central wavelength $\lambda_0 = 810$ nm, central frequency $\omega_0 = 4.65 \times 10^6$ GHz, and supposing a Gaussian beam shape in each photon path, obtaining the result shown in the Fig. 23c with a 92% of fidelity with the experimentally prepared state. By way of comparison, the total decreasing of the off-diagonal elements in the density matrix was observed, in the calculation of the behavior of the $|\Psi^+\rangle$ state after passing through a 1 m of decoherence medium, see Fig. 23d. The fidelities

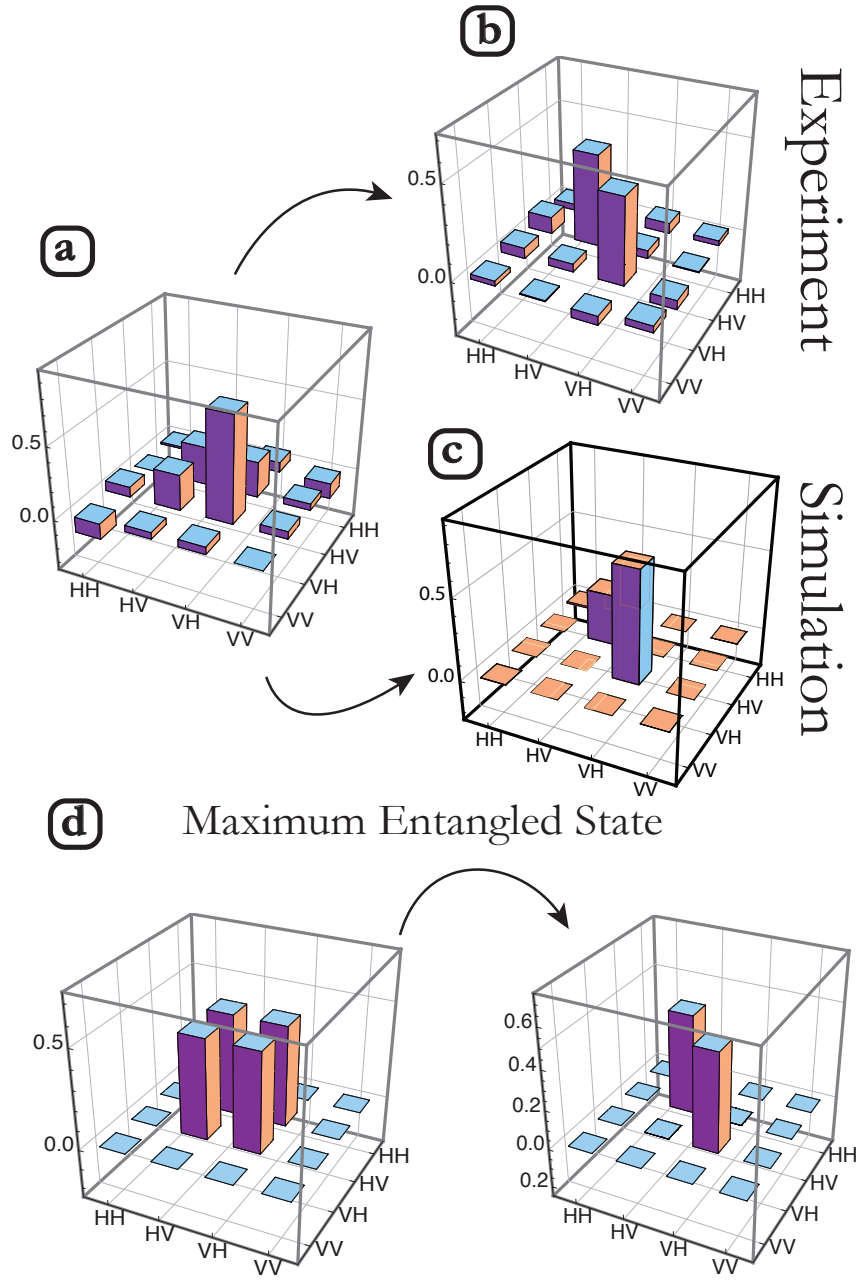

Figure 23: The experimental result of the quantum tomography is shown in (a) for the input state and (b) for the final state after the PMF. (c) The theoretical simulation of (b) achieves a 91.8% with the model here presented. (d) Here is shown the simulation of the $|\phi^+\rangle$ (maximally entangled state) behavior after the decoherence interaction with the environment.

between the experimental input (output) and calculated output, are presented in the table 22. As a matter of facts, we found a good accuracy in the description of the PMF as a tool of controlled decoherence over photons, which is supported by the fidelity between the calculated and the experimental output state which is 0.92.

Table 22: A summary of the fidelities calculated, the $F_{Exin-Exout}$ is the fidelity of the final experimental state against the initial experimental one, the $F_{Exin-Cout}$ is the fidelity of the experimental input state with the theoretical output expected state, and the $F_{Exout-Cout}$ is the fidelity of the final experimental state against the final calculated one.

State	$F_{Exin-Exout}$	$F_{Exin-Cout}$	$F_{Exout-Cout}$
ρ_{Exin}	0.46	0.56	0.92

Repeating the analysis performed previously (Fig. 22) but now on the experimental state, We estimated the fidelities as a function of the rotational angle of the environment to evaluate the effects of the experimental input, see Fig. 24a. Here, it is clear that no matter the value of the rotational angle the fidelity does not reach a value higher than ~ 0.58 at a fixed length (1 m) after the PMF environment, the state is not any more recoverable as the original input in a collective and non-collective scenario. We evaluate the entanglement in the Wooters metric [20], it means, the amount of information extractable from the measurement of only one part of the system, the quantifier of quantum entanglement used here is the *Entanglement of Formation* $\mathcal{E}$ (EoF). The maximum amount of information extractable of the state of a whole system, measuring only one of its parts is quantifiable through the *mutual information* [155]. In the quantum case this expression is given in terms of the von Neumann entropy and is represented by, $I(\rho_{AB}) = S(\rho_A) + S(\rho_B) - S(\rho_{AB})$. However, if we assume a generalization of the classical measure of correlations, considering a complete unidimensional set of projections acting locally on a subsystem B [19], appears another way to obtain the mutual information, which is not equivalent in general to $I(\rho_{AB})$ and define as $J(\rho_{AB})_{\{\Pi_j^B\}} = S(\rho_A) - S(\rho_{A|\{\Pi_j^B\}})$, where the conditional entropy is given by $S(\rho_{A|B}) \equiv S(\rho_{A|\{\Pi_j^B\}}) = \sum_j p_j S(\rho_{A|\Pi_j^B})$, with probabilities $p_j = \mathrm{T}r(\Pi_j^B \rho_{AB} \Pi_j^B)$, and the density matrix after the measurements on B is $\rho_{A|\Pi_j^B} = \frac{\Pi_j^B \rho_{AB} \Pi_j^B}{tr(\Pi_j^B \rho_{AB} \Pi_j^B)}$[19, 156, 157]. The minimal difference between the two versions of the mutual information is called the *Quantum Discord* $\mathcal{D}$. Complementary, the *classical correlation* (by Henderson & Vedral [18]) introduced a quantity which gives the account of the maximum classical information that is pos-

sible to be extracted from the subsystem A when a set of positive operator valued measurements have been carried out on the subsystem B. These quantifiers will give us the information about the quantumness of the information contained in the physical system.

The calculation of the quantum information correlations described above, for a fixed angle ($0\ rad$), as a function of the environment length shows that the classical correlations remain constant. However, the entanglement and the other quantum correlations decrease totally, for the experimental input at $100\lambda_0 \sim 0.23$ m. Initially, the experimental input has a value of 0.32 for $\mathcal{E}$ while the concurrence ($\tilde{C}$) was 0.26. After the quantum system passes through the PMF the entanglement for the output state has been decreased to 0.0024, and the concurrence to 0.032. Nevertheless, we calculated the correlations for the experimental input depending on both the environment length and the rotational angle. In the non-collective decoherence environment, an angular position ($0.94\ rad$) in which the $\mathcal{E}$ (Eof) is constant and as high as the initial value (0.32) emerge, as shown in Fig. 24c. Around this value, we observe a symmetric organization similar to a Gaussian distribution which offers a non-zero region for the entanglement useful for the implementation of protocols such as teleportation. Furthermore, just changing the environment to a collective decoherence a bowl shape is present in the behaviour of the entanglement and two angle values, $0\ rad$ and $1.57\ rad$, keep the value of the $\mathcal{E}$ (Eof) as high as the maximum available due to the characteristics of the state. However, the values in the bounds of the bowl shape are not the same, the first maximum has the same value as the original maximum input and is allocate at $0\ rad$, while the other end at $1.57\ rad$ has a value of about 0.21 for $\mathcal{E}$ (Eof), as shown in the Fig. 24d. Despite the existence of the entanglement is not completely crucial to achieve advantages, with quantum states over their classical counterparts, as has been theoretically and experimentally suggested [47, 150, 151], this demeanour open the possibility to implement conditions of death and revival of correlations, just changing the angular position of decoherence environments like the PMF. This evidence suggests the PMF as a useful tool to transport and control quantum information codified in polarisation basis, and even to integrate protocols of superactivation in which the control of correlations will require.

2.5 Conclusions

We show here that the physical behavior of a PMF corresponds with a long birefringent crystal which could be a useful device to control coherence on photonic qubits.

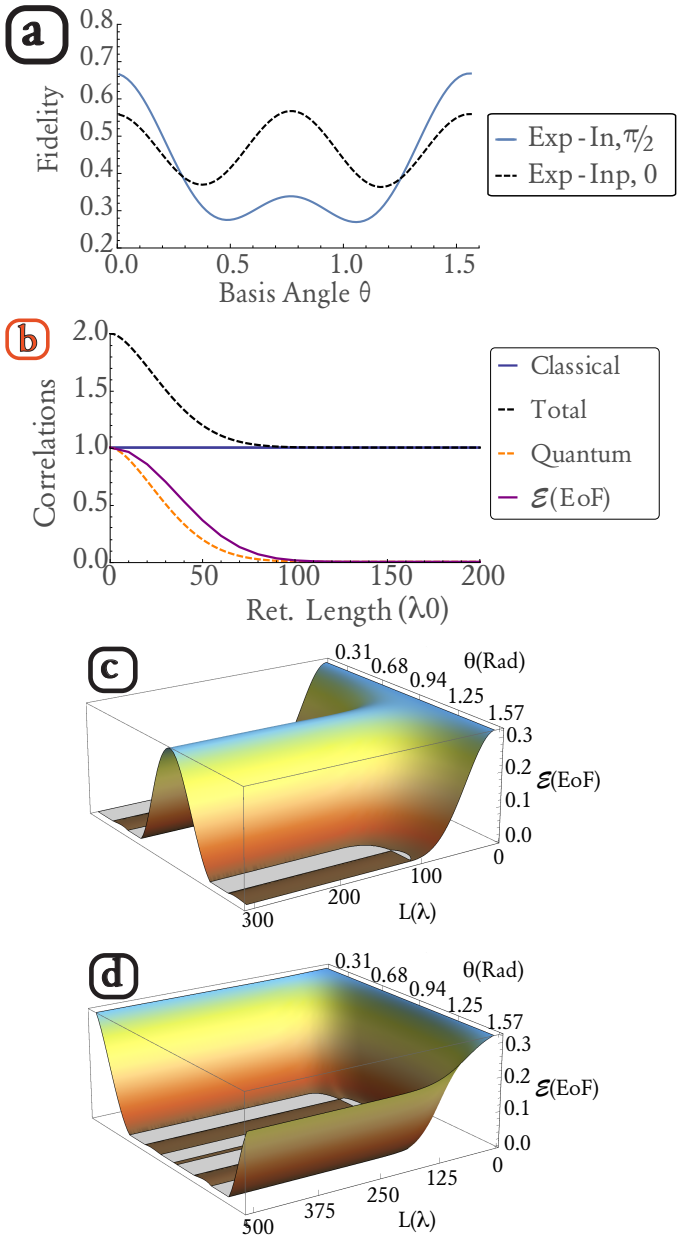

Figure 24: This plot shows the computed fidelities and correlations for the generated experimental input state in different scenarios: a) fidelities for both the collective ($\pi/2$) and independent (0) environments, and b) quantum correlations as a function of the retardation length for the non-collective decoherent environment with fixed rotational angle (0 rad); the total, classical, and quantum correlations (quantum Discord), and the entanglement of formation (EoF) $\mathcal{E}$. The latter is plotted as a function of the rotational angle and the retardation length for c) independent and d) collective environments.

It is important to remark that the quantum characteristics of the system counted by the quantum correlations, including entanglement, survive for the different scenarios (collective and non-collective) of decoherence without a critical dependence of the retardation length. However, the survival characteristic occurs only in the specific range of angles which depends on the symmetry of the environment. In this sense, the precise control of this angles will guaranty an efficient tool to control the decoherence which could be implemented together with protocols to enhance the robustness of the quantum state of interest. Experimentally we verify the accuracy of the model for a non-maximally entangled bipartite state of photons. Nevertheless, the experiment about the constant rotation of the PMF fiber has not been achieved yet due to the difficulty of controlling the rotation of both ends of the PMF fiber at the same time without inducing torsion in the material.

Chapter 3

QUANTUM PROTOCOL: QUANTUM GAMES WITH PHOTONS

3.1 Introduction

Game theory is a well established branch of mathematics whose formalism has a vast range of applications from the social sciences, biology, to economics. Motivated by quantum information science, there has been a leap in the formulation of novel game strategies that lead to new (quantum Nash) equilibrium points whereby players in some classical games are always outperformed if sharing and processing joint information ruled by the laws of quantum physics is allowed. We show that, for a bipartite non zero-sum game, input *local* quantum correlations, and *separable* states in particular, suffice to achieve an advantage over any strategy that uses classical resources, thus dispensing with quantum nonlocality, entanglement, or even discord between the players' input states. This highlights the remarkable key role played by pure quantum coherence at powering some protocols. Finally, we propose an experiment that uses separable states and basic photon interferometry to demonstrate the locally-correlated quantum advantage.

In 1944, von Neumann developed a formal framework of game theory [158], namely of understanding the dynamics of competition and cooperation between two or more competing parties that hold particular interests. In another seminal work, twenty years later, Bell discovered the intrinsic, fundamental nonlocal character of quantum theory [10], the fact that there exist quantumly correlated (entangled) particles whose measurement gives results that are impossible in classical physics—the so-called violation of Bell inequalities [11, 29]. Such Bell nonlocality and entanglement turned out to be of key relevance in the development of quantum information science and technology [2]. In fact, quantisation protocols for strategy games exemplify a physical process whereby entanglement or nonlocality are used as a fundamental resource [77, 159–171]. This establishes a connection between game theory and quantum information and, as such, introduces the existence of certain advantages over the foregoing classical results [77, 159–171], and extends the set of cases that find solution to the interaction formalism [158, 172, 173] into the quantum realm [159, 160]. Such quantum features are reflected, e.g., in the increase of efficiency and payoffs, emergence of new equilibria, and novel game strategies which

are simply not possible in the classical domain [164, 169–171]. These achievements signalled an interest about the nature of such a quantum advantage, and introduced questions related to the properties of physical systems and the mathematical structure that underlies the novel game strategies [77, 161–165]. Advantages of different kind became evident when quantisation rules were applied to different sort of games, and most of these scenarios pointed out quantum entanglement as a precursor of such effects [159, 160, 166–171]. Furthermore, Bell nonlocality has been recently shown

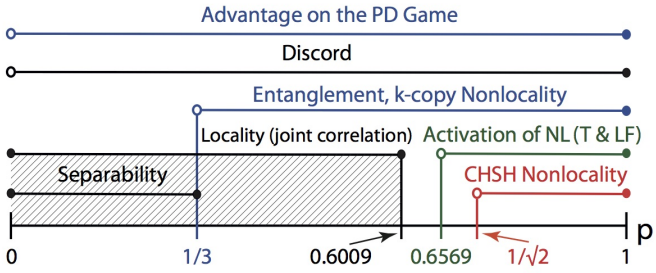

Figure 31: **Some quantum properties for two-qubit Werner-like states.** The schematics highlights locality (for the joint correlation), entanglement, CHSH-nonlocality, k-copy nonlocality, activation of nonlocality through tensoring and local filtering, and discord, for the Werner-like states $\rho_{W\text{-}l}(p) = p|\psi\rangle\langle\psi| + \frac{(1-p)}{4}\mathbb{1}\otimes\mathbb{1}$, $|\psi\rangle = \frac{1}{\sqrt{2}}(|00\rangle + i\,|11\rangle)$, $0 \leq p \leq 1$. These states can lead to a PD game advantage in the whole p-region.

to provide an advantage when deciding conflicting interest games [161–163]. In this regard, and mostly inspired by strategies of this sort, the activation of quantum nonlocality has been put forward [174, 175]. In particular, k-copy nonlocality or superactivation [176], and activation of nonlocality through tensoring and local filtering [177], although seminal for protocols based on nonlocality (e.g., quantum cryptography), are ultimately limited by the presence of entanglement [174]. This said, here we explore other kind of correlations that highlight local states as a possible resource for introducing a quantum advantage (see Fig. 31, shaded region). In particular, we ask whether there is, beyond entanglement or nonlocality, another underlying fundamental quantum feature as quantum coherence that warrants the emergence of the above-mentioned advantages. This consideration is also motivated by a recent experimental demonstration of a *zero-sum* game that exhibits a quantum gain for players that do not share entanglement [165].

Table 31: Payoff matrix for the PD game. The first (second) entry in the parenthesis denotes Alice's (Bob's) payoff. In the classical game, the strategy (*C*,*C*) defines a Pareto optimal (joint maximum gain), and (*D*,*D*) a Nash equilibrium.

Alice\Bob	C	D
C	(3,3)	(0,5)
D	(5,0)	(1,1)

The Prisoners' Dilemma

The Prisoners' Dilemma (PD) game is a celebrated bipartite non-zero sum game in classical game theory [172, 173] whereby two parties, say Alice (*A*) and Bob (*B*), have to decide between two strategies in an independent way: to defect (*D*) or cooperate (*C*). The retribution to the players decision is conditioned to the pair of choices, as shown in TABLE 31. The classical PD game reveals the existence of a set of strategies from which unilateral movement of the players diminishes their payoff—a Nash equilibrium (NE)— and a set of strategies whereby the players simultaneously do best—a Pareto optimal [172]. The dilemma arises due to the choice problem between the equilibrium and the optimal gain.

The PD sum game has been extended to the quantum domain by Eisert *et al.* [160], who proposed the use of initial maximally entangled states and unitary operators to define a strategy of purely quantum character that removes the decision dilemma [160]. Thus, the interaction between players can be cast in a quantum circuit that generates, via the action of a two-qubit operator $\hat{\mathcal{J}}(\delta)$, an initial state of the form:

$$|\psi_{in}(\delta)\rangle = \cos\frac{\delta}{2}\,|00\rangle + i\sin\frac{\delta}{2}\,|11\rangle\,, \tag{3.1}$$

where $\delta \in [0, \pi/2]$. Here, the possible outcomes of the classical strategies *C* and *D* are assigned to the computational basis states $|0\rangle$ and $|1\rangle$, respectively, and the strategy space of each player has a Hilbert space structure that couples through a tensor product. In Fig. 32(a), the operator $\hat{\mathcal{J}}(\gamma) = \exp\{i\gamma\hat{D}\otimes\hat{D}/2\}$ generates input entangled states[160]. After that, the players execute, unilaterally, their movements acting with the unitary parameterised operator ($i = A, B$),

$$\hat{U}_i(\theta_i, \phi_i) = \begin{pmatrix} e^{i\phi_i}\cos\frac{\theta_i}{2} & \sin\frac{\theta_i}{2} \\ -\sin\frac{\theta_i}{2} & e^{-i\phi_i}\cos\frac{\theta_i}{2} \end{pmatrix}, \tag{3.2}$$

particularly, $\hat{C} = \hat{U}(0,0)$ and $\hat{D} = \hat{U}(\pi,0)$ reduce to the classical strategies. Finally, an operator that destroys the entanglement generated by $\hat{\mathcal{J}}(\delta)$ is applied before projecting the output state onto the usual 4-dimensional space basis, giving

rise to a probability distribution above the four possible classical states, from which the expected payoff for each player is determined. The unitary operator Eq. (3.2) was introduced as a tool in the quantisation of non-zero sum games in [160], the so-called two-parameter strategy set. However, it was pointed out that such an operator defined a set of strategies that did not consider the natural counterstrategy of the quantum strategy $\hat{Q}$ (see Results), and hence did not represent a general conclusion for other quantisation formalisms [178]. Such an observation was addressed in [179], and incorporated to account for generalised two-parameter strategies in [180–182], also to consider the presence of dephasing [183], and for multiplayer quantum games [14,33]. In spite of this restriction on the strategic space defined by the strategy $\hat{Q}$ [160], Eq. (2) has been used as the starting point in more elaborated constructions that allow for the analysis of game behaviour in the quantum domain [180–182].

In this chapter, we analyse the PD game and demonstrate that *local*, and even further, *separable* quantum input states suffice to achieve an advantage over any classical strategy. This result is in contrast with previous approaches to quantum games that consider entanglement or Bell nonlocality as required resources for achieving a quantum advantage [159–162, 169]. Our finding is two-fold: First, we show that neither nonlocality nor entanglement can be regarded as the underlying fundamental properties responsible for the PD quantum advantage: we find purely discord-correlated states (zero entanglement) that also achieve such an advantage. Second, we show, by extending the set of Werner-like (*W-l*) states $\rho_{W\text{-}l}(p)$, that there exist (non-zero discord) input states for which the discord does not play any role at reaching this advantage. We also provide an optical setup that implements the locally-powered game strategy, and perform numerical experiments that demonstrate our findings. The analysis here presented is performed (although not limited) for the case of a two-parameter strategy set. In Discussion we address its extension to a more general three-parameter strategy set.

Local quantum correlations as a resource in the PD game.

In contrast to the use of entangled states as a strategy for 'quantising' the PD game (Fig. 32(a)) [160, 169], we explore a different feature and use the following input states (Fig. 32(b)) as the feeding resource for performing the quantum PD game:

$$\rho_{in}(p,\delta) = \frac{(1-p)}{4}\mathbb{I} + p\,|\psi_{in}(\delta)\rangle\,\langle\psi_{in}(\delta)|\,, \tag{3.3}$$

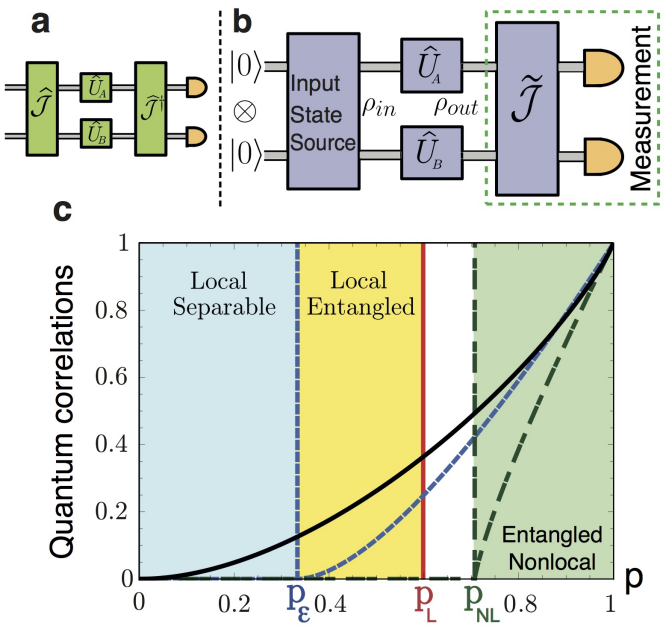

Figure 32: **Quantum Prisoners' Dilemma setup and classification of input correlations.** (**a**) Eisert *et al.* two players game protocol [160], (**b**) our setup uses a source of input $\rho_{in} \equiv \rho_{in}(p,\delta)$ (e.g., Werner-like) states, one qubit gates to represent the players' moves, and the measuring process (dashed rectangle). The measurement is taken as the projection onto the basis generated by $\tilde{\mathcal{J}} \equiv \tilde{\mathcal{J}}(\delta)$ in the usual 4-dimensional basis, (**c**) quantum correlations of input $\rho_{W\text{-}l}(p)$ states: discord $\mathcal{D}$ (solid-black), entanglement of formation $\mathcal{E}$ (dashed-blue), and CHSH-nonlocality (doubly-dashed green).

where $\mathbb{I}$ is the 4×4 identity matrix, and $p \in [0,1]$ acts as a control of the statistical mixture $\rho_{in}(p,\delta)$, and allows a direct comparison with the protocol of Fig. 32(a) [160]. In Fig. 32(b), the measurement process is made in a basis controlled by the same δ parameter, which allows the control of the degree of correlations that is 'destroyed' in the final step of the protocol, just before the projection onto the usual basis; i.e., the quantum operator $\tilde{\mathcal{J}} \equiv \tilde{\mathcal{J}}(\delta)$ inside the dashed rectangle of Fig. 32(b) is defined such that $\tilde{\mathcal{J}} = \hat{\mathcal{J}}^{\dagger}$in the same way as the entangling operator of Fig. 32(a) [160].

Every separable (non-entangled) state is local. However, there exist entangled states which are also local. For general two-qubit states of the form $\rho := p\rho' + \frac{(1-p)}{4}\mathbb{I}$, $0 \leq p \leq 1$, being ρ' an arbitrary two-qubit state, a locality bound has been reported [184]. In our protocol, we identify $\rho' = |\psi_{in}(\delta)\rangle \langle\psi_{in}(\delta)|$ such that $\rho \equiv \rho_{in}(p,\delta)$, and hence the locality bound reads $p_L \approx 0.6009$; i.e., entangled states with $p \leq p_L$ are local (see the full local-entangled (LE) region, yellow area in Fig.32(c)). Furthermore,

we also account for the set of local, but separable (LS) states (see the blue Region in Fig. 32(c)).

In what follows, we first specialise to *W-l* states $\rho_{in}(p) := \rho_{in}(p, \pi/2) \equiv \rho_{W\text{-}l}(p)$ as inputs, and the correlation parameter δ is fixed to $\pi/2$ for the initial state, and only varied at the measurement. We then generalise our results to input states $\rho_{in}(p, \delta)$, and consider the δ parameter being varied at both the input state and the final measurement process. For comparison, we also compute metrics to quantify quantum correlations such as discord $\mathcal{D}$, entanglement of formation $\mathcal{E}$, and CHSH-nonlocality; see Methods section for definitions.

3.2 Theoretical Results

Quantum local PD payoffs for the Werner-like states.

The quantum properties of the states $\rho_{in}(p)$ are shown in Fig. 32(c), where several distinctive regions can be identified: *local-separable* ($0 \leq p \leq p_{\mathcal{E}} = 1/3$), local-entangled ($1/3 < p \leq p_L \approx 0.6009$), and entangled-nonlocal ($p \geq p_{NL} = 1/\sqrt{2}$) states (see Methods section). Furthermore, the *W-l* states also highlight quantum correlations at zero entanglement ($p \leq 1/3$) [93], which are captured here by means of the discord [19, 156, 157]. Building on this, we take an approach that is not based on entangled [160] or nonlocal [161, 162] input states. Instead, we choose local-separable $\rho_{in}(p \leq 1/3)$ input states ($\mathcal{E} = 0$, Fig. 32(c)), while the players' quantum moves remain ruled by $\hat{U}_i$, to test whether a quantum strategy based on such states removes the choice problem in the PD game. We calculate the corresponding PD payoffs for the *W-l* input states; for player A this reads:

$$\begin{aligned}\pi_A[\theta_i, \phi_i, p, \delta] \;=\; & \frac{9}{4} - \frac{p}{4}\Big\{ f(\theta_{AB}) + g(\theta_{AB}) \sin\left(\phi_A + \phi_B\right) + \\ & 4 \sin\delta \Big[f^2\Big(\frac{\theta_{AB}}{2}\Big) \cos 2(\phi_A + \phi_B) - g^2\Big(\frac{\theta_{AB}}{2}\Big) + \\ & \frac{5}{2}\Big(\partial_{\frac{\theta_B}{2}} g\Big(\frac{\theta_{AB}}{2}\Big)\Big)^2 \cos 2\phi_B - \frac{5}{2}\Big(\partial_{\frac{\theta_A}{2}} g\Big(\frac{\theta_{AB}}{2}\Big)\Big)^2 \cos 2\phi_A - \\ & g(\theta_{AB})\Big(\frac{3}{4}\sin\left(\phi_A - \phi_B\right) + \partial_{\phi_B} g(\phi_{AB})\Big)\Big]\Big\},\end{aligned} \tag{3.4}$$

with $f(\theta_{AB}) := \cos\theta_A \cos\theta_B$ and $g(\theta_{AB}) := \sin\theta_A \sin\theta_B$. Player B's payoff is obtained from equation (3.4) by exchanging indexes A and B ($i = A, B$). In Fig. 33, we plot the players' payoffs as function of their strategies. We obtain a payoff distribution for which the solution criteria can be evaluated in order to find equilibrium strategies [172]; the classical solution criteria remain valid in the quan-

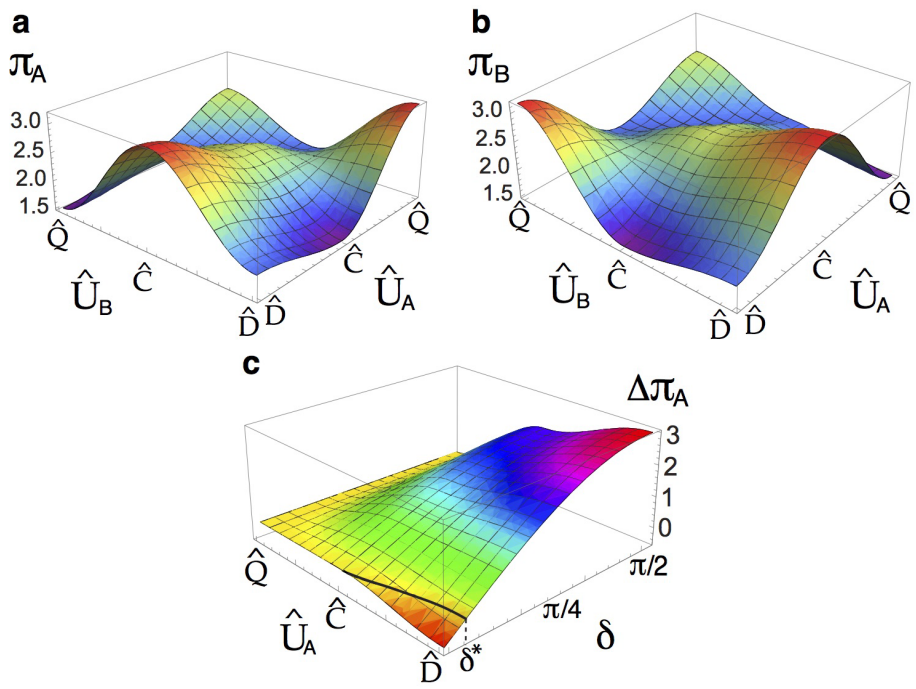

Figure 33: **Players payoffs and Nash inequality for the quantum PD game.** (**a**) Alice and (**b**) Bob's payoff functions for the initial mixed-separable-discorded state $\rho_{in}(p = 1/3)$ as function of the strategy space; $(\hat{Q}, \hat{Q})$, with $\hat{Q} = \hat{U}(0, \pi/2)$, is the quantum strategy that removes the dilemma. (**c**) The left-hand-side value in equation (3.5), $\Delta\pi_A$, is plotted as a function of the players strategies and the measurement parameter δ. The Nash inequality takes positive values almost anywhere the surface, except at the red region below the black curve; e.g, for the particular strategy $(\hat{D}, \hat{Q})$, the inequality is not satisfied for $\delta < \delta^* = \arcsin(1/7)$. Since p is just a global factor in equation (3.5), this behaviour holds even for input states with zero entanglement.

tum context, and thus we introduce a $(\hat{Q}, \hat{Q})$ strategy, with $\hat{Q} = \hat{U}(0, \pi/2)$, that removes the choice problem in the PD game [160]. This result arises 'naturally' by fixing $\delta = \pi/2$ and $p = 1$ at both the input state and the measurement stage of our protocol. A thorough examination of the payoff functions, equation (3.4), reveals that whilst p controls the magnitude of the players' payoff, δ modifies the shape of their distributions. This demonstrates that our *local* input state ($p \leq 1/3$) keeps unaffected the equilibrium properties of the quantum version of the PD game as shown in Fig. 33(a) and (b) for the particular case $p = 1/3$ and $\delta = \pi/2$. We then ask what happens to the Nash Equilibrium if both p and δ are modified at a given time, for which we next compute the corresponding Nash inequality.

Nash equilibria of the game.
In a finite game of normal form $\{N, \{S_i\}_{i=0}^n, \{\pi_i\}_{i=1}^n\}$, a strategy chain s^* is NE to the i-th player if and only if $\pi_i(s_i^*, s_{-i}^*) \geq \pi_i(s_i, s_{-i}^*), \forall s_i \in S_i$, where S_i is the strategy space of player i, and π denotes the payoff function. We evaluate this criterion with respect to the quantum strategy $(\hat{Q}, \hat{Q})$, and for player A we obtain

$$\begin{aligned} \Delta\pi_A &:= \pi_A(\hat{Q}, \hat{Q}) - \pi_A(s_i, \hat{Q}) \\ &= p\Big[\sin\delta\Big(1 + \cos^2\frac{\theta_A}{2}\cos 2\phi_A + \frac{5}{2}\sin^2\frac{\theta_A}{2}\Big) + \frac{\cos\theta_A - 1}{4}\Big] \geq 0. \end{aligned} \tag{3.5}$$

Note that $\pi_A(\hat{U}, \hat{U}) \equiv \pi_A(\theta_i, \phi_i, p, \delta)$. We reach the same result for $\Delta\pi_B$. This inequality does not depend on the value of p, and hence it holds even for zero entanglement input states; since we are interested in the quantum case, $p = 0$ is discarded. Thus, δ becomes a crucial factor when deciding whether this Nash inequality is satisfied. We highlight the novelty of the result equation (3.5): the quantum advantage, here reported, *does not* require neither the maximal entanglement condition $\delta = \pi/2$ (nor any $\mathcal{E} > 0$ at all), nor that of nonlocality to be fulfilled; instead, the quantum strategy $(\hat{Q}, \hat{Q})$ is a NE when the player A moves its strategy from $\hat{C}$ to $\hat{D}$, for $\sin\delta \geq f(\theta) = (1 - \cos\theta)/(11 - 3\cos\theta)$. For the specific strategy $(\hat{D}, \hat{Q})$, the critical value δ^* is given by $\sin\delta^* = f(\pi) = 1/7$, as explicitly shown in Fig. 33(c). For clarity, in Fig. 34(a) we plot the player A's payoff for the particular $(\hat{Q}, \hat{Q})$ (brown-upper) and $(\hat{D}, \hat{Q})$ (blue-lower) strategies, in terms of the entanglement δ and mixing p parameters. The vertical-dashed line on the $p = 1$ plane marks the critical δ^* at which the dominant strategy, i.e., the strategy giving a NE, changes. Hence, two regions arise for any $p > 0$: i) $\delta \geq \delta^* = \sin^{-1}(1/7)$, the quantum strategy $(\hat{Q}, \hat{Q})$ is the NE and Pareto optimal such that the choice dilemma is removed as can be seen for π_A in Fig. 34(b); ii) $\delta < \sin^{-1}(1/7)$, the game does not present a strict NE but two at $(\hat{Q}, \hat{D})$ and $(\hat{D}, \hat{Q})$, the payoff for player A is greater when choosing the former rather than the latter strategy, as shown in Fig. 34(c) (the opposite arises for player B–not shown). This asymmetry implies again a choice problem in the game such that the dilemma is not removed in this region. Figures 34(b) and (c) have been obtained for $p = 1/3$, and show that the advantage over any classical strategy is still achieved for separable states.

We stress that the quantum advantage in the PD game, here reported, is not a consequence of entanglement at the input state of the game. In general, as long as $\rho_{in}(p)$ can be generated, the quantum solution for removing the prisoners' dilemma is achieved. This means that, for these particular input states, the quantum advantage in the non-zero sum game has been extended to a more general kind of quantum

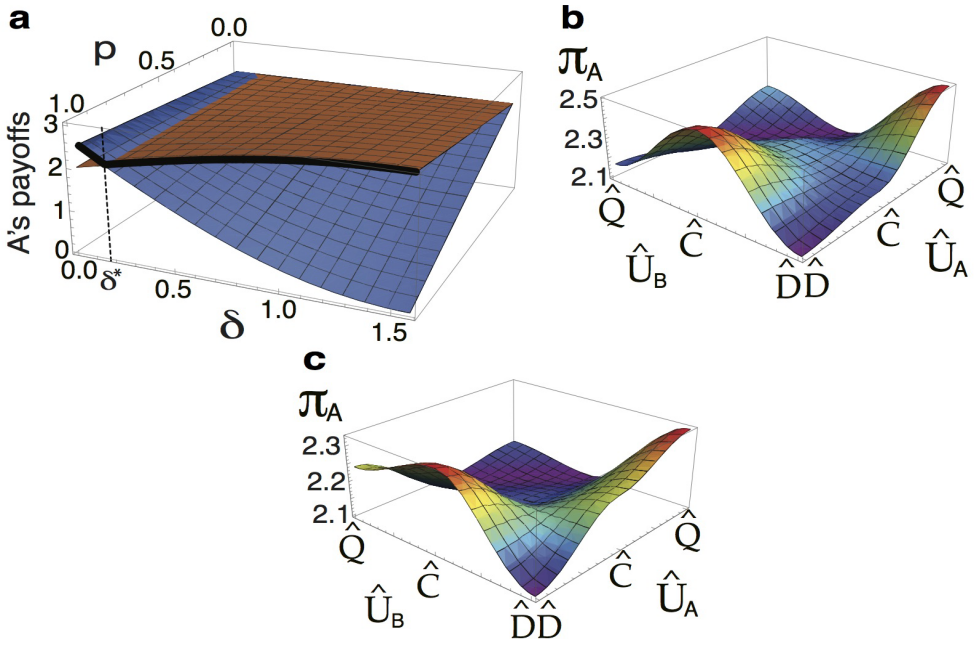

Figure 34: **Nash equilibrium analysis for the Werner-like initial state:** (**a**) Player A's payoffs for $(\hat{Q},\hat{Q})$ (brown-upper), and $(\hat{D},\hat{Q})$ (blue-lower) strategies as functions of both the entanglement δ and the mixing p parameters. The black-solid curve at $p=1$ shows the behaviour of the Nash equilibrium before and after the critical point $\delta^*=\sin^{-1}(1/7)$ (vertical-dashed line). Strategies space profile for player A payoffs with (**b**) $\delta=0.2>\delta^*$, and (**c**) $\delta=0.05<\delta^*$ for the mixed input state $\rho_{in}(p=1/3)$.

correlations, beyond entanglement, here quantified by the quantum discord. This is indeed emphasized, as mentioned above, by the quantum properties displayed by the states equation (3.3), as plotted in Fig. 32(c) for $\delta=\pi/2$. Indeed, for $p\leq p_L$, $\rho_{in}(p)$ is local; furthermore, if the resource states $p\leq 1/3$, then the input states are local-separable and not related whatsoever to either entanglement or nonlocality. In Fig. 32(c), we also find that discord is present in the whole p-region $0<p\leq 1$. This said, a new question arises: how essential is quantum discord as a resource for the quantum advantage here reported? To address this question, we extend our analysis to input states with a more general structure, as given by $\rho_{in}(p,\delta)$.

Generalisation to input states $\rho_{in}(p,\delta)$.

If we now control the input state degree of correlations by varying δ in equation (3.3), Nash inequality holds as follows: for the strategy $(\hat{D},\hat{Q})$ (or equivalently, for $(\hat{Q},\hat{D})$), $\Delta\pi_A:=\frac{p}{2}\left(-3+5\cos 2\delta_1\right)\geq 0$, and for the strategy $(\hat{Q},\hat{Q})$, $\Delta\pi_A:=$

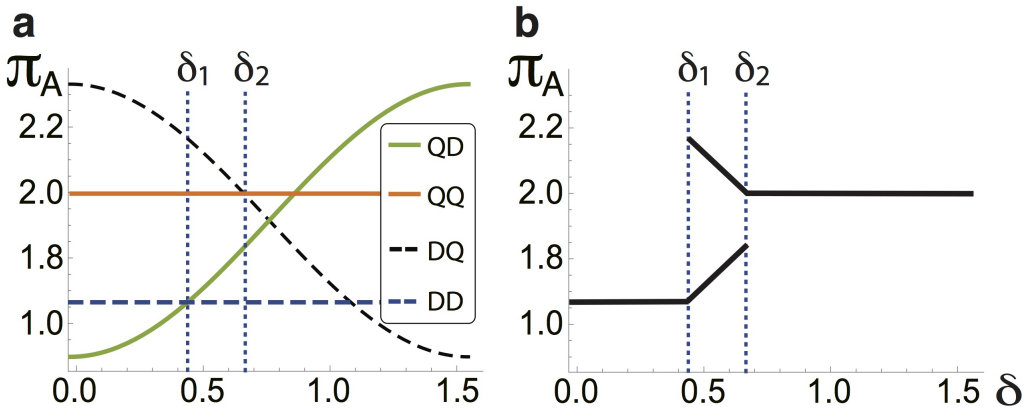

Figure 35: **Payoffs for general states $\rho_{in}(p,\delta)$:** (**a**) the control of the initial state correlations, and $\tilde{\mathcal{J}}(\delta)$ imply thresholds at $\delta_1 = \sin^{-1}\sqrt{1/5}$, and $\delta_2 = \sin^{-1}\sqrt{2/5}$, (**b**) strategies reaching the Nash equilibrium in the regions defined by δ_1 and δ_2.

$\frac{p}{2}(1 - 5\cos 2\delta_2) \geq 0$. Three regions arise, as indicated in Figs. 35(a) and 35(b), by means of $\delta_1 = \sin^{-1}\sqrt{1/5}$, and $\delta_2 = \sin^{-1}\sqrt{2/5}$. The payoff for the players in the $(\hat{Q},\hat{Q})$ strategy will be constant in the same way that for the $(\hat{D},\hat{D})$ strategy. This behaviour is crucial for values greater than δ_2 because the Nash equilibrium is reached, and the dilemma is removed. The key parameters δ_1 and δ_2 obtained here for the considered mixed states coincide with those reported by Du *et al.* [169] for just pure states. This is because p only affects the size but not the shape of the payoff functions. For example, by computing the Nash inequality for A's payoff in the $(\hat{Q},\hat{Q})$ and $(\hat{D},\hat{Q})$ strategies, p holds as a global parameter and does not affect the bounds of the inequality. Finally, we show that by considering the *W-l* states $\rho_{in}(p)$ and just controlling the degree of correlations in the final operator $\tilde{\mathcal{J}}(\delta)$, we reach the quantum advantage which removes the game dilemma for δ values smaller than those reported before [169], and, crucially, $\delta^* < \delta_2$, even for separable states. For the sake of completeness, we analyse the quantum advantage in the PD game, i.e., the two regions defined by the δ_2 bound, from which the quantum $(\hat{Q},\hat{Q})$ strategy removes the dilemma, in terms of the quantum properties of the input $\rho_{in}(p,\delta)$ states. We plot the entanglement of formation (Fig. 36(a)), non-locality given by CHSH inequality violation, k-copy nonlocality (SA) [176], and activation through tensoring and local filtering [177] (NL Act.) (Fig. 36(b)), and quantum discord (Fig. 36(c)), all of them as functions of the correlation δ, and mixing p parameters (see the Methods section for definitions). We distinguish two principal regions in Fig. 36: Region I ($\delta \geq \delta_2$, and $p \leq p_L$, upper left rectangles) in which it is possible to find local-entangled states, and more interestingly, separable states which are able to remove the choice

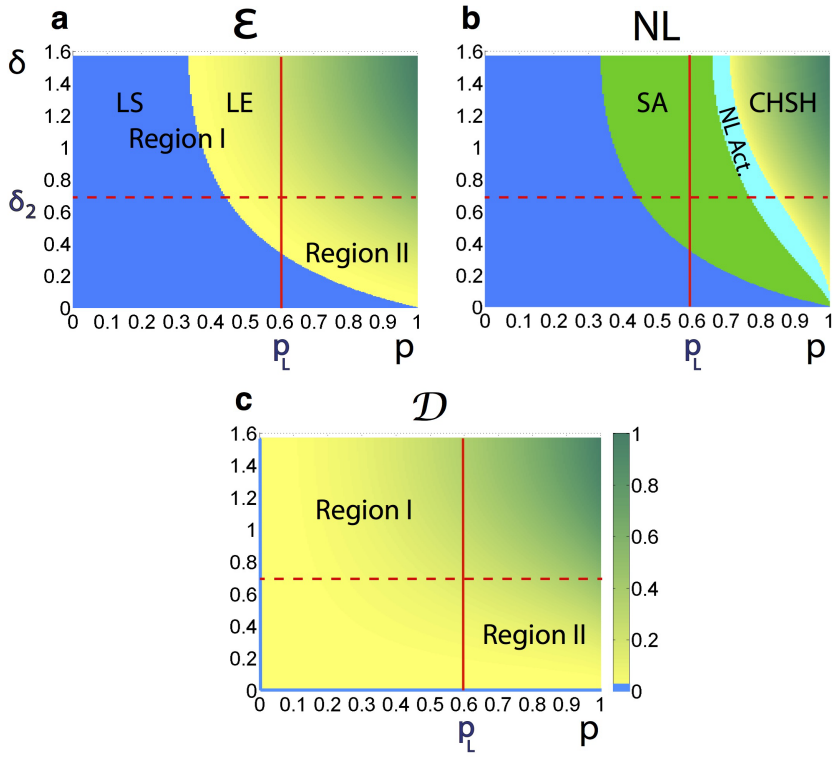

Figure 36: **Quantum properties of the input states $\rho_{in}(p,\delta)$ and quantum advantage bound.** As a function of δ and p, we plot: (**a**) Entanglement of Formation ($\mathcal{E}$): the blue area represents the set of separable and therefore local states, and all the states $p \leq p_L \approx 0.6009$, as depicted by the vertical line $p = p_L$, are also local (for the joint correlation) [184]; these allow the identification of the local-entangled (LE) region of states, (**b**) non-locality (NL) properties: $CHSH$ inequality violation, k-copy nonlocality or superactivation (SA) of non-locality (green-solid area), and activation of non-locality (NL Act.) through tensoring and local filtering (cyan-solid area), and (**c**) quantum discord ($\mathcal{D}$): the Region I ($\delta \geq \delta_2$, $p \leq p_L$, upper left rectangles) spans non-zero discord states that even though local, allow a quantum advantage; the Region II ($\delta < \delta_2$, $p > p_L$, lower right rectangles) portrays non-local and local non-zero discord states for which the choice dilemma is not removed. The bound $\delta \geq \delta_2 = \sin^{-1}\sqrt{2/5}$, for which the quantum advantage holds, is depicted by a horizontal red-dashed line.

dilemma as they admit the quantum $(\hat{Q},\hat{Q})$ strategy to be the NE and Pareto optimal (see Fig. 35). This implies that there exist local quantum states that can be seen as a powering resource for performing quantum strategies that outperform any possible classical strategy in a PD game. In Region II ($\delta < \delta_2$, and $p > p_L$, lower right rectangles), there are states with different nonlocal properties (Fig. 36(a) and (b)) admitting no quantum advantage for removing the choice dilemma in the PD game.

It is worth pointing out that the nonlocal properties here analysed are bounded by entanglement, i.e., all of them cover sets of states smaller than or equal to the one representing the entangled states. On the other hand, Fig. 36(c) clearly shows that even for some discord-correlated states, the dilemma is not removed in this region, hence explicitly showing the existence of non-zero discord states that exhibit no quantum advantage. Thus, discord on its own cannot be regarded as a fundamental measure (beyond entanglement) that underpins the quantum advantage.

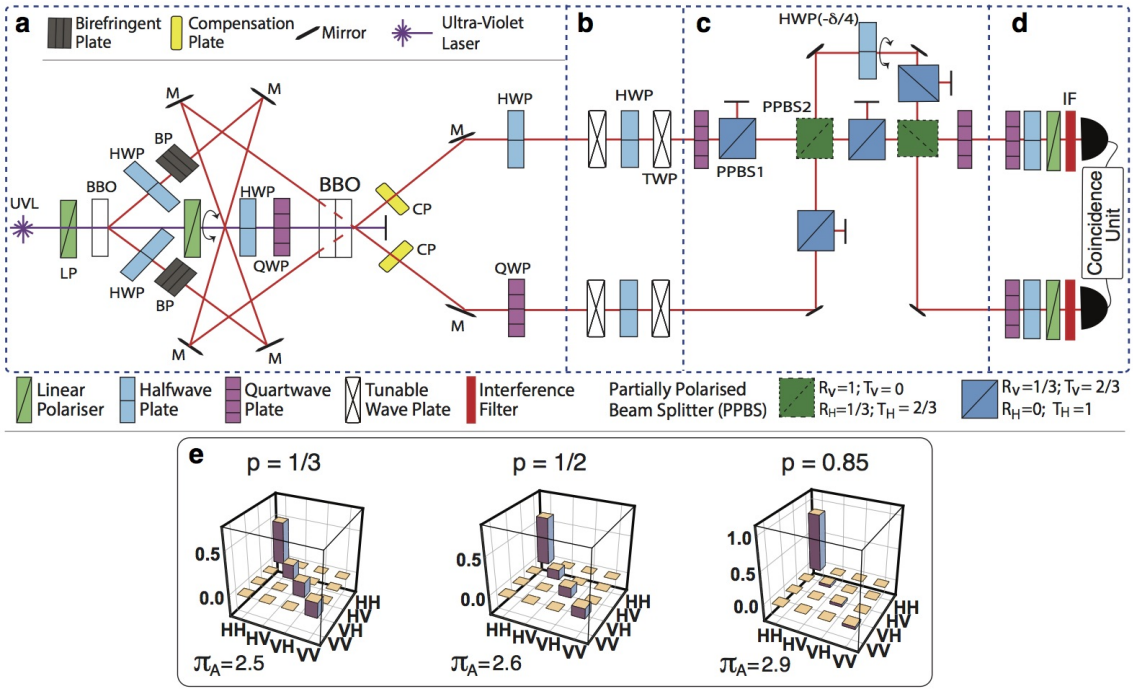

Figure 37: **Experimental setup to demonstrate the local quantum advantage in the PD game.** Dashed boxes: (**a**) protocol that generates the input states starting from $|VV\rangle$: a Werner state is created and successive applications of an X and a π-phase gates lead to $\rho_{in}(p)$ (equation (3.3)), (**b**) the individual action of the players on each qubit, $\hat{U}_A$ and $\hat{U}_B$, (**c**) implementation of the quantum operations $\pi/2$-phase shift, C-NOT, $e^{-i\frac{\delta}{2}Y} \cdot Z$, C-NOT, $\pi/2$-phase shift (Y and Z are the usual Pauli gates), (**d**) the standard tomography protocol to reconstruct the final state which gives the players payoffs, (**e**) expected tomographies and player A's payoffs for separable ($p = 1/3$), local-entangled ($p = 1/2 \leq p_L$), and non-local ($p = 0.85 > p_{NL} = 1/\sqrt{2}$) input states; $\delta = \pi/2$, and chosen strategy $(\hat{Q}, \hat{Q})$.

3.3 Experimental proposal for demonstrating the locally-correlated quantum advantage.

The described quantum PD game based on local input states can be experimentally tested, e.g., by optical means. In Fig. 37 we give a setup that uses an optical encoding of horizontal ($|H\rangle$) and vertical ($|V\rangle$) polarisation states as qubits. The experimental process is divided into four main steps: preparation of the initial state (Fig. 37(a)), setting the players' strategies (Fig. 37(b)), tailoring a quantum operation on the output state (Fig. 37(c)), and detection of the game's result via quantum state tomography (Fig. 37(d)). In Fig. 37(a), a laser beam is sent, through a linear polariser defining the input, to the first nonlinear crystal (BBO-β barium borate type I) as $|H\rangle$. After the first BBO crystal the state holds $|VV\rangle$, we then use a couple of half-wave plates (HWP) rotated azimuthally $\theta = \pi/8$ to apply a Hadamard gate to each qubit such that $|V\rangle$ is transformed into $\frac{1}{\sqrt{2}}(|H\rangle - |V\rangle)$, and hence a superposition of all basis states is generated [61]. Sequentially, a birefringent environment (a set of quartz or BBO plates) is applied to each photon path and tuned to the maximum decoherence, which only affects the off-diagonal elements of the density matrix [41, 54, 61], thus setting the state $\rho_1 = \mathbb{I}/4$. After the first BBO crystal, the non-converted remaining light is transformed into $\frac{1}{\sqrt{2}}(|H\rangle + |V\rangle)$ by a HWP and pre-compensated through a quarter-wave plate (QWP), then directing it to a second set of BBOs which comprises a couple of crystals with mutually-perpendicular optical axes to create a maximally entangled state [64]. By combining the rays that passed through the first and second BBOs, the Werner state $\rho = p|\Psi^-\rangle\langle\Psi^-| + \frac{1-p}{4}\mathbb{I}$ is produced, where $|\Psi^-\rangle = \frac{1}{\sqrt{2}}(|HV\rangle - |VH\rangle)$ is a Bell basis state. We next apply a σ_x-gate to the upper path through a HWP with $\theta = \pi/4$ as a rotating angle, thus transforming $|\Psi^-\rangle$ into the $|\Phi^+\rangle = \frac{1}{\sqrt{2}}(|HH\rangle + |VV\rangle)$ Bell state. Then, a $\pi/2$-phase shift gate is applied to the lower path using a QWP with $\theta = 0$ and hence producing $\rho_{in}(p, \pi/2)$ (equation (3.3)), the input state of our quantum PD game. Here, p can be tailored by allowing control of the intensity ratio between the converted light in the first BBO and the converted light in the second BBOs [61]: $0 \leq p \leq 1$ could be tuned by adjusting the rotation angle of a linear polariser with respect to its optical axis located on the unconverted path just after the first BBO; p can then be measured from the total irradiance (I_T) after the second conversion, and the partial irradiance (I_P) of the light converted in the first BBO, as $p = \frac{I_T - I_P}{I_T}$. Thus, the local $\rho(p = 1/3)$ input state can be achieved by setting $I_P = 2I_T/3$.

Figure 37(b) implements the actions of the players (operator $\hat{U}_i$ in equation (3.2)) by means of a set of wave plates, where the phase ϕ corresponds to the retarding angle of

each plate, i.e., $\phi = \pi$ for a HWP, and $\phi = \pi/2$ for a QWP. The angle θ corresponds to the perpendicular rotation of the centre half wave plates, referred to their optical axis. In Fig. B1, we use a special kind of wave plate that does not have a defined angle ϕ, the so-called tunable wave plate (TWP), which allows us to generate $0 \leq \phi \leq 2\pi$. In Fig. 37(c) we start from the output state ρ_{out} (Fig. 32(b)) generated in the previous step. To test the NE inequality, equation (3.5), we apply a phase gate by means of a QWP on the lowermost path, and resort to the use of a quantum Controlled-NOT gate which comprises a set of three partially polarised beam splitters (PPBS) [185–188], where the two PPBS1s completely transmit the photons with $|H\rangle$ and $1/3$ of the $|V\rangle$ polarisation, while the PPBS2 completely reflects $|V\rangle$ and $1/3$ of the $|H\rangle$ polarisation. Then, a HWP with $\theta = -\frac{\delta}{4}$ acts as a controller of the δ parameter over the control output of the first C-NOT gate (uppermost path), and additionally, a symmetrical arrangement of another C-NOT, and a QWP($\theta = 0$) completes the quantum operator $\tilde{\mathcal{J}}(\delta)$. Finally, the measurement process is depicted in Fig. B1(d); a standard quantum state tomography protocol [100], which requires a set of 16 measures is performed in order to obtain the final state of the system and the result of the game.

In Fig. 37(e), we have performed a numerical experiment in order to obtain the Alice's payoffs based on the local-separable $\rho_{in}(p = 1/3)$, local-entangled $\rho_{in}(p = 1/2)$, and the non-local $\rho_{in}(p = 0.85)$ states, for the $(\hat{Q}, \hat{Q})$ strategy. In so doing, we have considered the following feasible experimental parameters: laser wavelength $\lambda = 351$ nm, converted central wavelength $\lambda_0 = 702$ nm, retardation length $153\,\lambda_0$ and $306\,\lambda_0$, spectral bandwidth $\Delta\lambda = 10$ nm, and birefringent plates with a constant difference of $\pi/2$ between them for their rotation angles. These simulations are in excellent agreement with the result that is obtained by simply following the abstract circuit of Fig. 32(b). We would like to stress that the main contribution of this work is that the "prisoner's dilemma quantum advantage" is achieved in the three different considered scenarios, regardless the nonlocal or entanglement features of the considered quantum input states. Thus, the mentioned experiment is currently a proposal. This said, it is amenable to experimental demonstration with currently available quantum optics and Information technologies (e.g., see appendix B for a description).

3.4 Discussion

Purely *local* and/or *separable* input quantum states have been harnessed as a resource in the PD game, and we have shown that such a strategy gives a clear advantage

over the original bipartite non-zero sum game that makes use of just classical resources. In particular, we have also shown that neither entanglement nor any nonlocal property is strictly required at the input of the game in order to achieve a quantum $(\hat{Q}, \hat{Q})$ strategy that removes the PD dilemma and hence outperforms any classical strategy. First, our results have been explored for Werner-like states with known nonlocal properties, but also extended to a more general class of correlation-parameter-dependent states (equation (3.3)). Second, we have shown that within the set of discord-correlated states, there exist some states for which the PD choice problem is not removed, thus implying that quantum discord is neither a necessary condition for achieving the above-described quantum advantage. These results point out the interesting and relevant role played by separable quantum states (and therefore locality) when designing quantum strategies that outperform those based on classical resources, and suggest that such a key resource actually arises from basic quantum interference mechanisms, i.e., quantum coherence, whose description as a physical resource is a rapidly growing conceptual development [189].

Even though we have focused in the PD version in which both players choose their strategies from the particular set of two-parameter strategies (Eq. (2)), we next demonstrate that our findings can be extended to more general scenarios [180, 181, 183]. In the case of a three-parameter set of strategies, it is known that there is no pure strategy being a Nash equilibrium because for every strategy of Alice, there exists a counterstrategy available for Bob [178]. However, it is possible to have a mixed strategy Nash equilibrium that is non unique [180]. If we assume that Alice and Bob can carry out the following set of strategies [180, 183]

$$U(\theta, \phi, \psi) = \begin{pmatrix} e^{i\phi}\cos(\theta/2) & ie^{i\psi}\sin(\theta/2) \\ ie^{-i\psi}\sin(\theta/2) & e^{-i\phi}\cos(\theta/2) \end{pmatrix}, \tag{3.6}$$

they can reach a mixed equilibrium when Alice chooses $U(0, 0, \psi)$ and $U(0, \pi/2, \psi)$ with the same probability, and Bob chooses $U(\pi, \phi, 0)$ and $U(\pi, \phi, \pi/2)$ with the same probability [180, 183]. Despite the lack of uniqueness of the above equilibrium, a unique equilibrium can be found by applying the local point effect [190]. However, our main aim is to show that our findings can be extended to this scenario and that the major analysis on the role of quantum (e.g. Bell non-local, entangled local, or just local) correlations holds. For doing so, we demonstrate that the optimality of the mixed quantum strategies with respect to the classical strategies behave in the same way as for the case of the two-parameter strategy considered above.

Assuming that Alice and Bob choose the aforementioned quantum mixed strategies

and apply them to our initial input state $\rho_{in}(p,\delta)$, Alice's payoff becomes:

$$\pi_A(M_A^{\text{Quan}}, M_B^{\text{Quan}}) = \frac{1}{4}\left(9 - 4p - 5p\cos\left(2\delta\right)\right), \tag{3.7}$$

where $M_A^{\text{Quan}} = \{\frac{1}{2}, \frac{1}{2}, U(0,0,\psi), U(0,\pi/2,\psi)\}$ and
$M_B^{\text{Quan}} = \{\frac{1}{2}, \frac{1}{2}, U(\pi,\phi,0), U(\pi,\phi,\pi/2)\}$. Now, assuming that Alice decides to play the classical mixed strategy $M_A^{\text{Class}} = \{\frac{1}{2}, \frac{1}{2}, \hat{C}, \hat{D}\}$ instead of the above quantum mixed strategy, while Bob keeps his quantum movement, it is straightforward to show that the inequality $\Delta\pi_A = \pi_A(M_A^{\text{Quan}}, M_B^{\text{Quan}}) - \pi_A(M_A^{\text{Class}}, M_B^{\text{Quan}}) \geq 0$ leads to

$$\frac{p}{4}\left(1 - 3\cos^2\delta\right) \geq 0. \tag{3.8}$$

This comparison between the quantum mixed strategies and the classical one shows that the new payoff inequality does not depend on the input state parameter p. Hence, our findings regarding the actual role played by quantum (local or non-local) correlations in game behaviour remain valid for this more general scenario. Finally, we remark that a description of the focal equilibrium available in the considered three-parameter strategy is beyond the scope of this work and is left as a further development for the interested reader.

The simulated experiment for computing the tomography of the final states of the game, as well as their associated payoff functions (Fig. B1), show that our findings are amenable (although not restricted) to being tested with current photonics technology, as the involved optical devices follow well established, achievable laboratory parameters. We stress that since our PD protocol makes use of disentangled states as captured by equation (3.3), their optical generation, via the component $\rho' = |\psi_{in}(\delta)\rangle\langle\psi_{in}(\delta)|$ of the mixed state $\rho_{in}(p,\delta)$, can be facilitated by the fact that 'imperfect' *W-l* states are more likely to be obtained in the laboratory, in addition to the fact that different (p,δ)-states can be achieved by varying the tilt angle of the second BBO, and by modifying the length of the compensator plates in Fig. B1, thus facilitating the photon interferometry here devised to demonstrate the quantum advantage.

3.5 Concluding Remarks

A general finite-dimensional bipartite AB system is represented by a density matrix or quantum state $\rho \in D(\mathbb{C}^{d_A} \otimes \mathbb{C}^{d_B})$, with $d_A, d_B \geq 2$, where $D(\mathbb{H}) := \{\rho \in PSD(\mathbb{H}) | \text{Tr}(\rho) = 1\}$ stands for the set of density matrices of the complex Hilbert space $\mathbb{H}$, with PSD the set of *positive semidefinite* complex matrices, i.e., the

matrices ρ such that $\forall\,|\phi\rangle \in \mathbb{H} : \langle\phi|\,\rho\,|\phi\rangle \geq 0$. Here, we focus on the quantum properties of our two-qubit input states $\rho_{in}(\delta, p)$ as shown in Fig. 36, where we have emphasised the locality region ($p \leq p_L$) which is limited by the value $p_L \approx 0.6009$ (vertical line), according to the best known bound [184]. This locality means that a Hidden Variable Model can be found to reproduce the same joint correlation of Alice and Bob $\mathrm{Tr}(A \otimes B\rho_{AB})$ predicted by quantum mechanics, where A and B are observables on the state of Alice and Bob, respectively [184]. The aforementioned nonlocal quantum features of the input states plotted in Fig. 36 for performing the PD game are described in the section C.1 and appendix A.

We remark that we have mainly focused on generating the sufficient conditions for the purely quantum strategy $(\hat{Q}, \hat{Q})$ to solve the dilemma in a realistic scenario. This is why we consider an initial state perturbed by a white noise, as well as a non maximally entangled measurement basis. Furthermore, we extend our discussion to the more general case in which not only the entanglement of the measurement basis is varied, but also the entanglement in the ρ' component of the input state, i.e., we consider the variation of the same correlation parameter δ at both the beginning and the end of the PD game. Related results for the threshold in the NE inequality have been reported [191], but for some restricted input entangled states.

The experimental confirmation of quantum behaviors as the here described requires the exploration of physical systems promising to build hardware structure for quantum processing. However, the identification of systems with reliable quantum properties needs the characterization of the physical capabilities which will be tuning the quantum states within it,e.g., the photoexcitation process in nanostructure complexes. Hence, on the analysis of perovskites systems and the photophysical characterization as reliable tools for this tasks, the next part of this document will be focused.

Part II

Coherence and correlations in perovskites systems

Chapter 4

PHOTOPHYSICS OF THE HYBRID HALIDE ORGANOMETAL PEROVSKITE STRUCTURE

Clarification Note

Before the implementation of a single photon source with structured materials such as perovskites, first, it is necessary to identify the physical characteristics that make this material suitable for such a development. In this chapter we study the Methilamonium halide perovskite by focusing on its photoluminescence (PL) under the presence of: aceptor materials such as PCBM, electric field, and excess of iodine ions. All this aims to understanding the correlation between the PL response and the structure of the material.

This chapter incorporates the results of two published papers to which I mainly contributed with the realization and analysis of the PL measurements, under the supervision of Dr. Richard Hildner, from the University of Bayreuth. These experimental test were related with the real-time observation of ions movement, the blinking, the confocal observation, and the combination of the IS technique with PL visualisation with the support of A. Guerrero and J. Bisquert of different number of samples under study. The Huettner AG (Cheng Li, Yu Zhong, Anna Gräser) prepare different the samples used and the micro-lithography for the electrodes over the perovskite film, the Anna Köhler AG (Thomas Unger, Kostantin Deichsel) perfomed the measurement of PL quenching under the iodine atmosphere, and the experimental estimation of the parameters of the Perovskite based solar cell.

4.1 Introduction:

Blinking-Intermittency Process and Ions Movement in Perovskites Films

The unprecedented development of solution-processed inorganic-organic halide organometal perovskite-based solar cells (e.g., $CH_3NH_3PbI_{3-x}Cl_x$ and $CH_3NH_3PbI_3$), with power conversion efficiency (PCE) evolving from 3.8% [192] to 20.1% [193], has proposed the characterization of these materials as a significant breakthrough in the last few years [104, 105]. A number of different methods are employed, ranging from crystallographic study [194, 195], photo-physical investigation [139, 196, 197], to electrical characterisation [198, 199], etc. Currently, both scientific and technical interests concentrate on the further improvement of the PCE and decrease the

energy loss during the light conversion process approaching the Shockley-Queisser Limit [200–203]. Nonetheless, not only by the highly promising performance for optoelectronic applications, such as solar cells, light-emitting diodes, lasers, among others, we will investigate the Inorganic-organic halide organometal perovskites, But also, by their potential applications on the quantum information scenario preparing as a reliable single-photon source towards the experimental realization of quantum protocols. However, the little knowledge on the underlying photophysics, especially on a microscopic scale, hampers the further improvement of devices based on perovskite structures [104, 204, 205].

Among various characterisation approaches, it is well known that the PCE of solar cells is correlated with its photoluminescence (PL) property, which is an indication of the charge carrier recombination pathways [206]. Briefly, the charge carrier recombination is considered as a combined process of (1) trap/defects-assisted (first order) (2) electron-hole bimolecular (second order) and (3) Auger recombination (third order)[207, 208]. To achieve the ideal maximum PCE, or the Shockley-Queisser Limit, [209] the device has to perform as a "good radiator",[210] that is, to maximise the radiative bimolecular recombination based on the detailed balance model. In reality, perovskites have demonstrated outstanding performance in the applications such as light emitting diodes[211] and lasers.[104, 212] Nevertheless, the appearance of dark areas, or PL inactive domains in perovskite films, have been reported.[213–218] These dark areas in PL images indicate the existence of non-radiative recombination pathways, which are detrimental to the energy conversion and can be passivated by chemical treatment.[208, 213, 219] Recently more and more evidence demonstrates that this non-radiative recombination is associated with the migration/segregation of ions in the film.[217, 220] Therefore, the study of ionic dynamic becomes an emergent issue.

Although individual perovskite nanoparticles have been intensively studied by confocal PL microscopy [221–223], the knowledge on the perovskite film (i.e., ensemble of perovskite subdomains on films as grains) [224] is still far from being fully understood. This is mainly due to the complex boundary conditions, broad distribution of particle sizes and trap sites [214]. In this chapter, by one side both conventional PL characterisation and the spatial-temporally-resollved PL imaging is applied to investigate perovskite films, revealing the possible factors hindering PCE towards the Shockley-Queisser limit. Other authors have been related these observations to the presence of ions/ defects, however, the underlying fundamental physics and

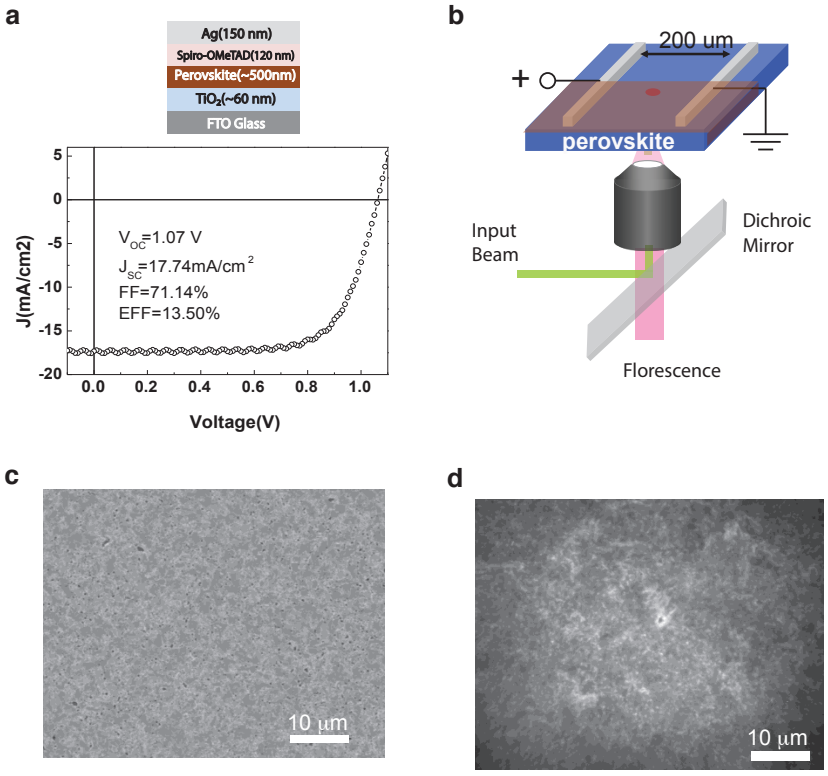

Figure 41: (a) Current density-voltage (J-V) curve of a perovskite solar cell under AM 1.5G illumination, with the structure depicted in upper part. (b) Schematic diagram of a confocal PL imaging microscopy. (c) SEM image of a perovskite film on a glass substrate. (d) PL image of the perovskite film (not the same area). The excitation source is a 532 nm pulse laser with an intensity of ~40 mW/cm^2, the exposure time is 50 ms on CCD camera.

the detailed microscopic processes concerning to trap/defect status, ion migration, etc., still poorly understood. In this sense, we employ correlated wide-field PL microscopy and impedance spectroscopy (IS) on perovskite films to in-situ investigate both the spatial and temporal evolution of these PL inactive areas under external electrical fields.

We attribute the formation of PL inactive domains to the migration and accumulation of iodine ions under external fields. Hence we are able to characterise the kinetic processes and determine the drift velocities of these ions. In addition, we show that I_2 vapor directly affects the PL quenching of a perovskite film, which provides evidence that the migration/segregation of iodide ions plays an important role in the PL quenching and consequently limits the PCE of organo-metal halide based

perovskite photovoltaic devices.

Ultrafast spectroscopy has gained success on characterisation of the charge carrier generation/recombination process ($\sim$ ns timescale or even faster) in perovskites.[206, 224] However, the contribution of ions/defects with timescales of ~ 10 s is still not fully elucidated.[139, 218, 225] In this chapter, correlated wide-field PL imaging microscopy [217, 226] and impedance spectroscopy (IS) [227–229] serve as a powerful tool to investigate the ionic/electronic dynamic process in perovskite films. Furthermore, we demonstrate a method which allows to directly visualise the migration of ions within a perovskite film.

4.2 Experimental Methods

This research considers a wide range of methods from the fabrication of a solar cell and a thin film of perovskite to the optical characterization, these are briefly in the following described. The description of the PL Imaging Experiment is expanded, differently from the published version, to give an additional technical detail.

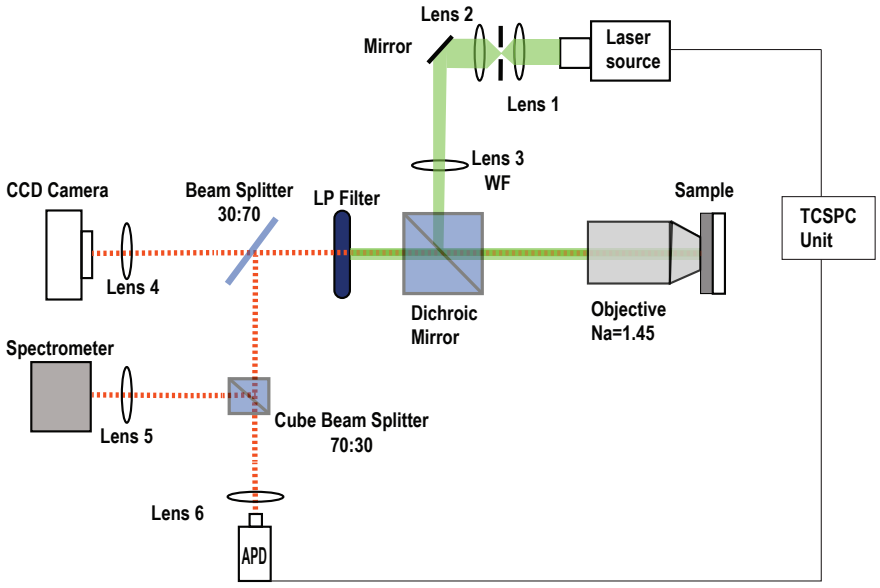

Figure 42: Sketch of the experimental setup. The light crossing through a telescope arrangement which acts as a spatial filter via the pinhole involved; the beam is then directed toward the sample, crossing first a dichroic mirror which reflects the wavelength of the illumination and allows the passing of the fluorescence. The 70 % of the fluorescence from the sample is focused in a CCD camera to follow the PL behavior. The remaining 30% could be employed in the spectrum and lifetime measurements.

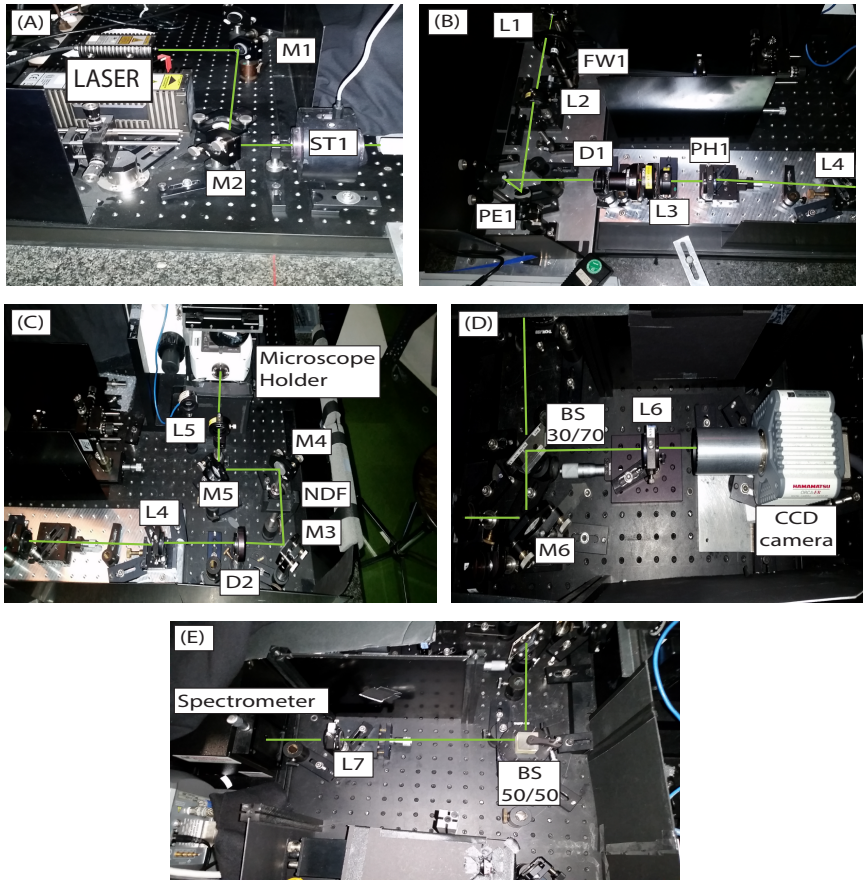

Figure 43: Pictures of the experimental setup. This involves: (a) laser illumination with a picoseconds pulsed laser (LDH-C-450B or LDH-P-FA 530L) crossing through a shutter (ST1), (b) a telescope array of lenses (L1 and L2) to collimate the beam, and a Neutral Density Filter Wheel (FW1) to control the intensity. The height of the optical path is varied with a periscope (PE1), and put into a diaphragm (D1) and a spatial filter with two lenses (L3 and L4) and a pinhole (PH1) with 40 μm diameter; (c) the coherent light sent to the microscope holder is addressed through a set of mirrors (M3, M4, M5) and focused with bi-convex lens (L5) in the chamber. We focused the light on the sample with an immersion oil 60X microscope objective; (d) the 70% of the light emission from the sample is focused on the CCD camera with a biconvex lens (L6); finally, (e) the 30% of the remaining light is focused to the spectrometer with a Beam Splitter (BS) and a biconvex lens (L7).

Perovskite Solar Cell Fabrication

Perovskite solar cells Device Fabrication and Characterisation. CH_3NH_3I (MAI) was purchased from Tokyo Chemical Industry (TCI) company, and Spiro-OMeTAD (2,2',7,7'-Tetrakis-(N,N-di-4-methoxyphenylamino)-9,9'-spirobifluorene) was pur-

chased from Merck company. All the other chemicals were purchased from Sigma-Aldrich and were used as received.

Fluorine-doped tin oxide ($F : SnO_2$) transparent conducting glasses were cut and patterned by Zn power and HCl solution. FTO glasses were washed with acetone, 2% hellmanex diluted in deionized water, deionized water and isopropanol successively for 10 min each. Then by spraying a solution of Titanium diisopropoxide bis(acetylacetonate) (0.6 mL) in ethanol (21.4 mL) at $450°C$ for 90 min in ambient atmosphere, a compact TiO_2 layer (~ 50 nm) was deposited.

MAI and lead chloride ($PbCl_2$) (3:1 molar ratio) was dissolved in anhydrous N,N-Dimethylformamide (DMF). Then, this precursor solution was spin-coated on the TiO2/FTO substrates at 3000 rpm for 60 s. After drying for approximately 30 min, the as-spun films were annealed at $100°C$ for 90 min. Following that, Spiro-OMeTAD solution was prepared by dissolving 72.3 mg Spiro-OMeTAD, 26.3 μL Lithium-bis(trifluoromethanesulfonyl)imide (Li-TFSI) solution (520 mg Li-TFSI in 1 mL acetonitrile), and 43.2 μL 4-tert-butylpyridine in 1 mL chlorobenzene. This hole transport layer (HTL) was deposited by spin-coating at 4000 rpm for 30 s. All device fabrication steps were carried out within a nitrogen gas filled glovebox. The whole of the device was exposed in a dry box (ambient atmosphere with humidity < 5%) for more than 12h. Finally, a 150 nm silver electrode was deposited by thermal evaporation in a chamber with a pressure of approximately 1×10^{-6} mbar. The effective electrode area was $9\ mm^2$ or $16\ mm^2$.

J-V measurements were performed under inert environment with a Keithley 2400 source measure unit under $100\ mW/cm^2$ illumination from an AM 1.5 solar simulator. The active area of $4\ mm^2$ and $9\ mm^2$ were defined by the overlap of a black mask aperture area, the FTO and the evaporated top electrode. The light intensity was calibrated before by a Silicon detector. There was no pre-biasing process. The scanning speed is 0.9 V/s.

Perovskite Film Fabrication for PL Experiment

CH_3NH_3I (MAI) was purchased from Tokyo Chemical Industry (TCI Deutschland GmbH, Eschborn, Germany), and all other chemicals were purchased from Sigma-Aldrich and used as received. Glass substrates were washed and cleaned with acetone and isopropanol for $10\ min$ each in ultrasonic baths. Then, these glass substrates were treated within an ozone chamber for approximately $10\ min$. Following that, in a nitrogen glovebox (both water and oxygen less than $10\ ppm$), the per-

ovskite precursor, i.e., MAI and $PbCl_2$ (3:1) in anhydrous N,N-dimethylformamide (DMF), was spin-coated on glass substrates at $3000\ rpm$ for $60\ s$. Then, these as-spun films were annealed at $100°C$ in the nitrogen atmosphere for $60\ min$. Subsequently, $20\ mg/mL$ phenyl-C61-butyric acid methyl ester (PCBM) dissolved in chlorobenzene were coated on the film at $2000\ rpm$ for $30\ s$ as a quencher layer. In the end, $40\ mg/mL$ poly(methyl methacrylate) (PMMA) dissolved in butyl acetate (anhydrous, 99%) was spin-coated on the perovskite film at $2000\ rpm$ for $60\ s$ acting as a protection layer. For the experiment of PL imaging under electrical field, perovskite film on glasses were transferred into an evaporation chamber with pressure of 1×10^{-6} mbar, and ~ 100 nm thickness of gold was deposited by thermal evaporation through a shadow mask. The electrode distance was $200\ \mu m$ and the interdigitating electrode geometry provided a ratio between channel width W and length L, W/L of 500.

PL Imaging Experiment:

The setup used for PL imaging of perovskite films was based on a home-built confocal microscope, see Fig.42 and Fig.43. The sample was illuminated by a laser with wavelength of either 450 or 532 nm (LDH-C-450B or LDH-P-FA 530L, 20 MHz repetition rate, 70 ps pulse duration, Picoquant), resulting in excitation of free charge carriers. The laser is cleaned with an spacial filter formed by a couple of achromat lenses and a pinhole with a diameter $\sim 0.66\lambda/2NA$ with λ as the central wavelength of the laser.

The excitation power can be controlled by neutral density attenuation filters and was set to $\approx\ 40mWcm^{-2}$ in the sample plane. The laser light was spatially filtered and directed to the microscope, which was equipped with an infinity-corrected high-numerical-aperture oil-immersion objective (60×, numerical aperture of 1.45, Olympus). The perovskite film was placed in the focal plane of the objective lens, and the sample position was controlled by a piezostage (Tritor 102 SG, from piezosystem Jena) with a resolution of $0.1\mu m$. An additional lens (wide-field lens) was flipped into the excitation beam path to focus the laser light into the back focal plane of the microscope objective. This allowed for illumination of a large area with $\approx 60\ \mu m$ diameter in the sample plane.

The PL signal was collected by the same objective, passed a long-pass filter (LP 467 -OD 6 or LP545 -OD 6, AHF) to suppress residual laser light, and was imaged onto a CCD camera (Orca-ER, Hamamatsu). This home-built system is able to measure

lifetimes of fluorescent emissions limited only by the laser repetition rate to process up to 50 ns of duration. This temporal measurement is achieve with the synchronization between the laser trigger and the avalanche photodiode (APD) countig, and a time-correlated single photon counting (TCSPC) system (Timeharp200, picoquant). The TCSPC system measures the intensity of the process detected by the APD delayed to the laser trigger for consecutive delays to construct a histogram which represents the

For electric field dependent measurement, the PL was recorded with a constant 20 V DC voltage being applied between the Au electrodes. We have done an estimation on the noise level of the PL intensity measurement as follows. The laser power stability is better than 3% (r.m.s.); to be conservative, we use 3% in the following, i.e., $S_{Laser} = 0.03$. The CCD's dark current amounts to 0.03 electrons per pixel per second, i.e., with the used exposure times of $< 100\ ms$, this dark current is < 0.003 electron per pixel per exposure. As will be clear from the numbers calculated below, this dark current is negligible and will not be considered further. The readout noise of the CCD-camera is 8 electrons (r.m.s.). The measured and displayed signals are given in AD counts (i.e., after signal amplification and Analog-Digital conversion). The resulting conversion factor is 4.6 electrons per AD count according to the manufacturer. Finally, the created electrons have to be converted into detected photons to estimate the photon shot noise contributing to the signal. In the emission range of the samples around $800\ nm$, the quantum efficiency of the CCD amounts to 30%. For the data shown in Figure 46 b,d, we estimate the noise level in the high signal regime starting at around $100\ s$. Here, the average signal is $2200\ AD$ counts, corresponding to $10,120$ electrons or $33,700$ photons. For the readout noise, we then obtain $S_{CCD} = 0.0008$. From the number of detected photons, the shot noise is $S_{Shot} = 0.005$. Hence, in total, the noise level is $s = \sqrt{S_{Laser}^2 + S_{CCD}^2 + S_{Shot}^2} = 0.03$, which translates into $67\ AD$ counts. Comparing this noise level to the observed signal fluctuations of about $\pm 150\ AD$ counts in Figure 46d, it is clear that these fluctuations cannot arise from noise. For the data shown in Figure 47, the situation is slightly different: using the displayed AD counts of around 500 in the high signal regime starting around $80\ s$, we obtain a noise level of $16\ AD$ counts following the same procedure as above. Hence, in the presence of the PCBM quencher layer, the observed fluctuations are largely determined by the noise level in these experiments.

PLQE Measurements Under Iodine Atmosphere:

Photoluminescence quantum efficiency (PLQE) was taken using an integrating sphere and a laser diode at a 485-nm wavelength (PicoQuant GmbH, Berlin, Germany). The spectra are spectrally corrected for grating, charge-coupled device (CCD) and fibre efficiencies. The Time-Correlated Single Photon Counting PL transients are measured with a TCSPC setup (FluoTime 200, PicoQuant GmbH). The excitation source was a pulsed laser diode with a 485-nm wavelength with 2- to 10-MHz repetition rate and a pulse duration of about 140 ps.

The PL of a perovskite film was measured under iodine atmosphere. For this, a perovskite film was placed in an atmospherically sealed measuring chamber with quartz glass windows. Before starting the measurement, we heated the chamber to roughly $50°C$ using a heat-gun in order to prevent condensation of solid iodine onto the windows and the perovskite film. The photoluminescence measurements under iodine were performed using an 80 mW laser (PGL V-II) with a wavelength of 532 nm. The spectra were recorded using a spectrometer (QE Pro from Ocean Optics) and matching optical fibre. A filter (OG 590 nm) was used to filter the emission light.

Initially the PL was measured under a pure nitrogen atmosphere to obtain a reference value. Subsequently, a vial with solid iodine was connected to the gas inlet pipeline and thus the chamber was filled with a mixed iodine/nitrogen atmosphere. Upon connecting the iodine vapour, we measured a PL spectrum every 3 s to observe the progress of the PL intensity. After the PL intensity stabilised on a lower level, the iodine was disconnected from the gas pipeline and flushed the measurement chamber with pure nitrogen.

Experimental Real-Time Observation Technique:

The Fig.41b depicts the schematic of a wide-field PL imaging microscope, a detailed description has been reported previously [230]. The Fig.41c and Fig.44a illustrates the scanning electron microscopy (SEM) image of a perovskite film on glass, while Fig.41d is the PL image of the same film on a similar scale (yet not of the same region). The SEM image in Fig.41c shows the perovskite film possesses densely packed grains ranging from 100 nm to 800 nm in size, which is consistent with the PL image (Fig.41d). We note that on the surface of the device, the spatial distribution of the PL intensity is not uniform. This may be ascribed to the inhomogeneous distribution of composition and defects. Note that it has been reported that the

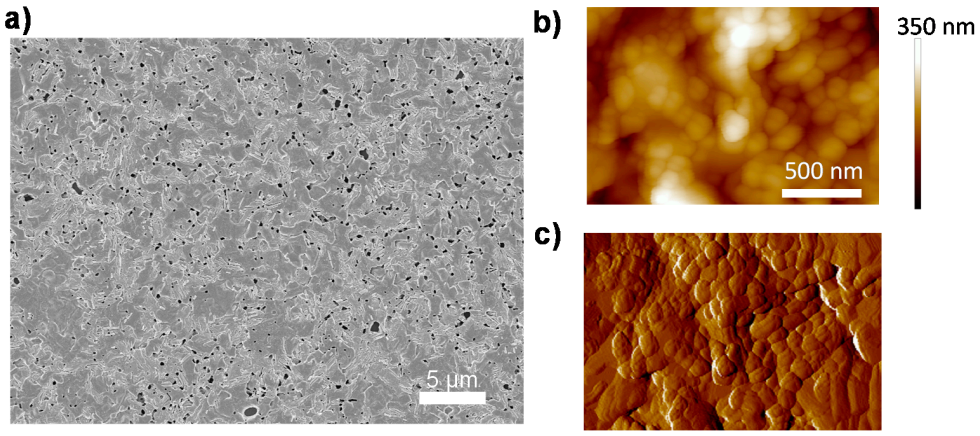

Figure 44: Morphology characteristics of a $CH_3NH_3PbI_{3-x}Cl_x$ perovskite film. (a) Scanning electron microscopy (SEM) image; (b) atomic force microscopy (AFM) topography image; and (c) AFM phase image. The color bar in (b) indicates height.

presence of oxygen and moisture may result in a significant increase of the PL. [230, 231] Here, to rule out the influence of ambient atmosphere, we deposited a polymethyl methacrylate (PMMA) layer with $\sim$ 200 nm thickness on top of the perovskite film as a protection layer. In addition, the device was in direct contact with the microscope immersion oil during the whole PL characterisation.

Impedance Spectroscopy:

The setup to measure impedance spectroscopy is similar to that described previously for PL analysis. However, in this case the DC voltage source to polarise the sample was a potentiostat equipped with a frequency analyser (Zahner Potentiostat, Zenium). A small AC perturbation was applied and the differential current output was measured to calculate the impedance response. The frequency window was kept small ranging between 10 kHz$-$100 mHz to minimize the measurement time. Each frequency scan took less than 1 minute and a delay time of 5 minutes was used between scans to carry out the PL measurements. The light source was turned off after the PL measurement and the new IS scan was taken under dark conditions. For measurements at a DC voltage of 2 V the delay time was reduced to 30 s and this enabled the observation of the accumulation of ions at the interface. Alternatively, devices where measured systematically under a range of applied bias using a high sensitivity potentiostat (Autolab PGSTAT-30) to cover a lower frequency range down to 5 mHz.

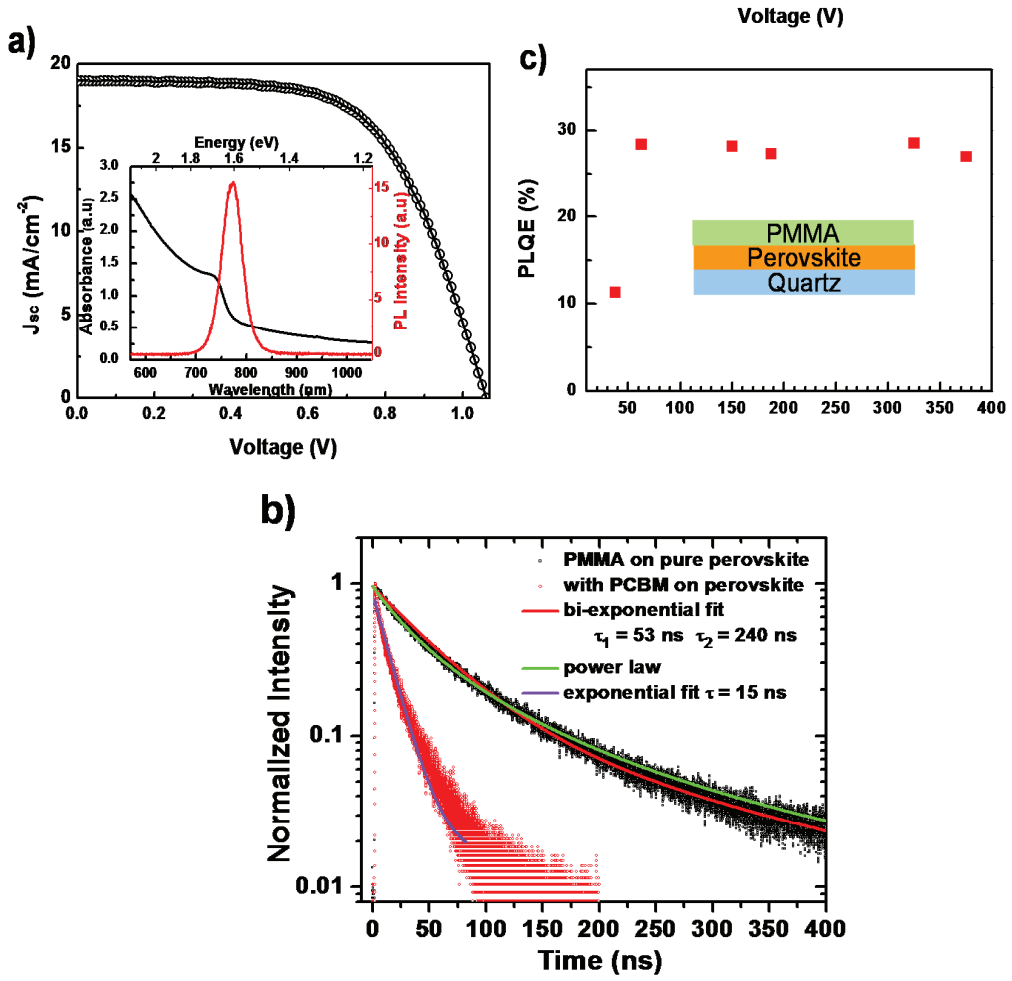

Figure 45: (a) Current-Voltage (J–V) curve measurement of a perovskite solar cell. The inset shows the photoluminescence (PL) and UV-VIS absorption spectra of a perovskite film; (b) Time-resolved photoluminescence measurement on a perovskite film with (red dots) and without (black dots) a PCBM quencher layer, together with fit lines; (c) Photoluminescence quantum efficiency (PLQE) of a perovskite thin film as a function of laser intensity. The inset shows the schematic of the device.

4.3 Analysis of Physical Properties

Blinking-Intermittency Process in Perovskites

The $CH_3NH_3PbI_{3-x}Cl_x$ perovskite films, were prepared by spin-coating of a mixed halide precursor solution($CH_3NH_3I : PbCl_2 = (3 : 1)$) on quartz glass substrates, followed by a thermal annealing step in a nitrogen glovebox. The detailed fabrication process has been described in previous work [232]. The morphology of the film is shown in Fig. 44. A uniform perovskite film is deposited on quartz substrate with

only minor pinhole density due to gas release during annealing [233] (Fig. 44a). We also employ atomic force microscopy (AFM) to investigate the microscopic structure of the film, shown in Fig. 44b, c. It is evident that the perovskite film is composed of densely-packed grains, which are ranging from 100 nm to 800 nm in size.

The UV-VIS optical absorption and PL spectra of $CH_3NH_3PbI_{3-x}Cl_x$ perovskite thin film recorded, with commercial spectrophotometers at room temperature are shown in the inset of Fig. 45a. The absorption edge is located at around 769 nm, which is consistent with previous other works [211]. For the PL analysis, the film is being excited by a 532-nm laser, and the emission peak is centred at around 780 nm. This small Stokes-shift (energy difference between optical absorption and emission), is attributed to the small vibrational relaxation in perovskite[139]. Incorporating this perovskite film into a typical perovskite solar cell architecture results in the performance shown in Fig.45a. From the light current-voltage (J-V) curve measurement, we obtain the open circuit voltage $V_{oc} = 1.06V$, short circuit current $J_{sc} = 182.9\, mA/cm^2$, fill factor $FF = 62.3\%$, and a Power Conversion Efficiency (PCE) calculated of 12.5%.

By monitoring the PL decay after photo-excitation, we can investigate the charge carrier recombination kinetics. The Fig. 45b presents the normalised time-resolved PL behaviour of this perovskite film under pulsed laser excitation at 485 nm, with and without a phenyl-C61-butyric acid methyl ester (PCBM) layer, respectively. The PL decay of the pure perovskite film can not be described by a mono-exponential decay but a power-law dependence. The best bi-exponential fit would give a dominant short decay component of about 52 ns.

Solid lines in Fig. 45b represents the fits to bi-exponential decays, power-law decays and to exponential decay. For the quenched PL decay with PCBM, a diffusion model as describes by Stranks et al. [139] should actually be applied. Using for simplicity, an exponential fit, a decay time of 15 ns is obtained. This result shows the action of the quencher layer which enhances the free charge carrier recombination through the decreasing of the diffusion length of the species created in the photo-excitation process (free charge carriers and bound excitons). We also carry out steady-state photoluminiscence quantum efficiency (PLQE) measurements [234] on perovskite films with a PMMA layer as a function of the excitation intensity using a wavelength of 485 nm to study the recombination. As shown in Fig.45c, in the initial low excitation intensity regime, PLQE rises proportional to the laser intensity. We

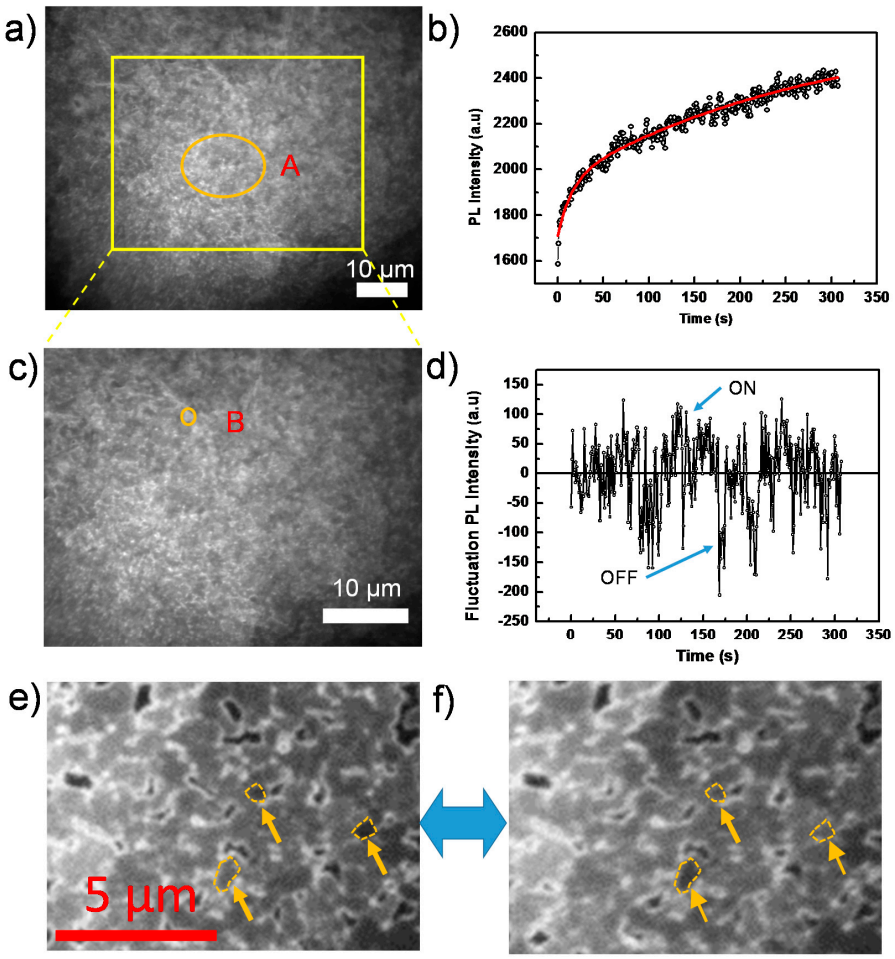

Figure 46: (a) Wide-field PL image of a perovskite film taken from a sequence of 400 consecutively-recorded images with an exposure time of 50 ms, an interval time of 500 ms and an excitation intensity of 44 mW/cm^2; (b) PL intensity trajectory extracted from Area A in the sequence of images in (a). The red line is the fit by an exponential function; (c) Enlarged view of the yellow square area of (a); (d) PL intensity trajectory extracted from Area B in (c) after subtraction of the exponentially increasing base line; (e,f) Individual grains in "ON" and "OFF" states, respectively, indicated by yellow arrows.

consider this increase associated with the probable trap-filling process, as well as the increase of exciton density of the photogenerated species [213, 235]. In detail, due to the low temperature solution processing of the perovskite film, there can be various defect states within the crystallised bulk and surface, such as vacancies, interstitials, substitutions, etc. [236–238].

These defects could act as trap-assisted recombination (Shockley-Read-Hall re-

combination) centers, via which the free charge carriers can undergo non-radiative recombination processes [239]. These recombination centers would lead to shorter carrier life times and a lower open circuit voltage (V_{oc}). When illuminated, these sub-bandgap traps would be filled and stabilised by photogenerated electrons/holes, reducing the non-radiative recombination probability and consequently increasing the V_{oc} under light soaking [240, 241]. For the higher excitation intensity, the PLQE would reach a saturated value, indicating that all traps associated with the non-radiative recombination have been filled [208, 213, 235].

This scenario is consistent with our experimental data. However, we note that the PLQE is still quite low, around 30%, which is supposed to approach unity according to the detailed balance model [209, 210]. This implies that besides the trap-assisted recombination, there exists an additional non-radiative recombination pathway. In order to understand the detailed mechanism, which suppresses the further increase of PL intensity, we employ spatially- and temporally-resolved PL microscopy to investigate the perovskite film locally on the level of individual grains.

The detailed experimental setup, which is displayed in Fig. 42, has been described in a previous paper [242]. Briefly, we use a home-built optical confocal microscope, which can be operated using wide-field illumination and a charge-coupled device (CCD) camera as a detector to obtain PL images of large areas (diameter $\sim 60\mu m$) of a sample. We are able to record typically sequences of up to 2000 PL images with exposure times as short as 50 ms per image. This enables us to track the temporal/spatial evolution of the PL intensity from a perovskite film under continuous laser illumination of the pulse laser.

Here, to rule out the possible influence of environmental effects on the perovskite films, i.e., oxygen and water molecules [216, 243], we spin-coated a polymethyl methacrylate (PMMA) layer with a $\sim 200\ nm$ thickness on the top of the perovskite film as the protection layer. In addition, the PMMA layer was in direct contact with the immersion oil of the microscope objective during the whole PL characterisation, which further prevents oxygen from diffusing into the film.

The Fig. 46a is an example of a wide-field PL image sequence from a perovskite film, which agrees generally with the SEM result, showing ensembles of grains on the film and the appearance of pinholes on the surface. Note that, due to the diffraction limit, grains with a size smaller than $\sim 300nm$ cannot be resolved with our microscope and, thus, appear as blurred structures. However, we still observe the existence of dark crystal grain/particle boundaries. The observation of dark

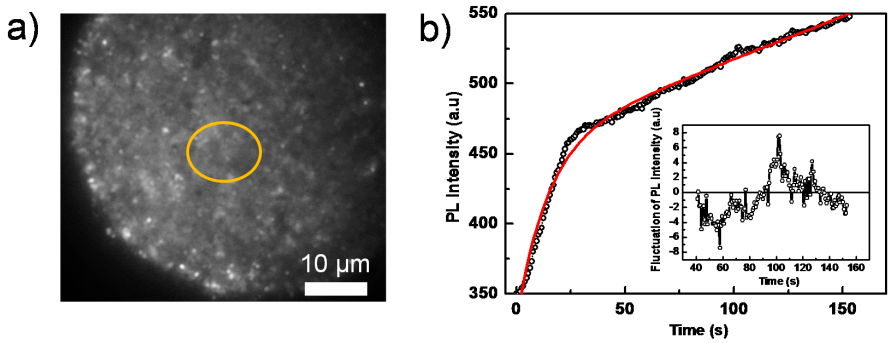

Figure 47: (a) Wide-field PL image of a perovskite film, covered with a PCBM quencher layer, taken from a sequence of 200 consecutively recorded images with an exposure time of 100 ms, an interval time of 500 ms and an excitation intensity of 280 mW/cm^2; (b) PL intensity trajectory extracted from the yellow circled area in the sequence of images in (a). The red line is the fit by a bi-exponential function. The inset shows the relative fluctuations of the PL intensity after subtraction of the bi-exponential fit function.

grain boundaries (non-radiative recombination centers) has also been observed by higher resolution confocal microscopy, as demonstrated by deQuilettes et al. [214] for example.

The Fig.46b shows the PL intensity as a function of time, obtained by extracting the integrated PL of the orange circled Area A in Fig.46a from each image of the sequence. We find that the PL intensity continuously increases during the light soaking process, as shown in Fig.46b. This increase, which agrees with the previous PLQE measurement, has also been reported in other papers [223, 235, 244] and is attributed to trap filling processes.

Here, we note that the time dependence of the PL intensity in Area A, shown in Fig.46b, is fitted by a bi-exponential function with time constants of $\sim 14\,s$ and $\sim 280\,s$ and pre-factors of 230 and 690, respectively. This implies that there exist two distinct trap-filling processes, that is a quick one and a much slower one. We propose that the quick process is associated with the direct filling of defect states in the perovskite film [222]. These defects originate from the symmetry breaking of the perfect bulk crystalline structure in the vicinity of the surface or grain boundary, where well-defined facets are lacking [238]; while, for the slower one, we assume that it is ascribed to the formation and migration of defect states in the perovskite film under light illumination. Recently, more and more studies have been carried out in this field, investigating the roles of defect formation/migration on the hysteresis

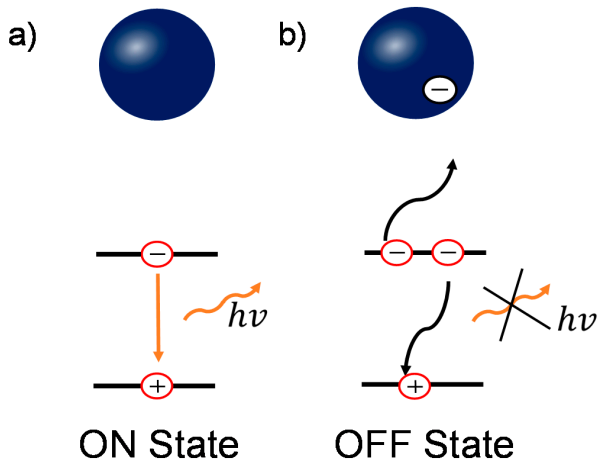

Figure 48: Schematic diagrams of the relationship between the charged grains and blinking behaviour in perovskite. (a) In the uncharged states, the dominant recombination pathway is bi-molecular recombination; (b) In the charged states, the non-radiative three-carrier Auger recombination plays an important role. Each blue ball represents an individual perovskite grain.

and long-term (seconds to minutes) phenomena [225, 229, 245]. Hoke et al. [246] observed the presence of an iodine-rich phase in mixed halide perovskite under light irradiation. Chen et al. [215] detected the light activation and accumulation of ion by light soaking, resulting in PL quenching in the perovskite film.Yuan et al. [247] attributed the degradation of perovskite structures to the ion migration via light or external electron beam. Hentz et al. [248] also observed the formation of an iodine-rich region induced by an external region induced by an external electron beam.

The overall continuous PL intensity enhancement, shown in Fig.46b, is superimposed by strong PL intensity fluctuations beyond experimental noise. This behaviour is reminiscent of random switching between ON (highly emissive state) and OFF (weakly emissive state) in the emission trajectory, which is known as blinking or PL intermittency [249]. Although the blinking behavior has been observed in perovskite nanocrystals [145, 221, 223], it is still not fully studied on compact films composed of the densely-packed perovskite grains [224].

To reveal the underling mechanism, we investigate individual grains avoiding averaging over ensembles in the film. Fig.46c displays an enlarged view of the yellow boxed area in Fig. 46a, and an individual grain is highlighted by the orange circle labeled with B. The PL intensity trajectory of this grain B, after subtraction of a

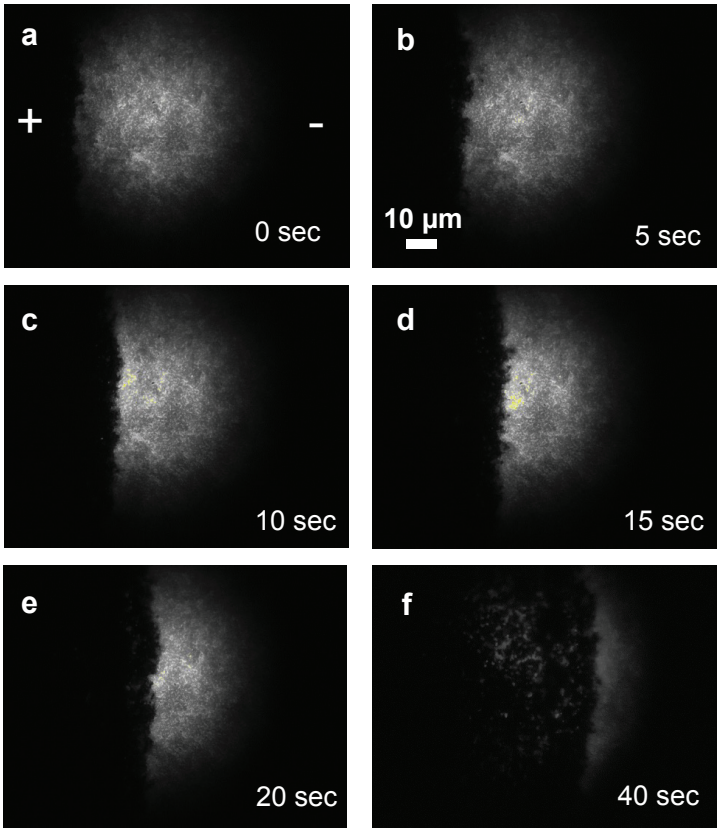

Figure 49: Time dependent PL images of a perovskite film under an external electric field ($\approx 10^5\ Vm^{-1}$). The "+" and the "-" signs indicate the polarity of the electrodes, the excitation intensity is $40mW/cm^{-2}$ and the exposure time per image is $50\ ms$.

continuous bi-exponentially-increasing baseline, shows a typical blinking behaviour, that is random distribution of ON/OFF states in the PL intensity trajectory, as shown in Fig.46d. Additional areas with this behaviour for individual grains in are shown in Fig. 46 e, f. Here, some ON or OFF states remain over the 20 s after the light interaction, which indicates a significantly slow dynamic process at this scale.

To further investigate the processes giving rise to blinking, we performed PL imaging on perovskite films coated with a PCBM layer, which acts as a PL quencher layer. Compared to the pure perovskite film, the overall PL intensity reduces significantly despite using higher excitation intensities (see Fig.47a). This PCBM layer effectively separates the photogenerated charge carriers (free electron/hole or weakly bound excitons) [250], because PCBM serves as an electron acceptor and consequently quenches the radiative charge recombination. The Fig.47b shows the integrated PL intensity of the yellow circled area in Fig.47a as a function of time, which can

be well fitted by a bi-exponential function with time constants of 5.4 s and 14.6 s, respectively. This is consistent with the results displayed in Fig.45b, in which a faster (quenched) PL decay is due to the PCBM quencher layer. It is interesting to note that although the overall PL still increases as a function of time, the blinking amplitude significantly reduces below the noise level (the ratio between the fluctuation and the average emission intensity), both in the whole film and in individual grains, as shown in the inset of Fig.47b.

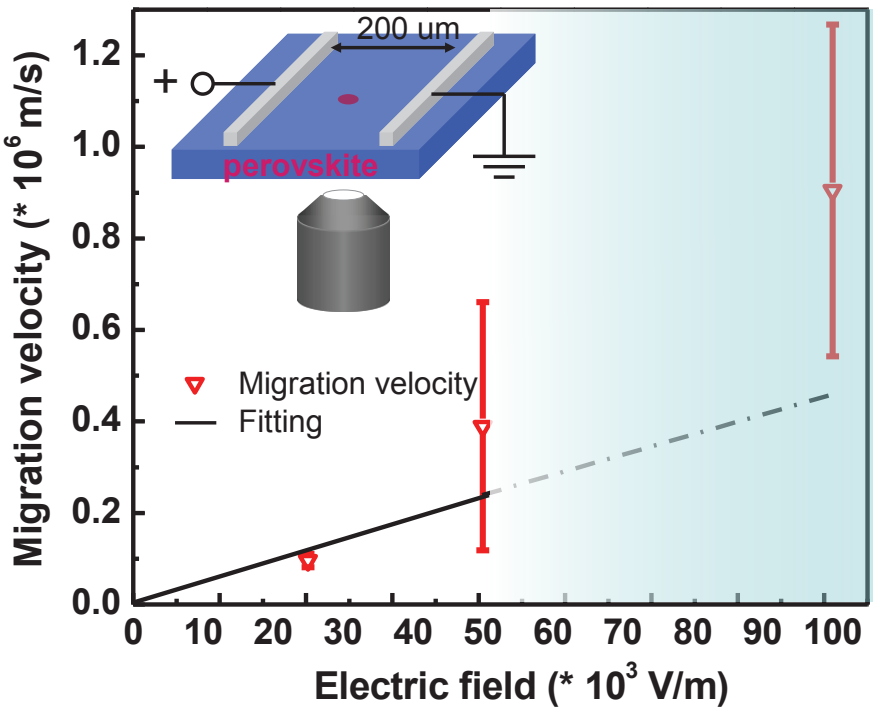

Figure 410: Field dependence of the ionic migration velocity. Inset: the schematic diagram of the setup. The black line is the fitting line based on first two points (lower voltages) considering the weight of error. Dashed line is the extension of the fitting line, because at high voltage, the perovskite film exhibits decomposition. The coloured gradient indicates the more chemical decomposition under higher voltage.

Based on the previous results, combining both the conventional PL characterisation and widefield PL imaging, we can reveal the underlying physics in the enhancement and quenching of the PL. Though there are several models to interpret the blinking behavior [249, 251, 252], the presence of OFF states in perovskite film/nanoparticles is commonly attributed to additional charges due to charge trapping process [222–224]. If there is no charge trapped in perovskite grains, shown in Fig.48a, the dominant decay process is bi-molecular recombination (for medium carrier densities)

[235], which is radiative during the recombination process, denoted as the "ON" state. In contrast, when photogenerated charges are trapped in the grain, either by surface or bulk defect states, the ionized surrounding enhances Auger recombination [224, 253]. This process involves a recombination of an electron and a hole, followed by a process of energy transfer to a third carrier instead of photon emission, as shown in Fig.48b. This process is non-radiative and therefore renders the grains dark in PL imaging, denoted as the "OFF" state. The PL emission recovers to the "ON" state when these trapped charges release. This Auger recombination statistically reduces the PL intensity in the whole film, resulting in the loss in V_{oc} and PCE [200, 202].

Note that the long durations of more than $20\ s$ of "ON" and "OFF" states are similar to the slow response in electrical transient behaviour, such as hysteresis and light-induced degradation [224, 247]. This implies that it can be associated with the same mechanism, i.e., ion migration. These ions can be driven by the external electrical field and consequently accumulate, enhancing the Auger recombination locally [224]. In addition, these ions are also able to migrate between grains within the film [224, 225].

Covering the perovskite film is with a PCBM quencher layer, the PL blinking is significantly suppressed (insets in Figure 47b). This is ascribed to two possible reasons: First, PCBM has been demonstrated to be a good candidate to passivate traps in perovskites, leading to a charge de-trapping process [254]. In addition, the insertion of PCBM suppresses the ionic migration among the grains of perovskite, leading to a further reduction of PL blinking [255]. Second, the Auger recombination is proportional to the third power of charge carrier density n^3 [207]. Owing to the effective charge transfer process at the perovskite/PCBM interface, the negative charge carrier density (n_e) inside the perovskite significantly decreases, giving rise to the decrease of the Auger recombination contribution.

Analysis of Data: How Fast are The Ions?

It has been proposed that the migration/segregation of ions plays an important role on the decay of PL intensity [52, 214, 216, 220, 243]. These ions can be driven by an external electrical field. Therefore, we recorded time dependent PL images on films with laterally interdigitated electrodes with channel lengths of $\sim 200\mu m$ (see Fig. 41 and inset in Fig.410). Applying a constant electric field of $\sim 10^5\ V/m$, we observe that initially the PL intensity in the bright areas exhibits a uniform decrease

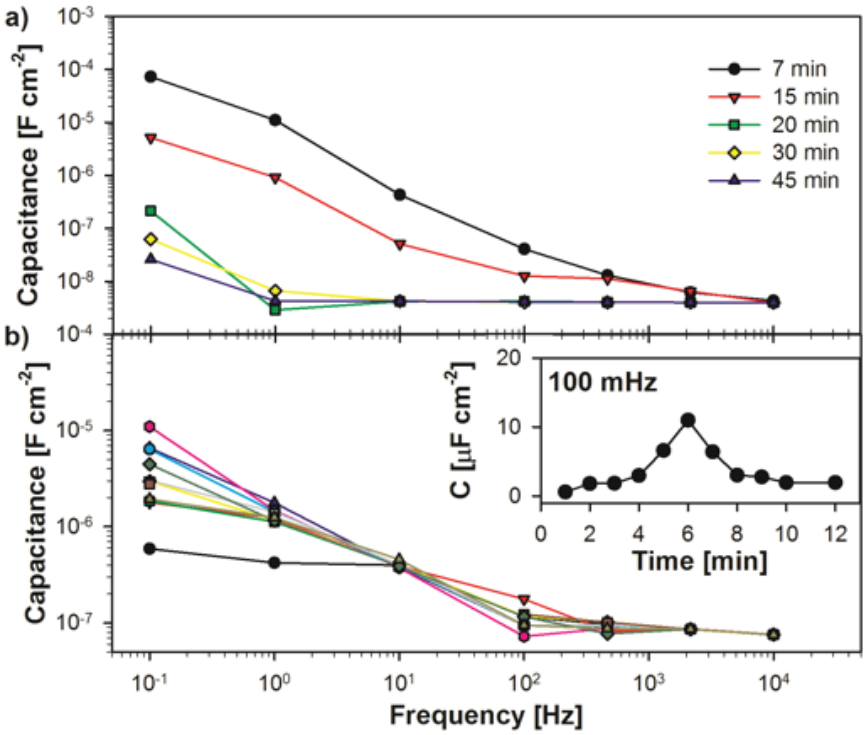

Figure 411: Capacitance-frequency plot of measurements were carried out simultaneously during PL measurement by applying a DC bias of a) 1V and b) 2V. The inset shows the evolution of the capacitance at 100 mHz with time.

as the device is connected with the external electrical circuit. This is attributed to the charge extraction by the external electrical field, which decreases the population of photogenerated charge carriers. Interestingly, under the constant electrical field, a front forms that separates bright and dark domains and that moves from the positive electrode towards the negative one, as shown sequentially in Fig.49.

Note, that in the immediate vicinity on the bright side of the migrating front (Fig. 49(c) and (d) for instance), the PL intensity is abnormally high. This implies that at this boundary an electrochemical reaction occurs (see below). Taking into account the direction of the front, from positive towards negative electrode, we assign this movement of PL dark area is attributed to the migration/accumulation of negative ions, that is, iodide ions in perovskite.[214, 217] This observation is consistent with previous studies on the ionic migration, in which iodide ions serve as a main contribution for the hysteresis behavior [227, 228, 232, 256, 257] and field driven [258, 259]. As shown in Figure 49, it takes $\sim 50s$ to turn the whole PL image (diameter is around $60\mu m$) to dark area, under the electrical field of $10^5\ V/m$.

Therefore, the analysis of the kinetics of the migrating front enables to directly estimate the velocity of ionic migration.

To investigate this ionic motion, we characterise the velocity of the migrating front as a function of external electrical field. By varying the strength of the field, we obtain that the migration velocity is proportional to the field within the error, as shown in Fig410. Ignoring the ion diffusion, this movement of the front can be described by a simple ionic mobility theory:[260]

$$\nu = \mu E \tag{4.1}$$

Here, ν is the drift velocity of ion movement, μ is the mobility of ions, and E is the electrical field across the whole channel. By fitting the field dependent ionic migration (two lower voltages), the mobility of iodide ions is obtained $(5 \pm 2) \times 10^{-12} m^2/Vs$. This value is close to the ionic migration mobility obtained in $CH_3NH_3PbI_3$[258, 261], the discrepancy between the two values (one order of magnitude difference) may be due to the different defect density, film fabrication process (using $PbCl_2$ instead of PbI_2 as the precursor) or nature of grain boundaries. Based on the Einstein relation:[260]

$$D = \mu k_B T \tag{4.2}$$

where D is the diffusion constant, k_B is Boltzmann's constant and T is the absolute temperature,we obtain the diffusion constant D of $(1.0 \pm 0.4) \times 10^{-13} m^2/s$, which also agrees with the value $\sim 10^{-12} m^2/s$, obtained by [262] Here, note that the last point $(1 \times 10^5 V/m)$ deviates from the fitting line. This is attributed to the degradation of the perovskite film under the high electrical fields, consistent with the grazing incidence wide angle x-ray scattering (GIWAXS) results performed under different electrical fields.

To further understand ionic motion within the film we reversed the bias and monitored the time evolution of the dark area. We observe that, under the reversed electrical field, the dark regions are recovering to the bright areas again, and the recovery speed is much slower. This asymmetry may be associated with electric field induced chemical reactions, [262] and will be further addressed below. It is also observed that after 12 hours disconnected with the external electrical field, the dark area returns to bright (not shown here). This reversible phenomenon is consistent with the iodide ion diffusion process characterised in previous papers [217, 256].

We optimized the laser power for fast acquisition and low excitation intensity. We note, that the laser excitation power may play an important role in PL quantum

efficiency [212] and dynamics [146, 256]. Wang et al.[263], for example, found a photodriven transformation in $CsPbX_3$ nanostructures Xing et al. [264] observed a decreased activation energy for ion migration under light illumination and the presence of migrating ions has direct implications on slow dynamic optical processes in perovskite-based devices as has been recently reviewed by Panzer et al.[146].

Impedance Spectroscopy

IS has been demonstrated to be a powerful tool to explore the microscopic processes in perovskite solar cells, especially the migration of ionic charges [229, 262, 265]. In this work, we carried out IS measurements with the aim to electrically monitor how ions are piling up at one electrode and to correlate with the PL measurements by performing both measurements quasi-simultaneously. In a typical IS measurement a Direct Current (DC) bias is applied to polarise the sample and a small Alternate Current (AC) perturbation is superimposed. As we have seen, ionic concentration shifts as a function of time showing a constant mobility. Therefore, the combination of the two methods allows us to implement this additional parameter in the interpretation of the IS results. The differential current output is measured, which offers information on the capacitive and resistive processes taking place in an operating device. For perovskite devices it has previously been demonstrated that the response in the low frequency region is related to electrode polarisation of ions by generation of a Helmholtz layer and charge compensation by the external electrode.[265]

As shown in Fig.411(a), initially a DC bias of 1V was applied in the dark to induce ion migration towards the electrodes by using a potentiostat equipped with a frequency analyser, which is able to acquire impedance spectroscopy in-situ. The PL image was recorded at every end of each IS cycle. It is important to note that under this very mild field of only 1V applied between the contacts no noticeable advance front is observed, though as established above (Fig.410) we can assume a constant mobility. Hence, a lower voltage gives us sufficient time to carry out the respective IS cycles. Furthermore, IS measurements are very sensitive to changes at the interface level between perovskite layer and contacts. Indeed, Fig. 411(a) shows the capacitance-frequency plot as a function of time. After the first IS measurement scan (7 minutes) the capacitance at low frequencies (0.1 Hz) is initially in the range of $\sim 70 \mu F cm^{-2}$ which is a typical capacitance value produced from piling up ions at one interface due to electrode polarisation [265]. Interestingly, as the polarisation time increases, this low frequency capacitance decreases with lowest value observed ($20\ nF cm^{-2}$) after 45 minutes of applied bias which could be the

result of an electrochemical reaction leading to the generation of neutral species (i.e. PbI_2)[258]. PbI_2 is neutral and as such will not give rise to a capacitive response, for this reason the capacitance will reduce with time as the material forms. The detailed electrochemical reaction will be addressed in the following part.

Subsequently, IS measurements were carried out with a polarisation of 2 V (Fig.411(b)) with a shorter delay time (1 min). These conditions allow monitoring how the ions accumulate at one interface as a function of the time and the electrochemical reaction leading to neutral species at the electrode. Initially, the capacitance in the low frequency region is low as no ions are present in the interface ($0.7\mu\ Fcm^{-2}$) and this increases with the time to reach a maximum capacitance value ($10\ \mu Fcm^{-2}$) observed at 6 min indicating that after this time most of the electrode surface is covered by charged ions that have migrated from the bulk of the perovskite layer. Note that capacitances are not as high as in the previous experiment as some of the interfacial area has already reacted in the previous experiment leading to inactive areas. After this time the capacitance begins to decrease as shown in the inset of Fig.411(b) similar to the effect observed for polarisation at $1\ V$. Capacitances of $\sim 2\ \mu Fcm^{-2}$ are observed after 12 min of polarisation indicating that the charged species covering the electrode have mostly reacted to generate neutral species. A different set of measurements, with the same device structure, were carried out where the capacitance was measured as a function of the applied bias (Fig.412(a)) in the dark. In this set of experiments, the frequency range was increased to cover still lower frequencies (down to 5 mHz). As expected noise increases in this region as a consequence of the slow response of mobile ions to the small AC perturbation. The electrode polarisation capacitance increases with the applied bias exponentially. The observation of a variation of the capacitance with voltage, shown in Fig.412(b), is a clear indication of charge accumulation at the interface. A number of previous studies have clearly shown that the large low frequency capacitance of perovskite solar cells in the dark can originate from the mobile ion accumulation[146, 265]. In principle, if the ions move freely in the solid medium the structure of the interface consists on a double layer and a diffuse layer that is controlled by the applied voltage. For a symmetric electrolyte the Gouy-Chapman model gives the capacitance [263]

$$C = \frac{\epsilon\epsilon_0}{L_D} \sinh\left(\frac{qV}{2k_BT}\right) \tag{4.3}$$

Where V is the potential drop between the metallic contact and the absorber bulk, ϵ_0 is the permittivity of vacuum, ϵ is the dielectric constant of perovskite, and k_BT is the thermal energy, q is the charge. The ion Debye length L_D is therefore given

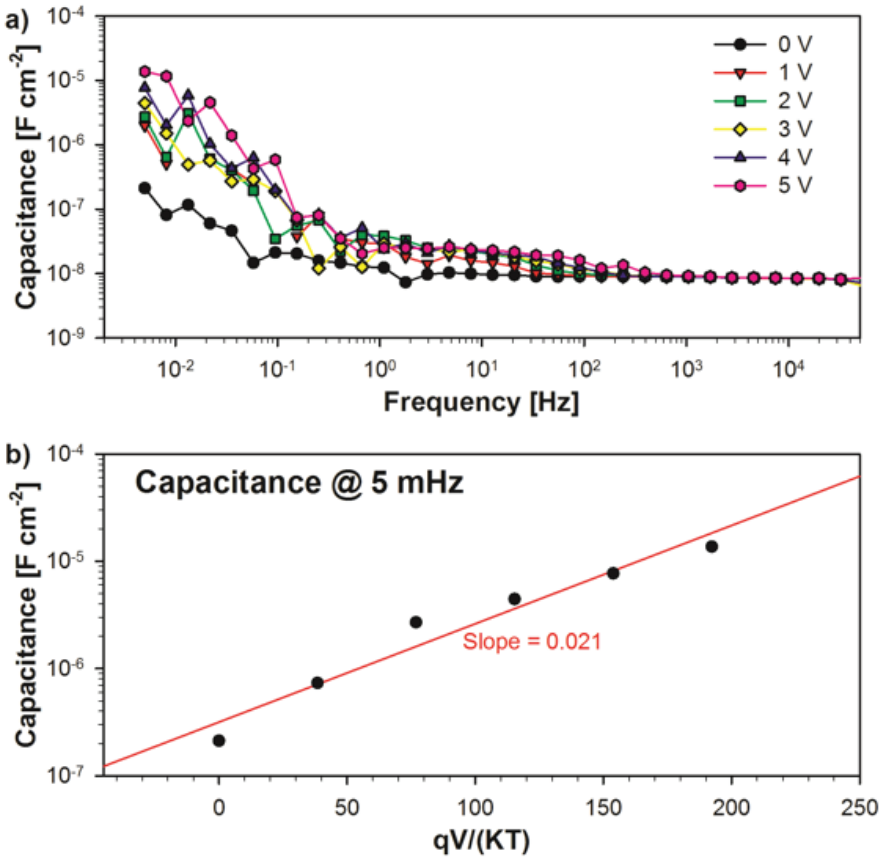

Figure 412: a) Capacitance-frequency plot of measurements carried out in the dark as a function of the applied bias. b) Exponential relationship of capacitance as a function of external voltage measured at 5 mHz.

by:

$$L_D = \sqrt{\frac{\epsilon\epsilon_0 k_B T}{q^2 N}} \tag{4.4}$$

Here N accounts for the equilibrium density of ionic charges in the bulk material. Eq.4.3 indicates that the extension of disequilibrium of ionic distribution at the interface is of size L_D. The capacitance at zero bias is:

$$C_1 = \frac{\epsilon\epsilon_0}{L_D} \tag{4.5}$$

The thermalised distribution of ions in Eq.4.3 can be approximated by the formula:

$$C = C_0 e^{\frac{\alpha q V}{k_B T}} \tag{4.6}$$

With $C_0 = C_1$ and a parameter $\alpha = 1/2$ that corresponds to the thermalised accumulation of freely diffusing ions according to their electrochemical potential.

However, the experimental observations reported in Fig. 412 show that $\alpha = 1/2$ is far from being satisfied. Since $\alpha \approx 0.02$, as shown in Fig. 412(b), it is apparent that the rise of capacitance does not correspond simply to the thermalised distribution of ions, but to an exponential distribution of states characterised by a temperature parameter T_0 as $\alpha = T/T_0$[264]. This exponential distribution of states is a common occurrence in ionic and electronic systems that are characterised by a large degree of disorder. For example, a distribution of states has been observed in the intercalation of Li^+ ions into WO_3 electrochromic thin films [266] and also for the insertion of Li into ultra-thin Ge layer in Si/Ge battery cathodes [199].

The observation of an exponential density of states for the accumulation of ions close to the perovskite/Au electrode interface indicates that ions become immobilised in the host material with the given distribution. According to the observation of the large changes of capacitance reported above, we can assume that such a distribution is not intrinsically formed at the interface but rather has been caused by the prolonged voltage applied to the symmetric cell. Therefore, a special layer is formed at the interface which is richer in I_2 and reduces the ability to take ions from the bulk. Tentatively we assume that reaction at the metal surface produces a film of PbI_2 that contains the exponential distribution suggested in Eq.4.6. This observation would consistent with the formation of a PbI_2 layer under a continuous electrical bias, and the electrochemical reaction proposed as [259]:

$$MAPbI_3 \longrightarrow PbI_2 + MA^+ + I^- \tag{4.7}$$

$$2I^- \longrightarrow I_2 \uparrow + 2e^- \tag{4.8}$$

In addition, Li et al. [232] observed that after long term biasing at the positive electrode, the ratio between iodine and lead is away from the stoichiometric ratio of perovskite, suggesting the formation of PbI_2. Further more, there exists PbI_2 signal after electrical biasing characterised by GIWAXS measurement. Deng et al.[218] also obtain the PbI_2 signal by investigating the PL signal near the positive electrode.

Photoluminescence Characterisation Within Iodine Vapour

To further understand the role of iodide ions on the PL performance of device, we recorded time dependent PL spectra under an iodine vapour atmosphere with configuration displayed in Fig.413(a). As shown in Fig.413(b), as the I_2 vapour (mixed with N_2 gas flow) was introduced into the chamber, the PL intensity immediately decreases. After 30 s, the PL intensity decreased by around two orders magnitude. Then the I_2 saturated gas was turned off and the chamber was purged with pure

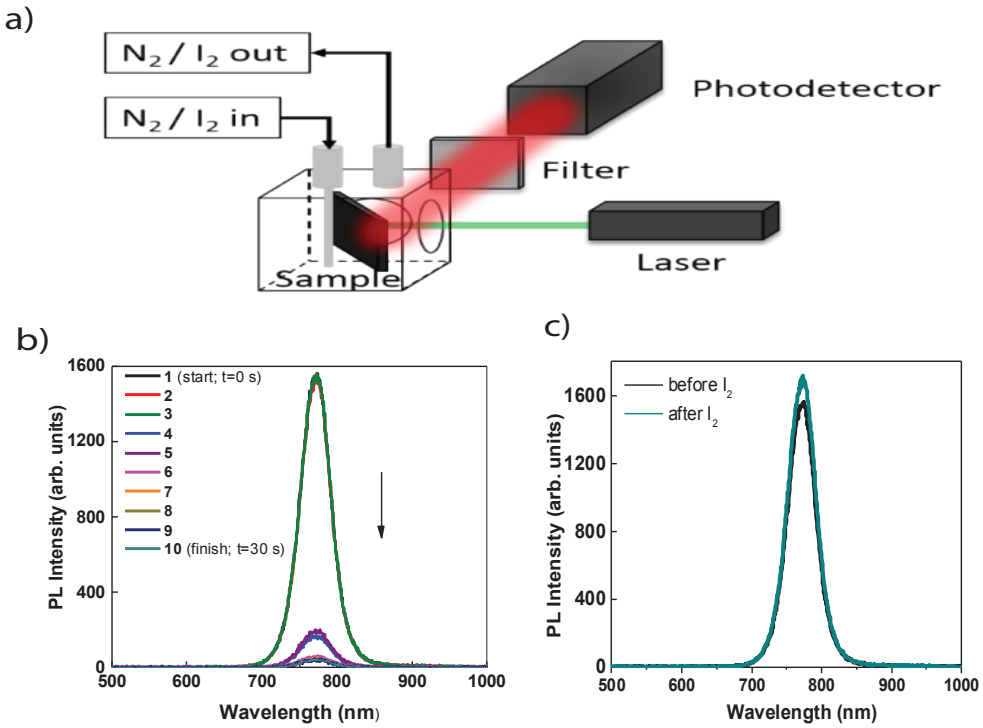

Figure 413: a) Schematic diagram of the PL quenching/recovery experiment using I_2 saturated N_2 and pure N_2 vapour, respectively. The excitation source is a laser with wavelength of 532 nm. b) Temporal evolution of the PL intensity of a perovskite film in I_2 vapour. PL spectra were recorded every 3 s. c) Recovery of PL intensity of perovskite film after 5 min in a pure N_2 atmosphere.

N_2 leading to a recovery of the PL intensity to its original value after $\sim 5\ min$. The optical absorption of iodide vapour [267] does not affect the excitation (532 nm) or the emission signal (∼780 nm). This PL quenching is only associated with the influence of iodine doping in the perovskite film. Wang et al.[268] proposed the chemical reaction of perovskite materials exposure to the high concentration of iodine vapour. The proposed chemical reaction reads as:

(i) under visible or ultraviolet light

$$I_2 \xrightarrow{h\nu} 2I^{\cdot} \tag{4.9}$$

$$2I^- + 2I^{\cdot} \xrightarrow{h\nu} 2I_2^{\cdot -} \tag{4.10}$$

(ii) under darkness

$$I^- + I_2 \overset{\leftarrow}{\rightarrow} I_3^- \tag{4.11}$$

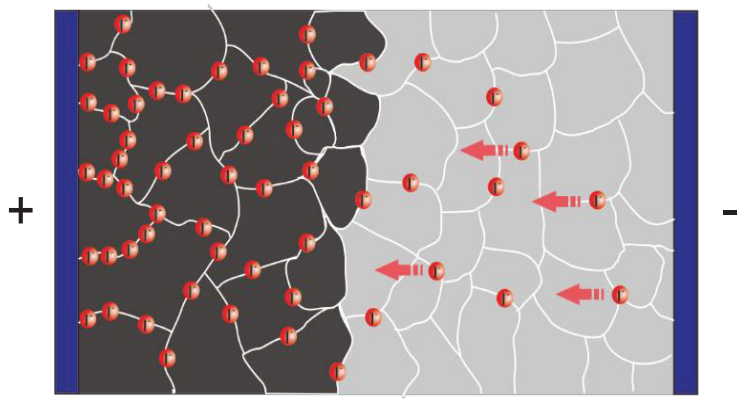

Figure 414: Schematic diagram of the influence of iodide ion migration on the PL intensity under an external electric field. The electric field drives the ions, leading to the accumulation of these ions which enhance the nonradiative recombination in these individual grains. These grain boundaries serve as the main pathways for the ionic migration.

With assistance of light, atomic iodine ($I^{\cdot}$) is generated in the iodine vapour based on Eq.4.9. Then these atomic iodines can react with iodide ions (I^{-}), forming $I_2^{\cdot -}$ based on Eq.4.10. $I_2^{\cdot -}$ can further react with MA^{+} ions, leading to the degradation of perovskite materials. According to Eq.4.11, triiodide ions (I_3^{-}) are formed in the iodine vapour. I^{-} can further participate the following reaction with MA^{+} ions. Both of the above reactions will lead to the degradation of perovskite, forming CH_3NH_2 gas and PbI_2. Here, note that, in this work, under relatively low concentration iodine vapour, the reversible change of PL intensity suggests the reversible chemical reaction, rather than irreversible structure degradation [218]. Currently, the detailed microscopic process is still under investigation, however this rather simple experiment elucidates the direct and reversible influence of accumulated iodide.

4.4 Model of Photoluminescence Quenching Under External Electrical Fields

Now, we can provide a picture on the evolution of PL dark areas on the perovskite film under external electrical field. This enhanced non-radiative recombination pathway includes both the trap-assisted recombination [269] and possible Auger-like recombination due to the charged mobile defects [217, 220]. Under external fields, as shown in Fig.414, the mobile ions obtain sufficient energy to overcome the activation energy [257, 270] and start to drift. These accumulated charges enhance the local electrical field [214]. It is known that the excited states are significantly influenced

by its surrounding, e.g. ionized grains [271], which results in the PL quenching [220, 272]. By employing time-of-flight secondary ion mass spectrometry with PL microscopy, deQuilettes et al. [273] find that excess iodide ions are driven by an optical field away from the illuminated region. Subsequently, this redistribution of iodide ions gives rise to the rising of PL intensity under continuum light illumination by decreasing the local iodide ion concentration. Nevertheless, how the excess iodide ions contribute to the nonradiative recombination is still not fully elucidated. Iodide interstitials [236, 274], acting as shallow defects, should not lead to significant charge recombination. Agiorgousis et al. [275] suggest that both lead dimers and iodide trimers may form with strong covalent bonds at defects, performing as strong-covalency induced recombination centres. The detailed understanding, however, is still under investigation.

Here, it is necessary to mention that during this experiment, we cannot completely rule out the migration or reorientation of $MA+$ ions under an electrical field [216, 268], though the recent evidences in literature point toward iodine. Previous works proposed that the migration of MA+ ions and Pb vacancies may play a role in the hysteresis of perovskite solar cells [229, 276]. However, Eames et al. [257] estimated that the diffusion coefficient of MA^+ ions is four orders of magnitude lower than the one of iodide ions. In addition, the direct observation of accumulation of negative ions at the positive side suggests the main contribution of halide ions rather than other defects [215, 232]. This may be attributed to the low mobility and higher activation energy for other defects, e.g., Pb vacancies, MA^+ ions, etc [277]. In this work, we observed the migration of ions in relatively low electric field ($\approx 10^5 Vm^{-1}$), so the phase change should also not be the main reason.

The exact ionic migration pathway is still unclear. Due to the large density of defect states in the perovskite film, ascribed to the low-temperature film fabrication, the defect facilitated ion migration may play an important role. Beside moving through bulk point defects, more and more evidence indicates that the grain boundary, where large amount of defects exist due to the lack of perfect crystalline structure, serves as the main ionic migration channel [225, 278, 279]. Due to the loss of the half chemical bond at grain boundary, these defects, e.g., iodide vacancies or iodide interstitials sites, facilitate the ionic migration through defect site replacing [225]. In addition, at temperature 330 K under external electric field, decomposed PbI_2 was observed, migrating along external field [259]. Therefore, field-induced structure decomposition/distortion may also play a role in ionic migration.

The Fig. 49 demonstrates that movement of PL inactive area migrates grain by grain. This suggests that under external electric field, with the assistance of grain boundaries, iodide ions drift toward and accumulate at the positive electrode. When the concentration of iodide ion reaches a certain threshold, PL quenching is observed. By investigating the ion migration properties in perovskite films and single crystal, Xing et al. [264] found that the activation energy of ions strongly depends on the size of grain. In addition, the research on the grain size dependence of ionic migration, characterised by PL microscopy is processing in the Huettner group. However, this is beyond the scope of this chapter.

In addition, a different case is observed when the ion does not act merely as an spectator but lead to chemical reactions with the surrounding materials. Obviously, in this case the rate of the reactions may be limited by the ions supply and this will follow diffusive limitations. In the case of perovskite solar cells, it looks like we are able to remove 1-3 iodide ions from each unit cell according to previous results [280].

It is necessary to mention that the moving front in Fig. 49 might not be actually ions migration but the reaction product between the perovskite and the excess ions. In fact, this impressive flat profile of the fronts as shown in Figure 2 are not usually observed in diffusive processes and rather implies that a certain threshold value of accumulated iodine is responsible for this phenomenon. In addition, it is noted that the velocity of moving front across the whole channel is not a constant, suggesting an ionic space charge effect. The detailed process is under investigation.

Beside in perovskite solar cells, ion migration also plays an important role in perovskite light emitting diodes (LEDs) and the herein presented experiments can help to shine light into respectively observed dynamics. For instance, in typical perovskite LEDs [281, 282], considering a dielectric constant of $CsPbX_3$ quantum dots ($\epsilon_r \approx 5$) [283] and polymer transport layer ($\epsilon_r \approx 3$), the electric field dropped on this perovskite layer is in the order of $10^7 Vm^{-1}$. These fields are even larger than those applied in this experiment (Fig.410), which renders even faster migration velocities. For example, Tan et al. [211] observed respective time dependent performance and hysteresis behaviour. The timescale of increases in external quantum efficiency of the LEDs under pulsed voltage is less than $0.01\ s$.

4.5 Concluding Remarks

In summary, we use both photoluminescence (PL) characterization and wide-field PL imaging as a function of time to investigate the spatially- and temporally-resolved PL in $CH_3NH_3PbI_{3-x}Cl_x$ perovskite films. Further, continuously increasing the excitation intensity during the light soaking was observed the PL "blinking" or PL intermittency behavior in individual grains of these films.Further, Realising a continuous increase of the PL intensity during light soaking, was observed the PL "blinking" or PL intermittency behaviour in individual grains of these films. A significant suppression of the PL blinking in perovskite films coated with a phenyl-C61-butyric acid methyl ester (PCBM) layer was observed. This suggests that the PL intermittency is attributed to Auger recombination induced by photoionized defects/traps or mobile ions within grains (trap-filling process). This photoionized process results in the PL blinking which prevents to reach SQ-limit so far.

Complementary, we demonstrate a direct method to visualise ion migration in an electric field in organolead halide perovskite films through wide-field PL imaging microscopy. It is evident that local stoichiometric variations due to external electrical field have a significant impact on the local PL performance, and therefore influence the solar cells performance. This field driven inhomogeneity is associated with iodide ions migration, which is confirmed by both IS characterisation and PL quenching under I_2 vapour. By employing PL imaging microscopy in combination with IS, we further characterize the dynamic processes of these iodide ions when monitoring the migration of PL inactive areas under external electrical fields in lateral-configured electrode devices. Hence, wide-field PL imaging microscopy provides an in situ approach to investigate ionic migration, which has obvious impact on photovoltaic performance, such as J-V hysteresis and chemical degradation. This provides a powerful tool to investigate the influence of grain boundaries, crystal size or passivation procedures in perovskite thin films. To further improve the performance and stability of perovskite solar cells, it is important to carefully control the defect/ions migration within the operating device, either by decreasing the defect density in the bulk (crystalline size and quality) or alleviating the long-term biasing effect in the vicinity of electrode. This finding paves the way to provide a guideline on the further improvement of perovskite opto-electronic devices and complement the research of this kind of architectures towards single photon emitters.

Chapter 5

TRIHALIDE PEROVSKITE QUANTUM DOTS AS A RELIABLE SINGLE PHOTON QUANTUM SOURCE

5.1 Introduction

The dynamical development of quantum technologies has defined some quantum information protocols without classical counterpart like teleportation[12], quantum cryptography [67], big numbers factoring algorithm (Shor's algorithm)[284], search algorithms (Grover's algorithm)[285], quantum key distribution[286], and schemes that surpass the classical equivalent like decision strategies (Quantum Games)[47], Quantum Fourier Transform [287], quantum simulation, and quantum walks[288]. Nevertheless, current realizations of these algorithms require a physical system which can be prepared in the quantum state wanted. It means, to achieve the quantum control over the physical representation of the qubit which belongs in turn to a two-level system. In this way of thinking, the production of pure quantum states of light becomes necessary and reliable through the building of controllable single photon sources[70, 71]. Different efforts have been addressed in this direction, for example, measuring the resonant fluorescence of Quantum dots (QDs) in a microcavity[114–116], using a three-level atom in an optical cavity[117], observing the fluorescence from a single nitrogen-vacancy[118], counting the emissions from defects in Silicon Carbide [119], analysing molecules trapped in solids[120], setting QDs in silicon photonic circuits[121], recording emissions from excitons originated at oxygen defects in carbon nano tubes[122], or employing highly diluted organic molecules [123]. Nowadays, a new material with the possibility to control the fluorescent emission with an electric field is joining to these initiatives[53].

The quickly increase of the Power Conversion Efficiency (PCE) of the inorganic-organic trihalide perovskite materials from 6.5%[113] to 9.7%[112] in only one year attracted the attention of the scientific community of solar cells[104]. Currently, these materials achieve a PCE of 22.7%[129], and nowadays the structural, electronic and optical properties motivate the creation and the enhancement of existing light-emitting devices [105]. The typical crystal structure ABX_3 of Perovskites, where A and B are cations bounded by anions X, offers a versatile and stable combination just changing its constituent halides, see Fig. 51. This molecular structure can be

synthesise as Hybrid Organic-Inorganic Perovskite (HOIPs) counting with around $1,346$ stable structures with 16 organic cations, 4 halide anions (Cl, I, Br, F) and 3 group-IV cations (Pb, Sn, Ge) in defined combinations [132]. In this variety of combinations, it is found the methylammonium (MA) in the $MA-SnX_3$ structure with tunability of emissions over a wavelength range higher than 900 nm but with a high tendency to the degradation at contact with the air[289]. Besides, we consider the exhaustively explored material for optoelectronics applications, the Methylamonium (MA) trihalide Perovskite ($CH_3NH_3PbX_nY_{3-n}$)[146, 201, 218, 219, 224, 229, 247, 259, 265, 268, 279]. This compound is spectrally tuneable in the UV-VIS-NIR range changing the halides components and has a direct band-gap which ensure a high emission efficiency [134]. Structures all-inorganics also integrates the Perovskite family in which the Cs replaces the organic cation (MA, Formamidinium-FA, etc.) obtaining $CsPbX_3$, with X as Br, I, or a mixture. This last structure was prepared by first time in 1958 by Moller [290, 291]. However, until 2016 the structure was synthesized in monodisperse Quantum Dots (QDs) of $\sim 4-15$ nm of the side with cubic perovskite crystal structure. Protesescu *et al.*[102] proposed these QDs and have exhibited high photoluminescence efficiency ($> 50\%$) in a tunable range of emission ($400-700$ nm). Also, the mentioned structures count with a volume per unitary cell of $\sim 216\ \ nm^3$ resulting in a packing efficiency of 0.001 besides of their easy manufacturing in solution and favorable stability at cryogenic and room temperature. These features highlighted the QDs Cs-based perovskites over the other well-studied materials alternatives like $CdSe$ and $PbSe$ [292]. Additionally, the perovskite structure is a candidate to solve the scalability problem in the quantum information protocols, in the sense of increasing the number of qubits accessible to be controlled and the decreasing of the coding errors. In this direction, some alternatives require the control of the system electro-optical response to the preparation of quantum states, the detection arrangement which interacts in a controlled way with the quantum system, and the hardware for the hosting and transmission of qubits. In this direction, here we present a protocol, employing optical characterization, to find the adequate parameters in the manufacturing of single photon sources making use of inorganic perovskites as QDs. Considering that these materials with high packing efficiency and homogeneous distribution as QDs allow the control of its Photoluminescence (PL) emission through the regulation of the free charge carriers recombination within them through the ions movement mechanism, as shown in recent research[53]. This molecular structure defines a promising candidate to become the bridge between the photonic and the

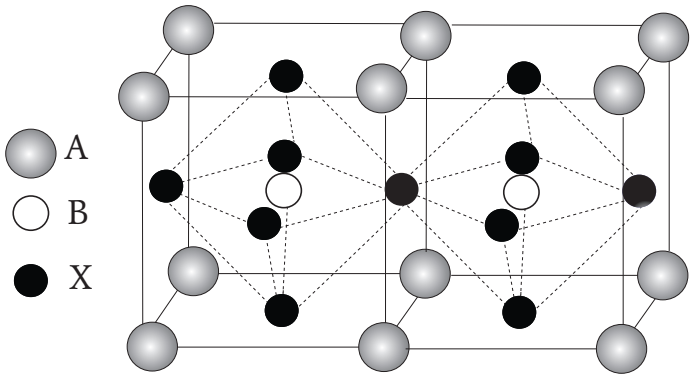

Figure 51: Scheme of the ABX_3 structure which is characterized by an inner octahedron ($(BX_6)^{4-}$). The corners in the orthogonal directions generate an infinite three-dimensional framework ($(BX_3)^{-}$). The cations A^+ define the shape, charge distribution and size of the final structure.

superconducting qubits in the formulation of a hybrid computational scheme for quantum information.

5.2 Experimental Methods:

Quantum dot Samples:

In [293], the perovskite samples preparation is detailed. As a brief description, octadecene and $PbBr_2$ were deposit in a neck flask and heated to 120 ° C. Time after, the oleic acid and the oleylamine were injected into the mixture and heated up to 150° C to mix with cesium oleate. Afterward, through centrifugation, the QDs were precipitated and redispersed in hexane, to finally in a glovebox be stored, without contacting water nor oxygen. Before setting the sample in the optical system, the QDs in solution was diluted ($1 : 100$ - $1 : 10^4$) vol/vol in toluene. Finally, an amount of 10 μl of the sample was homogeneously deposited over a coverslip using a spin-coat at 7000 RPM in an inert atmosphere of N_2.

Photoluminescence (PL) spectra and Hanbury Brown-Twiss (HBT) Measurements:

We use two different home-built confocal microscope to visualize the signal of the fluorescence emission. The first employ in the detection path a CCD camera (Hamamatsu Orca) in widefield and confocal mode, a spectrometer coupled to a CMOS camera (Princeton Acton 2500 series+ Sensicam camera), and the Avalanche

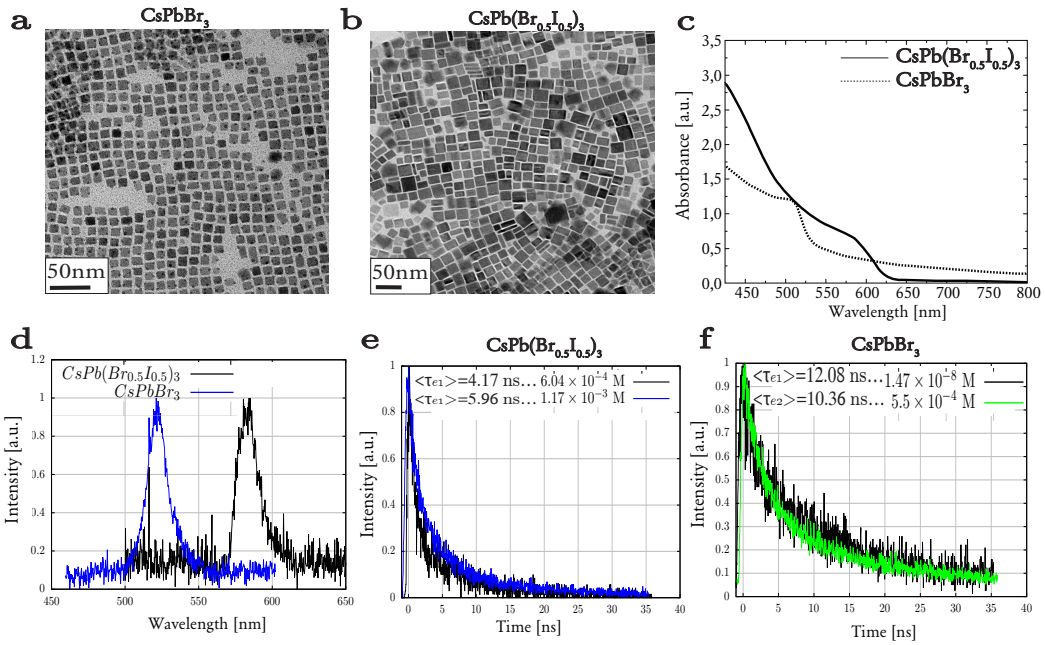

Figure 52: Optical and morphological characteristics of $CsPbBr_3$ and $CsPb(Br_{0.5}I_{0.5})_3$ perovskites. In both Transmission Electron Microscope (TEM) images the scalebar represents 50 nm for (a) $CsPbBr_3$ perovskite, and (b) $CsPb(Br_{0.5}I_{0.5})_3$ to visualize the morphology. (c) the absorbance spectrum of perovskites, the dashed line is the absorbance for $CsPbBr_3$ and the solid line for $CsPb(Br_{0.5}I_{0.5})_3$. (d) The compounds emission spectra presents maxima emission peaks at 525 nm for $CsPbBr_3$ and at 580 nm for $CsPb(Br_{0.5}I_{0.5})_3$ as expected [103, 145, 292]. The exciton average lifetime $\langle \tau_e \rangle$ measurements of (e) $CsPb(Br_{0.5}I_{0.5})_3$ at concentrations of 6.04×10^{-4} M and 1.17×10^{-3} M, and (f) $CsPbBr_3$ at concentrations of 1.47×10^{-8} and 5.5×10^{-4} in both cases the behavior is better fitted by a bi-exponential behaviour.

photodiode (APD) connected to a TCSPC card (Timeharp-200-picoquant). We used a pulsed laser diode (LDH-P-C-4508B, Picoquant-20 MHz repetition rate), attenuated with neutral density filters, as the excitation source. In the second setup, we use a CW laser at 488 nm, spatial filtered, to exciting the sample in the HBT measurements. Posteriorly, we split the beam through a dichroic mirror and address it to the sample with a scanning mirror and a set of telecentric lenses. This set allows the accurate movement of the spot over the sample in a confocal mode able to resolve down to $\sim$ 360nm with a microscope objective of $NA = 0.85$. The fluorescence response travels way back crossing over a Long Pass filter (LP514) afterward, a $70 : 30$ beam splitter divided this light and focused it in a CCD camera (DV887DCS-BV, Luca Andor Technology) in one arm. The other arm was

directed through another $50:50$ beam splitter and finally coupled to single photon counters (SPCM-AQR-15, EG&G) connected between them through a TCSPC card (Timeharp 200-picoquant) which save the correlations to the computer, see Fig. B1.

5.3 Results and discussions:

We analyse two compositions of Cs-based perovskite compounds with the absorption spectra shown in the Fig. 52c, and a maximum emission peak measured in the spectra around $\lambda = 525$ nm for $CsPbBr_3$ and at $\lambda = 580$ nm for $CsPb(Br_{0.5}I_{0.5})_3$ as shown in Fig. 52d. We prepare these compounds at different dilutions ranging from $\sim 10^{-8}$ M up to $\sim 10^{-3}$ M corresponding to the molar masse, and volume of a single perovskite cell for each compound. These concentrations define the amount of fluorescence bright spots on the field of view of our microscope in a maximum diameter of $\sim 40\mu$ m. In each concentration, the fluorescent emission lifetime was measured and fitted better by a bi-exponential behaviour with two time constants (τ_1 and τ_2) corresponding to the effective single-exciton lifetime and the respective amplitudes (w_1 and w_2) which can be related to the average exciton lifetime of the quantum dots ensemble through $\langle \tau_e \rangle = \sum_i^2 w_i \tau_i$ accounting for both the nonradiative and radiative processes[292]. Each compound was measured and analyzed for two different concentrations we calculated the average exciton lifetime for each QD ensemble. For $CsPb(Br_{0.5}I_{0.5})_3$, we found a value of $\langle \tau_e \rangle = 4.17$ ns ($\tau_1 = 5.19$ ns, $\tau_2 = 0.76$ ns, $w_1 = 0.77$, $w_2 = 0.23$) for a concentration of 6.04×10^{-4} M, and $\langle \tau_e \rangle = 5.96$ ns ($\tau_1 = 7.99$ ns, $\tau_2 = 1.71$ ns, $w_1 = 0.68$, $w_2 = 0.31$) for a concentration of 1.17×10^{-3} M. For $CsPbBr_3$, the exciton average lifetime was of $\langle \tau_e \rangle = 12.08$ ns ($\tau_1 = 13.01$ ns, $\tau_2 = 1.73$ ns, $w_1 = 0.92$, $w_2 = 0.08$) for a concentration of of 1.47×10^{-8} M, and $\langle \tau_e \rangle = 10.36$ ns ($\tau_1 = 12.63$ ns, $\tau_2 = 2.52$ ns, $w_1 = 0.78$, $w_2 = 0.22$) for a concentration of 5.5×10^{-4} M, all these measurements were performed at room temperature, Fig.52e-f. We can observe a difference of around 6 ns between the composites with iodine and the one with Bromide only of the average emission times. This difference is an indication that the injection of iodine into the perovskite structure is decreasing the efficiency of the Auger process responsible for the excitons decay to form free carriers of charge [292, 294–297]. In such a way, a different value of the emission lifetime is the result of the dynamics between the radiative and the nonradiative processes. Even more, the switching process in the fluorescence emission (intermittency or blinking) will depend on the local conditions of highly diluted samples due to the non-radiative events (e.g., nonradiative Auger recombination). In this sense, the characterization of the in-

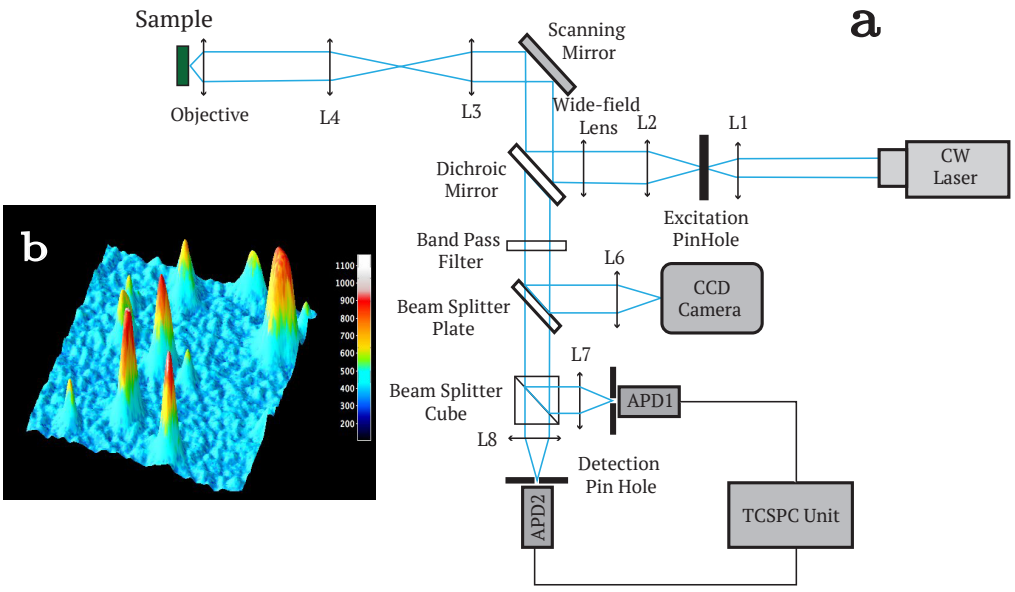

Figure 53: (a) The experimental setup (L and PH corresponds to Lens and PinHole respectively): a CW laser at 488 nm is focused and spatially filtered through the lens set L1 and L2 and the excitation pinhole. Later, the beam travel to the sample through a Dichroic and a Scanning mirror which allows the movement of the light on the sample surface in the same focal plane through the telecentric lenses system (L3, and L4). Finally, we focus the beam with an objective of 0.85 NA on the material in confocal mode. This last illumination mode was able to be changed using a wide-field lens before the dichroic mirror. The fluorescence response from the material directed through a Bandpass filter to avoid the laser reflection signal and via a 70:30 beam splitter the resulting beam was divided. One arm focus on a CCD Camera with the L6 and the other arm was set in a Hanbury-Brown and Twiss interferometer form by a 50:50 beam splitter cube, L7, L8 two detection pinholes and two avalanche Photodiodes (APD 1 and 2) connected to a time-correlated single photon counting system (TCSPC). (b) A 3D profile of $10\ \times 10\ \mu m$ of the sample where the z coordinate represents the intensity in false color and x, y are spatial coordinates.

termittency behavior gives us a better understanding of the local photophysics in each compound. We explore the PL emission intensity resulting from the sequential variation of the pumping excitation power on each perovskite sample selected. The highest pump power over the materials lead to the photobleaching threshold. The Fig. 54a shows the spectral answer of the $CsPb(Br_{0.5}I_{0.5})_3$ with a concentration of 6.04×10^{-4} M being excited with intensities of $8.3\times10^{2}\ W/cm^2$, $2.5\times10^{3}\ W/cm^2$, $3.1\times10^{4}\ W/cm^2$, and $3.1\times10^{5}\ W/cm^2$. The upper part corresponds to the sequential images of the sample spectra with an exposure time of 50 ms each and an

excitation power marked on it. The lower frame is the relative intensity of the spectra in which the shaded region represents the change of excitation power on the sample. Here, we appreciate a proportional and stable answer to the excitation pumping at the beginning of the sequence until around twenty seconds of excitation. However, the response of the sample to higher intensities ($\sim \times 10^4 - \times 10^5\ W/cm^2$) was proportional but unstable exhibiting a "sudden drop" on the PL emission indicating that the amount of photons on the sample has saturated the radiative processes, in turn, enhancing the nonradiative ones as the charge carrier recombination leading to the photobleaching behavior for $3.1 \times 10^4\ W/cm^2$ [53]. Nevertheless, we observed a small plateau after sixty seconds with an intensity of around 3000 counts (notably high in comparison with the background of 200 counts in average) which is an indication that the system is currently responsive and not entirely photobleached yet, see Fig. 54 (a). After $3.1 \times 10^5\ W/cm^2$, the sample is photobleached decreasing the PL answer notably. This sequential analysis was performed with the same excitation intensity levels over the $CsPbBr_3$ (with 1.47×10^{-8} M) showing a photobleaching reaction (around $2.5 \times 10^4\ W/cm^2$) earlier than the previous perovskite composite. We developed the experiment with an integration time of 500 ms due to the lower intensity response of this sample. In this case, after the sample is photobleached the higher pumping do not produce a proportional PL answer from the sample as shown in the Fig. 54b for $3.33 \times 10^5\ W/cm^2$. With this procedure, we established the pumping excitation range for our samples at room temperature. Complementary, the recognizing of conditions for blinking appearing at low dilutions could guide us toward the single emitters preparation because the PL intermittency or "Blinking" could be used as a signal of few emitters spatially isolated in highly diluted samples [298]. In this sense, we select different regions on two samples with the same concentration ($5.5 \times 10^{-4}\ M$) of $CsPbBr_3$ in which was identified the blinking signature. In each location, we have taken an average of 100 confocal images of the chosen sample piled in a sequential time series with the integration time inscribed on the images, as shown in the upper parts of the Figures 55-56.

To analyze the blinking response due to the pumping power then these QDs were organized into two sets. The first couple of QDs received a fluency of $1.3 \times 10^4\ W/cm^2$ nearly to the damage threshold in which both sites show different behaviors, see Fig.55. The QD1 shows a steady emission in which the maximum variations on the intensity are around 3800 counts, however, the minimum intensity emitted is 2200 counts which compares with the background signal on average 600 counts is at least four times higher, then, this is not representative of blinking

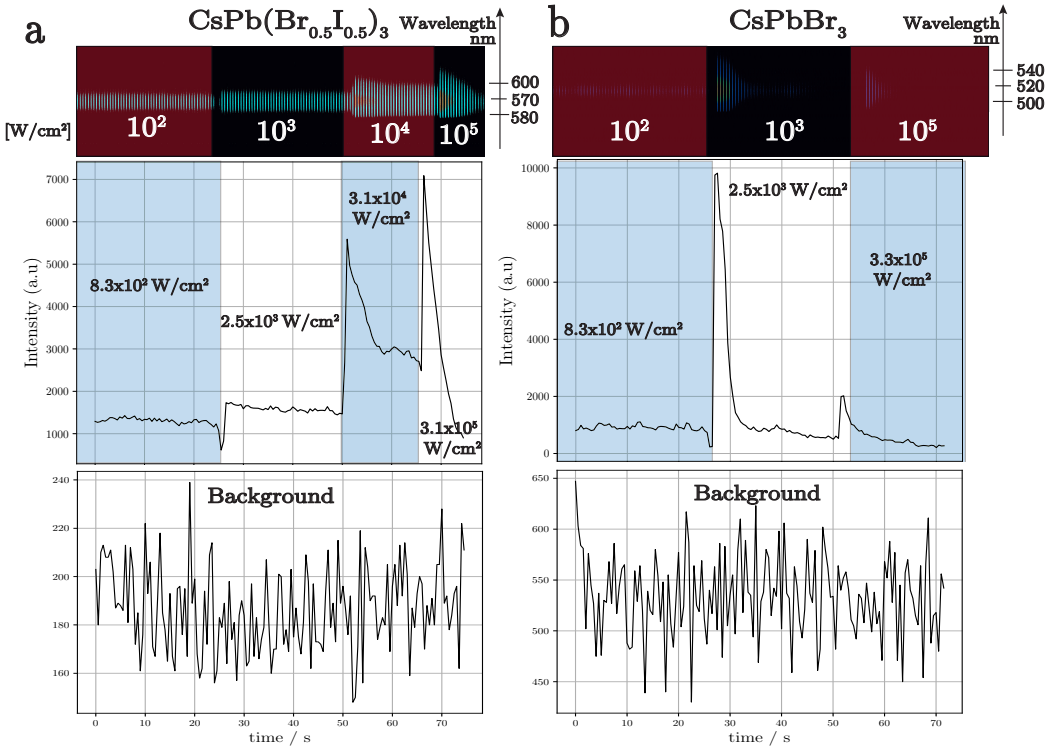

Figure 54: The stacking of sequential spectra from the samples allows the analysis of the intensity response of the (a) $CsPb(Br_{0.5}I_{0.5})_3$ saved with 500 ms of exposure time per spectrum under excitations intensity of $8.3 \times 10^2\ W/cm^2$, $2.5 \times 10^3\ W/cm^2$, $3.1 \times 10^4\ W/cm^2$, and $3.1 \times 10^5\ W/cm^2$ marking the changes of the excitation intensity by the shaded areas. Corresponding for (b)$CsPbBr_3$ at 500 ms of exposure time and excitations intensity of $8.3 \times 10^2\ W/cm^2$, $2.5 \times 10^3\ W/cm^2$, $3.3 \times 10^5\ W/cm^2$. The upper frame shows the real image of the sample spectra in fake color to enhance the intensity by picture indicating the changes of excitation intensity with shaded regions. The lower frame corresponds to the total intensity profile of the fluorescence response obtained from the upper section. In the bottom, the background measurements for the experiments (a) with 190 counts in average, and (b) with an average of 550 counts.

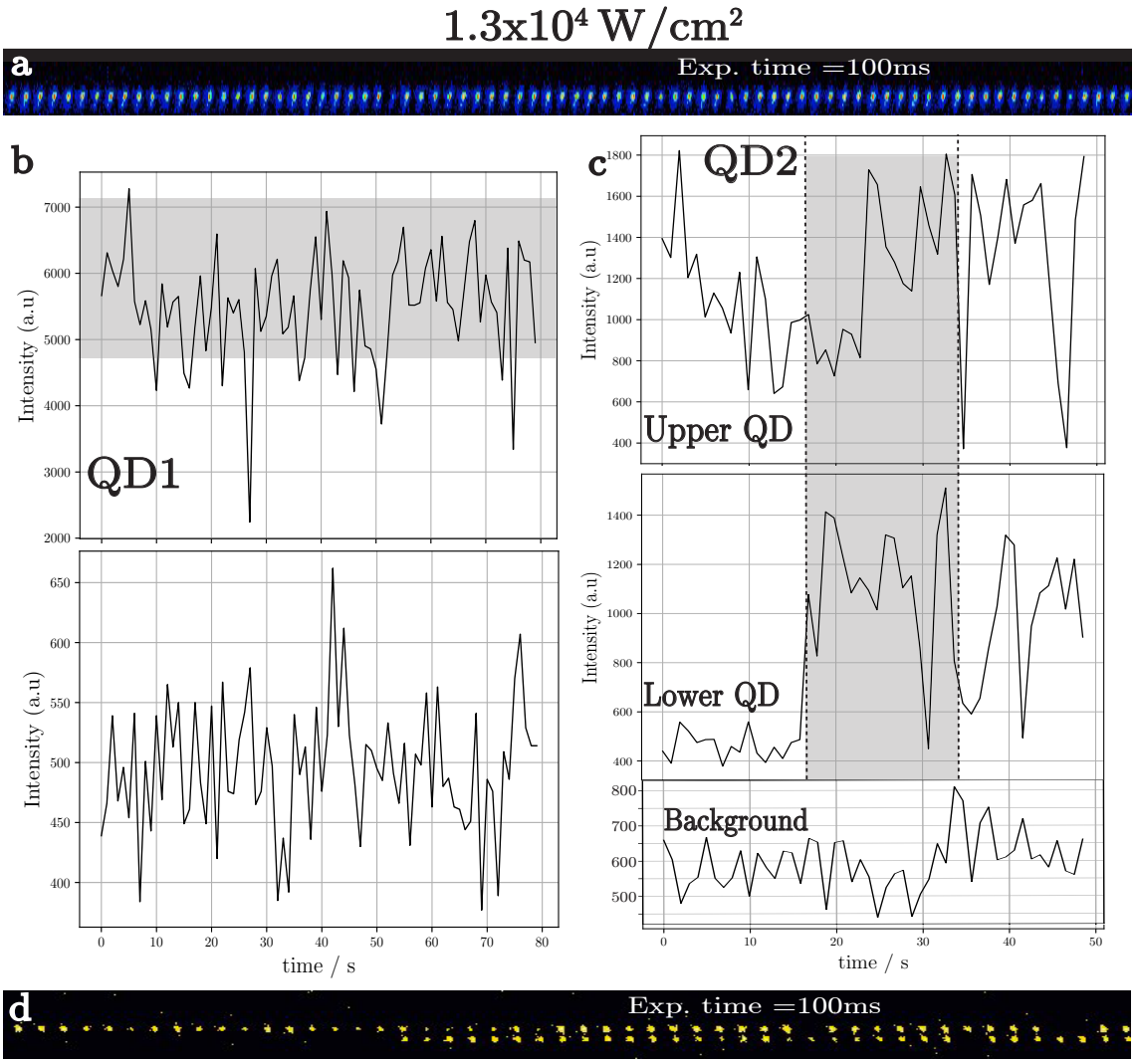

Figure 55: The $CsPbBr_3$ perovskite excited with $1.3 \times 10^4\ W/cm^2$ of intensity near to the damage threshold of the material. (a) Sequential confocal images, with a exposure time of 100 ms and saved each 1 s, of the fluorescence response of the QD1 corresponding to the Intensity response profile in (b), here we observe the emission value in comparison with the background plotted in the lower part. In the same experiment, (c) the QD2 received the same intensity but under the appearance of another QD which is activate 15 s later, the grey region shows the simultaneous activation of this QDs, as shown in (d) the sequential set of confocal images of the experiment.

behavior, as shown in Fig.55a. This behavior means these emissions belong to a small agglomerate of QDs and not single emitters. This tendency changed in the QD2, Fig. 55c-d, showing variations of the fluorescence fifteen seconds after begins the excitation. The appearing of a nearby QD neighbor is the reason for the change in the intensity shown in the grey area in Fig.55c, the lower frame Fig. 55d, which finally produces a double blinking sequence in which is observable the change in the emission state analyzing both QD separetly (Fig. 55c upper and lower frame). Here, the blinking operation is clear due to the minimum intensity emitted in both cases (upper and lower frame) are ~ 600 counts, as high as the background value, and the maximum emission is three times higher than the background signal showing an appreciable ON-OFF change. The other QDs were excited with $85\ W/cm^2$, a value smaller than the photobleaching limit, and we achieve two scenarios again. The QD3, shown in the Fig. 56a presents regions of blinking and multi-level emission becoming a mixture of conditions of the set before analyzed. And the QD4, despite a slight variation in the intensity profile of emission it is not blinking as shown in Fig. 56c. In this QD the blinking graphical analysis shows a change not higher than 7000 counts and the minimum fluorescence emission is around 11000 counts. Comparing with the background signal (shown in the lower frame of the Fig. 56 c) this does not represent an OFF-state. And as shown in Fig. 56d, then we observe that the blinking is not present and the conditions for the two-level behavior are not accomplished.

Henceforth, the idea to analyze the photophysical behavior of the QDs determines two significant features of the preparation of single photon sources. First, this experimental analysis allows distinguishing the local conditions of each QDs as a protocol to find specific environments employing the PL responses correlated with time. And second, the average lifetime of the emitter in the excited state defines the lag time to emit a single photon, i.e., the repetition frequency of emission of a single photon[145].

Single Photon Source with Perovskites

We use a CW laser ($\lambda = 488nm$) in a Hanbury Brown-Twiss (HBT) interferometer connected to a Time-Correlated Single Photon Counting (TCSPC) system (see methods and Fig.B1) to analyze the emissions of $CsPb(Br_{0.5}I_{0.5})_3$, with a concentration of 1.7×10^{-5} M, the QD to analyse was allocated employing the optical identification already described. The blinking signature shows two state emissions which are characteristic of single emitters a similar phenomenon occurs on atoms

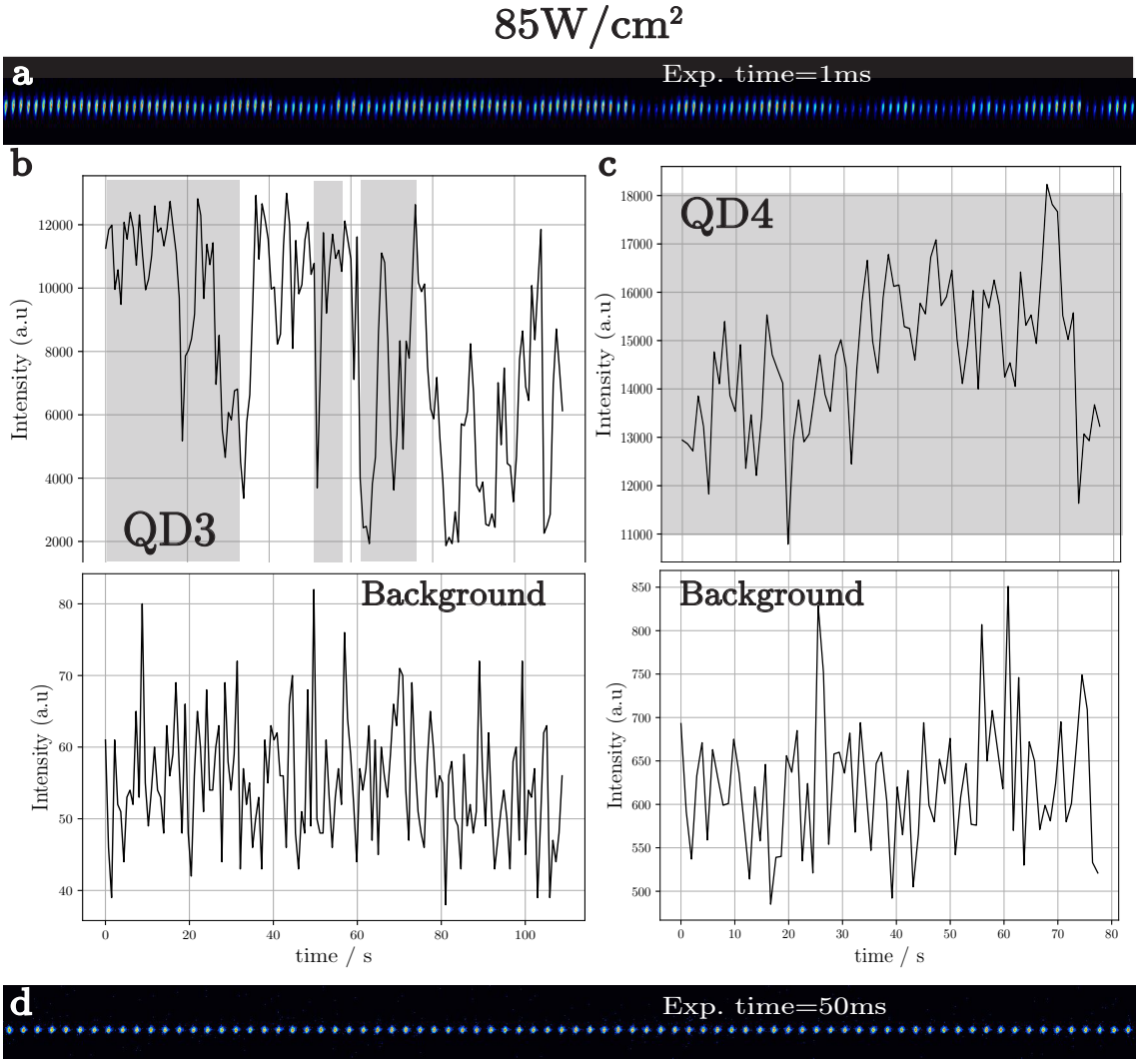

Figure 56: $CsPbBr_3$ perovskite excited with a intensity smaller than the damage threshold of the material, $85\ W/cm^2$. The QD3 presents a combination of conditions not observed in (a) the sequential stack of confocal images but signaled by changes in the intensity response profile in (b) with the shaded region. The bottom panel shows the background taken during the measurement of QD3 (~ 55 counts). The confocal image sequence shows a possible single QD, however, in agreement with the profile data, the emission behavior could correspond to a couple of emitters closely located. The QD4 shows (c) the intensity response with a variation of 7000 counts from the total, however in regards to the background data (~ 800 counts) the minimum emission (11000 counts) is at least 12 times higher. (d) shows the sequential stack of confocal images of the QD4.

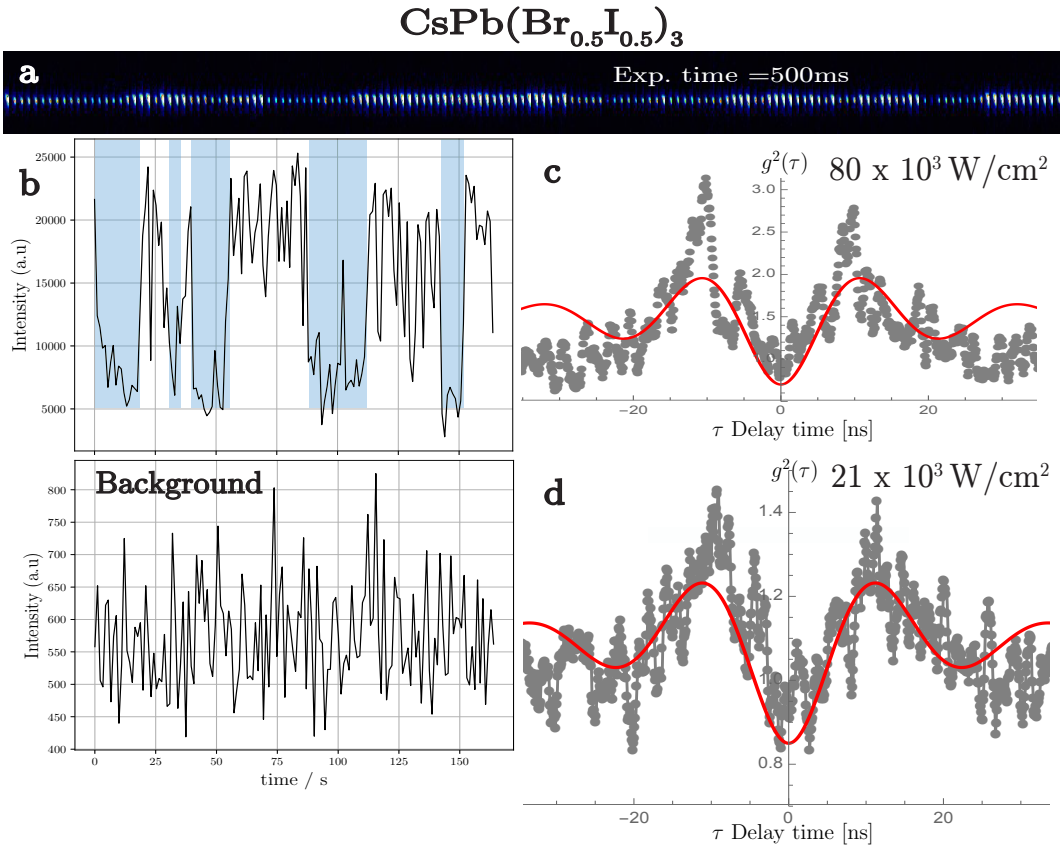

Figure 57: (a) The upper frame corresponds to the confocal image of the fluorescence emission saved at 500 ms of exposure time per picture of $CsPb(Br_{0.5}I_{0.5})_3$ at 1.17×10^{-5} M. (b) The intensity response profile, extracted from the confocal images, shows on-off emission process similar to the quantum jump in single emitters. However, in comparison with the background signal in the bottom (~ 550 counts), the minimum emission of the QD is around ten times higher. With the Hanbury-Brown-Twiss setup, already described in methods, the system displays the performance given by the grey points for an excitation intensity of (c) 2.1×10^4 W/cm^2 and (d) 8.0×10^4 W/cm^2. This behavior fitted with the red line corresponds to the $g^{(2)}$ function of the resonance fluorescence experiments previously discussed [299, 300]. However, the sub-Poissonian response was not clear possibly due to the background noise and the existence of a few additional emitters in the same site which avoid achieving a minimum value of $g^{(2)}(\tau)$.

in which is known as quantum jumps [299]. In this case, the minimum emission intensity is 5000 counts around nine times higher than the background (600 counts), and the maximum emission is 24000 counts (forty times higher than the background) which make clear the ON-OFF behavior, Fig. 57a-b. However, the notable difference between minimum emission and the background signal could mean that we are observing a small cluster of QDs and not only one. In this way, to achieve information about the nature of light emitted it is necessary to measure the degree of second-order coherence $g^{(2)}$. We select the excitation and the detection paths through optical filters during the measurement process for 1800 s in two QDs with excitation powers around $80 \times 10^3 \ W/cm^2$ and $21 \times 10^3 \ W/cm^2$ on the QDs. We achieve the behavior shown in the Fig. 57c-d in which the central depth does not achieve the zero as expected in an isolated quantum system and the $g^{(2)}$-function does not show a regular increase up to 1. Nevertheless, accounting for the background correction due to additional emitters and the fact that we were working nearly to the damage threshold of the QDs, we employ the second-order coherence function for the fluorescence resonance scattering in the high excitation power regime to fit our experimental data. In this regime the Raby frequency is greater than the radiative decay rate of the system ($\Omega \gg \gamma_s$) and the $g^{(2)}$-function reads [299, 300]:

$$g^{(2)}(\tau) = 1 - \left(\cos(q\gamma_s|\tau|) + \frac{3}{2q} \sin(q\gamma_s|\tau|) \right) e^{-\frac{3\gamma_s|\tau|}{2}} \tag{5.1}$$

where $q = \left(\frac{\Omega^2}{\gamma_s^2} - \frac{1}{4} \right)^{1/2}$, and through the fitting we obtained the parameters $q = 7.365$ and $\gamma_s = 65 \ MHz$, finding a Raby frequency of $\Omega/ = 479 \ MHz$ for an excitation intensity of $8.0 \times 10^4 \ W/cm^2$ and $q = 5.36, \ \gamma_s = 75 \ MHz$ ($\Omega = 399 \ MHz$) for $2.1 \times 10^3 \ W/cm^2$, as shown in Fig. 57. These results suggests a Quantum Yield of 0.31 and shows the correspondence between the excitation intensity applied and the Raby frequency produced in this perovskite structure. Here we can consider that the $g^{(2)}$-function hide the Sub-Poissonian behavior of the light because, by one way the emission of few additional QDs, or by the other way the high excitation power generates a value greater than one [300]. Nevertheless, considering that the antibunching does not always means a photo-counting statistics Sub-Poissonian[301], the antibunching phenomenon can be contemplate in the sense of the function behavior,i.e., $g^{(2)}(0) < 1$ and $g^{(2)}(0) < g^{(2)}(\tau \sim 10 \ ns)$, as is shown in the Fig. 57. Additionally, the high number of excitation photons on the sample stimulated the saturation of the radiative process on the perovskite QDs which contribute to masking the single emission.

The same procedure was follow in the measurement of $CsPbBr_3$ perovskite with a concentration of 2.8×10^{-6} M. However, the measured answer not evidenced the expected behavior (not shown here).

5.4 Concluding Remarks

We identify essential features for the single photon emitters preparation from QDs of optoelectronic materials with the protocol here described. The characteristics identified involve an appropriate value for the excitation power, an adequate concentration of perovskite QDs, and a blinking signature. In a similar fashion as single atoms, the Perovskite QDs behave like a two-level system under conditions that are observable from the fluorescence blinking pattern. The long exciton lifetime of the $CsPb(Br_{0.5}I_{0.5})_3$ in comparison with $CsPbBr_3$ suggest a favorability of the radiative process instead of the non-radiative ones which constitute an advantage in the applications of light emission. Employing these tools, we observed the mixed behavior of the $g^{(2)}$-function divided into intervals, because despite not having achieved a total dip at τ from 0 to ~ 10 ns the $g^{(2)}(0) < 1$ and $g^{(2)}(0) < g^{(2)}(\tau = 10)$ which corresponds to *antibunching* tendency. However, after $\tau \sim 10$ ns the function behavior changed getting $g^{(2)}(\tau = 10) > g^{(2)}(\tau)$ which indicate that the measurements reveal antibunching behavior but a not a sub-Poissonian light in the $CsPb(Br_{0.5}I_{0.5})_3$ Perovskite QD. We produce a source with statistical emission bounded between the Poissonian and Sub-Poissonian behavior achieving a $g^{(2)} = 0.85$ for $CsPb(Br_{0.5}I_{0.5})_3$ in a concentration of 1.7×10^{-5} M with a repetition frequency $1/\tau \sim 200$ MHz. These results suggest the QDs of $CsPb(Br_{0.5}I_{0.5})_3$ as an alternative in the implementation of quantum computing hardware based on optoelectronics materials.

Chapter 6

SUMMARY

Employing the fact that for a specific range of angles which depends on the symmetry of the environment the quantum correlations, including entanglement, survive for the different scenarios (collective and non-collective) of decoherence without a critical dependence of the retardation length. In this thesis, we show, in **Chapter 3**, that a PMF corresponds with a long birefringent crystal, and could be a useful as coherence control device on entangling qubits. This phenonema was experimentally for a non-maximally entangled bipartite state of photons Verified.

In the **Chapter 4**, we particularly analyze the Prisoners' dilemma game for two an three players. Here, we employed a Werner-like state to evaluate, a difference from other authors, the importance of the entanglement or discord as correlations to keep the called "quantum advantage" in this algorithm. This advantage represents the additional amount of information that the quantum player has over the classical one. We concluded through the analysis of different nonlocality metrics that the important correlation in this algorithm is the "quantum superposition" and not the entanglement or discord. Finally, we proposed an experimental setup to verify these findings.

The **Chapter 5** describes the photoluminescence characterisation (PL) of the MA-halide perovskite material under different conditions: changing the laser excitation intensity, including additional PMMA material as oxidation stabiliser, and phenyl-C61-butyric acid methyl ester (PCBM) as electron acceptor, including an constant potential, and an saturated atmosphere with I_2 vapour. These scenarios were with PL spectroscopy analyzed, Impedance spectroscopy and a mixture of both techniques. This last constituted an in situ technique to visualize ion migration in organolead halide perovskite films under the action of a constant electric field. We further characterize the dynamic processes of these iodide ions at monitoring the migration of PL inactive areas under external electrical fields in lateral-configured electrode devices. Hence, wide-field PL imaging microscopy provides an approach to investigate ionic migration, which has an impact on photovoltaic performance, such as J-V hysteresis and chemical degradation. This procedure provides an effective tool

to investigate the influence of grain boundaries, crystal size or passivation procedures in perovskite thin films. This finding paves the way to provide a guideline on the further improvement of perovskite optoelectronic devices and complement the research of this kind of architectures towards single photon emitters.

In the **Chapter 6**, we identify essential features for the single photon emitters preparation from QDs of Cs-halide Perovskites materials. The characteristics identified involve an appropriate value for the excitation power, an adequate concentration of perovskite QDs, and a blinking signature. In a similar fashion as single atoms, the Perovskite QDs behave like a two-level system under conditions that are observable from the fluorescence blinking pattern. Here, we compared $CsPb(Br_{0.5}I_{0.5})_3$ with $CsPbBr_3$ to produce the single emitter source. We observed the mixed behavior of the $g^{(2)}$-function divided into intervals, because despite not having achieved a total dip at τ from 0 to ~ 10 ns the $g^{(2)}(0) < 1$ and $g^{(2)}(0) < g^{(2)}(\tau = 10)$ which corresponds to *antibunching* tendency. However, after $\tau \sim 10$ ns the function behavior changed getting $g^{(2)}(\tau = 10) > g^{(2)}(\tau)$ which indicate that the measurements reveal antibunching behavior but a not a sub-Poissonian light in the $CsPb(Br_{0.5}I_{0.5})_3$ Perovskite QD. In despite to not achieve an ideal source ($g^{(2)} = 0.0$), we produce a source with statistical emission bounded between the Poissonian and Sub-Poissonian behavior achieving a $g^{(2)} = 0.85$ for $CsPb(Br_{0.5}I_{0.5})_3$ in a concentration of 1.7×10^{-5} M with a repetition frequency $1/\tau \sim 200$ MHz. These results suggest the QDs of $CsPb(Br_{0.5}I_{0.5})_3$ as an alternative in the implementation of quantum computing hardware based on optoelectronics materials.

Finally, the advance training achieved in this research and the different ideas proposed here were the main resource to the implementation of a laboratory in Quantum Optics and Information, and another focused in spectroscopy of temporal molecular events named “Ultrafast spectroscopy laboratory” as described in the **Appendix**. As a collateral result of the laboratory implementation, we develop an FPGA -based cost-efficient coincidence counting module to process the signals sent by the single photon counting devices in experiments to test the quantum information theory concepts.

Appendix A

DETERMINATION CRITERIA AND ACTIVATION OF NON-LOCALITY

Clarification Note

The criteria here defined are adapted and selected from [47].

A.1 Non-locality Criteria

the input states $\rho_{in}(\delta, p)$ in a general finite-dimensional bipartite AB system is represented by a density matrix or quantum state $\rho \in D(\mathbb{C}^{d_A} \otimes \mathbb{C}^{d_B})$, with $d_A, d_B \geq 2$, where $D(\mathbb{H}) := \{\rho \in PSD(\mathbb{H}) | \mathrm{Tr}(\rho) = 1\}$ stands for the set of density matrices of the complex Hilbert space $\mathbb{H}$, with PSD the set of *positive semidefinite* complex matrices, i.e., the matrices ρ such that $\forall\, |\phi\rangle \in \mathbb{H} : \langle\phi|\, \rho\, |\phi\rangle \geq 0$. Here, we focus on the quantum properties of our two-qubit input states $\rho_{in}(\delta, p)$ which means that a Hidden Variable Model can be found to reproduce the same joint correlation of Alice and Bob $\mathrm{Tr}(A \otimes B \rho_{AB})$ predicted by quantum mechanics, where A and B are observables on the state of Alice and Bob, respectively [184]. The aforementioned nonlocal quantum features of the input states plotted in Ch.3, Fig. 36, for performing the PD game are described as follows.

Entanglement:

As consider in the Ch.2, the metric of quantum entanglement used here is the *Entanglement of Formation* $\mathcal{E}$ proposed by Wootters [20] defined as,

$$\mathcal{E}(\rho_{AB}) = h\left(\frac{1}{2}\left[1 + \sqrt{1 - \tilde{C}(\rho_{AB})^2}\right]\right), \tag{A.1}$$

where $h(x) = -x \log_2 x - (1-x)\log_2(1-x)$ is the classical binary entropy, and $\tilde{C}(\rho_{AB}) = \max\{0, \lambda_4 - \lambda_3 - \lambda_2 - \lambda_1\}$ the *concurrence*. The λ_i's refer to the square root of the eigenvalues to the auxiliary operator of the system $\rho_{AB}\tilde{\rho}_{AB}$ arranged in decreasing order, and $\tilde{\rho}_{AB} = (\sigma_y \otimes \sigma_y)\rho^*_{AB}(\sigma_y \otimes \sigma_y)$ [20]. The relationship between $\mathcal{E}$ and the $\tilde{C}$ is bi-univocal: $\mathcal{E}(\rho_{AB}) = \tilde{C}(\rho_{AB}) = 1$ for a maximally entangled state, and $\mathcal{E}(\rho_{AB}) = \tilde{C}(\rho_{AB}) = 0$, for a separable state. In any other case $\mathcal{E}(\rho_{AB}) < \tilde{C}(\rho_{AB})$. Besides of the analysis about the behaviour of the entanglement.

It is important to include also another metrics related with the amount of information obtained from the different measurements over the system.

Bell inequalities:

In 1964 J. S. Bell [10] defined a criterion to evidence the *spooky reaction at distance* postulated by Einstein, Podolsky and Rosen time before [3] to argue the incompleteness of the Quantum Mechanics. This early standard as *Bell inequalities* known, was considered a way to determine the amount of non-locality and entanglement indistinctly. As an ansatz, J. Bell considered a pair of one-half-spin particles in a singlet spin state and moving to opposite directions in which it can perform the measurement of the spin components $\hat{\sigma_1}$ and $\hat{\sigma_2}$. Here, if the value of the measure of $\hat{\sigma_1} \cdot \vec{a}$, with $\vec{a}$ as an unit vector, is $+1$, hence, the measurement of $\hat{\sigma_2} \cdot \vec{a}$ should be -1. By this hand, considering additional variables with influence over the measurement, i.e., λ and $\vec{a}$ determine the result A of measuring $\hat{\sigma_1} \cdot \vec{a}$, with $\vec{a}$ and the measurement value B of measuring $\hat{\sigma_2} \cdot \vec{b}$ is defined by $\vec{b}$ and λ n the same sense. In that way,

$$A(\vec{a}, \lambda) = \pm 1, \;\; B(\vec{b}, \lambda) = \pm 1, \tag{A.2}$$

and being $\rho(\lambda)$ the probability distribution of λ the expectation value of the product of the two measurements is

$$E(\vec{a}, \vec{b}) = \int d\lambda \rho(\lambda) A(\vec{a}, \lambda) B(\vec{b}, \lambda), \tag{A.3}$$

a quantity that should be equal to the expected value in the usual sense:

$$\langle \hat{\sigma_1} \cdot \vec{a} \hat{\sigma_2} \cdot \vec{b} \rangle = -\vec{a} \cdot \vec{b}. \tag{A.4}$$

However, Bell shows in general that eqn. A.3 $\neq$ eqn. A.4, and additionally if $\vec{c}$ is another unitary vector that:

$$1 + E(\vec{b}, \vec{c}) \gg |E(\vec{a}, \vec{b}) - E(\vec{a}, \vec{c})| \tag{A.5}$$

This last was the form derived by Bell of the called *Bell's inequalities* [10]. Currently, we recognise the existence of entangled but local states in structures as Werner and Werner-like for an specific value of p as presented in the Chap.3. A new formulation of the proof for the Bell's theorem is called the CHSH-nonlocality (Clauser-Horne-Shirmony-Holt nonlocality)

CHSH-Nonlocality:

Given $\rho \in D(\mathbb{C}^2 \otimes \mathbb{C}^2)$, the Clauser-Horne-Shimony-Holt (CHSH) inequality [11] considers two dichotomic observables per party (eigenvalues ± 1), namely

(A_1, A_2, B_1, B_2), and it takes the form:

$$|B_\rho(A_1, A_2, B_1, B_2)| := |E_{11} + E_{12} + E_{21} - E_{22}| \leq 2, \tag{A.6}$$

where $E_{ij} := \mathrm{Tr}\left[(A_i \otimes B_j)\,\rho\right]$, $i, j = 1, 2$. It is said that ρ violates the CHSH inequality if and only if $M(\rho) := \mu + \widetilde{\mu} > 1$, where $\mu, \widetilde{\mu}$ are the biggest two eigenvalues of the matrix $U_\rho := T_\rho^T T_\rho \in M_{3\times3}(\mathbb{R})$, with $T_\rho := [t_{nm}] \in M_{3\times3}(\mathbb{R})$, with elements $t_{nm} := \mathrm{Tr}[\rho(\sigma_n \otimes \sigma_m)]$, σ_k, $k = 1, 2, 3$, the Pauli matrices. This arises from the fact that $\max B_\rho := |\max_{A_1,A_2,B_1,B_2} B_\rho| = 2\sqrt{M(\rho)}$ [302]. Then, using the Tsirelson's bound [303], $\max B_\rho \leq 2\sqrt{2}$, it follows $0 \leq M(\rho) \leq 2$, showing nonlocality in the interval $1 < M(\rho) \leq 2$. Instead of $M(\rho)$, we could work with $B(\rho) := \sqrt{\max\{0, M(\rho) - 1\}}$ given that, for pure states, the former equals the concurrence: $C(|\psi\rangle) = B(|\psi\rangle)$ [304]. However, in order to have a direct comparison with $\mathcal{E}$, in Fig. 36(b), we compute nonlocality through the CHSH inequality, by plotting $\mathrm{CHSH}(\rho) := h([1 + \sqrt{1 - B(\rho)^2}]/2)$, where $h(x)$ is the binary entropy.

A.2 Non-locality Activation

k-copy nonlocality (superactivation):

Given $\rho \in D(\mathbb{C}^2 \otimes \mathbb{C}^2)$, if ρ is useful to teleportation then is k-copy nonlocal [305], i.e., ρ admits *superactivation* of nonlocality [176]. Usefulness to teleportation can be numerically tested by computing the Fidelity of Teleportation, which can be written as $\mathcal{F}(\rho) = \frac{2F(\rho)+1}{3}$, where F denotes the Fully Entangled Fraction [306], which for two qubits reads $F(\rho) = \max\{\eta_i, 0\}$, with η_i's the eigenvalues of the matrix $M = [M_{mn}]$, of elements $M_{mn} = \mathrm{Re}\left(\langle\psi_m|\,\rho\,|\psi_n\rangle\right)$, and $\{|\psi_n\rangle\}$ the so-called magic basis $|\psi_{ab}\rangle := i^{(a+b)}(|0, b\rangle + (-1)^a\,|1, 1 \oplus b\rangle)/\sqrt{2}$ [307]. ρ is useful to teleportation if and only if $\mathcal{F} > 2/3$ [306]. In our case, as shown in Fig. 36(b), the set of states that can be super-activated coincides with the whole set of entangled states (although this fact does not hold in general).

Activation of nonlocality through tensoring and local filtering:

Given $\rho \in D(\mathbb{C}^{d_1} \otimes \mathbb{C}^{d_2})$ for subsystems A and B with arbitrary dimensions d_1 and d_2 respectively and, defining P_{CHSH} as the set of states that do not violate the CHSH inequality, even after local filtering, we say that $\rho \in P_{CHSH}$ admits *activation* of nonlocality through tensoring and local filtering [177] if there exists a state $\tau_\rho \in P_{CHSH}$ such that $\rho \otimes \tau_\rho \notin P_{CHSH}$. The latter is equivalent to have

$\mathrm{Tr}\left(\tau_\rho\left(\rho^{\mathrm{T}}\otimes H_{\pi/4}\right)\right) < 0$, with $H_{\pi/4} := \mathbb{I}_2\otimes\mathbb{I}_2 - \frac{1}{\sqrt{2}}(\sigma_x\otimes\sigma_x + \sigma_z\otimes\sigma_z)$, with T denoting transposition [177]. A theorem [177] establishes the existence of such matrices τ_ρ in the space $D\big(\bigotimes_{i=1}^{2}(\mathbb{C}^{d_i}\otimes\mathbb{C}^2)\big)$ for any entangled ρ. Although the existence of such a matrix τ_ρ is already guaranteed, the theorem does not explicitly tell us how to calculate it. We have numerically tested this activation [177] by looking for a state τ_ρ with positive partial transpose with respect to the first subsystem, $\tau_\rho^{T_1}\geq 0$ (say $\mathbb{C}^{d_A}\otimes\mathbb{C}^2$) [308, 309], since this implies $\tau_\rho\in P_{CHSH}$ [310]. Thus, we solved the optimisation problem $\sigma(\rho) := \min_{\tau_\rho}\mathrm{Tr}\left(\tau_\rho\left(\rho^{\mathrm{T}}\otimes H_{\pi/4}\right)\right)$ under constrains $\tau_\rho\geq 0 \ \wedge \ \tau_\rho^{T_1}\geq 0$ [177]. Even though the considered activation of the nonlocality region covers the whole entangled states [177], the region for which we are indeed able to find the ancillary matrix required for the activation is represented by the cyan solid area (which covers the CHSH inequality violation region) in Fig. 36(b).

Other nonlocality metrics

I have shown here a family of states in which the entanglement and the nonlocality are not synonyms or conditionals. In the wide way of analysis and verification of nonlocal properties of states exists additional metric such as the *Local filtering or hidden nonlocality (HN)*, the *Superactivation tensoring factor* $k(d, f_d)$, and the *Fidelity of Teleportation(FoT)*, between others. A brief review of these techniques can be found in Ducuara *et al.* [175], and a more detailed description in [176, 305, 307] and [311].

Appendix B

BUILDING A LABORATORY IN....

At the very beginning of this doctoral research, the main problem was the local infrastructure limitation. Fortunately, some cooperations mainly between Universidad del Valle-Colombia and Universität Bayreuth-Germany allowed the development of the present research plan. Nevertheless, we never leave aside the idea of local experimental implementations. Searching financial founds we receive regional and national grants which enable the implementation of laboratories for the study of computational systems in photons, and the analysis of photo-physical features of molecules with the equipment that I described as follows:

B.1 Quantum Information

In the beginning, this infrastructure would allow us, for instance, the implementation of universal quantum gates, the generation and detection of Bell states, and the experimental demonstration of nonlocality from the violation of Bell's inequalities toward the activation of this feature through filtering techniques. The main parts of the system currently used are described briefly in the following:

The laser source

As excitation source we implemented a Ti: Sa pulse laser from Avesta company, model TiF-100 (see Fig. Fig.B1A), with tuneable pulse range ($40 - 90$ fs), and wavelength ($715 - 800$ nm). This source produced the SHG (second Harmonic generation) with a BBO crystal of 0.2 mm width turning the wavelength to a range of $355 - 400$ nm. This last wavelength range is involved in the preparation of entangled photons through the Spontaneous Parametric Downconversion (SPDC) process.

The optical system

After the laser, we control the pulse width with a pulse compressor system using an SF10 Prism Pair (Newport inc.) to compensate the pulse dispersion produced by the additional optics, see Fig.B1B. The laser beam travels toward an SHG system which generates the pumping light for the SPDC system (employing a $\beta - BBO$ of 1 mm width). However, the SHG has an efficiency of $\sim 30\%$, and through a

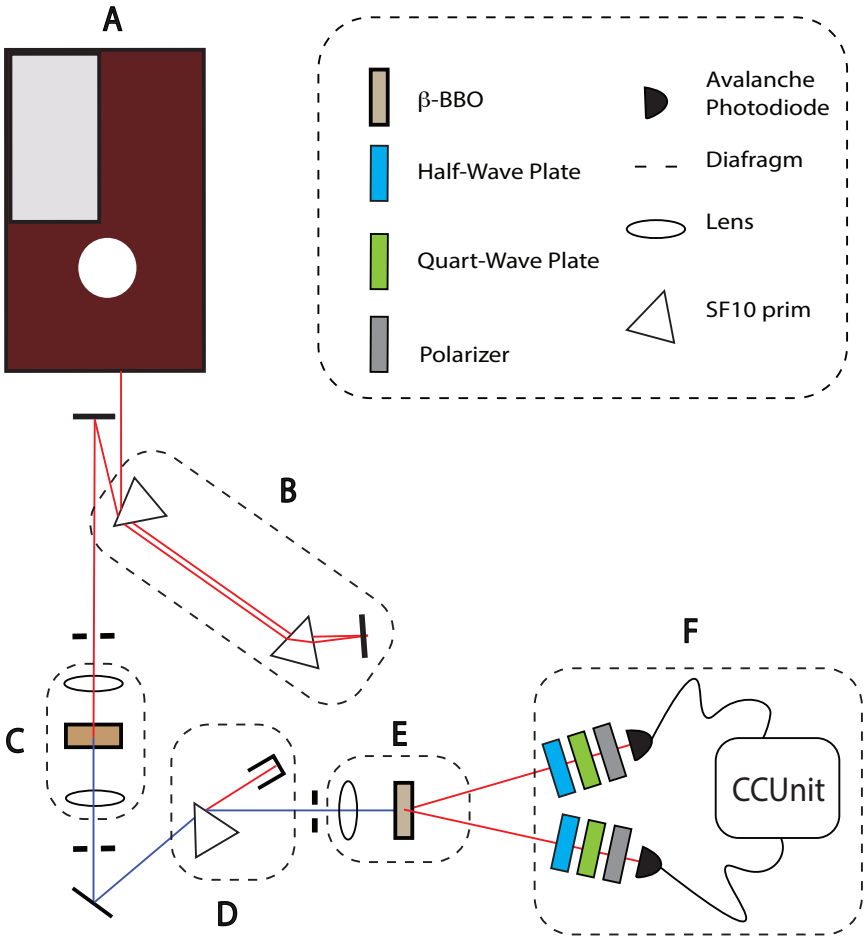

Figure B1: Quantum Information and Optics Laboratory (Universidad del Valle). A: The Ti: Sa pulsed laser source ($40-80$fs) produces an emission range of $715-800$ nm. B: The pulse compressor system compensates the group velocity dispersion (GVD) induced by optics. C: The SHG system changes the emission ranges to $355-400$ nm. D: Te harmonics separator deviates the non-converted light from the SHG. E: The SPDC source again changes the emission range to $715-800$ nm, but with entangled polarisation photons. F: The quantum tomography incorporates half-wave and quart-wave plates, and polariser coupled to a pair of SPCM connected to a CCU to determine the probable quantum state of the system.

prism, the harmonics are separated, see section Fig. B1D. Finally, this new laser source produces temporally correlated photons entangled in the polarisation basis and through the quantum tomography protocol are analyzed.

The Detection system

The analysis of the prepared states is achieved using the quantum tomography protocol proposed by D. F. James *et al.* [100]. This procedure employs sixteen (16) and four (4) independent measurements to describe quantum states of two- and one-qubit system. The analyzed light crosses over polarisation analysis plates (Half-wave and quart-wave plates, and a polarizer) to project the photons on the orthogonal basis to determine the contribution of each polarization basis on the total state. The electronic counting in realizes by a couple of Single Photon Counting Module (SPCM-AQRH series Excelitas technologies) connected to a Coincidence Counting Unit (CCU), see Fig. B1 F, which stores the measurements in the computer for the final post-processing procedure.

B.2 Molecular Spectroscopy

As a useful tool to characterize and understand the intramolecular behavior of the matter and its interaction with light a spectroscopy laboratory was posed, as a consequent of this research plan, and currently is in development. Employing the knowledge acquired during my research stay in Germany I defined a versatile system with a wide range of excitation wavelengths and control for the laser delay. This experimental setup will be able to perform single molecule spectroscopy, fluorescence correlation spectroscopy, and pump-probe spectroscopy.

The laser source

A Ti: Sa pulse laser from Avesta company, model TiF-20 (see Fig. Fig.B2) with tuneable pulse range ($12 - 40$ fs), and wavelength ($715 - 800$ nm) is the principal excitation source. This pulse laser is split to produce SHG (pulse width $\sim fs$) and Supercontinuum light (pulse width $\sim ps$)with an optical fiber of photonic crystal (femtowhite 800 NKT Photonics). This arrangement constitutes a versatile excitation system useful for a wide range of molecules which keeps temporal information in the fs and ps order, unfolding potentialities to perform experimental procedures as Time-correlated Single Photon Counting (TCSPC) to measure molecular emissions lifetime.

The optical system and measurement procedure

The central laser source is divided twice through 50:50 beam splitter cubes. The first branch cross a neutral filter wheel, which controls the intensity without changing the wavelength, and a mechanical shutter controls the laser input toward the collimation

and preparation optics. The double lens setup (telescope optical arrangement) performed the collimation, and the linear polarizers and waveplates controlled the polarisation content. A mechanical delay is added to identify changes in the emission spectrum correlated with the delay on the excitation, see Fig.B2 D. The second beam splitter divided the second branch in two ways to produce, in one way SHG and supercontinuum light in the other arm. Folding mirrors marked with arrows realized the selection of the wavelength, as shown in the Fig. B2. Before the light arrives at the sample, is collimated again and optically filtered within the excitation band, Fig. B2 G and H. Further, the excitation light is selected with a dichroic mirror (Band Pass Filter) and addressed to an immersion objective (NA=1.25, 60X), shown in detail in the Fig. B2 I. The same dichroic mirror directs the emission response from the sample toward a cube beam splitter 70:30 which sends the 70% of the emission to a low dispersion spectrometer. The remaining 30% arrives at an Avalanche Photodiode (APD) connected to a TCSPC system which synchronizes the repetition rate of the central laser to account the time duration of intramolecular events. These techniques allow the molecular characterization of the photophysical process as the fluorescence lifetime, the charge transfer rate, and the single molecule spectrum, among others. Additionally, the implementations here described open new local research lines and set the appropriate conditions to contribute in a fundamental way to the global advance of these branch of knowledge.

Finally, as part of this implementation, we proposed an electronic device which could serve both laboratories for counting signals from the APDs, as describe the next annex.

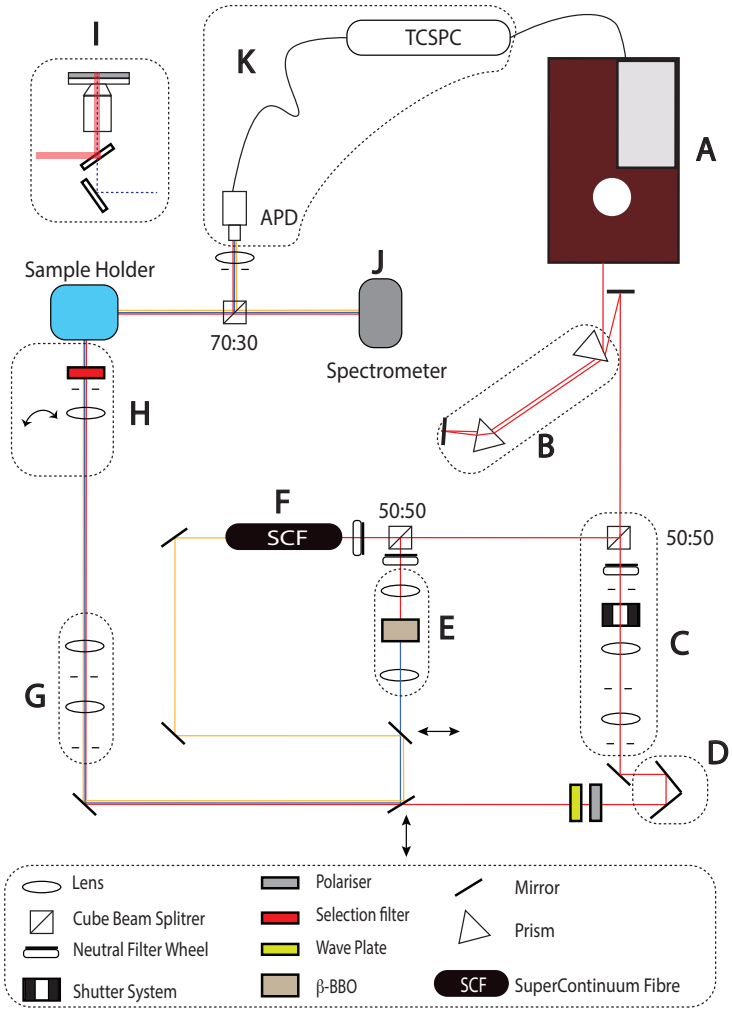

Figure B2: Ultrafast Spectroscopy Laboratory (Universidad del Valle). A: The Ti: Sa pulsed laser source ($12 - 40$fs) produces an emission range of $715 - 800$ nm. B: The pulse compressor system compensates the group velocity dispersion (GVD) induced by optics. C: A neutral filter wheel and a mechanical shutter perform the control of the input Intensity, and the two-lenses setup collimates the crossing radiation. D: A mechanical delay allows following the behavior of the absorbed energy by the sample with fs in resolution. E: SHG system changes the main emission range from the central NIR wavelength to $355 - 400$ nm. F: the Supercontinuum fiber system produces a continuous band of coherent emission in the visible spectrum. G: the Second collimation system ensures the correction of the divergences induced by the optics. H: the excitation filter selects the illumination wavelength to define the energy band in which the molecular system should respond. In this dashed box is include the widefield lens which moves the focal plane of the system in such a way to enable the homogeneous illumination over the sample. I: The sample holder in cross-section view, a dichroic mirror collects the illumination in the same range of the excitation light, a broad spectrum mirror address the response from the sample toward the spectrometer. J: Low dispersion spectrometer to record the emission spectra from the samples as a part of the detection system. K: An APD counts the signal from the sample and sends it toward the TCSPC protocol to create a correlated histogram, with the pulse repetition rate of the central laser, which finally gives us the lifetime of the radiant emissions from the sample.

Appendix C

PHOTON COINCIDENCE DETECTION

C.1 Introduction

The state-of-the-art technologies of pulse counter electronics offer a significant range of commercial devices, but such systems are usually expensive due to the complicated logic used for this task. The use of counting electronics in conjunction with photon counters can be used, for example, to perform experimental tests in Quantum Optics and Quantum Information Science. In the next chapter, it is present the development and implementation of a low-cost module for multi-photon coincidence statistics with detection windows of a few nanoseconds. The detection of Transistor-Transistor Logic (TTL) signals retrieved from a signal generator characterize the counting device implemented in an optical setup. A Field Programmable Gate Array (FPGA) analyzes and stores the detected output signals (TTL pulses) in a computer. The first experimental proof-of-principle incorporated this module in the tests of quantum information and molecular spectroscopy techniques at CIBioFi.

In less than three decades, a new technological revolution has been boosted by harnessing the fundamental principles of quantum mechanics, and the superposition and entanglement of quantum states have been at the core of such a development. This, however, implies a big challenge for testing and implementing remarkable protocols such as quantum computation, cryptography, and teleportation in quantum information science [47, 312–314]. In the case of optical technologies, the detection of individual pulses and photon-coincidences is fundamental [315, 316], and setups for Light Detection and Ranging (LIDAR) [317], Fluorescence Correlation Spectroscopy (FCS) [318, 319], molecular life-time emissions and quantum entanglement and correlations quantification [152, 157, 319, 320], between others, rely on this feature in a crucial way. Thus, photon statistics [321–323] through the coincidence counting (detection of photons-simultaneously or within a small time window) provide a key ingredient in Science and Engineering.

Most of the time-dependent statistics of photons in different experimental schemes has been made possible thanks to a Time to Amplitude Converter (TAC) protocol, which allows for the measurement of the time interval between incident pulses, from “start” to “stop”, and generates an output pulse that is proportional to this time

interval. This action is commonly implemented in experimental setups used for the characterisation of molecular systems such as "Time Correlated Single Photon Counting" (TCSPC) [324, 325]. Such a counting technique produces a histogram that represents the characteristic time scale of the analysed molecular system. The TAC process involves a time whereby the counting electronics is reseted to restart the measurement, the so-called *dead-time* of the protocol. This said, such a procedure for coincidence counting of multiple photons is nowadays expensive and easily saturable due to current dead-time intervals around 125 ns and saturated count rate of 8 MHz in reverse mode operation [326], and even for 16 MHz [327].

Time-to-Digital Converter (TDC) is another procedure that employs the "start-stop" principle. This can be entirely implemented on a digital basis, thus avoiding the use of ADC (Analog-to-Digital) protocols that limit TDC applications to deep sub-micron technologies [328]. This is due firstly, to a frequent recalibration against a primary quartz oscillator time base to determine the required conversion slope, and secondly to an early usage of two analog processes: an analog ramp time-to-amplitude converter (which also involves a recycling time) in conjunction with a pulse-height analyser [329]. Current TDC based on 65 nm CMOS technology could achieve a maximum frequency in the 5-10 GHz range and reach a maximum around 100-200 ps for the measurement accuracy [328]. Further, an even a shorter time accuracy can be achieved if one clock period is asynchronously subdivided into smaller time intervals [330–334]. Combining this technique with photon detectors such as the Avalanche Photodiode (APD), the sampling would be limited by the maximum rate allowed by the detector. This method can be employed in diverse experiments, ranging from, e.g., materials surface reconstruction in the measure of the Time-of-Flight (ToF) of photons from a transmitter to a target and back to the detector [335], fluorescence life-time imaging [336], to TCSPC [331, 332]. In this direction, in our work we implement a useful tool for research by means of a purely digital procedure which offers an appropriate sampling rate useful for several purposes (e.g., quantum information technology and molecular spectroscopy) that is cost-efficient compared to different devices available in the market. This implementation adds some improvements compared to its predecessor model [316, 337, 338], which include an increment in the number of input signals capable of being analysed in one device. In addition, such a module uses a faster electronics and wireless connections to reach the balance of cost efficiency.

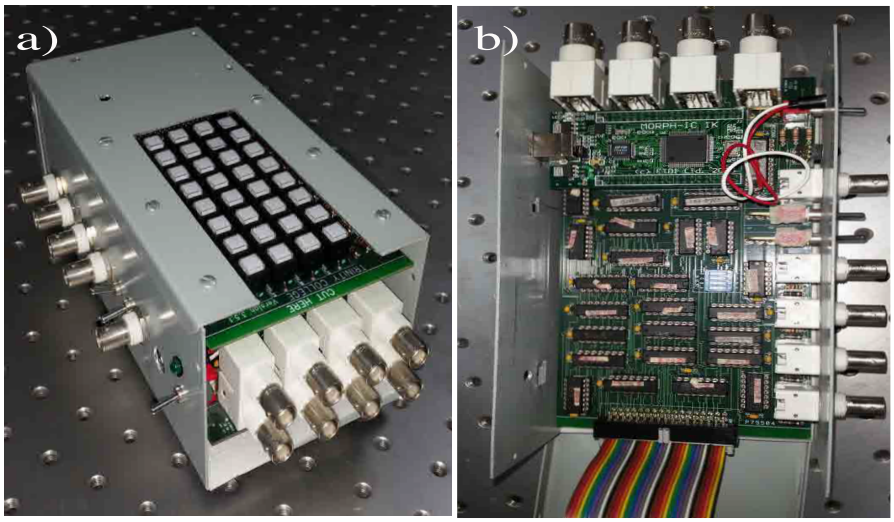

Figure C1: Cards that exhibit the electronics of the first implemented coincidence counting module in our laboratory based on Branning's work [316]: a) the electronics for the detection of the signals, and the final presentation of the coincidence counting module Branning's version. The $8 \times 4 = 32$ buttons on top show the 8 channels by 4 inputs that can be handled by the device. This ensures up to four-coincidences analysis in each available channel, b) the structural location of the electronics logic that allow us the manipulation of the entry signals. In this work, this module was expanded up to eight inputs and eight-fold coincidences.

C.2 Experimental Development

Counting module assembly

In 2009, Branning *e*t al. [316] posed to change the TAC protocol by implementing a set of logic gates. This assembly used a TTL pulse sent by a commercial photo counter to modify the pulse width, then defined the coincidence, and finally used a Peripheral Interface Controller (PIC) to count and store the data in a computer. After this, the PIC was replaced by a Field Programmable Gate Array (FPGA) that developed the same functionality as its predecessor but became better suited and adaptable [337]. This development is appealing due to the cost-efficiency of these devices, and besides, this also allows the scalability to $4N$ inputs but using $N - 1$ different Coincidences Counting Modules (CCM) [338].

We initially used a third generation proof board of Branning's CCM [339] and assembled a device as shown in figure C1. This CCM was built on electronic boards of four layers each one. In one of them, we located the different electronic devices, NANDs, ORs, and Multiplexors. In the second card, the manual selection of input signals and the hosting of switches was configured, as can be seen in figure C1(a),

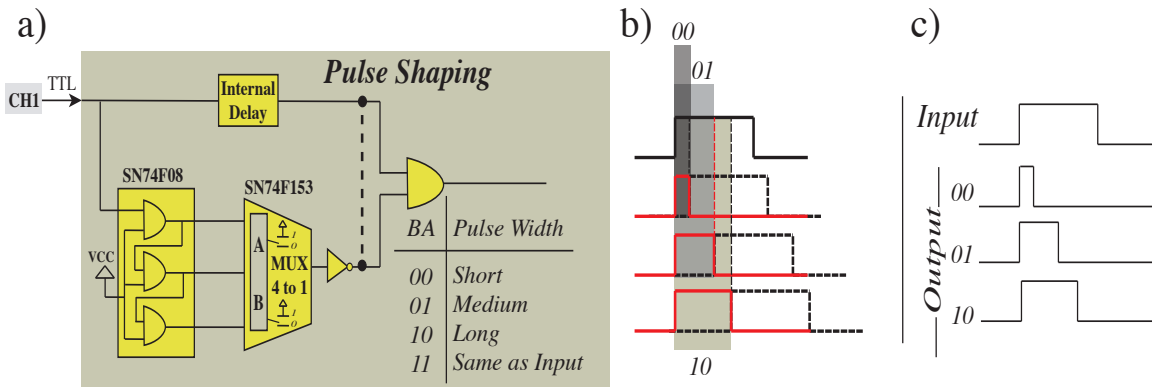

Figure C2: Schematics of the pulse shaping process followed by the input in a given channel. a) Graphical description of the stages followed by the input signal from CH1 to the output of the shaping process. Vertical dashed line accounts for the key signal shape and final output. b) Sketch of the MUX inverted output signal in the lower path, delayed as a function of the A, B status selectors, as compared to the pulse in the upper path as indicated by the dashed line of a). The difference between the delay of the pulses in b) defines c) the final shape of the pulse after passing through the total shaping process.

and C1(b). Those devices are protected by a metallic box to preserve their electronic components, and to allow for an easier manipulation of the counting module. The main limitation of this module, however, is the reduced number of inputs (4) for the Single Photon Counting Modules (SPCM), given that, for example, state-of-the-art quantum optics experiments can entangle up to ten photons, and use around 20 APDs for their detection [323]. In this sense, recent efforts have expanded other counting strategies with different techniques that are able to reach up to 32 [318], and even 48 inputs [340].

In this work, we report the implementation of a photon-counter coincidence module with a short response time (a few ns), and use as a counting device an FPGA DE0-nano model [341]. In this module, we expand Branning *e*t al. initial proposal, by increasing the number of inputs up to 8 as well as the coincidences (8-fold). In our implementation, we used integrated circuits of fast series (SN74FXXX) of different logical arrays, and a wireless module to communicate the data to a software analyser. The stages followed in the coincidence counting process are as follows: i) pulse shaping, ii) selection of the input signal, iii) counting, and iv) storing the acquired data. We next describe these steps.

Shaping the input pulses

A description of the pulse shaping process is schematically given in figure C2(a). First, the signal splits into two equal and temporal synchronised signals, next both of them are delayed but subjected to the following two-path rule. In the upper path, the delay is controlled through a double inverter logic circuit which is equivalent in time to the application of two digital gates. In the lower path, the delay is defined by the selectors A and B, where "0" and "1" denote "off" and "on" states, respectively. This delay finally defines the width of the output pulse from the MUX which is inverted as is shown in figure C2(b). The positions of the selectors AB define the number of logical AND gates that the signal should pass through. This variable (number of gates crossed by the signal) is directly related to the width's output signal, e.g., if the selectors are set in the "00" position, the signal will pass over one logical gate (with a minimal operation speed of ~ 2.2 ns, and a maximal of ~ 6.6 ns [342]) plus the Multiplexing operation (range $3.7 - 12$ ns [343]), and a final AND gate giving a resulting output pulse between 6.0 and 19.0 ns as shown in section C.3. If the operational conditions (voltage and temperature) are constant despite the operational range of the logical gates, these devices typically work with the average value of their range plus the accumulative uncertainties due to buffer operation. Thus, for the case of the "00" selector we can define a typical value of $\sim 13.0 \pm 2.5$ ns. This selector "00" accomplishes the minimum delay (shown in figure C2(b)), where the red curve represents the final output width of the signal and the shadowed area (with the respective label) remarks the delay between the incoming pulses. Finally, such a minimum delay between the two paths translate into the minimum signal width as sketched in the figure C2(c). In the same sense, if the selectors are in the "01" position, the addition of one AND gate influences the final width in an average value of $\sim 16.5 \pm 2.6$ ns. Otherwise, if the "10" position is selected (maximum delay), two additional AND gates are added to the process, and the width of the output signal increases to a range between 9.9 and 32.2 ns, with a typical operation value of $\sim 21.0 \pm 2.8$ ns.

Selecting the input signal

All the input pulses are shaped as explained before but only the modules' user defines the number of inputs that are to be considered in the coincidence process. The selection of the signals is implemented via a switching system that allows the following: to select a channel (or channels) for detection and counting the pulses, and then, counting the coincidences between signals. As sketched in figure C3, each

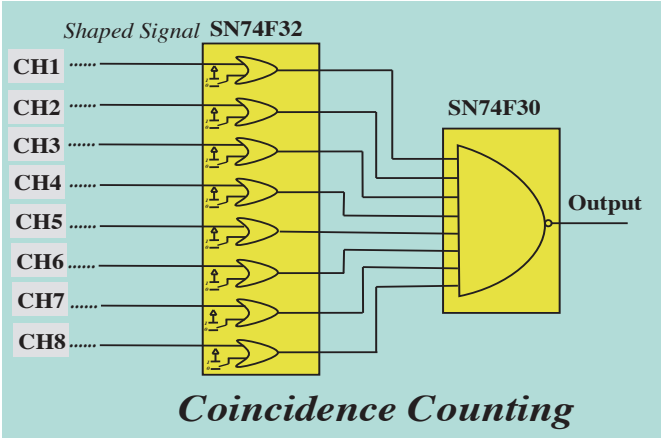

Figure C3: Scheme of signals selector: OR-gates (SN74F32) are applied on each shaped pulse, and over the logical state of switches manually defined. Only the selected signals get involved in the coincidence process performed by an AND-gate with multi-inputs (SN74F30).

input channel (from 1 to 8) passes through the shaped process and is compared with the logic state of a switch ("0" or "1") connected to the OR-gate-SN74F32. Next, the logic resulting is transmitted to the coincidence channel performed by the AND-gate-SN74F30 to be finally counted. The coincidence protocol is just the logical comparison of the selected pulses in a defined time interval which will depend on the operation speed of the logical gates involved. In this setup, the coincidence interval ranges between 3 and 13 ns, depending on the operational speed of the SN74F32 and the SN74F30 gates [344, 345] with a typical value of $\sim 8.0 \pm 1.4$ ns. To sum up, the pulse shaping of the input signals only guaranties the overlap between signals from different channels and the coincidence window defines how close the upper flank of the involved signals are. This coincidence is set to "high" or "true" if only both upper flanks are within the coincidence interval defined by the operation time of the consecutive OR and AND gates, i.e., the definition of a coincidence is only limited by the electronics logical response time at the gate, and by the number of followed buffers.

Counting, saving and data acquisition

For this purpose, the final pulses are counted and stored for later acquisition in readable files in a computer. This is developed by means of an FPGA of programmable logic and connections under *VHSIC*[1] *Hardware Description Language (VHDL)*. A MORPH-1C-II system [346] has been recently introduced, in four channels protocols

[1]Acronym for Very High Speed Integrated Circuits

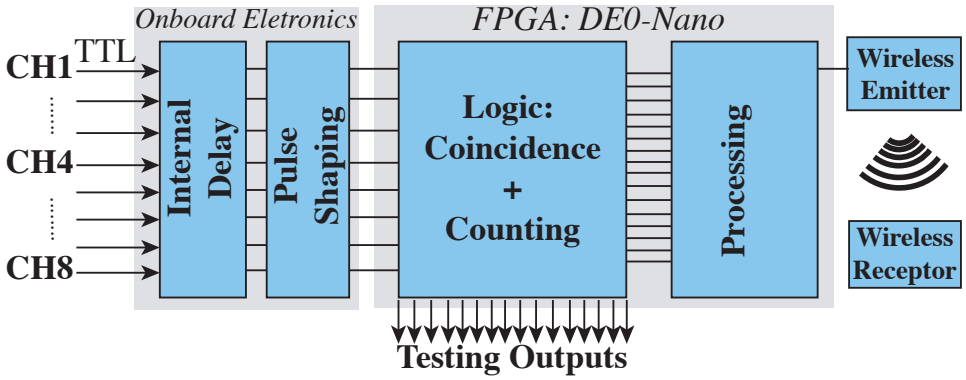

Figure C4: Scheme of the input processing and data transmission protocols. Each input signal is delayed, shaped, and counted. If the selection process defines more than one input, then the coincidence will be counted and saved. These data were collected during a defined period, the so-called *i*ntegration time, $2\,\mu\text{s} \leq \tau_{count} \leq 1$ s, and were finally sent through an intercommunication wireless port to a receptor module by packages that were stored in a computer.

[339], due to its Multi Protocol Synchronous Serial Engine that allows programming and re-programming by means of a USB port in a fraction of a second, i.e., of at least 0.2 s [347]. This implementation, however, has a practical drawback since it requires programming every time that a lack of power supply arises and, operatively speaking, a plug-&-play usage with this kind of FPGA is not possible. Another hurdle arises from this model's processing capability due to the fact that an increment in the number of possible input signals implies an increment of the number of selecting switches, as shown in figure C1(a) and figure C3. As an alternative, this switching system can be included in a software interface using the logical elements of the FPGA instead of hardware buttons. In the latter, an FPGA with a larger number of logical elements is to be required.

In our implementation, we resort to an FPGA with a ROM memory for the counting process as the DE0 nano [341] from the Cyclone™IV family [347]; this device has two headers of 40 pins each one, where 72 pins are input/output, 4 power pins, and 4 GND pins; connection to a USB port for its output signals and 23 pins for connection to a JTAG interface (standard protocol to develop debugging tools [348]). Another key feature of this model is the maximum acceptable frequency of 153 MHz for the input signals, and a larger number of logical elements: 22.320 compared to 4.608 of the MORPH-1C-II. These features allow the detection of different physical systems that range from the single photon counting and coincidences through to the radioisotopes in positron emission tomography [349].

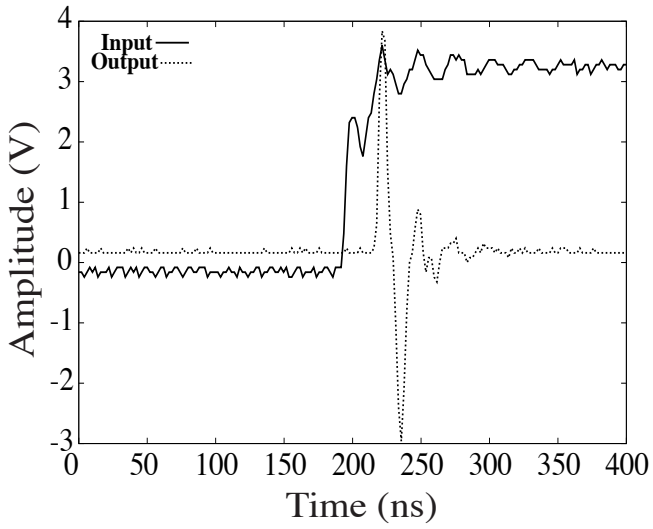

Figure C5: Comparison between an input signal of 10 KHz and the output response of the configuration "00" during the pulse shaping stage.

For programming this FPGA, we used the compilation environment Quartus™. The particular code used here can create eight registers of independent counts of 16 bits available each one to define the channel of the register. This number of channels stems from the module inside that compares the selected input signals between them to count coincidences in the FPGA. To obtain the saved data, we used XBee modules that allow the wireless communication between the FPGA and a designated computer [350]. This process relies on the time needed to send the data by the transmission module (τ_{send}). In order to overcome lacks in the processing, it is useful to define integration times to count in the FPGA in the same order ($\tau_{count} \sim \tau_{send}$). The required variables in the process of wirelessly data sending are the *sending rate* (number of data send per second) and the *bit length* ("size" of the data), which depend on the number of channels to count. These variables determine the file transmission and reception, and are set in the code that is implemented within the FPGA and the XBee (X−CTU) module. Finally, the file arrives to a reception module that is connected to a computer to visualise and analyse the counts, as schematically shown in figure C4.

Device estimated cost

The total cost involved in the construction of the coincidence counting device can be estimated as follows: i) FPGA DE0-nano ~ 190 USD, ii) PCBs (assembling cards) ~ 50 USD, iii) the complete set of fast series circuits (SN74FXXX) ~ 30 USD,

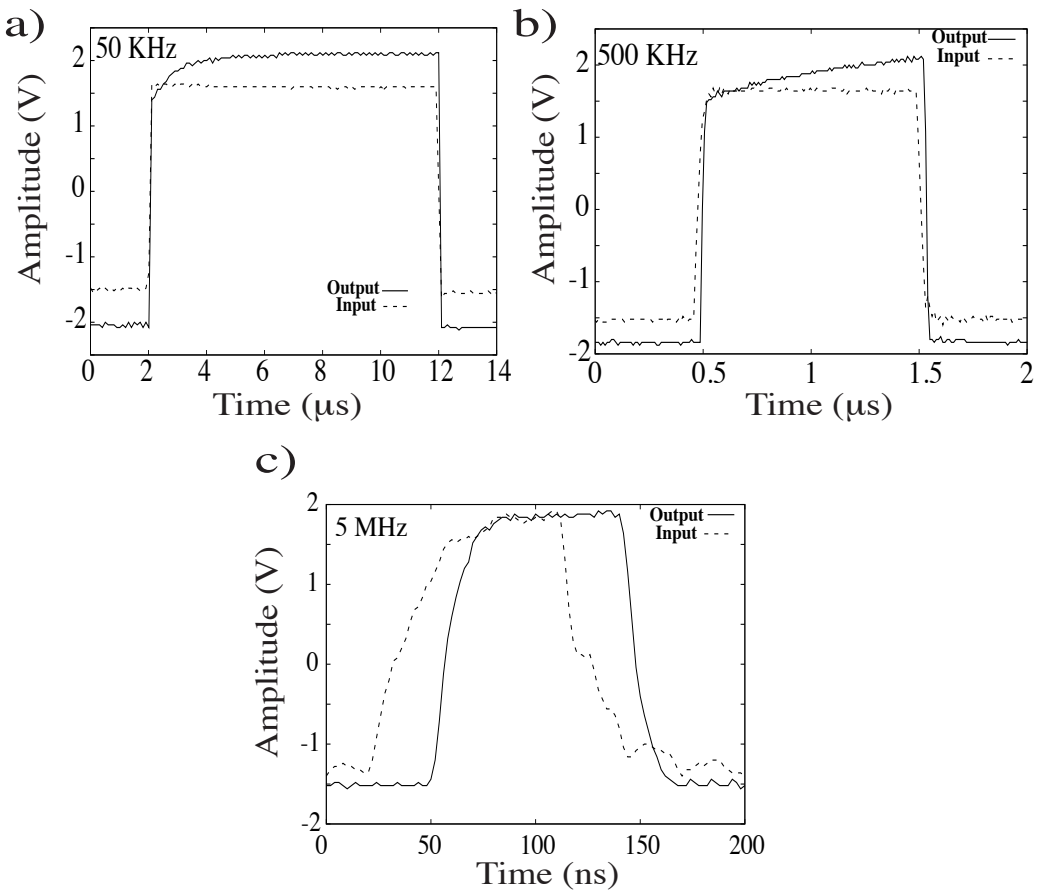

Figure C6: Input signals of different frequencies in the "11" configuration: a) the 50 KHz signal presents a rounded corner due to the amplification response of the pulse shaping stage: the time-scale of the pulse width is enough to see the maximum amplification of about $\sim 33\%$ between the output and the input signals, b) in the 500 KHz pulse, the amplification process is also reached, but this exhibits a cut-off due to the increase of the repetition frequency, and c) an input pulse of 5 MHz is used in the module: the amplification is not evident and an apparent time shift exhibited by the output signal at FWHM around $\sim 16\%$ of its width takes place. This is attributed to the usage of a trigger signal that did not allow for a proper compensation of the output signal.

iv) additional electronics and housing (switches, cables, LEDs, BNC connectors, metallic box) ~ 200 USD. These give an approximate total of about 470 USD. This is to be contrasted with typical commercial devices available in the market (with similar features) that can be well above 2500 USD (e.g., Canberra Model 2040 and National Instruments modules).

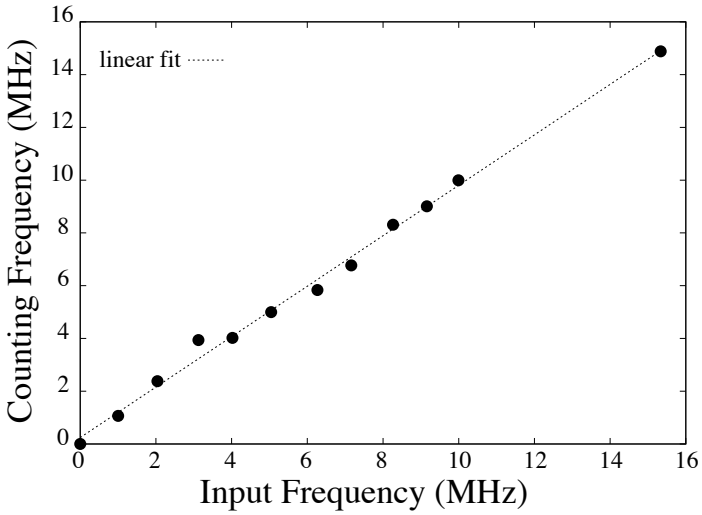

Figure C7: Single channel counting rate for the "11" configuration. The functional dependence is linear, with calculated slope $m = 0.9561 \pm 0.0213$. An almost identical result was obtained for the "00" configuration (not shown).

C.3 Device Response and Discussion

The coincidence counting module was carefully checked in each one of the previously mentioned stages. In figure 5 we show the effect of the pulse shaping in the configuration "00" over a square input signal in the counting module. Here, we observe that the output exhibits a damped oscillator-like behaviour, possibly due to the response time at the logic circuits. This input signal has a frequency of 10 KHz, which means an average width of ~ 0.1 ms, and the shaping process produces an output of ~ 15 ns; this represents a reduction of at least five orders of magnitude of the former width. Although the plot shows a delay of a few nanoseconds between the input and the output signals, this difference is comparably small: $\sim 10^{-4}$ % of the input pulse width. We also verified the output signal in the configuration "11" with signals generated by a square pulse generator set at three different frequencies (50 KHz, 500 KHz, and 5 MHz).

In this test we find a slight increment in the amplitude of the input signals as can be seen in figure C6. This could be achieved due to the amplification performed by the shaping electronics at this stage and the impedance of the cables used for this experiment. However, this amplification process takes a time comparable to the time scale of these inputs to reach a maximum value. This behaviour is responsible for the apparently "round corner" on the top of the output signal in figure C6(a). When

the frequency is changed, say by one order of magnitude, the shaping is constant, but in a closer look, the former "round corner" is clearly an slope related to the time needed to achieve the stability of the logical process, as shown in figure C6(b). In addition, frequencies in the range of MHz exhibit an alteration of the output pulse and a "non-evident" voltage amplification process. This means that the amplification procedure is slower than the period of the input signal, and the maximum amplitude is not reached before the temporal width vanishes. For the case of a 5 MHz input signal, the output signal is delayed as observed in figure C6(c). We estimate the uncertainty due to this time shift presented by the output signal at FWHM around $\sim 16\%$ of its width. This is due to the time taken by the logical gates to operate and to the usage of an oscilloscope trigger signal that did not allow us to produce a proper compensation of the output signal. This amplification is not really an issue because for the logic gating the importance holds on the flanks of the signals that determine the counting process. On the other hand, this process helps to maintain the fidelity of the signal inside the counting module due to the fact that it preserves the temporal features of the input signal and increases the voltage that enhance the robustness of the signal against the possible dispersions inside the module.

This visualisation issue, however, does not compromise the functioning of the counting device, since the amplifying response during the shaping stage does not affect the efficiency of the counting process due to the fact that the counting frequency is proportional to the input frequency, as shown in figure C7. We found that, in the configuration "11", the frequency of the input signal is proportional to the counting frequency by a constant value 0.9561 ± 0.0213. The "00" configuration exhibits a likewise proportionality with a very similar constant.

C.4 Concluding Remarks

We have built a cost-efficient (compared to commercial prices) counting module device of eight inputs, as well as eight-fold coincidence channels that exhibit key features that can be used in different areas of science, engineering and the medical sciences, and in particular, in quantum and non-linear optics. These features allow us to perform a more in depth analysis about incident photons in quantum optics and quantum information experiments. The reported counting module has a response time of a few nanoseconds and works for incident signals with frequencies up to 150 MHz. This module is currently being implemented in our laboratory for the detection of Werner-like states which have recently been proposed as a novel resource for quantum game strategy in a protocol that requires neither quantum entanglement

nor nonlocality as a resource [47]. We work on the FPGA programming to improve the module for data transfer in quantum tomography of one and two polarisation photonic qubits experiments.

The device here implemented for photon coincidence detection shall also be used in quantum interferometry, and photo-luminiscence detection in molecular spectroscopy experiments.

Appendix D

COMPUTATIONAL CODES

I developed the computational used codes in Python 3.6.5 and Wolfram Mathematica 11.3. We analyzed in Python the images from the spectrometers and the TCSPC data. The tomography protocol, the calculation of information correlations, and the resulting Jones's matrices in optical setups, in Mathematica, were performed. If the reader needs the codes for educational use, please contact me by e-mail to carlos.melo@correounivalle.edu.co or Carlos.melo@uni-bayreuth.de, and I will send it back.

BIBLIOGRAPHY

[1] Dirk Bouwmeester and Artur Ekert. *The Physics of Quantum Information*. Ed. by Anton Zeilinger. first. Vol. 01. Berlin Heidelberg: Springer Verlag, 2000.

[2] Michael A. Nielsen and Isaac L. Chuang. *Quantum Computation and Quantum Information: 10th Anniversary Edition*. Cambridge University Press, 2010.

[3] A. Einstein, E. Podolsky, and N. Rosen. "Can Quantum Mechanical Description of Physical Reality Be considere Complete?" In: *Phys. Rev.* 47 (1935), pp. 777–780.

[4] Daniel Salart, Augustin Baas, Cyrill Braciard, Nicolas Gisin, and Hugo Zbinden. "Testing the speed of 'spooky action at a distance'". In: *Nature* 454 (Aug. 2008), pp. 861–864.

[5] Valerio Scarani, Wolfgang Tittel, Hugo Zbinden, and Nicolas Gisin. "The speed of quantum information and the preferred frame: analysis of experimental data". In: *Phys. Lett. A* 276 (Oct. 2000), pp. 1–7.

[6] Amir D. Aczel. *Entanglement: The Greatest Mystery in Physics*. Ed. by Terry Bain. First. Basic Books. 39 West 14th Street, room 503: Four Walls Eight Windows, Sept. 2002.

[7] R. P. Feynman. "There's plenty of room at the bottom". In: *J. Micro. Sys.* 1 (1992), pp. 60–66.

[8] Richard P. Feynman. "Quantum Mechanical Computers". In: *Opt. News* 11 (Feb. 1985), pp. 11–20.

[9] David Deutsch. "Quantum theory, the Church-Turing principle and the universal quantum computer". In: *Proc. Roy. Soc. Lon.* 400 (July 1985), pp. 97–117.

[10] J. Bell. "On the Einstein Podolsky Rosen paradox," in: *S. Physics* 1 (1964), pp. 195–200.

[11] J. F. Clauser, M. A. Horne, A. Shimony, and R. Holt. "Proposed experiment to test local hidden-variable theories". In: *Phys. Rev. Lett.* 23 (1969), pp. 880–884.

[12] Charles H. Bennett, Gilles Brassard, Claude Crépeau, Richard Jozsa, Asher Peres, and William K. Wootters. "Teleporting an unknown quantum state via dual classical and Einstein-Podolsky-Rosen channels". In: *Phys. Rev. Lett.* 70 (Mar. 1993), pp. 1895–1899.

[13] Artur K. Ekert. "Quantum cryptography based on Bell's theorem". In: *Phys. Rev. Lett.* 67 (Aug. 1991), pp. 661–663.

[14] Charles H. Bennett, Gilles Brassard, and N. David Mermin. “Quantum cryptography without Bell’s theorem”. In: *Phys. Rev. Lett.* 68 (Feb. 1992), pp. 557–559.

[15] Ian A. Walmsley and Michael G. Raymer. “Towards quantum-information processing with photons”. In: *Science* 307 (2005), p. 1733.

[16] Timothy C. Ralph and Robert W. Boyd. “Better Computing with Photons”. In: *Science* 318 (2007), p. 1251.

[17] E. Knill. “Quantum computing with realistically noisy devices”. In: *Nature* 434 (Mar. 2005), pp. 39–44.

[18] L. Henderson and V. Vedral. “Classical, quantum and total correlations”. In: *J. Phys. A* 34 (2001), pp. 6899–6905.

[19] H. Ollivier and W. H. Zurek. “Quantum discord: A measure of the quantumness of correlations”. In: *Phys. Rev. Lett.* 88 (2001), p. 017901.

[20] W. K. Wootters. “Entanglement of formation of an arbitrary state of two qubits.” In: *Phys. Rev. Lett.* 80 (1998), pp. 2245–2248.

[21] R. Horodecki, P. Horodecki, M. Horodecki, and K. Horodecki. In: *Rev. Mod. Phys.* 81.865 (2009).

[22] B. Hensen et al. “Loophole-free Bell inequality violation using electron spins separated by 1.3 kilometres”. In: *Nature* 526 (Oct. 2015), pp. 682–686.

[23] the BIG Bell test Collaboration. “Challenging local realism with human choices”. In: *Nature* 557.7704 (2018), pp. 212–216.

[24] T. D. Ladd, F. Jelezko, R. Laflamme, Y. Nakamura, C. Monroe, and J. L. O’Brien. “Quantum Computers”. In: *Nature* 464 (Mar. 2010), pp. 45–53.

[25] S. Haroche and J. Wineland. *Nobel Prize Lecture*. 2012.

[26] W. H. Zurek. In: *Rev. Mod. Phys.* 75 (2003), p. 715.

[27] J. Preskill. *Lecture Notes on Quantum Computation*. California Institute of Technology. 2009.

[28] S. J. Freedman and J. S. Clauser. “Experimental Test of Local Hidden-Variable Theories”. In: *Phys. Rev. Lett.* 28 (1972), pp. 938–941.

[29] A. Aspect, P. Grangier, and G. Roger. “Experimental Tests of Realistic Local Theories via Bell’s Theorem”. In: *Phys. Rev. Lett.* 47 (1981), pp. 460–463.

[30] A. Aspect, J. Dalibard, and G. Roger. “Experimental Test of Bell’s Inequalities Using Time- Varying Analyzers,” in: *Phys. Rev. Lett.* 49 (1982), pp. 91–94.

[31] A. Zeilinger. “Experiment and the foundations of quantum physics”. In: *Rev. Mod. Phys.* 71.2 (1999), p. 288.

[32] M. A. Horne and A. Zeilinger. *in Microphysical Reality and Quantum Formalism*. Ed. by A. van der Merwe, F. Seller, and G. Tarozzi. Kluwer, Dordrecht, 1988.

[33] J. D. Franson. "Bell inequality for position and time". In: *Phys. Rev. Lett.* 62 (1989), pp. 2205–2208.

[34] D. C. Burnham and D. L. Weinberg. "Observation of Simultaneity in Parametric Production of Optical Photon Pairs". In: *Phys. Rev. Lett.* 25 (1970), pp. 84–87.

[35] Sheng-Kai Liao et al. "Satellite-to-ground quantum key distribution". In: *Nature* 549 (Aug. 2017), pp. 43–47.

[36] Warren S. Warren. "The Usefulness of NMR Quantum Computing". In: *Science* 277 (1997), p. 1688.

[37] Gerard J. Milburn. "Quantum Measurement and Control of Single Spins in Diamond," in: *Science* 330 (2010), p. 1188.

[38] Heinz-Peter Breuer and Francesco Petruccione. *The Theory of Open Quantum Systems*. Oxford University Press, 2003.

[39] S. Takahashi, I. S. Tupitsyn, J. van Tol, C. C. Beedle, D. N. Hendrickson, and P. C. E. Stamp. "Decoherence in crystals of quantum molecular magnets." In: *Nature* 476 (2011), p. 76.

[40] D.Leibfried, R. Blatt, C. Monroe, and D. Wineland. "Quantum dynamics of single trapped ions". In: *Rev. Mod. Phys.* 75 (2003), pp. 281–324.

[41] Paul G. Kwiat, Andrew J. Berglund, Joseph B. Altepeter, and Andrew G. White. "Experimental Verification of Decoherence-free subspace". In: *Science* 290 (2000), p. 498.

[42] O. Jimenez Farias, C. Lombard Latune, S. P. Walborn, L. Davidovich, and P. H. Souto Ribeiro. "Determining the Dynamics of Entanglement." In: *Science* 324 (2009), pp. 1414–1417.

[43] Jin-Shi Xu, Xiao-Ye Xu, Chuan-Feng Li, Cheng-Jie Zhang, Xu-Bo Zou, and Guang-Can Guo. "Experimental investigation of classical and quantum correlations under decoherence." In: *Nat. Comm.* 1 (2010), p. 7.

[44] G. Puentes, Dirk Voigt, Andrea Aiello, and J.P. Woerdman. "Tunable spatial decoherers for polarization entangled photons". In: *Opt. Lett.* 31 (2006), p. 2057.

[45] Animesh Datta and Anil Shaji. "Quantum Discord and Quantum Computing-An Appraisal". In: *Int. J. Quan. Info.* 9 (2011), pp. 1787–1805.

[46] E. Knill and R. LaFlamme. "Power of one bit of quantum information". In: *Phys. Rev. Lett.* 81 (1998), pp. 5672–5675.

[47] Carlos Andres Melo-Luna, Cristian E. Susa, Andrés F. Ducuara, Astrid Barreiro, and John H. Reina. “Quantum Locality in Game Strategy”. In: *Sci. Rep.* 7 (2017), pp. 1–11.

[48] E. Knill. “Physics: Quantum computing”. In: *Nature* 463 (2010), pp. 441–443.

[49] Erwin Lang, Richard Hildner, Hanna Engelke, Peter Osswald, Frank Würthner, and Jürgen Köhler. “Comparison of the Photophysical Parameters for Three Perylene Bisimide Derivatives by Single-Molecule Spectroscopy”. In: *Chem. Phys. Chem.* 8 (July 2007), pp. 1487–1496.

[50] Abey Issac, Richard Hildner, Dominique Ernts, Catharian Hippius, Frank Würthner, and Jürgen Köhler. “Single molecule studies of calix[4]arene-linked perylene bisimide dimers: relationship between blinking, lifetime and/or spectral fluctuations”. In: *Phys. Chem. Chem. Phys.* 14 (Aug. 2012), pp. 10789–10798.

[51] A. Isaac, R. Hildner, C. Hippius, F. Würthner, and J. Köhler. “Stepwise Decrease of Fluorescence Versus Sequential Photobleaching in a Single Multichromophoric System”. In: *ACSNano* 8.2 (2014), p. 1708.

[52] Cheng Li, Yu Zhong, Carlos Andres Melo-Luna, Thomas Unger, Konstantin Deichsel, Anna Gräser, Jürgen Köhler, Anna Köhler, Richard Hildner, and Sven Huettner. “Emission Enhancement and Intermittency in Polycrystalline Organolead Halide Perovskite Films”. In: *Molecules* 21 (2016), p. 1081.

[53] Cheng Li, Antonio Guerrero, Yu Zhong, Anna Gräser, Carlos Andres Melo-Luna, Jürgen Köhler, Juan Bisquert, Richard Hildner, and Sven Huettner. “Real-Time Observation of Iodide Ion Migration in Methylammonium Lead Halide Perovskites”. In: *Small* 1701711 (2017), pp. 1–10.

[54] Carlos Andres Melo-Luna and John H. Reina. “Experimental quantum control of entangled photonic qubits under decoherence”. to be submitted. 2018.

[55] Carlos Andres Melo-Luna, M. Ritter, R. Hildner, J. Köhler, Stephan Förster, and John H. Reina. “Trihalide Perovskite Quantumdots as a Reliable Quantum Source”. to be submitted.

[56] Erick Ipus, Carlos Andres Melo-Luna, Luis Giraldo, Otto Vergara, and John H. Reina. “Implementation of a Cost-Efficient Device for Wireless Photon Coincidence Detection”. to be submitted, arXiv:1706.04927. 2018.

[57] Scott Aaronson. *Quantum Computing since Democritus*. Cambridge University Press, 2013.

[58] Mark M. Wilde. *Quantum Information Theory*. cambridge university press, 2013.

[59] Paul G. Kwiat, Klaus Mattle, Harald Weinfurter, and Anton Zeilinger. “New High-Intenssity Source Polarization-Entangled Photon Pairs”. In: *Phys. Rev. Lett.* 75.24 (1995), p. 4337.

[60] Paul G. Kwiat, Edo Waks, Andrew G. White, Ian Appelbaum, and Philippe H. Eberhard. “Ultrabright source of polarization-entangled photons”. In: *Phys. Rev. A* 60.2 (1999), R773.

[61] Y.-S. Zhang, Y.-F. Huang, C.-F. Li, and G.-C. Guo. “Experimental preparation of the Werner state via spontaneous parametric down-conversion”. In: *Phys. Rev. A* 66 (2002), p. 062315.

[62] M. P. Almeida, F. de Melo, M. Hor-Meyll, A. Salles, S. P. Walborn, P. H. Souto Ribeiro, and L. Davidovich. “Environment-Induced Sudden Death of Entanglement”. In: *Science* 316 (2007), pp. 579–582.

[63] Nicholas A. Peters, Joseph B. Altepeter, David Branning, Evan R. Jeffrey, Tzu-Chieh Wei, and Paul G. Kwiat. “Maximally Entangled Mixed States: Creation and Concentration”. In: *Phys. Rev. Lett.* 92.13 (2004), p. 133601.

[64] A. G. White, D. F. V. James, W. J. Munro, and P. G. Kwiat. “Exploring Hilbert space: Accurate characterization of quantum information.” In: *Phys. Rev. A* 65 (2001), p. 012301.

[65] Jin-Shi Xu, Chuan-Feng Li, Ming Gong, Xu-Bo Zou, Cheng-Hao Shi, Geng Chen, and Guang-Can Guo. “Experimental Demonstration of Photonic Entanglement Collapse and Revival”. In: *Phys. Rev. Lett.* 104.100502 (2010).

[66] D. Bouwmeester, J.W. Pan, K. Mattle, M. Eibl, H. Weinfurter, and A. Zeilinger. “Experimental Quantum Teleportation”. In: *Nature* 390 (1997), pp. 575–579.

[67] Charles H. Bennett, Francois Bessette, Gilles Brassard, Louis Salvail, and John Smolin. “Experimental Quantum Cryptography”. In: *J. Cryptology* 5 (1992), pp. 3–28.

[68] Alberto Politi, Jonathan C. F. Matthews, and Jeremy L. O’Brien. “Shor’s Quantum Factoring Algorithm on a Photonic Chip”. In: *Science* 325 (2009), pp. 1221–1.

[69] Xi-Lin Wang et al. “Experimental Ten-Photon Entanglement”. In: *Phys. Rev. Lett.* 117.210502 (2016).

[70] Kazuya Takemoto, Yoshihiro Nambu, Toshiyuki Miyazawa, Yoshiki Sakuma, Tsuyoshi Yamamoto, Shinichi Yorozu, and Yasuhiko Arakawa. “Quantum key distribution over 120 km using ultrahigh purity single-photon source and superconducting single-photon detectors”. In: *Sci. Rep.* 5.14383 (2015).

[71] J. Nilsson et al. “Quantum teleportation using a light-emitting diode”. In: *Nature Photonics* 7 (2013).

[72] Q. A. Turchette, C. J. Hood, W. Lange, H. Mabuchi, and H. J. Kimble. “Measurement of Conditional Phase Shifts for Quantum Logic”. In: *Phys. Rev. Lett.* 75.25 (Dec. 1995), p. 4710.

[73] J. I. Cirac and P. Zoller. “A scalable quantum computer with ions in an array of microtraps”. In: *Nature* 404 (Apr. 2000), pp. 579–581.

[74] A. Imamoglu, D. D. Awschalom, G. Burkard, D. P. DiVincenzo, D. Loss, M. Sherwin, and A. Small. “Quantum Information Processing Using Quantum Dot Spins and Cavity QED”. In: *Phys. Rev. Lett.* 83.20 (Nov. 1999), p. 4204.

[75] A. Rauschenbeutel, P. Bertet, S. Osnaghi, G. Nogues, M. Brune, J. M. Raimond, and S. Haroche. “Controlled entanglement of two field modes in a cavity quantum electrodynamics experiment”. In: *Phys. Rev. A* 64.050301(R) (Oct. 2001).

[76] Michael N. Leuenberger and Daniel Loss. “Quantum computing in molecular magnets”. In: *Nature* 410 (Apr. 2001), pp. 789–793.

[77] *Quantum strategic game theory*. 3. Innovations in Theoretical Computer Science Conference. 2012.

[78] Lieven M. K. Vandersypen, Matthias Steffen, Gregory Breyta, Costantino S. Yannoni, Mark H. Sherwood, and Isaac L. Chuang. “Experimental realization of Shor’s quantum factoring algorithm using nuclear magnetic resonance”. In: *Nature* 414 (Dec. 2001), p. 883. URL: http://dx.doi.org/10.1038/414883a.

[79] Neil A. Gershenfeld and Isaac L. Chuang. “Bulk Spin-Resonance Quantum Computation”. In: *Science* 275 (Jan. 2009), pp. 350–356.

[80] Isaac L. Chuang, Lieven M. K. Vandersypen, Xinlan Zhou, Debbie W. Leung, and Seth Lloyd. “Experimental realization of a quantum algorithm”. In: *Nature* 393 (May 1998), pp. 143–146.

[81] E. Knill, Isaac L. Chuang, and R. Laflamme. “Effective pure states for bulk quantum computation”. In: *Phys. Rev. A* 57 (Sept. 1998), pp. 3348–3363.

[82] Jonathan A. Jones, Vlatko Vedral, Artur Ekert, and Giuseppe Castagnoli. “Geometric quantum computation using nuclear magnetic resonance”. In: *Nature* 403 (Feb. 2000), p. 869.

[83] Immanuel Bloch. “Quantum coherence and entanglement with ultracold atoms in optical lattices”. In: *Nature* 453 (June 2008), pp. 1016–1022.

[84] Thierry Giamarchi, Christian Rüegg, and Oleg Tchernyshyov. “Bose–Einstein condensation in magnetic insulators”. In: *Nature Physics* 4 (Mar. 2008), pp. 198–204.

[85] Ilya Fushman, Dirk Englund, Andrei Faraon, Nick Stoltz, Pierre Petroff, and Jelena Vuckovic. “Controlled Phase Shifts with a Single Quantum Dot”. In: *Science* 320 (May 2008), pp. 769–772.

[86] Lucio Robledo, Jeroen Elzerman, Gregor Jundt, Mete Atatüre, Alexander Högele, Stefan Fält, and Atac Imamoglu. “Conditional Dynamics of Interacting Quantum Dots”. In: *Science* 320 (May 2008), p. 772.

[87] J. M. Raimond, M. Brune, and S. Haroche. “Colloquium: Manipulating quantum entanglement with atoms and photons in a cavity”. In: *Rev. Mod. Phys.* 73.3 (July 2001), p. 565.

[88] C. Monroe, D. M. Meekhof, B.E. King, W. M. Itano, and D. J. Wineland. “Demonstration of a Fundamental Quantum Logic Gate”. In: *Phys. Rev. Lett.* 75 (Dec. 1995), pp. 4714–4717.

[89] Asher Peres. *Quantum Theory: Concepts and Methods*. Ed. by Alwyn van der Merwe. Kluwer Academic Publisher, 2002.

[90] Nicolas Gisin Asher Peres. “Maximal violation of Bell’s inequality for arbitrarily large spin”. In: *Phys. Lett. A* 162 (Dec. 1992), p. 15.

[91] S. Popescu. “Bell’s inequalities and density matrices: Revealing “hidden” nonlocality”. In: *Phys. Rev. Lett.* 74 (1995), p. 2619.

[92] Sandu Popescu and Daniel Rohrlich. “Quantum Nonlocality as an Axiom”. In: *Foundation fo Physics* 24.3 (July 1994), p. 379.

[93] R. F. Werner. “Quantum states with Einstein-Podolsky-Rosen correlations admitting a hidden-variable model”. In: *Phys. Rev. A* 40 (1989), p. 4277.

[94] M. Horodecki and P. Horodecki. “Reduction criterion of separability and limits for a class of distillation protocols”. In: *Phys. Rev. A* 59.6 (1999), pp. 4206–4216.

[95] Flavien Hirsch, Marco Tulio Quintino, Joseph Bowles, and Nicolas Brunner. “Genuine Hidden Quantum Nonlocality”. In: *Phys. Rev. Lett.* 111 (2013), pp. 160402–4.

[96] Tong-Jun Liu, Cen-Yang Wang, Jian Li, and Qin Wang. “Experimental preparation of an arbitrary tunable Werner state”. In: *Eur. Phys. Lett* 119.14002-5 (July 2017).

[97] Jin-Shi Xu, Chuan-Feng Li, Cheng-Jie Zhang, Xiao-Ye Xu, Yong-Sheng Zhang, and Guang-Can Guo. “Experimental investigation of the non-Markovian dynamics of classical and quantum correlations”. In: *Phys. Rev. A* 82.042328 (Oct. 2010).

[98] Jin-Shi Xu, Kai Sun, Chuan-Feng Li, Xiao-Ye Xu, Guang-Can Guo, Erika Andersson, Rosario Lo Franco, and Giuseppe Compagno. “Experimental recovery of quantum correlations in absence of system-environment back-action”. In: *Nat. Comm.* 4.2851 (Nov. 2013).

[99] Manuel Erhard, Robert Fickler, Mario Krenn, and Anton Zeilinger. “Twisted photons: new quantum perspectives in high dimensions”. In: *Light: Science & Applications* 7 (Mar. 2018), pp. 1–11.

[100] Daniel F. V. James, Paul G. Kwiat, William J. Munro, and Andrew G. White. “Measurement of qubits”. In: *Phys. Rev. A* 64 (2001), p. 052312.

[101] Michael Kasha. “Characterization of Electronic Transitions in Complex Molecules”. In: *Dis. Faraday Soc.* 9 (July 1950), p. 14.

[102] Loredana Protesescu, Sergii Yakunin, Maryna I. Bodnarchuk, Franziska Krieg, Riccarda Caputo, Christopher H. Hendon, Ruo Xi Yang, Aron Walsh, and Maksym V. Kovalenko. “Nanocrystals of Cesium Lead Halide Perovskites ($CsPbX_3$, X = Cl, Br, and I): Novel Optoelectronic Materials Showing Bright Emission with Wide Color Gamut”. In: *Nano Lett.* 15 (2015), p. 3692.

[103] Gabriele Raino, Georgian Nedelcu, Loredana Protesescu, Maryna I. Bodnarchuk, Maksym V. Kovalenko, Rainer F. Mahrt, and Thilo Stöferle. “Single Cesium Lead Halide Perovskite Nanocrystals at Low Temperature: Fast Single-Photon Emission, Reduced Blinking and Exciton Fine Structure”. In: *ACS Nano* 10.2 (2016), p. 2485.

[104] Samuel D. Stranks and Henry J. Snaith. “Metal-halide perovskites for photovoltaic and light-emitting devices”. In: *Nature Nanotechnology* 10 (2015), pp. 391–402.

[105] Brandon R. Sutherland and Edward H. Sargent. “Perovskite Photonic Sources”. In: *Nature Photonics* 10 (2016), p. 295.

[106] John H. Reina, Cristian E. Susa, and Richard Hildner. “Conditional quantum nonlocality in dimeric and trimeric arrays of organic molecules”. In: *Phys. Rev. A* 97 (2018), pp. 063422–11.

[107] M. Celebrano, P. Kukura, A. Renn, and V. Sandoghdar. “Single-molecule imagin by optical absortion”. In: *Nature Photonics* 290 (Jan. 2011), pp. 95–98.

[108] W.E. Moerner and M. Orrit. “Illuminating Single Molecules in Condensed Matter”. In: *Science* 283 (1999), pp. 1670–1676.

[109] Chris Gell, David Brockwell, and Alastair Smith. *Handbook of Single Molecule Fluorescence Spectroscopy*. Oxford University Press, 2006.

[110] Y. L. A. Rezus, S. G. Walt, R. Lettow, A. Renn, G. Zumofen, S. Gotzinger, and V. Sandoghdar. “Single-Photon Spectroscopy of a Single Molecule”. In: *Phys. Rev. Lett.* 108 (Mar. 2012), pp. 093601–5.

[111] C. Hettich, C. Schmitt, J. Zitzmann, S. Kühn, I. Gerhardt, and V. Sandoghdar. “Nanometer resolution and Coherent Optical Dipole Coupling of two individual Molecules”. In: *Science* 298 (Oct. 2002), pp. 385–389.

[112] Hui-Seon Kim et al. “Lead Iodide Perovskite Sensitized All-Solid-State Submicron Thin Film Mesoscopic Solar Cell with Efficiency Exceeding 9%”. In: *Sci. Rep.* 2.591 (2012).

[113] Jeong-Hyeok Im, Chang-Ryul Lee, Jin-Wook Lee, Sang-Won Park, and Nam-Gyu Park. “6.5% efficient perovskite quantum-dot-sensitized solar cell”. In: *Nanoscale* 3 (2011), pp. 4088–4093.

[114] Xing Ding et al. “On-Demand Single Photons with High Extraction Efficiency and Near-Unity Indistinguishability from a Resonantly Driven Quantum Dot in a Micropillar”. In: *Phys. Rev. Lett.* 116.020401 (2016).

[115] Charles Santori, David Fattal, Jelena Vučković, Glenn S. Solomon, and Yoshihisa Yamamoto. “Indistinguishable photons from a single-photon device”. In: *Nature* 419 (2002), 594 EP -.

[116] Yu-Ming He, Yu He, Yu-Jia Wei, Dian Wu, Mete Atatüre, Christian Schneider, Sven Höfling, Martin Kamp, Chao-Yang Lu, and Jian-Wei Pan. “On-demand semiconductor single-photon source with near-unity indistinguishability”. In: *Nature Nanotechnology* 8 (Feb. 2013).

[117] Axel Kuhn, Markus Hennrich, and Gerhard Rempe. “Deterministic Single-Photon Source for Distributed Quantum Networking”. In: *Phys. Rev. Lett.* 89.6 (2002), p. 067901.

[118] Christian Kurtsiefer, Sonja Mayer, Patrick Zarda, and Harald Weinfurter. “Stable Solid-State Source of Single Photons”. In: *Phys. Rev. Lett.* 85.2 (2000), p. 290.

[119] A Lohrmann, B C Johnson, J C McCallum, and S Castelletto. “A review on single photon sources in silicon carbide”. In: *Rep. Prog. Phys.* 80 (2017), p. 034502.

[120] T. Basché, W. E. Moerner, M. Orrit, and H. Talon. “Photon Antihunching in the Fluorescence of a Single Dye Molecule Trapped in a Solid”. In: *Phys. Rev. Lett.* 69.10 (1992).

[121] Iman Esmaeil Zadeh, Ali W. Elshaari, Klaus D. Jöns, Andreas Fognini, Dan Dalacu, Philip J. Poole, Michael E. Reimer, and Val Zwiller. “Deterministic Integration of Single Photon Sources in Silicon Based Photonic Circuits”. In: *Nano Letters* 16.4 (2016).

[122] Igor Aharonovich, Dirk Englund, and Milos Toth. “Solid-state single-photon emitters”. In: *Nature Photonics* 10 (2016).

[123] B. Lounis and W. E. Moerner. “Single photons on demand from a single molecule at room temperature”. In: *Nature* 407.28 (2000), p. 491.

[124] Feng Liu et al. “Highly Luminescent Phase-Stable CsPbI3 Perovskite Quantum Dots Achieving Near 100% Absolute Photoluminescence Quantum Yield”. In: *ACS Nano* 11 (Sept. 2017), pp. 10373–10383.

[125] Ian L. Braly, Dane W. deQuilettes, Luis M. Pazos-Outón, Sven Burke, Mark E. Ziffer, David S. Ginger, and Hugh W. Hillhouse. “Hybrid perovskite films approaching the radiative limit with over 90% photoluminescence quantum efficiency”. In: *Nature Photonics* 12.6 (2018), pp. 355–361.

[126] Chenghao Bi, Shixun Wang, Wen Wen, Jifeng Yuan, Guozhong Cao, and Jianjun Tian. "Room-Temperature Construction of Mixed-Halide Perovskite Quantum Dots with High Photoluminescence Quantum Yield". In: *J Phys. Chem. C.* 122 (Feb. 2018), pp. 5151–5160.

[127] Nikolaos Droseros, Giulia Longo, Jan C. Brauer, Michele Sessolo, Henk J. Bolink, and Natalie Banerji. "Origin of the Enhanced Photoluminescence Quantum Yield in $MAPbBr_3$ Perovskite with Reduced Crystal Size". In: *ACS Energy Lett.* 3 (May 2018), pp. 1458–1466.

[128] R. Brunner, Y.-S. Shin, T. Obata, M. Pioro-Ladrière, T. Kubo, K. Yoshida, T. Taniyama, Y. Tokura, and S. Tarucha. "Two-Qubit Gate of Combined Single-Spin Rotation and Interdot Spin Exchange in a Double Quantum Dot". In: *Phys. Rev. Lett.* 107.14 (Sept. 2011), p. 146801.

[129] National Center for Photovoltaics (NCPV). *Efficiency Chart*. (Visited on).

[130] Constantinos C. Stoumpos and Mercouri G. Kanatzidis. "The Renaissance of Halide Perovskites and Their Evolution as Emerging Semiconductors". In: *Acc. Chem. Res* 48 (Sept. 2015), pp. 2791–2802.

[131] D. B. Mitzi, K. Chondroudis, and C. R. Kagan. "Organic-inorganic electronics". In: *IBM Journal of Research and Development* 45 (2001), pp. 29–45.

[132] Chiho Kim, Tran Doan Huan, Sridevi Krishnan, and Rampi Ramprasad. "Data Descriptor: A hybrid organic-inorganic perovskite dataset". In: *Sci. Data* 4.170057 (2017).

[133] Stefaan De Wolf, Jakub Holovsky, Soo-Jin Moon, Philipp Löper, Bjoern Niesen, Martin Ledinsky, Franz-Josef Haug, Jun-Ho Yum, and Christophe Ballif. "Organometallic Halide Perovskites: Sharp Optical Absorption Edge and Its Relation to Photovoltaic Performance". In: *Phy. Chem. Lett.* 5 (2014), pp. 1035–1039.

[134] Laura M. Herz. "Charge-Carrier Mobilities in Metal Halide Perovskites: Fundamental Mechanisms and Limits". In: *ACS Energy Lett.* 2 (2017), pp. 1539–1548.

[135] Feng Hao, Constantinos C. Stoumpos, Duyen Hanh Cao, Robert P. H. Chang, and Mercouri G. Kanatzidis. "Lead-free solid-state organic–inorganic halide perovskite solar cells". In: *Nature Photonics* 8 (May 2014), 489 EP -. URL: http://dx.doi.org/10.1038/nphoton.2014.82.

[136] Zhuo Wang, Binglong Lei, Xiaohong Xia, Zhongbing Huang, Kevin Peter Homewood, and Yun Gao. "$CH_3NH_2BiI_3$ Perovskites: A New Route to Efficient Lead-Free Solar Cells". In: *J. Phys. Chem. C* 122 (2018), pp. 2589–2595.

[137] Feliciano Giustino and Henry J. Snaith. "Toward Lead-Free Perovskite Solar Cells". In: *ACS Energy Lett.* 1 (2016), pp. 1233–1240.

[138] Nakita K. Noel et al. “Lead-free organic–inorganic tin halide perovskites for photovoltaic applications†”. In: *Energy Environ. Sci.* 7 (2014), p. 3061.

[139] Samuel D. Stranks, Giles E. Eperon, Giulia Grancini, Christopher Menelaou, Marcelo J. P. Alcocer, Tomas Leijtens, Laura M. Herz, Annamaria Petrozza, and Henry J. Snaith. “Electron-Hole Diffusion Lengths Exceeding 1 Micrometer in an Organometal Trihalide Perovskite Absorber”. In: *Science* 342.6156 (2013), pp. 341–344.

[140] Christian Wehrenfennig, Giles E. Eperon, Michael B. Johnston, Henry J. Snaith, and Laura M. Herz. “High Charge Carrier Mobilities and Lifetimes in Organolead Trihalide Perovskites”. In: *Adv. Mater.* 26 (2014), p. 1584.

[141] Tze Chien Sum, Nripan Mathews, Guichuan Xing, Swee Sien Lim, Wee Kiang Chong, David Giovanni, and Herlina Arianita Dewi. “Spectral Features and Charge Dynamics of Lead Halide Perovskites: Origins and Interpretations”. In: *Acc. Chem. Res* 49 (Jan. 2016), pp. 294–302.

[142] Michele Saba andFrancesco Quochi, Andrea Mura, and Giovanni Bongiovanni. “Excited State Properties of Hybrid Perovskites”. In: *Acc. Chem. Res* 49 (Dec. 2015), pp. 166–173.

[143] Peter Müller-Buschbaum, Mukundan Thelakkat, Thomas F. Fässler, and Martin Stutzmann. “Hybrid Photovoltaics - from Fundamentals towards Application”. In: *Adv. Energy Mater.* 7 (2017), p. 1700248.

[144] Lakshminarayana Polavarapu, Bert Nickel, Jochen Feldmann, and Alexander S. Urban. “Advances in Quantum-Con ned Perovskite Nanocrystals for Optoelectronics”. In: *Adv. Energy Mater.* 7 (2017), p. 1700267.

[145] Young-Shin Park, Shaojun Guo, Nikolay Makarov, and Victor I. Klimov. “Room Temperature Single-Photon Emission from Individual Perovskite Quantum Dots”. In: *ACS Nano* 9 (2015), pp. 10386–10393.

[146] Fabian Panzer, Cheng Li, Tobias Meier, Anna Köhler, and Sven Huettner. “Impact of Structural Dynamics on the Optical Properties of Methylammonium Lead Iodide Perovskites”. In: *Adv. Energy Mater.* 7 (2017), p. 1700286.

[147] J. L. O’Brien, A. Furusawa, and J. Vukovi. “Photonic Quantum Technologies”. In: *Nature Photonics* 3 (2009), pp. 687–695.

[148] C. Bennett and D. DiVincenzo. “Quantum information and computation”. In: *Nature* 404 (2000), p. 247.

[149] B. Vlastakis, G. Kirchmair, Z. Leghtas, S. E. Nigg, L. Frunzio, S. M. Girvin, M. Mirrahimi, M. H. Devoret, and R. J. Schoelkopf. “Deterministically Encoding Quantum Information Using 100-Photon Schrödinger Cat States”. In: *Science* 342.6158 (2013), pp. 607–610.

[150] Shunlong Luo, Shuangshuang Fu, and Nan Li. “Decorrelating capabilities of operations with application to decoherence”. In: *Phys. Rev. A* 82 (2010), p. 052122.

[151] L. Mazzola, J. Piilo, and S. Maniscalco. “Sudden Transition between Classical and Quantum Decoherence”. In: *Phys. Rev. Lett.* 104 (2010), p. 200401.

[152] C. E. Susa and J. H. Reina. “Correlations in optically controlled quantum emitters”. In: *Phys. Rev. A* 85 (2012), p. 022111.

[153] Andrew D. Yablon. *Optical Fiber Fusion Splicing*. Ed. by W. T. Rhodes. Vol. 103. Optical Series. 19 Schoolhouse Road Somerset, NJ 08873: Springer Verlag, 2005.

[154] Richard Jozsa. “Fidelity for mixed quantum states”. In: *J. Mod. Opt* 41.12 (1994), p. 2315.

[155] Berry Groisman, Sandu Popescu, and Andreas Winter. “Quantum, classical, and total amount of correlations in a quantum state”. In: *Phys. Rev. A* 72 (2005), p. 032317.

[156] K. Modi, A. Brodutch, H. Cable, T. Paterek, and V. Vedral. “The classical-quantum boundary for correlations: Discord and related measures”. In: *Rev. Mod. Phys.* 84 (2012), p. 1655.

[157] J. H. Reina, C. E. Susa, and F. F. Fanchini. “Extracting information from qubit-environment correlations”. In: *Sci. Rep.* 4 (2014), p. 7443.

[158] J. von Neumann and O. Morgenstern. *Theory of Games and Economic Behavior*. Princeton University Press, 1944.

[159] D. A. Meyer. “Quantum strategies.” In: *Phys. Rev. Lett.* 82 (1999), p. 1052.

[160] J. Eisert, M. Wilkens, and M. Lewenstein. “Quantum games and quantum strategies.” In: *Phys. Rev. Lett.* 83 (1999), p. 3077.

[161] A. Pappa. “Nonlocality and conflicting interest games”. In: *Phys. Rev. Lett.* 114 (2015), p. 020401.

[162] N. Brunner and N. Linden. “Connection between Bell nonlocality and Bayesian game theory”. In: *Nat. Comm.* 4 (2013), p. 2057.

[163] A. Iqbal and D. Abbott. “Constructing quantum games from a system of Bellâs inequalities.” In: *Phys. Lett. A* 374 (2010), p. 3155.

[164] R. Prevedel, A. Stefavov, Whalter, P., and A. Zeilinger. “Experimental realization of a quantum game on a one-way quantum computer.” In: *New J. Phys.* 9 (2007), p. 207.

[165] C. Zu. “Experimental demonstration of quantum gain in a zero-sum game.” In: *New J. Phys.* 14 (2012), p. 033002.

[166] S. C. Benjamin and P. M. Hayden. “Multiplayer quantum games.” In: *Phys. Rev. A* 64 (2001), p. 030301.

[167] C. Schmid. “Experimental implementation of a four-player quantum game.” In: *New J. Phys.* 12 (2010), p. 063031.

[168] L. Marinatto and T. Weber. “A quantum approach to static games of complete information”. In: *Phys. Lett. A* 272 (2000), p. 291.

[169] J. Du. “Experimental realization of quantum games on a quantum computer.” In: *Phys. Rev. Lett.* 88 (2002), p. 137902.

[170] C. F. Lee and N. F. Johnson. “Efficiency and formalism of quantum games.” In: *Phys. Lett. A* 67 (2003), p. 022311.

[171] A. Flitney and D. Abbott. “Advantage of a quantum player over a classical one in 2×2 quantum games.” In: *Proc. Roy. Soc. A: Math. Phys.* 459 (2003), p. 2463.

[172] R. B. Meyerson. *Game Theory: An Analysis of Conflict*. Cambridge. MIT Press, 1991.

[173] M. J. Osborne. *An Introduction to Game Theory*. Oxford: Oxford University Press, 2002.

[174] N. Brunner, D. Cavalcanti, S. Pironio, V. Scarani, and S. Wehner. “Bell nonlocality.” In: *Rev. Mod. Phys.* 86 (2014), p. 414.

[175] A. Ducuara, J. Madronero, and J. H. Reina. “On the activation of quantum nonlocality”. In: *Univ. Sci.* 21 (2016), p. 129.

[176] C. Palazuelos. “Superactivation of quantum nonlocality.” In: *Phys. Rev. Lett.* 109 (2012), p. 190401.

[177] Y. C. Liang, L. Masanes, and D. Rosset. “All entangled states display some hidden nonlocality.” In: *Phys. Rev. A* 86 (2012), p. 052115.

[178] S. C. Benjamin and P. M. Hayden. “Comment on “Quantum Games and Quantum Strategies””. In: *Phys. Rev. Lett.* 87 (2001), p. 069801.

[179] J. Eisert, M. Wilkens, and M. Lewenstein. “Eisert, Wilkens and Lewenstein Reply”. In: *Phys. Rev. Lett.* 87 (2001), p. 069802.

[180] J. Eisert and M. Wilkens. “Quantum games”. In: *J. Mod. Opt* 2543.47 (2000), p. 14.

[181] J. Du. “Phase-transition-like behaviour of quantum games”. In: *J. Phys. A* 36 (2003), p. 6551.

[182] A. P Flitney and L. C. L. Hollenberg. “Nash equilibria in quantum games with generalized two-parameter strategies,” in: *Phys. Lett. A* 363 (2007), p. 381.

[183] A. Nawaz. “Prisoners’ dilemma in the presence of collective dephasing”. In: *J. Phys. A* 45 (2012), p. 19.

[184] A. Acin, N. Gisin, and B. Toner. “Grothendieck’s constant and local models for noisy entangled quantum states”. In: *Phys. Rev. A* 73 (2006), p. 062105.

[185] N. K. Langford. “Demonstration of a simple entangling optical gate and its use in Bell-state analysis.” In: *Phys. Rev. Lett.* 95 (2005), p. 210504.

[186] R. Okamoto, H. F. Hofmann, S. Takeuchi, and K. Sasaki. “Demonstration of an optical quantum Controlled-NOT gate without path interference”. In: *Phys. Rev. Lett.* 95 (2005), p. 210506.

[187] N. Kiesel, C. Schmid, U. Weber, R. Ursin, and H. Weinfurter. “Linear optics Controlled-Phase gate made simple”. In: *Phys. Rev. Lett.* 95 (2005), p. 210505.

[188] A. Crespi. “Integrated photonic quantum gates for polarization qubits”. In: *Nat. Comm.* 2 (2011), p. 566.

[189] A. Streltsov, G. Adesso, and M. B. Plenio. “Quantum coherence as a resource”. In: *arXiv:1609.02439v2* (2016).

[190] C. Schellintg. *The Strategy of Conflict*. MA: Harvard University Press, 1960.

[191] A. Nawaz. “The strategic form of quantum prisoners’ dilemma”. In: *Chin. Phys. Lett.* 30 (2013), p. 050302.

[192] Akihiro Kojima, Kenjiro Teshima, Yasuo Shirai, and Tsutomu Miyasaka. “Organometal Halide Perovskites as Visible-Light Sensitizers for Photovoltaic Cells”. In: *J. Am. Chem. Soc.* 131.17 (2009), pp. 6050–6051.

[193] Woon Seok Yang, Jun Hong Noh, Nam Joong Jeon, Young Chan Kim, Seungchan Ryu, Jangwon Seo, and Sang Il Seok. “High-performance photovoltaic perovskite layers fabricated through intramolecular exchange”. In: *Science* 348.6240 (2015), pp. 1234–1237.

[194] Tze-Bin Song, Qi Chen, Huanping Zhou, Song Luo, Yang (Michael) Yang, Jingbi You, and Yang Yang. “Unraveling film transformations and device performance of planar perovskite solar cells”. In: *Nano Energy* 12 (2015), pp. 494–500.

[195] Qi Chen, Huanping Zhou, Ziruo Hong, Song Luo, Hsin-Sheng Duan, Hsin-Hua Wang, Yongsheng Liu, Gang Li, and Yang Yang. “Planar Heterojunction Perovskite Solar Cells via Vapor-Assisted Solution Process”. In: *J. Am. Chem. Soc.* 136.2 (2014), pp. 622–625.

[196] Giulia Grancini, Ajay Ram Srimath Kandada, Jarvist M. Frost, Alex J. Barker, Michele De Bastiani, Marina Gandini, Sergio Marras, Guglielmo Lanzani, Aron Walsh, and Annamaria Petrozza. “Role of microstructure in the electron-hole interaction of hybrid lead halide perovskites”. In: *Nature Photonics* 9 (2015), pp. 695–701.

[197] Hong-Hua Fang, Raissa Raissa, Mustapha Abdu-Aguye, Sampson Adjokatse, Graeme R. Blake, Jacky Even, and Maria Antonietta Loi. “Photophysics of Organic-Inorganic Hybrid Lead Iodide Perovskite Single Crystals”. In: *Adv. Funct. Mater.* 25 (2015), pp. 2378–2385.

[198] Osbel Almora, Isaac Zarazua, Elena Mas-Marza, Ivan Mora-Sero, Juan Bisquert, and Germà Garcia-Belmonte. "Capacitive Dark Currents, Hysteresis, and Electrode Polarization in Lead Halide Perovskite Solar Cells". In: *J. Phys. Chem. Lett.* 6.9 (2015), pp. 1645–1652.

[199] Rafael S. Sanchez, Victoria Gonzalez-Pedro, Jin-Wook Lee, Nam-Gyu Park, Yong Soo Kang, Ivan Mora-Sero, and Juan Bisquert. "Slow Dynamic Processes in Lead Halide Perovskite Solar Cells. Characteristic Times and Hysteresis". In: *J. Phys. Chem. Lett.* 5.13 (2014), pp. 2357–2363.

[200] Kristofer Tvingstedt, Olga Malinkiewicz, Andreas Baumann, Carsten Deibel, Henry J. Snaith, Vladimir Dyakonov, and Henk J. Bolink. "Radiative efficiency of lead iodide based perovskite solar cells". In: *Sci. Rep.* 4 (2014).

[201] Alessio Filippetti, Pietro Delugas, and Alessandro Mattoni. "Methylammonium Lead-Iodide Perovskite: Recombination and Photoconversion of an Inorganic Semiconductor Within a Hybrid Body". In: *Appl. Phys. Lett.* 106 (2015), p. 221104.

[202] Wolfgang Tress, Nevena Marinova, Olle Inganäs, Mohammad. K. Nazeeruddin, Shaik M. Zakeeruddin, and Michael Graetzel. "Predicting the Open-Circuit Voltage of $CH_3NH_3PbI_3$ Perovskite Solar Cells Using Electroluminescence and Photovoltaic Quantum Efficiency Spectra: the Role of Radiative and Non-Radiative Recombination". In: *Adv. Energy Mater.* 5 (2015).

[203] Wei E. I. Sha, Xingang Ren, Luzhou Chen, and Wallace C. H. Choy. "The efficiency limit of CH3NH3PbI3 perovskite solar cells". In: *Appl. Phys. Lett.* 106 (2015), p. 221104.

[204] Tze Chien Sum and Nripan Mathews. "Advancements in Perovskite Solar Cells: Photophysics behind the Photovoltaics". In: *Energy Environ. Sci.* 7 (2014), p. 2518.

[205] Yu-Che Hsiao, Ting Wu, Mingxing Li, Qing Liu, Wei Qin, and Bin Hu. "Fundamental physics behind high-efficiency organo-metal halide perovskite solar cells". In: *J. Mater. Chem. A* 3 (2015), p. 15372.

[206] Yasuhiro Yamada, Toru Nakamura, Masaru Endo, Atsushi Wakamiya, and Yoshihiko Kanemitsu. "Photocarrier Recombination Dynamics in Perovskite CH3NH3PbI3 for Solar Cell Applications". In: *J. Am. Chem. Soc.* 136 (2014), pp. 11610–11613.

[207] Laura M. Herz. "Charge-Carrier Dynamics in Organic-Inorganic Metal Halide Perovskites". In: *Annu. Rev. Phys. Chem.* 67 (2015).

[208] Nakita Kimberly Noel, Antonio Abate, Samuel David Stranks, Elizabeth Parrott, Victor Burlakov, Alain Goriely, and Henry J. Snaith. "Enhanced Photoluminescence and Solar Cell Performance via Lewis Base Passivation of Organic-Inorganic Lead Halide Perovskites". In: *ACS Nano* 8 (2014), pp. 9815–9821.

[209] William Shockley and Hans J. Queisser. “Detailed Balance Limit of Efficiency of p-n Junction Solar Cells”. In: *J. Appl. Phys.* 32 (1961), pp. 510–519.

[210] Owen D. Miller, Eli Yablonovitch, and Sarah R. Kurtz. “Strong Internal and External Luminescence as Solar Cells Approach the Shockley-Queisser Limit”. In: *IEEE J. Photovolt.* 2 (2012), pp. 303–311.

[211] Zhi-Kuang Tan et al. “Bright light-emitting diodes based on organometal halide perovskite”. In: *Nat. Nanotechnol.* 9 (2014), pp. 687–692.

[212] Jianpu Wang et al. “Interfacial Control Toward Efficient and Low-Voltage Perovskite Light-Emitting Diodes”. In: *Adv. Mater.* 27 (2015), p. 2311.

[213] Felix Deschler et al. “High Photoluminescence Efficiency and Optically-Pumped Lasing in Solution-Processed Mixed Halide Perovskite Semiconductors”. In: *J. Phys. Chem. Lett.* 5 (2014), pp. 1421–1426.

[214] Dane W. deQuilettes, Sarah M. Vorpahl, Samuel D. Stranks, Hirokazu Nagaoka, Giles E. Eperon, Mark E. Ziffer, Henry J. Snaith, and David S. Ginger. “Impact of microstructure on local carrier lifetime in perovskite solar cells”. In: *Sciencexpress* 10.1126 (2015), pp. 1–8.

[215] Sheng Chen, Xiaoming Wen, Rui Sheng, Shujuan Huang, Xiaofan Deng, Martin A. Green, and Anita Wing-Yi Ho-Baillie. “Mobile Ion Induced Slow Carrier Dynamics in Organic-Inorganic Perovskite CH3NH3PbBr3”. In: *ACS Appl. Mater. Interfaces* 8 (2016), pp. 5351–5357.

[216] Juan F. Galisteo-López, M.Anaya, M. E. Calvo, and H. Mı´guez. “Environmental Effects on the Photophysics of Organic-Inorganic Halide Perovskites”. In: *J. Phys. Chem. Lett.* 6 (2015), pp. 2200–2205.

[217] Ronen Gottesman, Laxman Gouda, Basanth S. Kalanoor, Eynav Haltzi, Shay Tirosh, Eli Rosh-Hodesh, Yaakov Tischler, and Arie Zaban. “Photoinduced Reversible Structural Transformations in Free- Standing CH3NH3PbI3 Perovskite Films”. In: *J. Phys. Chem. Lett.* 6 (2015), p. 2332.

[218] Xiaofan Deng, Xiaoming Wen, Cho Fai Jonathan Lau, Trevor Young, Jae Yun, Martin A. Green, Shujuan Huang, and Anita W. Y. Ho-Baillie. “Electric field induced reversible and irreversible photoluminescence responses in methylammonium lead iodide perovskite”. In: *J. Mater. Chem. C* 4 (2016), p. 9060.

[219] Daniel Louis Jacobs, Michael A. Scarpulla, Chen Wang, Benjamin R. Bunes, and Ling Zang. “Voltage Induced Transients in Methylammonium Lead Triiodide Probed by Dynamic Photoluminescence Spectroscopy”. In: *J. Phys. Chem. C* 120 (2016), p. 7893.

[220] Yuze Lin et al. “$\pi-$Conjugated Lewis Base: Ef cient Trap-Passivation and Charge-Extraction for Hybrid Perovskite Solar Cells”. In: *Adv. Mater.* 29 (2017), p. 1604545.

[221] Abhishek Swarnkar, Ramya Chulliyil, Vikash Kumar Ravi, Mir Irfanullah, Arindam Chowdhury, and Angshuman Nag. "Colloidal $CsPbBr_3$ Perovskite Nanocrystals: Luminescence beyond Traditional Quantum Dots". In: *Angew. Chem. Int. Ed.* 54 (2015), pp. 15424–15428.

[222] Takashi Tachikawa, Izuru Karimata, and Yasuhiro Kobori. "Surface Charge Trapping in Organolead Halide Perovskites Explored by Single-Particle Photoluminescence Imaging". In: *J. Phys. Chem. Lett.* 6 (2015), pp. 3195–3201.

[223] Yuxi Tian, Aboma Merdasa, Maximilian Peter, Mohamed Abdellah, Kaibo Zheng, Carlito S. Ponseca, Tonu Pullerits, Arkady Yartsev, Villy Sundstrom, and Ivan G. Scheblykin. "Giant Photoluminescence Blinking of Perovskite Nanocrystals Reveals Single-Trap Control of Luminescence". In: *Nano Lett.* 15 (2015), pp. 1603–1608.

[224] Xiaoming Wen, Anita Ho-Baillie, Shujuan Huang, Rui Sheng, Sheng Chen, HsienChen Ko, and Martin A. Green. "Mobile Charge Induced Fluorescence Intermittency in Methylammonium Lead Bromide Perovskite". In: *Nano Lett.* 15 (2015), pp. 4644–4649.

[225] Yongbo Yuan and Jinsong Huang. "Ion Migration in Organometal Trihalide Perovskite and Its Impact on Photovoltaic Efficiency and Stability". In: *Acc. Chem. Res.* 49 (2016), pp. 286–293.

[226] Sandheep Ravishankar, Osbel Almora, Carlos Echeverrı´a-Arrondo, Elnaz Ghahremanirad, Clara Aranda, Antonio Guerrero, Francisco Fabregat-Santiago, Arie Zaban, Germà Garcia-Belmonte, and Juan Bisquert. "Surface Polarization Model for the Dynamic Hysteresis of Perovskite Solar Cells". In: *J. Phys. Chem. Lett.* 8 (2017), p. 915.

[227] Ziv Hameiri, Arman Mahboubi Soufiani, Mattias K. Juhl, Liangcong Jiang, Fuzhi Huang, Yi-Bing Cheng, Henner Kampwerth, Juergen W. Weber, Martin A. Green, and Thorsten Trupke. "Photoluminescence and electroluminescence imaging of perovskite solar cells". In: *Prog. Photovolt. Res. Appl.* 23 (2015), pp. 1697–1705.

[228] Arman Mahboubi Soufiani, Ziv Hameiri, Steffen Meyer, Sean Lim, Murad Jehangir Yusuf Tayebjee, Jae Sung Yun, Anita Ho-Baillie, Gavin J. Conibeer, Leone Spiccia, and Martin A. Green. "Lessons Learnt from Spatially Resolved Electro- and Photoluminescence Imaging: Interfacial Delamination in $CH_3NH_3PbI_3$ Planar Perovskite Solar Cells upon Illumination". In: *Adv. Energy Mater.* 7 (2016), p. 1602111.

[229] Jon M. Azpiroz, Edoardo Mosconi, Juan Bisquert, and Filippo De Angelisa. "Defects Migration in Methylammonium Lead Iodide and their Role in Perovskite Solar Cells Operation". In: *Energy Environ. Sci.* 8 (2015), pp. 2118–2127.

[230] Bo Chen, Mengjin Yang, Xiaojia Zheng, Congcong Wu, Wenle Li, Yongke Yan, Juan Bisquert, Germà Garcia-Belmonte, Kai Zhu, and Shashank Priya. "Impact of Capacitive Effect and Ion Migration on the Hysteretic Behavior of Perovskite Solar Cells". In: *J. Phys. Chem. Lett.* 6 (2015), p. 4693.

[231] Abey Issac, Richard Hildner, Catharina Hippius, Frank Würthner, and Jürgen Köhler. "Stepwise Decrease of Fluorescence versus Sequential Photobleaching in a Single Multichromophoric System". In: *ACS Nano* 8 (2014), p. 1708.

[232] Cheng Li, Steffen Tscheuschner, Fabian Paulus, Paul E. Hopkinson, Johannes Kießling, Anna Köhler, Yana Vaynzof, and Sven Huettner. "Iodine Migration and its Effect on Hysteresis in Perovskite Solar Cells". In: *Adv. Mater.* 28 (2016), pp. 2446–2454.

[233] Hui Yu, Feng Wang, Fangyan Xie, Wenwu Li, Jian Chen, and Ni Zhao. "The Role of Chlorine in the Formation Process of "$CH_3NH_3PbI_{3-x}Cl_x$" Perovskite". In: *Adv. Funct. Mater.* 24 (2014), pp. 7102–7108.

[234] John C. de Mello, H. Felix Wittmann, and Richard H. Friend. "An Improved Experimental Determination of External Photoluminescence Quantum Efficiency". In: *Adv. Mater.* 9 (1997), pp. 230–232.

[235] Samuel D. Stranks, Victor M. Burlakov, Tomas Leijtens, James M. Ball, Alain Goriely, and Henry J. Snaith. "Recombination Kinetics in Organic-Inorganic Perovskites: Excitons, Free Charge, and Subgap States". In: *Phys. Rev. Appl.* 2 (2014).

[236] Wan-Jian Yin, Tingting Shi, and Yanfa Yan. "Unusual defect physics in $CH_3NH_3PbI_3$ perovskite solar cell absorber". In: *Appl. Phys. Lett.* 104. (2014).

[237] Andreas Baumann, Stefan Väth, Philipp Rieder, Michael C. Heiber, Kristofer Tvingstedt, and Vladimir Dyakonov. "Identification of Trap States in Perovskite Solar Cells". In: *J. Phys. Chem. Lett.* 6 (2015), pp. 2350–2354.

[238] Xiaoxi Wu, M. Tuan Trinh, Daniel Niesner, Haiming Zhu, Zachariah Norman, Jonathan S. Owen, Omer Yaffe, Bryan J. Kudisch, and Xiaoyang Zhu. "Trap States in Lead Iodide Perovskites". In: *J. Am. Chem. Soc.* 137 (2015), pp. 2089–2096.

[239] Gert-Jan A. H. Wetzelaer, Max Scheepers, Araceli Miquel Sempere, Cristina Momblona, Jorge Ávila, and Henk J. Bolink. "Trap-Assisted Non-radiative Recombination in Organic-Inorganic Perovskite Solar Cells". In: *Adv. Mater.* 27 (2015), pp. 1837–1841.

[240] Chen Zhao, Bingbing Chen, Xianfeng Qiao, Lin Luan, Kai Lu, and Bin Hu. "Revealing Underlying Processes Involved in Light Soaking Effects and Hysteresis Phenomena in Perovskite Solar Cells". In: *Adv. Energy Mater.* 5 (2015).

[241] Yehao Deng, Zhengguo Xiao, and Jinsong Huang. “Light-Induced Self-Poling Effect on Organometal Trihalide Perovskite Solar Cells for Increased Device Efficiency and Stability”. In: *Adv. Energy Mater.* 5.1500721 (2015).

[242] Andreas T. Haedler, Klaus Kreger, Abey Issac, Bernd Wittmann, Milan Kivala, Natalie Hammer, Jürgen Köhler, Hans-Werner Schmidt, and Richard Hildner. “Long-range energy transport in single supramolecular nanofibres at room temperature”. In: *Nature* 523 (2015), pp. 196–199.

[243] Yuxi Tian, Maximilian Peter, Eva Unger, Mohamed Abdellah, Kaibo Zheng, Tõnu Pullerits, Arkady Yartsev, Villy Sundström, and Ivan G. Scheblykin. “Mechanistic insights into perovskite photoluminescence enhancement: light curing with oxygen can boost yield thousandfold”. In: *Phys. Chem. Chem. Phys.* 17 (2015), pp. 24978–24987.

[244] Yuxi Tian et al. “Enhanced Organo-Metal Halide Perovskite Photoluminescence from Nanosized Defect-Free Crystallites and Emitting Sites”. In: *J. Phys. Chem. Lett.* 6 (2015), pp. 4171–4177.

[245] Ye Zhang et al. “Charge selective contacts, mobile ions and anomalous hysteresis in organic-inorganic perovskite solar cells”. In: *Mater. Horiz.* 2 (2015), pp. 315–322.

[246] Eric. T. Hoke, Daniel J. Slotcavage, Emma R. Dohner, Andrea R. Bowring, Hemamala I. Karunadasa, and Michael D. McGeheea. “Reversible photo-induced trap formation in mixed- halide hybrid perovskites for photovoltaics”. In: *Chem. Sci.* 6 (2015), pp. 613–617.

[247] Haifeng Yuan et al. “Degradation of Methylammonium Lead Iodide Perovskite Structures through Light and Electron Beam Driven Ion Migration”. In: *J. Phys. Chem. Lett.* 7 (2016), pp. 561–566.

[248] Olivia Hentz, Zhibo Zhao, and Silvija Gradecak. “Impacts of Ion Segregation on Local Optical Properties in Mixed Halide Perovskite Films”. In: *Nano Lett.* 16 (2016), pp. 1485–1490.

[249] Pavel Frantsuzov, Masaru Kuno, Boldizsar Janko, and Rudolph A. Marcus. “Universal emission intermittency in quantum dots, nanorods and nanowires”. In: *Nature Physics* 4 (2008), pp. 519–522.

[250] Valerio D’Innocenzo, Giulia Grancini, Marcelo J.P. Alcocer, Ajay Ram Srimath Kandada, Samuel D. Stranks, Michael M. Lee, Guglielmo Lanzani, Henry J. Snaith, and Annamaria Petrozza. “Excitons versus free charges in organo-lead tri-halide perovskites”. In: *Nat. Commun.* 5 (2014).

[251] Christophe Galland, Yagnaseni Ghosh, Andrea Steinbrück, Milan Sykora, Jennifer A. Hollingsworth, Victor I. Klimov, and Han Htoon. “Two types of luminescence blinking revealed by spectroelectrochemistry of single quantum dots”. In: *Nature* 479 (2011), pp. 203–207.

[252] Pascal Anger, Palash Bharadwaj, and Lukas Novotny. “Enhancement and Quenching of Single-Molecule Fluorescence”. In: *Phys. Rev. Lett.* 96 (2006).

[253] Al. L. Efros and M. Rosen. “Random Telegraph Signal in the Photoluminescence Intensity of a Single Quantum Dot”. In: *Phys. Rev. Lett.* 78 (1997), pp. 1110–1113.

[254] Yuchuan Shao, Zhengguo Xiao, Cheng Bi, Yongbo Yuan, and Jinsong Huang. “Origin and elimination of photocurrent hysteresis by fullerene passivation in $CH_3NH_3PbI_3$ planar heterojunction solar cells”. In: *Nat. Commun.* 5 (2014).

[255] Jixian Xu et al. “Perovskite-fullerene hybrid materials suppress hysteresis in planar diodes”. In: *Nat. Commun.* 6 (2015).

[256] Ronen Gottesman and Arie Zaban. “rovskites for Photovoltaics in the Spotlight: Photoinduced Physical Changes and Their Implications”. In: *Acc. Chem. Res* 49 (2016), p. 320.

[257] Christopher Eames, Jarvist M. Frost, Piers R.F. Barnes, Brian C. O’Regan, Aron Walsh, and M. Saiful Islam. “Ionic transport in hybrid lead iodide perovskite solar cells”. In: *Nat. Commun.* 6 (2015), p. 7497.

[258] Simone Meloni et al. “Ionic polarization-induced current-voltage hysteresis in $CH_3NH_3PbX_3$ perovskite solar cells”. In: *Nat. Commun.* 7 (2016), p. 10334.

[259] Yongbo Yuan, Qi Wang, Yuchuan Shao, Haidong Lu, Tao Li, Alexei Gruverman, and Jinsong Huang. “Electric-Field-Driven Reversible Conversion Between Methylammonium Lead Triiodide Perovskites and Lead Iodide at Elevated Temperatures”. In: *Adv. Energy Mater.* 6 (2016), p. 1501803.

[260] Zhengguo Xiao, Yongbo Yuan, Yuchuan Shao, Qi Wang, Qingfeng Dong, Cheng Bi, Pankaj Sharma, Alexei Gruverman, and Jinsong Huang. “Giant switchable photovoltaic e ect in organometal trihalide perovskite devices”. In: *Nat. Mater.* 14 (2015), p. 193.

[261] S. M. Sze. *Physics of Semiconductor Devices*. New York, USA: Wiley, 1981.

[262] Tae-Youl Yang, Giuliano Gregori, Norman Pellet, Michael Graetzel, and Joachim Maier. “The Significance of Ion Conduction in a Hybrid Organic-Inorganic Lead-Iodide-Based Perovskite Photosensitizer”. In: *Angew. Chem. Int. Ed.* 54 (2015), p. 7905.

[263] Yue Wang, Xiaoming Li, Sivaramapanicker Sreejith, Fei Cao, Zeng Wang, Mihaiela Corina Stuparu, Haibo Zeng, and Handong Sun. “Photon Driven Transformation of Cesium Lead Halide Perovskites from Few-Monolayer Nanoplatelets to Bulk Phase”. In: *Adv. Mater.* 28 (2016), p. 10637.

[264] Jie Xing, Qi Wang, Qingfeng Dong, Yongbo Yuan, Yanjun Fanga, and Jinsong Huang. "Ultrafast ion migration in hybrid perovskite polycrystalline thin films under light and suppression in single crystals". In: *Phys. Chem. Chem. Phys.* 18 (2016), p. 30484.

[265] Jordi Carrillo, Antonio Guerrero, Sara Rahimnejad, Osbel Almora, Issac Zarazua, Elena Mas-Marza, Juan Bisquert, and Germa Garcia-Belmonte. "Ionic Reactivity at Contacts and Aging of Methylammonium Lead Triiodide Perovskite Solar Cells". In: *Adv. Energy Mater.* 6 (2016), p. 1502246.

[266] Osbel Almora, Antonio Guerrero, and Germa Garcia-Belmonte. "Ionic charging by local imbalance at interfaces in hybrid lead halide perovskites". In: *Appl. Phys. Lett.* 108 (2016), p. 043903.

[267] Keith B. Oldham. "A Gouy-Chapman-Stern model of the double layer at a (metal)/(ionic liquid) interface". In: *J. Electroanal. Chem.* 613 (2008), p. 131.

[268] Shenghao Wang, Yan Jiang, Emilio J. Juarez-Perez, Luis K. Ono, and Yabing Qi. "Accelerated degradation of methylammonium lead iodide perovskites induced by exposure to iodine vapour". In: *Nat. Energy* 2 (2016), p. 16195.

[269] Juan Bisquert. *Nanostructured energy devices: Equilibrium Concepts and Kinetics*. Ed. by Taylor & Francis Group. 6000 Broken Sound Parkway NW, Suite 300, Boca Raton: CRC Press, 2015.

[270] Maria Stromme Mattsson. "Cation intercalation in sputter-deposited W oxide films". In: *Phys. Rev. B* 58 (1998), p. 11015.

[271] Marta Haro, Taeseup Song, Antonio Guerrero, Luca Bertoluzzi, Juan Bisquert, Ungyu Paik, and Germa Garcia-Belmonte. "Germanium coating boosts lithium uptake in Si nanotube battery anodes". In: *Phys. Chem. Chem. Phys.* 16 (2014), p. 17930.

[272] Simon George and N. Krishnamurthy. "Absorption spectrum of iodine vapor-An experiment". In: *Am. J. Phys.* 57 (1989), p. 850.

[273] Dane W. deQuilettes, Wei Zhang, Victor M. Burlakov, Daniel J. Graham, Tomas Leijtens, Anna Osherov, Vladimir Bulovic, Henry J. Snaith, David S. Ginger, and Samuel D. Stranks. "Photo-induced halide redistribution in organic–inorganic perovskite films". In: *Nat. Commun.* 7.11683 (2016), pp. 2–9.

[274] Andrei Buin, Patrick Pietsch, Oleksandr Voznyy, Riccardo Comin, Alexander H Ip, Edward H. Sargent, and Bruce Xu. "Materials Processing Routes to Trap-free Halide Perovskites". In: *Nano Lett.* 14 (2014), p. 6281.

[275] Michael L. Agiorgousis, Yi-Yang Sun, Hao Zeng, and Shengbai Zhang. "Strong Covalency-Induced Recombination Centers in Perovskite Solar Cell Material $CH_3NH_3PbI_3$". In: *J. Am. Chem. Soc.* 136 (2014), p. 14570.

[276] Yongbo Yuan, Jungseok Chae, Yuchuan Shao, Qi Wang, Zhengguo Xiao, Andrea Centrone, and Jinsong Huang. “Photovoltaic Switching Mechanism in Lateral Structure Hybrid Perovskite Solar Cells”. In: *Adv. Energy Mater.* 5 (2015), p. 1500615.

[277] Cheng Li, Antonio Guerrero, Yu Zhong, and Sven Huettner. “Origins and Mechanisms of Hysteresis in Organometal Halide Perovskites”. In: *J. Phys: Condens. Matter* 29 (2017), p. 193001.

[278] Yuchuan Shao et al. “Grain Boundary Dominated Ion Migration in Polycrystalline Organic- Inorganic Halide Perovskite Films”. In: *Energy Environ. Sci.* 9 (2016), p. 1752.

[279] Jae S. Yun, Jan Seidel, Jincheol Kim, Arman Mahboubi Sou ani, Shujuan Huang, Jonathan Lau, Nam Joong Jeon, Sang Il Seok, Martin A. Green, and Anita Ho-Baillie. “Critical Role of Grain Boundaries for Ion Migration in Formamidinium and Methylammonium Lead Halide Perovskite Solar Cells”. In: *Adv. Energy Mater.* 6 (2016), p. 1600330.

[280] Hui Yu, Haipeng Lu, Fangyan Xie, Shuang Zhou, and Ni Zhao. “Native Defect-Induced Hysteresis Behavior in Organolead Iodide Perovskite Solar Cells”. In: *Adv. Funct. Mater.* 26 (2016), p. 1411.

[281] Jizhong Song, Jianhai Li, Xiaoming Li, Leimeng Xu, Yuhui Dong, and Haibo Zeng. “Quantum Dot Light-Emitting Diodes Based on Inorganic Perovskite Cesium Lead Halides ($CsPbX_3$)”. In: *Adv. Mater.* 27 (2015), p. 7162.

[282] Guangru Li et al. “Highly Ef cient Perovskite Nanocrystal LightEmitting Diodes Enabled by a Universal Crosslinking Method”. In: *Adv. Mater.* 28 (2016), p. 3528.

[283] Vikash Kumar Ravi, Ganesh B Markad, and Angshuman Nag. “Band Edge Energies and Excitonic Transition Probabilities of Colloidal CsPbX3 (X= Cl, Br, I) Perovskite Nanocrystals”. In: *ACS Energy Lett.* 1 (2016), p. 665.

[284] Peter W. Shor. “Polynomial-Time Algorithms for Prime Factorization and Discrete Logarithms on a Quantum Computer”. In: *SIAM Review* 41.2 (1999), p. 303.

[285] *A fast quantum mechanical algorithm for database search*. Vol. STOC ’96. 28th. annual ACM Symposium on Theory of computing. ACM New York, 1996.

[286] Charles H. Bennett and Gilles Brassard. “Quantum Cryptography: Public key distribution and coin tossing”. In: *International Conference on Computers, systems and signal processing* 1 (1984), pp. 175–179.

[287] S. Dasgupta, C. H. Papadimitriou, and U. V. Vazirani. *Algorithms*. 1st. Mc Graw Hill Giher Education, 2008.

[288] Ashley Montanaro. “Quantum algorithms: an overviwe”. In: *npj Quantum Information* 2.15023 (2016).

[289] Qi Chen, Nicholas De Marco, Yang (Michael) Yanga, Tze-Bin Song, Chun-Chao Chena, Hongxiang Zhao, Ziruo Hong, Huanping Zhou, and Yang Yanga. "Under the spotlight: The organic—inorganic hybrid halide perovskite for optoelectronic applications". In: *Nano Today* 10 (2015), p. 355.

[290] CHR. KN. MØLLER. "A Phase Transition in Cæsium Plumbochloride". In: *Nature* 180 (Nov. 1957).

[291] CHR. KN. MØLLER. "Crystal Structure and Photoconductivity of Cæsium Plumbohalides". In: *Nature* 182 (Nov. 1958).

[292] Nikolay S. Makarov, Shaojun Guo, Oleksandr Isaienko, Wenyong Liu, Istvań Robel, and Victor I. Klimov. "Spectral and Dynamical Properties of Single Excitons, Biexcitons, and Trions in Cesium-Lead-Halide Perovskite Quantum Dots". In: *Nano Lett.* 16.4 (2016), p. 2349.

[293] Gang cheng Yuan, Cameron Ritchie, Maria Ritter, Sean Murphy, Daniel E. Gomez, and Paul Mulvaney. "The Degradation and Blinking of Single Perovskite Quantum Dots". In: *Phys. Chem. C* 10.1021 (2017).

[294] Juan A. Castañeda, Gabriel Nagamine, Emre Yassitepe, Luiz G. Bonato, Oleksandr Voznyy, Sjoerd Hoogland, Ana F. Nogueira, Edward H. Sargent, Carlos H. Brito Cruz, and Lazaro A. Padilha. "Efficient Biexciton Interaction in Perovskite Quantum Dots Under Weak and Strong Confinement". In: *ACS Nano* 10 (2016), p. 8603.

[295] C. J. Hwang. "I.ifetimes of Free and Bounti Excitons in High-Purity GaAs". In: *Phys. Rev. B* 8.2 (1973), p. 646.

[296] Kenichiro Tanaka, Takayuki Takahash, Takuma Bana, Takashi Kondoa, Kazuhito Uchidab, and Noboru Miurab. "Comparative study on the excitons in lead-halide-based perovskite- type crystals $CH_3NH_3PbBr_3$ $CH_3NH_3PbI_3$". In: *Solid State Communications* 127 (2003).

[297] Jing Li, Laihao Luo, Hongwen Huang, Chao Ma, Zhizhen Ye, Jie Zeng, and Haiping He. "2D Behaviors of Excitons in Cesium Lead Halide Perovskite Nanoplatelets". In: *J. Phys. Chem. Lett.* (2017).

[298] Kevin Wilma, Abey Issac, Zhijian Chen, Frank Würthner Richard Hildner, and Jürgen Köhler. "Tracing Single Electrons in a Disordered Polymer Film at Room Temperature". In: *Phy. Chem. Lett.* 7.1478 (2016).

[299] Rodney Loudon. *The Quantum Theory of Light*. Oxford University Press, 2010.

[300] G. Wrigge, I. Gerhardt, J. Hwang, G. Zumofen, and V. Sandoghdar. "Efficient coupling of photons to a single molecule and the observation of its resonance fluorescence". In: *Nature Physics* 4 (Dec. 2007), 60 EP.

[301] X.T.Zou and L.Mandel. "Photon-antibunching and sub-Poissonian photon statistics". In: *Phys. Rev. A* 41.1 (Jan. 1990), p. 475.

[302] R. Horodecki, P. Horodecki, and M. Horodecki. “Violating Bell inequality by mixed spin-1/2 states: necessary and sufficient condition”. In: *Phys. Lett. A* 200 (1995), p. 340.

[303] B. S. Cirel’son. “Quantum generalizations of Bell’s inequality”. In: *Lett. Math. Phys.* 4 (1980), p. 93.

[304] A. Miranowicz. “Violation of Bell inequality and entanglement of decaying Werner states”. In: *Phys. Lett. A* 327 (2004), p. 272.

[305] D. Cavalcanti, A. Acín, N. Brunner, and T. Vértesi. “All quantum states useful for teleportation are nonlocal resources”. In: *Phys. Rev. A* 87 (2013), p. 042104.

[306] M. Horodecki, P. Horodecki, and R. Horodecki. “General teleportation channel, singlet fraction, and quasidistillation”. In: *Phys. Rev. A* 60 (1999), p. 1888.

[307] J. Grondalski, D. M. Etlinger, and D. F. V. James. “The fully entangled fraction as an inclusive measure of entanglement applications”. In: *Phys. Lett. A* 300 (2002), p. 573.

[308] A. Peres. “Separability criterion for density matrices”. In: *Phys. Rev. Lett.* 7 (1996), p. 1413.

[309] M. Horodecki, P. Horodecki, and R. Horodecki. “Separability of mixed states: necessary and sufficient conditions”. In: *Phys. Lett. A* 223 (1996), p. 1.

[310] L. Masanes. “Asymptotic violation of Bell inequalities and distillability”. In: *Phys. Rev. Lett.* 97 (2006), p. 050503.

[311] Rajarshi Pal and Sibasish Ghosh. “Non-locality breaking qubit channels: the case for CHSH inequality”. In: *Journal of Physics A: Mathematical and Theoretical* 48.15 (2015), p. 155302. URL: http://stacks.iop.org/1751-8121/48/i=15/a=155302.

[312] John Preskill. *Quantum Computation Lecture Notes*. Caltech, 2016. URL: http://www.theory.caltech.edu/%7Epreskill/ph219/index.html#lecture.

[313] Michael A. Nielsen and Isaac L. Chuang. *Quantum Computation and Quantum Information: 10th Anniversary Edition*. Cambridge University Press, 2010.

[314] Y.-H. Kim, S. P. Kulik, and Y. Shih. “Quantum teleportation of a polarization state with a complete Bell State Measurement”. In: *Phys. Rev. Lett.* 86.7 (2000), pp. 1370–1373.

[315] S. Gaertner, H. Weinferter, and C. Kurtsiefer. “Fast and compact multichannel photon coincidence unit for quantum information processing”. In: *Rev. Sci. Inst.* 76 (2005), p. 123108.

[316] D. Branning, S. Bhandari, and M. Beck. “Low cost coincidence-counting electronics for undergraduated quantum optics.” In: *Am. J. Phys.* 77.7 (2009).

[317] Mathieu Chevrier and Giovanni Campanella. “How to build a LIDAR system with a time-to-digital converter”. In: *Analog App. Journal* 1Q (2017), p. 1.

[318] S. Gong, I. Labanca, I. Rech, and M. Ghioni. “A 32-channel photon counting module with embedded auto/cross-correlators for real- time parallel fluorescence correlation spectroscopy”. In: *Rev. Sci. Inst.* 85 (2014), p. 103101.

[319] Wolfgang Becker, ed. *Advanced Time-Correlated single Photon counting Applications*. Vol. 111. Springer Series in Chemical Physics. Switzerland: Springer, 2015.

[320] C. E. Susa and J. H. Reina. “Nonlocal fluctuations and control of dimer entanglement dynamics”. In: *Phys. Rev. A* 82 (2010), p. 042102.

[321] P. G. Kwiat and J. B. Alteper. “Optical technologies for quantum information science”. In: *Proc. SPIE, Quantum Communications and Quantum Imaging* 5161.87 (2004).

[322] C. Spengler and M. Huber. “Entanglement detection via mutually unbiased bases”. In: *Phys. Rev. A* 86.2 (2012), pp. 022311–1.

[323] X.-L. Wang et al. “Experimental Ten-Photon Entanglement”. In: *Phys. Rev. Lett.* 117 (2016), p. 210502.

[324] S. Antonioli, L. Miari, A. Cuccato, M. Crotti, I. Rech, and M. Ghioni. “8-channel acquisition system for time-correlated single-photon counting”. In: *Rev. Sci. Inst.* 84 (2013), p. 064705.

[325] Wolfgang Becker. *The bh TCSPC Handbook*. Sixth. Nahmitzer Damm 30, 12277 Berlin: Becker & Hickl GmbH, Dec. 2014.

[326] Joseh R. Lakowicz. *Principles of Fluorescence Spectroscopy*. Third. Center for Fluorescence Spectroscopy, University of Maryland School of Medicine, Baltimore: Springer, 2010.

[327] Matteo Crotti, Ivan Rech, and Massimo Ghioni. “Four Channel, 40 ps Resolution, Fully Integrated Time-to-Amplitude Converter for Time-Resolved Photon Counting”. In: *IEEE J. Solid-State circuits* 47.3 (Mar. 2012), p. 699.

[328] Stephan Henzler. *Time-to-Digital Converters*. Springer Series in Advanced Microelectronics 29. Lehrstuhl für Technische Elektronik Arcisstr. 21, 80290 München, Germany: Springer, 2010.

[329] M. Lampton and R. Raffanti. “A high-speed wide dynamic range time-to-digital converter”. In: *Rev. Sci. Inst.* 65.11 (Nov. 1994), p. 3577.

[330] Minjae Lee and Asad A. Abidi. “A 9 b, 1.25 ps Resolution Coarse–Fine Time-to-Digital Converter in 90 nm CMOS that Amplifies a Time Residue”. In: *IEEE J. Solid-State circuits* 43.4 (Apr. 2008), p. 769.

[331] Bojan Markovic, Simone Tisa, Federica A. Villa, Alberto Tosi, and Franco Zappa. "A High-Linearity, 17 ps Precision Time-to-Digital Converter Based on a Single-Stage Vernier Delay Loop Fine Interpolation". In: *IEEE Trans. Circ. Syst.—I* 60.3 (Mar. 2013), p. 557.

[332] *10-ps resolution hybrid Time to Digital Converter in a 0.18 μm CMOS technology*. New Circuits and Systems Conference (NEWCAS), 2014 IEEE 12th International. Trois-Rivieres, QC, Canada: IEEE, Oct. 2014.

[333] Min Zhang, Hai Wang, and Yan Liu. "A 7.4 ps FPGA-Based TDC with a 1024-Unit Measurement Matrix". In: *Sensors* 17.865 (Feb. 2017), p. 18.

[334] Jian Song, Qi An, and Shubin Liu. "A High-Resolution Time-to-Digital Converter Implemented in Field-Programmable-Gate-Arrays". In: *IEEE Transactions on Nuclear Science* 53.1 (Feb. 2006), p. 236.

[335] Ion Vornicu, Ricardo Carmona-Galan, and Angel Rodriguez-Vazquez. "A CMOS Imager for Time-of-Flight and Photon Counting Based on Single Photon Avalanche Diodes and In-Pixel Time-to-Digital Converters". In: *Romanian Journal of Information Science and Technology* 17.4 (2014), p. 354.

[336] Ryan M. Field, Simeon Realov, and Kenneth L. Shepard. "A 100 fps, Time-Correlated Single-Photon-Counting-Based Fluorescence-Lifetime Imager in 130 nm CMOS". In: *IEEE J. Solid-State circuits* 49.4 (Apr. 2014), p. 867.

[337] D. Branning and M. Beck. "An FPGA-based module for multiphoton coincidence counting". In: *Proc. SPIE, Advanced photon Counting Techniques VI* 8375 (2012).

[338] D. Branning and S. Khanal. "Note: Scalable multiphoton coincidence-counting electronics". In: *Rev. Sci. Inst.* 82 (2011), p. 016102.

[339] D. Branning. *Private Communication*.

[340] C. Zhang, W. Li, Y. Hu, T. Yang, G. Jin, and X. Jiang. "48-channel coincidence counting system for multiphoton experiment". In: *Rev. Sci. Inst.* 87 (2016), p. 113107.

[341] *DE0-Nano user manual*. v2.0. Terasic technologies. HsinChu, Taiwan, 2013.

[342] Texas Instruments. *Datasheet SN74F08 Quadruple 2-Input Positive-AND Gate*. (Visited on).

[343] Texas Instruments. *Datasheet SN54F153, SN74F153 Dual 1 of 4 Data Selectors/Multiplexers*. (Visited on).

[344] Texas Instruments. *datasheet SN54F32, SN74F32 Quadruple 2-Input Positive-OR Gates*. (Visited on).

[345] Texas Instruments. *datasheet SN54F30, SN74F30 8-input Positive-NAND Gates*. (Visited on).

[346] *Morphi-IC-II Datasheet*. 1.04. Future Technology Devices International Ltd (FTDI). Centurion Business Park, Glasgow, United Kingdom, 2011.

[347] *Cyclone IV Device Handbook*. Altera Corporation. San Jose, CA 95134, USA: IEEE, 2016.

[348] Kenneth Posse. *1687-2014 IEEE Standard for Access and Control of Instrumentation Embedded within a Semiconductor Device*. IEEE Computer Society, 2014.

[349] G. B. Ko, H. S. Yoon, S. Il Kwon, S. J. Hong, D. S. Lee, and J. S. Lee. "Development of FPGA-based Coincidence Units with Veto Function". In: *Biomed. Eng. Lett.* 1 (2011), pp. 27–31.

[350] *XBeeTM/XBee-PROTM OEM RF Modules*. M100232. MaxStream Inc. 355 South 520 West, Suite 180, 2007.

INDEX